NASA/CP—1998–207891

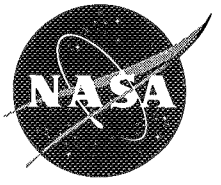

Third United States Microgravity Payload: One Year Report

P.A. Curreri, Compiler
Marshall Space Flight Center, Marshall Space Flight Center, Alabama

D. McCauley, Compiler
University of Alabama in Huntsville, Huntsville, Alabama

C. Walker, Compiler
Universities Space Research Association, Huntsville, Alabama

Proceedings of a conference held in
Washington, DC, February 10–11, 1997

November 1998

The NASA STI Program Office...in Profile

Since its founding, NASA has been dedicated to the advancement of aeronautics and space science. The NASA Scientific and Technical Information (STI) Program Office plays a key part in helping NASA maintain this important role.

The NASA STI Program Office is operated by Langley Research Center, the lead center for NASA's scientific and technical information. The NASA STI Program Office provides access to the NASA STI Database, the largest collection of aeronautical and space science STI in the world. The Program Office is also NASA's institutional mechanism for disseminating the results of its research and development activities. These results are published by NASA in the NASA STI Report Series, which includes the following report types:

- TECHNICAL PUBLICATION. Reports of completed research or a major significant phase of research that present the results of NASA programs and include extensive data or theoretical analysis. Includes compilations of significant scientific and technical data and information deemed to be of continuing reference value. NASA's counterpart of peer-reviewed formal professional papers but has less stringent limitations on manuscript length and extent of graphic presentations.

- TECHNICAL MEMORANDUM. Scientific and technical findings that are preliminary or of specialized interest, e.g., quick release reports, working papers, and bibliographies that contain minimal annotation. Does not contain extensive analysis.

- CONTRACTOR REPORT. Scientific and technical findings by NASA-sponsored contractors and grantees.

- CONFERENCE PUBLICATION. Collected papers from scientific and technical conferences, symposia, seminars, or other meetings sponsored or cosponsored by NASA.

- SPECIAL PUBLICATION. Scientific, technical, or historical information from NASA programs, projects, and mission, often concerned with subjects having substantial public interest.

- TECHNICAL TRANSLATION. English-language translations of foreign scientific and technical material pertinent to NASA's mission.

Specialized services that complement the STI Program Office's diverse offerings include creating custom thesauri, building customized databases, organizing and publishing research results...even providing videos.

For more information about the NASA STI Program Office, see the following:

- Access the NASA STI Program Home Page at ***http://www.sti.nasa.gov***

- E-mail your question via the Internet to help@sti.nasa.gov

- Fax your question to the NASA Access Help Desk at (301) 621–0134

- Telephone the NASA Access Help Desk at (301) 621–0390

- Write to:
  NASA Access Help Desk
  NASA Center for AeroSpace Information
  800 Elkridge Landing Road
  Linthicum Heights, MD 21090–2934

NASA/CP—1998–207891

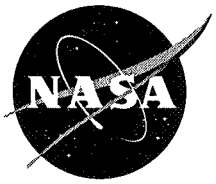

Third United States Microgravity Payload: One Year Report

P.A. Curreri, Compiler
Marshall Space Flight Center, Marshall Space Flight Center, Alabama

D. McCauley, Compiler
University of Alabama in Huntsville, Huntsville, Alabama

C. Walker, Compiler
Universities Space Research Association, Huntsville, Alabama

Proceedings of a conference held in
Washington, DC, February 10–11, 1997

National Aeronautics and
Space Administration

Marshall Space Flight Center

November 1998

Acknowledgments

The superb efforts and dedication of the STS–75 payload and orbiter crew, the mission and program managers, and mission operations personnel were critical to the completion of the mission's objectives and are sincerely appreciated. We wish to thank the Office of Life and Microgravity Science and Applications (OLMSA) and the Microgravity Research Division (MRD) at NASA Headquarters for their support, in particular the USMP–3 Program Scientist, Dr. Stephen Davison, without whom the success of the mission would not have been possible. We also wish to thank the NASA Marshall Space Flight Center's Public Affairs Office for their help in publicizing the results of the USMP–3 mission as well as all of the authors for contributing to this document.

Available from:

NASA Center for AeroSpace Information
800 Elkridge Landing Road
Linthicum Heights, MD 21090–2934
(301) 621–0390

National Technical Information Service
5285 Port Royal Road
Springfield, VA 22161
(703) 487–4650

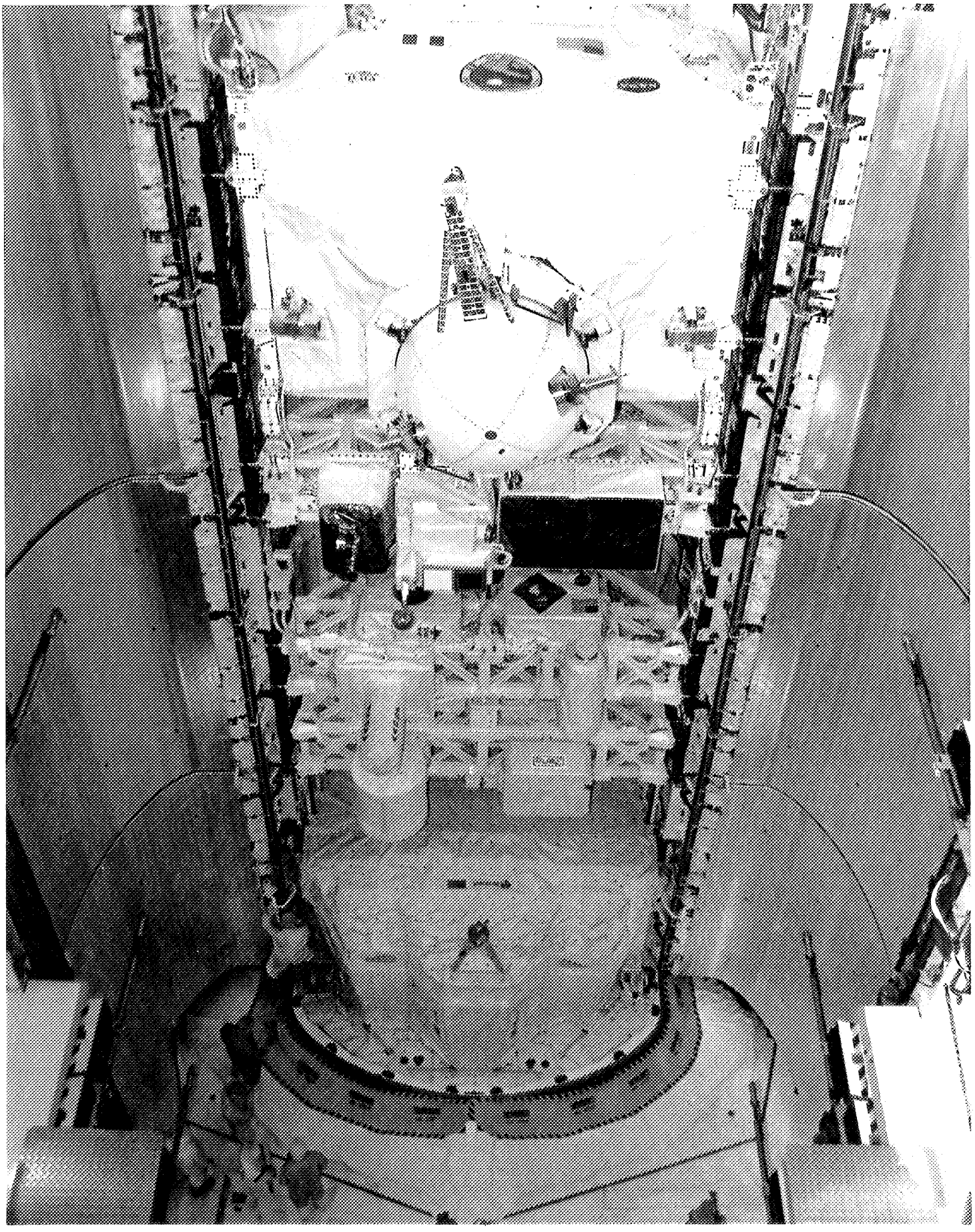

Zero
A
A
D
S
F

Table of Contents

THIRD UNITED STATES MICROGRAVITY PAYLOAD: ONE YEAR REPORT

Peter A. Curreri

USMP-3 Mission Scientist

George C. Marshall Space Flight Center

Overview

The Third United States Microgravity Payload (USMP-3) Space Shuttle mission was launched February 22, 1996 and landed March 9, 1996. The mission lasted 15 days and the Shuttle crew performed extensive microgravity science research during that time. The Principal Investigators (PI's) for the mission submitted science reports of their research findings to the Mission Scientist for USMP-3, and those reports were compiled into the USMP-3 One Year Report. The purpose of this report is to inform the microgravity science community and the public of the results of the experiments flown on the Shuttle mission.

The USMP-3 One Year Report represents the culmination of many years of sustained effort on the part of the investigators, mission management, and support personnel and is intended not only for the scientific community, but also for general public awareness and education. This mission gave the microgravity science community outstanding research opportunities to verify results obtained in previous flights, and to perform new experiments which contributed substantially and uniquely to the technological and commercial knowledge of the United States and its international partners. The results obtained and the lessons learned from this and future missions will lead us into a new era of microgravity research, to the Space Station and beyond.

USMP-3

The USMP-3 mission was launched on the 19th flight of the Space Shuttle *Columbia*, STS-75, on February 22, 1996. It carried four major microgravity experiments as well as the SAMS and OARE accelerometer systems. The USMP-3 experiments utilized microgravity to increase the fundamental understanding of materials processes: three studied formation of solid from the melt and one studied the critical point of a noble gas. The science payload also included three Middeck Glovebox investigations which studied the effect of microgravity on combustion processes. While the Glovebox investigations required intense crew involvement, the major USMP-3 experiments were controlled almost completely by telescience.

USMP-3 utilized two Mission-Peculiar Experiment Support Structures (MPESS) which were connected together and mounted behind the other STS-75 primary payload, the Tethered Satellite System (TSS). Science of opportunity by the USMP investigations was achieved during the TSS operations. After the TSS was lost on flight day-4, the USMP investigations went on to receive about 10 days of microgravity as the primary payload. The TSS safety

requirements mandated that the Shuttle crew operate with dual shifts. Thus, unlike previous USMP missions, there were no "quiet periods" (where the total crew was asleep) which would have allowed the microgravity investigations to perform the most sensitive microgravity experiments without crew-induced disturbances. In order to provide quiet periods for the USMP experiments, a concept for a crew display to monitor accelerations and provide real-time crew feedback was developed with the Payload Commander, Dr. Franklin Chang-Diaz, and was implemented during the mission. The results, as will be presented in the SAMS section, were comparable to "quiet time" accelerations during crew sleep. Thus, one lesson learned was that the crew acceleration feedback display could be quite effective and should be considered for use on future microgravity missions.

The major USMP-3 experiments were the Advanced Automated Directional Solidification Furnace (AADSF), the Isothermal Dendritic Growth Experiment (IDGE), Matérial pour l'Étude des Phenomènes Intéressants de la Solidification sur Terre et en Orbite ("Apparatus for the Study of Interesting Phenomena of Solidification on Earth and in Orbit") (MEPHISTO), and the Critical Fluid Light Scattering Experiment (Zeno).

The AADSF experiment was involved in gaining new understanding of fundamental crystal growth and its interaction with gravity. The furnace operated superbly. As the first crystal started to form, the temperature signature of the crystal nucleation was much more subdued than observed in Earth-based experiments. The telescience capability built into the AADSF was used to remelt and save the sample. Post-flight X-ray measurements showed void, or large pore, formation in the crystals, which has not been observed in Earth-grown crystals.

The IDGE experiment examined the formation of dendrites, which are tiny, pine tree-shaped crystals that commonly form as molten materials solidify. Dendrites are a concern in the production of most commercially important metal alloys because their structure has a strong influence on the mechanical properties the material. Previous studies on USMP-2 indicated that small deviations from theory in the growth rate and tip radius of the dendrites were due to the microgravity environment. USMP-3 data during the varying gravity resulting from the TSS being reeled out found that the variations are instead due to specimen size.

The MEPHISTO experiment studied how small disturbances in gravity can affect the production of metals and alloys by firing the Shuttle primary control jets and observing the impact. The experiment demonstrated that when the angle of the growing metal relative to the accelerations was carefully controlled the damage to the crystals by the resulting fluid flow could be eliminated. This and other solidification experiments from the USMP-3 provided unique data that is being applied to improve processes for making products ranging from alloys for airplane turbine blades to electronic materials.

The Zeno experiment used its exquisite temperature control of ± 3 micro-degrees to explore the behavior of xenon near its critical point. On USMP-3 the investigators were able to control the density changes by changing the temperature, which, although its impact is very small on Earth, became a major factor in the low gravity of the Shuttle. This allowed them to achieve their goal of getting stable, equilibrium measurements of the microscopic hydrodynamic fluctuations in the sample. At the end of the flight they were able to record and observe the sharpest phase

transition ever observed near room temperature; the phase boundary was observed with a precision of ± 20 micro-degrees.

The Glovebox experiments consisted of three combustion processes investigations:

- The Comparative Soot Diagnostics (CSD). The CSD investigation attempted to understand the soot production processes from flames burning in microgravity. NASA has flown fire detectors on Skylab and the Space Shuttle and has included them in the design for the *International Space Station (ISS).* CSD data will help improve their design by determining soot morphology in low gravity.

- The Radiative Ignition and Transition to Spread Investigation (RITSI). The RITSI investigation found that the flame spread behavior with the external flow velocity in microgravity showed a completely opposite trend from that found in normal gravity. The investigators also observed suprisingly complex smoldering growth patterns in microgravity.

- The Forced Flow Flame spreading Test (FFFT). The FFFT investigation studied the effects of flow speed and paper thickness for the flat paper samples, as well as the effect of flow speed, flow direction, and initial fuel temperature for the cylindrical fuels.

Key USMP-4 Personnel

Peter A. Curreri
NASA Marshall Space Flight Center
USMP-3 Mission Scientist

Stephen Davison
Universities Space Research Association/NASA HQ
USMP-3 Program Scientist

Sherwood Anderson
NASA Marshall Space Flight Center
USMP-3 Mission Manager

Rose Cramer
NASA Marshall Space Flight Center
USMP-3 Payload Operations Lead

Page intentionally left blank

USMP-3 Acronyms

AADSF	Advanced Automated Directional Solidification Furnace (USMP-2, USMP-3)
ARC	NASA Ames Research Center (Moffett Field, CA)
CCD	Charge-Coupled Device
CENG	Centre d'Etudes Nuclaires National de Grenoble (Grenoble, France)
CFD	Computational Fluid Dynamics
CMC	Center for Macromolecular Crystallography (UAB)
CMDS	Consortium for Materials Development in Space (UAH)
CMMR	Center for Microgravity and Materials Research (UAH)
CNES	Centre Nationale d'Études Spatiales ("National Center for Space Studies," French Space Agency)
CNRS	Centre National de la Recherche Scientifique (France)
CSD	Comparative Soot Diagnostics
DARA	Deutsche Agentur für Raumfahrtangelegenheiten ("German Agency for Space Affairs," German Space Agency)
DLS	Dynamic Light Scattering
ESA	European Space Agency
FFFT	Forced Flow Flamespreading Test
GBX	Glovebox
GCEL	Ground Control Experiments Laboratory (NASA MSFC)
IDGE	Isothermal Dendritic Growth Experiment
JPL	Jet Propulsion Laboratory (Pasadena, CA, managed by the California Institute of Technology)
JSC	NASA Johnson Space Center (Houston, TX)
KSC	NASA Kennedy Space Center (Cape Canaveral, FL)
LaRC	NASA Langley Research Center (Hampton, VA)
LeRC	NASA Lewis Research Center (Cleveland, OH)
LOS	Loss of Signal
MEPHISTO	Matérial pour l'Étude des Phenomènes Intéressants de la Solidification sur Terre et en Orbite ("Apparatus for the Study of Interesting Phenomena of Solidification on Earth and in Orbit")
MET	Mission Elapsed Time
MGBX	Middeck Glovebox
MPESS	Mission Peculiar Experiment Support Structure (Shuttle)

MSAD	Microgravity Science and Applications Division (NASA MSFC, also used to be the acronym for an OLMSA division at NASA Headquarters before name was changed to "Microgravity Research Division" (still Code UG))
MSFC	NASA Marshall Space Flight Center (Huntsville, AL)
NASA	National Aeronautics and Space Administration
NRC	National Research Council
OARE	Orbital Acceleration Research Experiment
PI	Principal Investigator
PIMS	Principal Investigator Microgravity Services (NASA LeRC)
POCC	Payload Operations and Control Center (NASA MSFC)
RITSI	Radiative Ignition and Transition to Spread Investigation
RPI	Rensselaer Polytechnic Institute (Troy, NY)
SAMS	Space Acceleration Measurement System
SEM	Scanning Electron Microscope
STS	Space Transportation System (Shuttle/external tank/solid rocket booster system, also a Shuttle mission designation)
TBE	Teledyne Brown Engineering
TEM	Transmission Electron Microscope
UAB	University of Alabama at Birmingham
UAH	University of Alabama in Huntsville
USMP-1	First United States Microgravity Payload (STS-52 Shuttle mission, launched in October 1992)
USMP-2	Second United States Microgravity Payload (STS-62 Shuttle mission, launched in March 1994)
USMP-3	Third United States Microgravity Payload (STS-75 Shuttle mission, launched in February 1996)
USMP-4	Fourth United States Microgravity Payload (STS-87 Shuttle mission, scheduled for launch in November 1997)
ZENO	Critical Fluid Light Scattering Experiment

Mission Information

Mission Designation:	STS-75 (75th Shuttle mission)
Orbiter:	*Columbia* (19th flight for this Shuttle)
Orbit Inclination:	28.45 degrees
Orbit Altitude:	160 nautical miles (184 statute miles)
Number of Orbits:	251 (6.5 million miles)
Major Payloads:	USMP-3 and TSS-1R
Launch:	February 22, 1996 @ 3:18 p.m. EST
Landing:	March 9, 1996 @ 8:58 a.m. EST at KSC
Mission Duration:	15 days, 17 hours, 41 minutes, 25 seconds (15/17:41:25)
Crew:	
Commander:	Lt. Col. Andrew M. Allen, U.S. Marine Corps (3rd mission)
Pilot:	Lt. Col. Scott J. Horowitz, U.S. Air Force (1st mission)
Payload Commander:	Dr. Franklin R. Chang-Diaz, Ph.D. (5th mission)
Mission Specialist:	Maurizio Cheli, ESA (1st mission)
Mission Specialist:	Claude Nicollier, ESA (3rd mission)
Mission Specialist:	Dr. Jeffrey A. Hoffman, Ph.D. (5th mission)
Payload Specialist:	Dr. Umberto Guidoni, Ph.D., Italian Space Agency (1st mission)

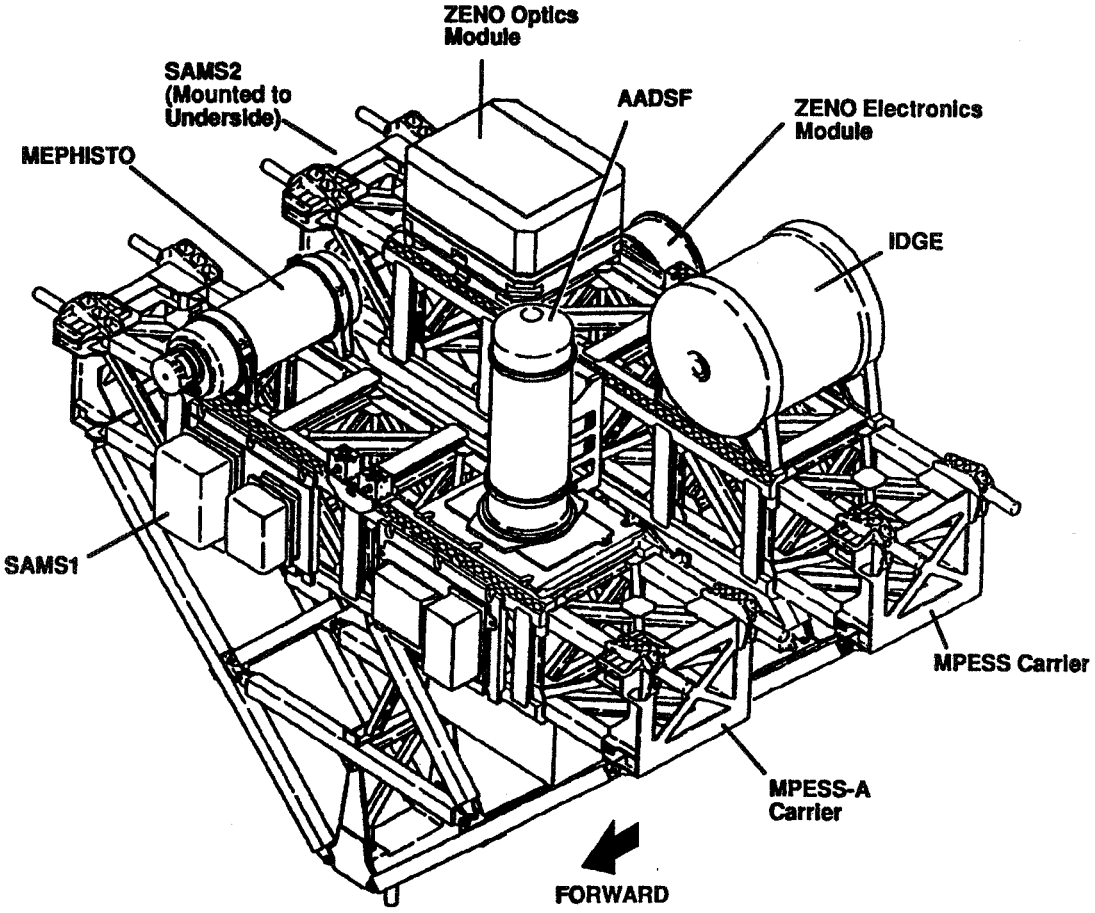

USMP-3 PAYLOAD

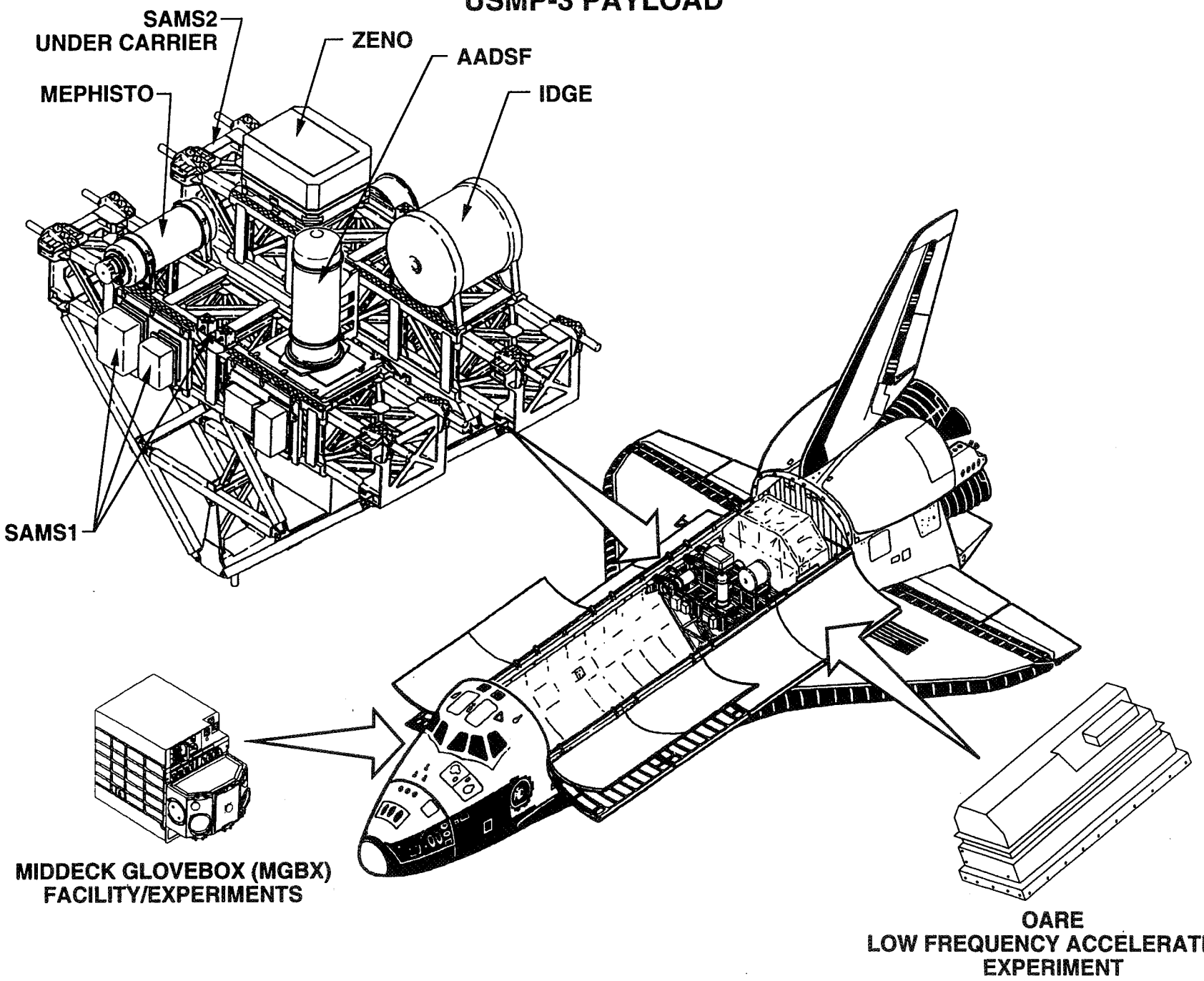

Study of Interesting Solidification Phenomena on the Ground and in Space (MEPHISTO)

J.-J. Favier, J. Iwan D. Alexander†, J.-P. Garandet,
Comissariat à l'Energie Atomique, DTA/CEREM/DEM/SPCM, 17 Rue des Martyrs, Grenoble Cedex 9, France

†Center for Microgravity and Materials Research, University of Alabama in Huntsville, Huntsville, Alabama 35899, USA

Abstract

Real-time Seebeck voltage variations in a Sn-Bi melt during directional solidification in the MEPHISTO spaceflight experiment flown on the USMP-3 mission, can be correlated with well characterized thruster firings and an Orbiter Main System (OMS) burn. The Seebeck voltage measurement is related to the response of the instantaneous average melt composition at the melt-crystal interface. This allowed us to make a direct comparison of numerical simulations with the experimentally obtained Seebeck signals. Based on the results of preflight and real-time computations, several well-defined thruster firing events were programmed to occur at specific times during the experiment. In particular, we simulated the effects of the thruster firings on melt and crystal composition in a directionally solidifying Sn-Bi alloy. The relative accelerations produced by the firings were simulated by impulsive accelerations of the same magnitude, duration and orientation as the requested firings. A comparison of the simulation results with the Seebeck signal indicates that there is a good agreement between the two. This unique opportunity allows us, for the first time, to quantitatively characterize actual g-jitter effects on an actual crystal growth experiment and to properly calibrate our models of g-jitter effects on crystal growth.

Introduction

The MEPHISTO program is the result of a cooperative effort that involves the French nuclear and space agencies Comissariat à l'Energie Atomique, CEA - Centre National d'Etudes Spatiales, CNES) and the National Aeronautics and Space Administration (NASA). Six space flights on the USMP carrier were initially planned, with odd-numbered missions being the responsibility of the French scientific teams and the even-numbered missions being the responsibility of the US. During the first flight of MEPHISTO in October 1992, bismuth-doped tin samples (Sn:0.5 at.% Bi) were used and experiments were carried out both below and above the morphological stability threshold. Exciting results were obtained [1] that opened new perspectives for research.

The first scientific objective of the USMP-3 flight was to investigate the g-jitter induced solutal segregation in planar front solidification. To do so, we requested well controlled gravity perturbations, mainly in the form of Primary Remote Control System (PRCS) burns. The other main scientific objective was to track the morphological stability threshold (i.e. the instability where the growth front goes from planar to cellular) with the finest accuracy possible. In comparison with the first flight, the USMP-3 alloys were slightly more concentrated (1.5% at. Bi), in order to check a possible soluto-convective effect. It should be noted that, in contrast, both the USMP-2 and USMP-4 MEPHISTO flights, (Professor Abbaschian, University of Florida, PI) featured bismuth based alloys with low tin concentrations. MEPHISTO is basically a directional solidification furnace, where three samples are simultaneously processed. An original point is that there are in fact two heating/cooling subsystems [2,3]; one of them is maintained at a fixed position to provide a reference interface, whereas the other is allowed to move for solidification and melting of the alloy. Sample #˘1 is dedicated to a measurement of the Seebeck voltage between the two ends, meaning that the system acts as its own thermocouple, with a "cold" and a "hot" reference junction (respectively the moving and fixed interfaces). The Seebeck voltage is then a measure of the undercooling at the growth front, a key feature being that the signal is obtained in real time. It is thus possible to run many experimental cycles on the same sample, which in turn allows to check the reproducibility of the process and to ensure a better accuracy of the results. On sample #˘2, the position and the velocity of the moving interface are obtained from an one line resistance measurement. At the end of the experimental cycle, a quench

freezes the structure of the solid-liquid front. Peltier pulse marking performed on sample #˘3 allow the determination of the shape of the interface at given time intervals. Moreover, thermocouples present in the liquid phase for both samples #˘2 and #˘3 are used to determine the temperature gradient and possible thermal fluctuations. The MEPHISTO facility ran for 312 hours, including 216 hours dedicated to scientific operation. During that time period, 24 solidification/fusion cycles were carried out. Five growth rates were preprogrammed (1.7, 3.7, 5.7, 12 and 24 mm/h) before the flight, but, thanks to teleoperation, we were able to use different growth rates to track the morphological stability threshold. For controlled gravity perturbations, we obtained 9 PRCS burns, ranging in duration from 10 to 25 seconds. In addition, an OMS burn and a 360° X-axis roll were also performed (see Table I). Last but not least, it should be noted that no anomalies were detected during the mission.

During the first flight of the MEPHISTO directional solidification experiment on NASA's USMP-1 mission in 1992, the impact of sudden effective gravity perturbations were clearly evidenced [1]. Real-time Seebeck voltage variations across a Sn-Bi melt showed a distinct variation that can be correlated with thruster firings (Fig. 1) [1]. The Seebeck voltage measurement is related to the response of the instantaneous average melt composition at the melt-solid interface [4]. This permitted a direct comparison of numerical simulations (and acceleration data) with the Seebeck signals obtained on USMP-1. Motivated by the results of the comparison, we used numerical simulations to predict the response of the Seebeck signal to thruster firings of various magnitudes and durations. The behavior of the signal is directly related to changes in interfacial composition caused by thruster-induced convective disturbances. Motivated by the observations made on USMP-1, one of the objectives of the USMP-3 MEPHISTO experiments was to quantitatively characterize g-jitter effects on an actual crystal growth experiment. To plan the USMP-3 MEPHISTO experiments, simulations were carried out for different solidification rates and g-jitter scenarios.

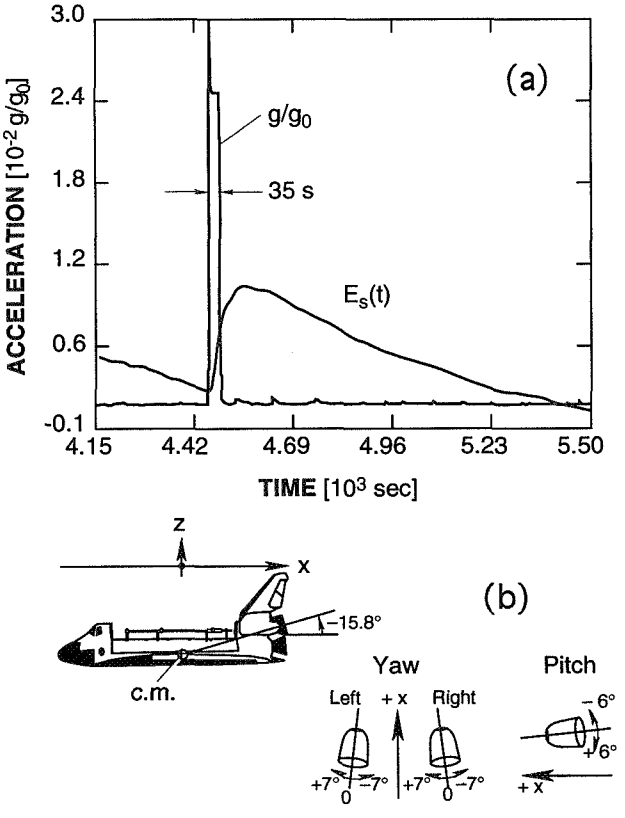

Fig. 1 (a) Acceleration vs. time for the OMS burn recorded on USMP-1 and the associated Seebeck signal , $E_S(t)$ [1]. (b) OMS engine alignment with the Orbiter.

There were several differences between the USMP-3 and USMP-1 experiments. First, a more concentrated alloy was solidified on USMP-3, and, second, Primary Reaction Control System (PRCS) thruster burns were requested at particular times during four separate growth runs. The Seebeck signal was recorded continuously and down-linked in real-time to the MEPHISTO experiment team at NASA's Marshall Space Flight Center. This allowed for quantification of the effects of "g-jitter" on convective-diffusive transport in the melt through the changes in average interfacial composition obtained from the Seebeck measurement. In addition, guided by SAMS acceleration data, we carried out simulations for comparison with the recorded Seebeck signals. The effects of thruster firings on the average composition was monitored in six separate experiments and for eleven separate acceleration disturbance events. Selected results from our ongoing post-flight analysis are described below.

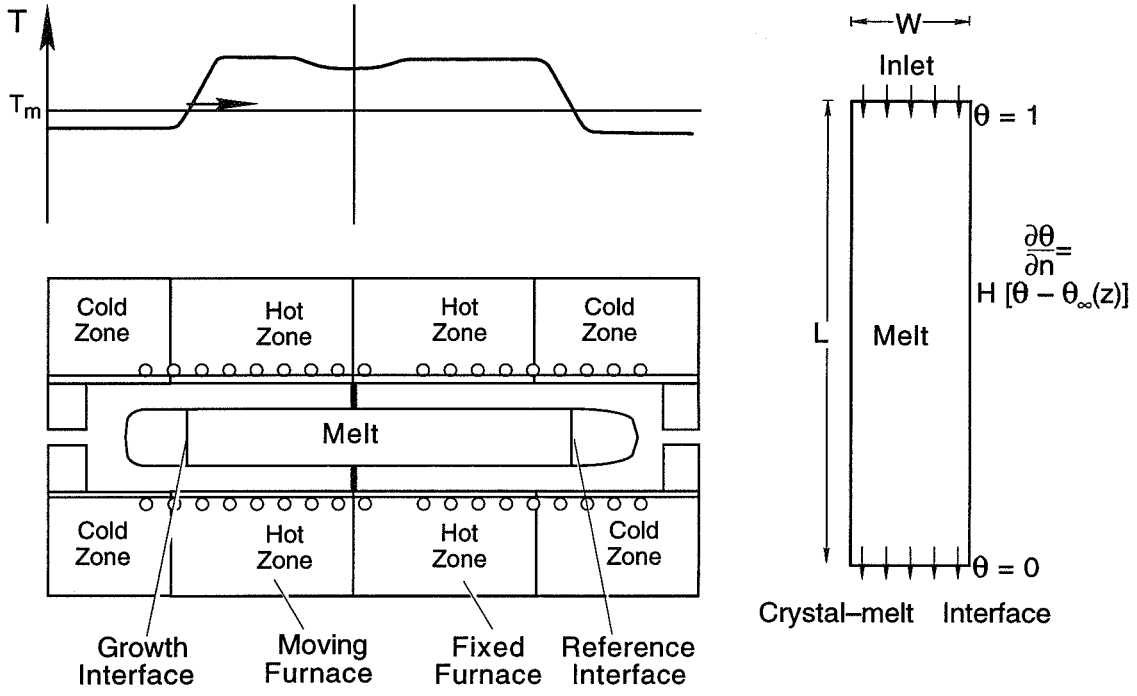

Fig. 2 The MEPHISTO set-up (bottom-left), temperature profile (top left) and computational model (right). T_m denotes the melting temperature.

Approach

A sketch of the experiment set-up is shown in Fig. 2. There are two furnaces. One is fixed. The other is translated. The applied temperature profile shown in Fig. 2 leads to a central cylindrical melt volume bounded by a moving and a stationary (or reference) solid-liquid interface. The melt composition at the moving and the stationary reference interfaces is not the same. For Sn-Bi there is a dependence of melting temperature on concentration. Thus, it follows that the melting temperature at the two interfaces will also be different. The Seebeck effect gives rise to a small but measurable voltage difference between these two interfaces. Measurement of this voltage difference allows us to determine the average temperature and, thus, the average composition of at the growing interface. The MEPHISTO set-up and the Seebeck measurements are discussed in more detail in [4].

The numerical model used to simulate the response of the tin-bismuth melt to particular types of g-jitter has been described elsewhere [5-7]. The essential features are outlined below. Solidification takes place as the furnace is translated along the ampoule (see Fig. 2). Directional solidification due to the furnace translation is simulated by supplying a two-component melt of

bulk composition c_∞ at a constant velocity Vg at the top of the computational space (inlet), and withdrawing a solid of composition $c_s = c_s(x,t)$ from the bottom (See Fig. 2). The crystal-melt interface is located at a distance L from the inlet; the width of the ampoule is W. The temperature at the interface is taken to be T_m, the melting temperature of the crystal, while the upper boundary is held at a higher temperature T_h. In the actual experiment, the temperature gradient along the ampoule wall ahead of the growing interface was essentially linear (195 K cm-1). Thus, we set a linear temperature gradient along the wall in the simulations. Furthermore, since we wish to confine our attention to compositional nonuniformities caused by buoyancy-driven convection, rather than variations resulting from non-planar crystal-melt interfaces, the interface is held flat. We expect that, given the large temperature gradient, changes in melting temperature due to compositional non-uniformity will not lead to significant changes in interface shape due to interfacial compositional inhomogeneity. Furthermore, because of the melt's low Prandtl number and the low magnitude accelerations, convection does not lead to significant deviations of the temperature from the conductive state, Thus, changes in the interface shape due to changes in the thermal field will be negligible. In an actual experiment, owing to the finite length of the ampoule, there is a gradual decrease in length of the melt zone during growth. In this model, transient effects related to the change in melt length are ignored. Since the MEPHISTO experiments involve melt lengths that far exceed the ampoule diameter, this does not preclude us from calculating the compositional transient. That is, we can start the calculations by solidifying from an initially uniform composition melt.

The dimensionless governing equations governing coupled convective-diffusive heat mass and species transfer in the melt were assumed to be those for a Boussinesq fluid with a linear dependence of density on temperature and composition. The boundary conditions imposed were those corresponding to plane front directional solidification at a translation rate Vg with a linear temperature gradient applied to the ampoule walls. Solute was preferentially rejected at the crystal-melt interface (k = 0.27 for this Sn-Bi alloy). The equations were solved using a Chebyshev spectral method.

Results

The PRCS firings produced an impulse acceleration with the largest component parallel to the solid liquid interface. Figure 3 shows the actual (uncorrected for drift) and predicted Seebeck signal for an experiment subject to two thruster burns (25 seconds and 10 seconds in duration) that produced an acceleration oriented parallel to the crystal-melt interface (i.e. perpendicular to the ampoule axis. Before the first burn, the Seebeck signal decreases monotonically. Immediately following the burn, the signal increases rapidly and reaches a maximum about 100 seconds after the termination of the burn. The signal then decreases slowly and eventually takes on almost the same slope that it had before the burn. The same behavior occurs following the second burn. After translation of the furnace was stopped. Solidification then ceases and the Seebeck signal increases as the average interfacial concentration decreases. Note that the actual Seebeck measurement shown has not been corrected for drift and, thus, the voltage does not return to its original value. For the response of the Seebeck signal predicted by computer simulation, there is an immediate rapid response to each of the firings. In addition, we see that the time taken for the Seebeck signal to reach a maximum value is approximately the same for the computed and measured signals.

Discussion

There is considerable interest in the effects of spacecraft residual acceleration, or "g-jitter" on experiments conducted in the low-gravity environment of a spacecraft, particularly since the object of conducting many of the experiments in low gravity is to avoid the effects of gravitational acceleration on earth. Understanding these effects is important when considering the design of orbital experiment facilities, the choice of orbital attitude for space laboratories and platforms, the optimal choice of experiment operating conditions and materials, as well as the scheduling of crew activities, quiet periods, pointing maneuvers and thruster firings used for attitude control.

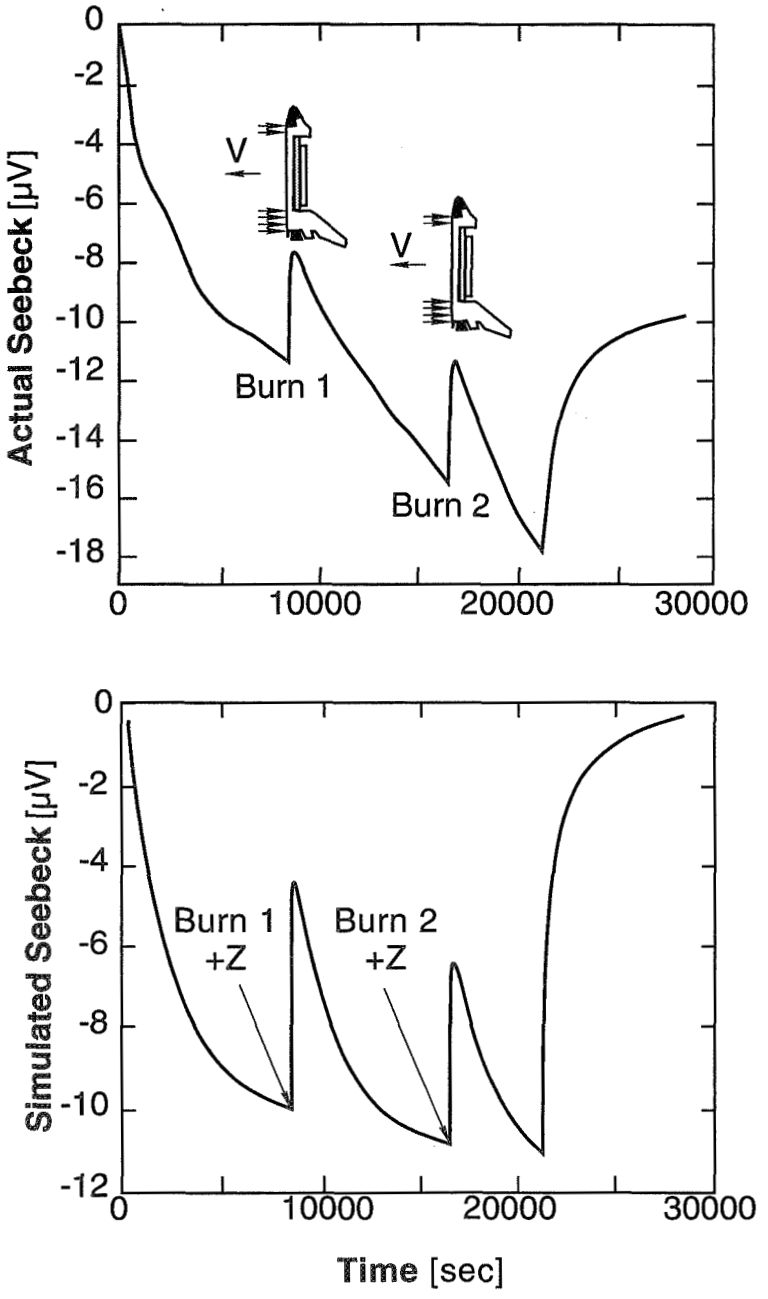

Fig. 3 (a) Actual and (b) predicted Seebeck signal for a 25 second and 15 second burn oriented parallel to the crystal-melt interface.

The USMP-3 MEPHISTO experiments permitted a quantitative correlation between well-characterized g-jitter recorded by spacecraft accelerometers and the response of a directionally solidifying alloy. Furthermore, the comparison of the results of the experiment with the predictions of numerical simulations carried out on the Alabama Research and Education Network's C-90 Supercomputer, will allow us to verify the degree to which such simulations can accurately predict experiment sensitivity to g-jitter accelerations. Without quantitative experimental verification, such predictions are of limited use and could lead to unnecessary design restrictions, an undesirable low gravity environment, or unsuitable experiment operating conditions

Ongoing work involves corrections of the raw Seebeck data, analysis of residual acceleration data measured by NASA's Space Acceleration Measurement System, and refinement of the computational simulations. This unique experiment showed use of simulations to assist in changes in experiment strategy greatly enhances the scientific return from limited opportunity spaceflight experiments. It is expected that ongoing work will yield benchmark comparisons between measured and predicted residual acceleration effects.

Acknowledgments

This work was carried out within the framework of the GRAMME agreement between CNES and the CEA, and was supported by the National Aeronautics and Space Administration through Grant NAG3-1740 and by the State of Alabama through the Center for Microgravity and Materials Research the Alabama Research and Education Network.

References

[1] J.J. Favier, J.P. Garandet, A. Rouzaud and D. Camel, J. Crystal Growth 140 (1994) 237.

[2] A. Rouzaud, J. Comera, P. Contamin, B. Angelier, F. Herbillon and J.J. Favier, J. Crystal Growth, 129 (1993) 173

[3] A. Rouzaud, J.J. Favier and D. Thevenard, Adv. Space Res., 8 (1988) 49

[4] J.-J. Favier, J.P. Garandet, A. Rouzaud and D. Camel, J. Crystal Growth, 113 (1991) 21.

[5] J.-J. Favier and A. Rouzaud, Revue Phys. Appl. 22 (1987) 713.

[6] J.I.D. Alexander, J. Ouazzani and F. Rosenberger, J. Crystal Growth 97 (1989) 285.

[7] J.I.D. Alexander, S. Amiroudine, J. Ouazzani and F. Rosenberger, J. Crystal Growth 113 (1991) 21.

[8] J.I.D. Alexander, in Materials and Fluids under Low Gravity, L. Ratke, H. Walter and B. Feuerbacher, eds.(Springer, Berlin, 1995) p. 95-102.

[9] J.I.D. Alexander, J.P. Garandet, J.J. Favier and A. Lizèe, "G-jitter effects on segregation during directional solidification of tin-bismuth in the MEPHISTO furnace facility", 97-02, in press J. Crystal Growth, 1997.

SECOND FLIGHT OF THE ZENO EXPERIMENT ON USMP-3

Robert W. Gammon, J. N. Shaumeyer, Matthew E. Briggs, Hacène Boukari, David Gent
Institute for Physical Science and Technology, Univ. of Maryland, College Park

and

R. Allen Wilkinson
NASA Lewis Research Center, Cleveland, Ohio

S2-25
011595
366209
P24

Gammon
Phone: 301-405-4791
FAX: 301-314-9404
email: rg2@umail.umd.edu

Shaumeyer
Phone: 301-805-4545
FAX: 301-805-4538
email:jeff.sha@jnt.com

Briggs
Phone: 301-581-9990
FAX: 301-581-4801
email: meb@mail.physics.utah.edu

Boukari
Phone: 301-405-4792
FAX: 301-314-9404
email:hb@roissy.umd.edu

Wilkinson
Phone: (216)-433-2075
FAX: (216)-433-8660
email: aw@lerc.nasa.gov

ABSTRACT

The second flight of the Zeno experiment in the USMP-3 flight has shown successful control of density perturbations near the window surfaces. These density changes were demonstrated to be arising from the rate of temperature change in the sample cell during the flight. These effects could be controlled by using decreasing ramp rates as Tc was approached. The cell window interference was carefully recorded to provide data about the phase of the interference close to the critical point and the effective window reflectivity. Correlograms were recorded from 500 mK down to 2 mK at 24 temperatures, 383 correlograms in all. The efforts to get closer were prevented by a long (>two week time constant) decay of a 1.3% density error caused by local heating from the 17μW laser beam. The phase boundary was located with unprecedented precision of ± 20μK. The complete experiment sequence was done with ground commanding and uploaded script files, bypassing the original autonomous-mode program sequence. More details of the experiment Science Requirements, the personnel, apparatus, and results are displayed on the Zeno homepage at http://www.zeno.umd.edu.

INTRODUCTION

All fluids exhibit universal, anomalous behavior in their thermodynamic and transport properties in the region of their liquid-vapor critical point. This is most dramatic when one looks at a critical fluid in an optical cell and sees the sample become an opaque with opalescence. This cloudiness is the consequence of the enormous thermodynamic fluctuations occurring in the fluid. The renormalization group calculations about critical thermodynamics have shown how to calculate the equilibrium divergences and how to relate different critical systems into universality classes. The theoretical calculation of transport processes such as thermal conductivity and viscosity in critical systems is much less developed.[1]

The goal of the Zeno experiment is to measure the decay rate of critical fluctuations in xenon close enough to the critical point to determine the limiting behavior. The experiment uses photon-correlation light-scattering spectroscopy to measure the characteristics of the density fluctuations as the critical point is approached. (Critical properties of xenon are: Tc=17.57 ∞C, Pc=58.4 atm, critical density=1.110 gm/cc.) The primary measurements are photon correlation functions, digitally processed in real time from the detected scattered-photon pulse stream. We also monitor the sample transmission which provides data about the local density and the sample turbidity when we get close to the critical point.

In this second flight we followed a timeline with only cooling steps of decreasing size and cooling rate in order to avoid problems found in the first flight with the locally perturbed density near the sample cell windows. We also took enough data far from Tc to characterize the sample cell reflectivity and thus provide a way to extract an accurate correlation range from the measured intensities. This data should also allow the analysis of the first flight data despite its density uncertainties.

In the following report we will give an overview of the apparatus, review the problems found in the first flight, describe the plan for the second flight, look at the second flight performance. This performance is summarized by the timeline plots of temperature, scattering intensity, and turbidity data. We show the improved control of density errors, the correlogram data, and our efforts so far to extract the correlation range. The surprise of a large density error from laser heating is discussed. Finally we show plots resulting from the slow temperature scan to locate the phase boundary (phase transition temperature). The reader is urged to look at the USMP-2 One Year Report[2] to see a discussion of the first Zeno flight and a bibliography of the field.

THE APPARATUS

The optical layout is shown in Fig. 1. The sample cell sat at the center of a three-concentric-cylinder thermostat (TH). This thermostat could be set with 1 μK resolution and it gave control of 1.5 μK RMS for periods of four hours (sampling 2/min with 5 sec. time constant). The shutters S 1-2 were used with one open and one closed to give two paths through the sample for the He-Ne LASER beam (633 nm), split by B1. Together with the filters F 1-2, two different intensities were available for the light scattering: 17 μW and 1.7 μW. The lenses L 1-2 focused the laser waist into the sample. The lenses L 2-4 imaged the scattering volume onto the pinhole

field stops A 2-4. The PD 1-2 are photodiodes used to measure the laser intensity before and after the sample by sampling behind the partial mirrors M 2-3. The photon counting detectors were the photomultipliers PMT 1-2. All these optical components were mounted on a 10 cm thick optical-honeycomb table and placed inside a temperature controlled (±0.1K on orbit), dry nitrogen filled, aluminum box. Overall external dimensions of the optics module were 102x84x56 cm^3. The box had a radiation panel on the top through which heat energy flowed to allow active control of the box temperature. The remaining outside surfaces were covered with multi-layer insulating blankets.

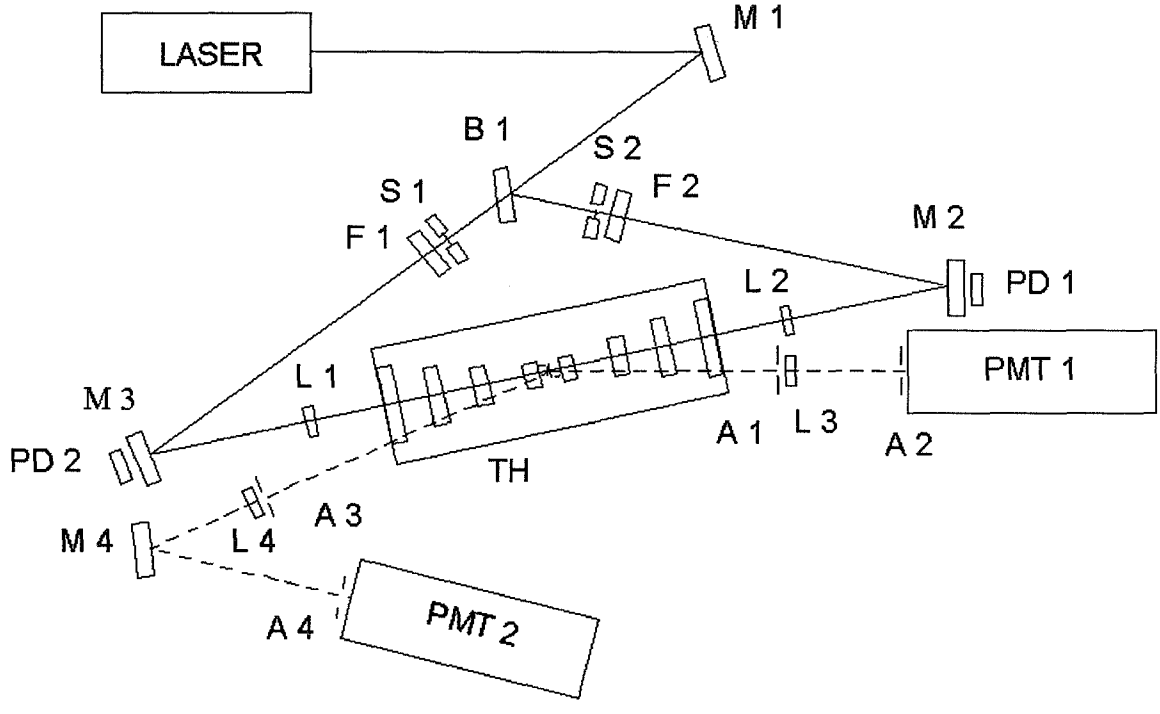

Fig. 1 Zeno optical layout. Components: He-Ne Laser, Mirrors M 1-4, Beam Splitter B 1, Shutters S 1-2, Filters F 1-2, Photodiodes PD 1-2, Lenses L 1-4, Apertures A 1-4, Photomultipliers PMT 1-2, and Thermostat TH. The sample cell is in the center of the three shell thermostat. The scattering angles are approximately 12 ° and 168 ° for either beam path chosen by shutter.

The sample cell was of unique design. A cross-sectional view is shown in Fig. 2. It featured stepped ("top-hat") windows which allowed a large sample volume (0.7 cm) while allowing the beams down the axis to pass through only a thin, 100 μm sheet of the fluid sample. The thin section limits the multiple scattering from the sample to less than 1% in our experiments. In the cell flown the windows were an epoxied stack of a larger sapphire widow and a smaller fused quartz window with AR coatings on the outer surfaces and no coatings on the inner surfaces next to the sample. All surfaces were superpolished. The fluid seals (to 70 bar) were crushed copper knife edges machined on the copper flanges. The remaining body parts were copper with some indium used to assure good thermal mating of the parts. The cell was filled to within 0.1 % of

the critical density, estimated by the symmetry of the sample volume and the centering of the meniscus when 2 mK below Tc. The filling and sealing valve is built into the cell wall.

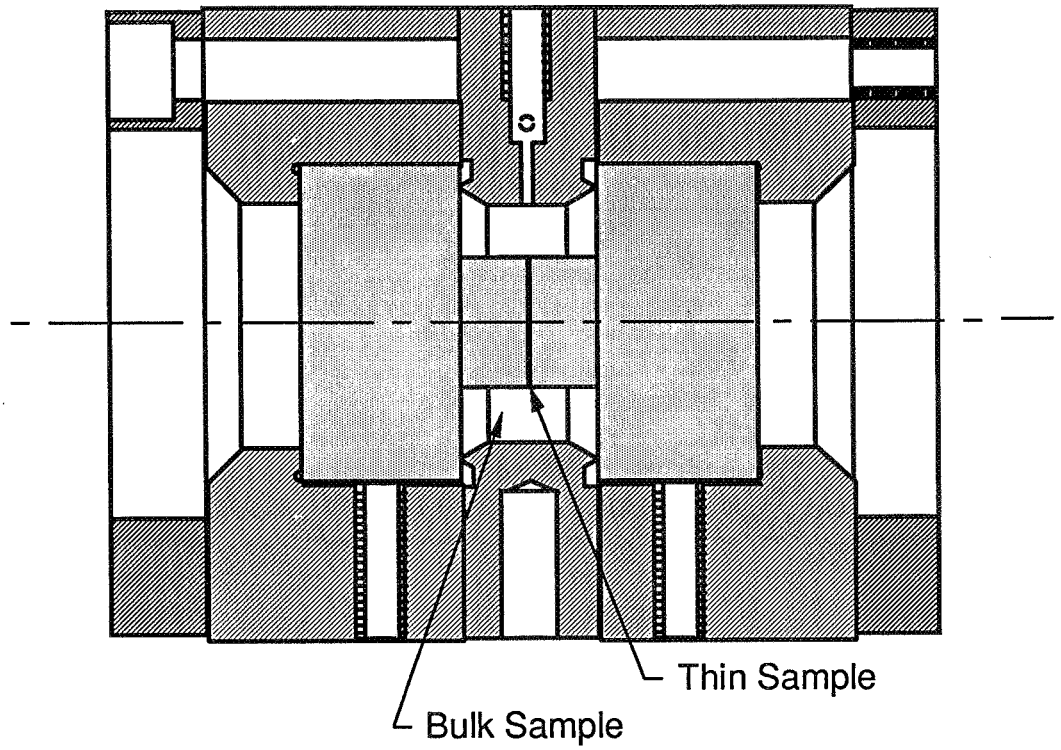

Fig. 2 Cross-section of the Zeno sample cell. Cylindrical sample wall flange is copper and is in mechanical/thermal contact with the copper window holders. The seals are crushed knife edges machined on the wall flange. The filling and sealing valve is built into the cell wall. The spacing of the inner window surfaces is 110 ± 1 μm in the central region. The outside dimensions are 3.8 cm dia. by 4.3 cm long.

The temperature control and measurement is based on using AC bridges which compare a thermistor and stable resistor (1 ppm/K) ratio with the ratio from a computer controlled inductive voltage divider. There are three nested, controlled aluminum cylinders providing the temperature control and setting a final gradient across the sample cell of < 1μK/cm. A fourth transformer is switched between five different half bridges, on command, to monitor the temperatures of the sample, the three controlled shells and a Pt calibration thermometer on the sample cell. The least count (digitization) resolution of the measurements is 1 μK and the measured RMS is 1.5 μK, just larger than the least count.

LESSONS FROM THE FIRST FLIGHT

The first flight featured an active timeline, mostly run by the autonomous mode of the flight computer. Three scanned searches for Tc were performed as well as one very long "zig-zag" search[1]. A temperature of 1 K from Tc was used for sample density homogenization. Temperature steps were done as fast as the thermostat would allow (up to 4.6 K/hr) or accelerated up to 60 mK/hr for steps less than 10 mK. During the flight we were puzzled and troubled by the fact that the transmission of the sample seemed to be drifting. There were also

very strong density over-shoot transients during temperature changes. Post-flight measurements showed that the instrument was reporting real sample property drifts. Further measurement and analysis showed that the interference effects from the inner cell windows were providing an extremely sensitive and useful check of the deviations in local sample density; we could see density changes less than 0.01%. We eventually concluded that we had managed to get the local density of the sample at the laser beam off by 1-2% from the critical density by our aggressive timeline and incomplete homogenization following the crossings to the two-phase region.

PLAN FOR THE SECOND FLIGHT

Thus, we made our plans for the second flight on the basis of testing for equilibration when 4 K from Tc ("mixing"), making sure that we did not cross into the two-phase region until the end of the experiment, a slow scan search for the phase boundary, and to limit the rate of temperature change so that we kept the density errors from lagging window surface temperatures to < 0.1%. This required using controlled ramps between temperature points with ever lower slopes. In the course of pre-flight testing we found that we could use much slower scanning rates during Tc searches and we eventually settled on rates of -100 μK/hr as a compromise rate for the search.

SECOND FLIGHT TIMELINE

During the second flight we operated with the flight computer in a paused state and controlled the sequence with a combination of uploaded sequence scripts and ground commanding. We actually carried out the planned timeline. The only changes from the ground baseline were that we waited until the drifts in the transmission (turbidity) signal corresponded to < 0.1%/hr before taking data or moving to next temperature. We equilibrated and took measurements at: 4K, 1.4K, 750 mK, 300 mK, 200 mK, 100 mK, 56 mK, 30 mK, 18 mK, 10 mK, 5.6 mK, 3 mK, 1.8 mK, 1.0 mK, 560 μK, 300 μK, and 180 μK. These temperatures are temperature distance above the nominal value of Tc. During the mission we used the data in hand to refine our estimate of the location of Tc on our temperature scale.

The timeline and experiment history is well illustrated by the flight data in Fig. 3, Fig. 4, and Fig. 5. Fig. 3 shows the sequence of temperatures seen by the sample over the course of the mission. In this log plot, the temperature steps and slopes all look the same but they are logarithmically decreasing. Fig. 4 shows the forward scattered intensity over the mission sequence. The sudden jump in count rate at Mission Elapsed Time day 10, hour 7:00 [MET 10/7:00] comes from the scheduled laser intensity change made at that point (sitting at 1 mK from Tc). The intensities following this change show very little drift. Fig. 5 shows that after the laser power was lowered from 17 μW to 1.7 μW, the turbidity jumped up and then began a strong, uncontrollable drift downward. We have concluded that this drift was real (though never seen on the ground at a power change!) and due to a low density region that had developed from laser heating of the inner window surfaces. When the laser power was changed, the density began moving back towards the average (critical) density. By that time the sample temperature was so close to Tc that this was going to take weeks to relax away. Unfortunately there were only four days of the mission left so we plunged on, taking the planned data. We were also

making needed adjustments in our estimate of the Tc location based on the data in hand (turbidity, intensity and decay rates).

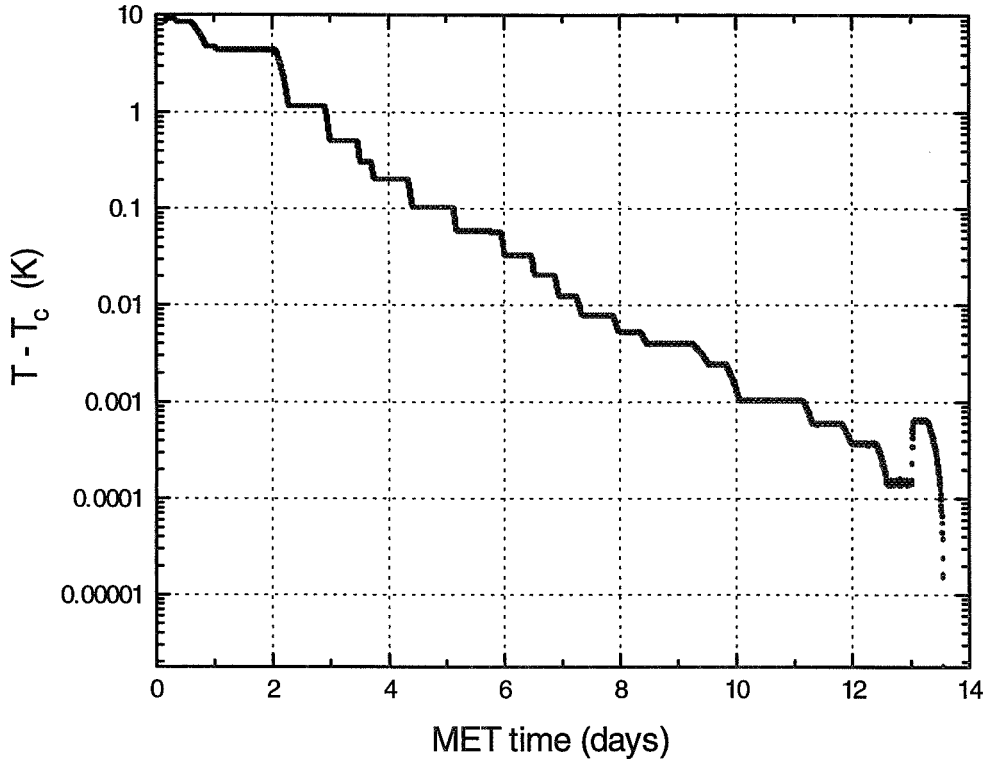

Fig. 3 The temperature timeline for the second Zeno flight. Notice that the sample did not cross into the two phase region until the last day of the mission.

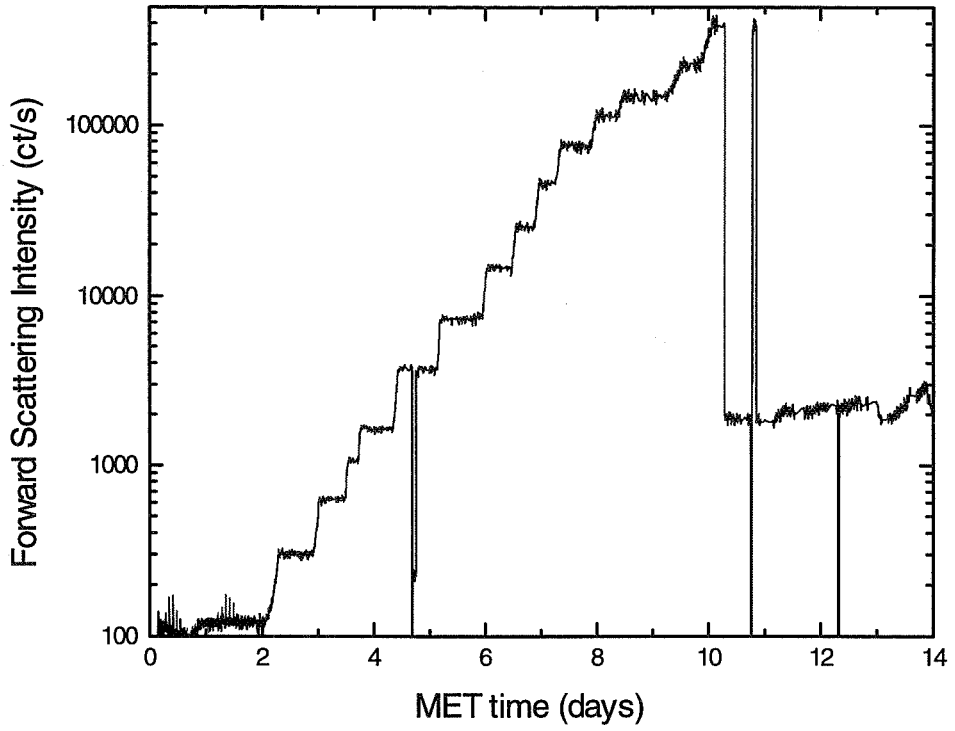

Fig. 4 Scattering intensity (photon count rate) versus Mission Elapsed Time (MET). At MET day 10 hour 7:00 the laser path was switched and the power lowered from 17 μW to 1.7 μW. The path change means that this detector began looking at backscattered light after this time.

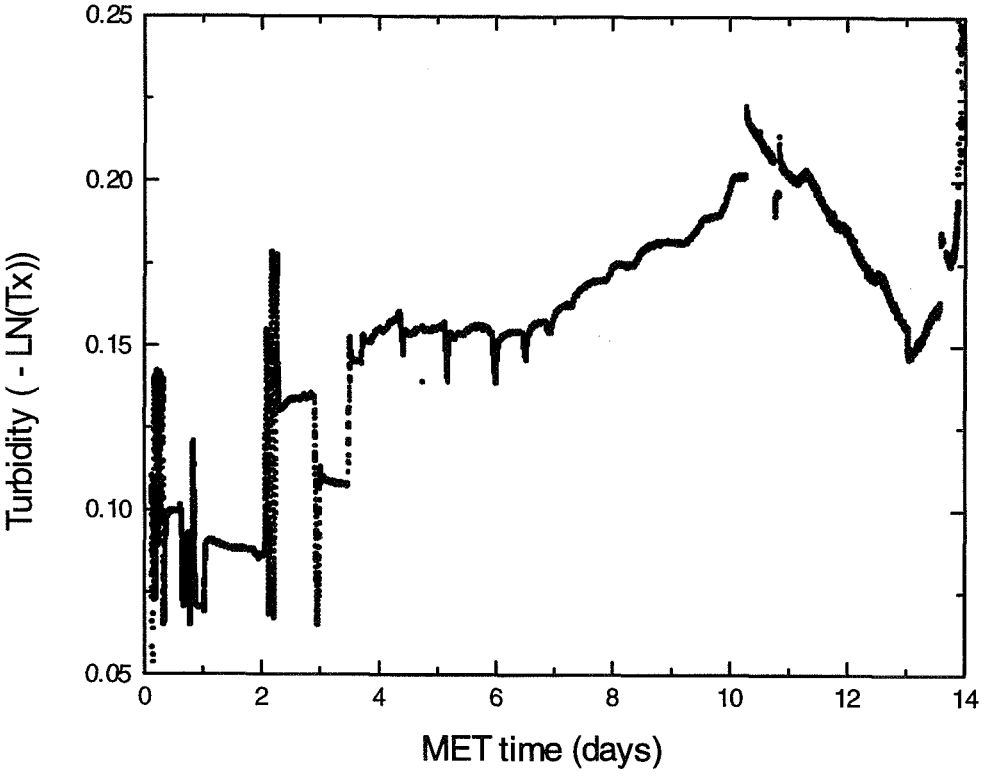

Fig. 5 Turbidity measurements over the mission. This is actually the turbidity-path-length product calculated from the natural log of the transmission Tx. A change of 0.01 in "turbidity" corresponds to a 1% change in Tx. Notice the dramatic response of this signal at the time of the path change/laser power change at MET day 10, hour 7:00 and the indication of phase separation on MET day 15.

DENSITY MONITORING

Fig. 6 shows a magnified section of the turbidity data from MET day 2. This plot shows the interference fringes from the windows. It also shows how the temperature scanning was stopped at positions of maximum slope so that the sensitivity of the interference was maximized for local density changes. In the first 10 days of the mission, with the laser power fixed at 17 μW, we could routinely achieve our goal of turbidity drifts of ≤ 0.001 /hr. After the power change, there was only a steady drift of the signal indicating a fairly large density error with very long time constant.

Fig. 7 is another section of turbidity data from MET days 4-8 that shows a phenomenon which is accentuated in low gravity. The figure shows the fairly large density transients occurring during

and following controlled ramps between temperatures. These transients are much smaller on the ground. The ramps used did not completely avoid density transients but they were small enough at each step that within a few hours the turbidity signal would again become stable (defined as equilibrium).

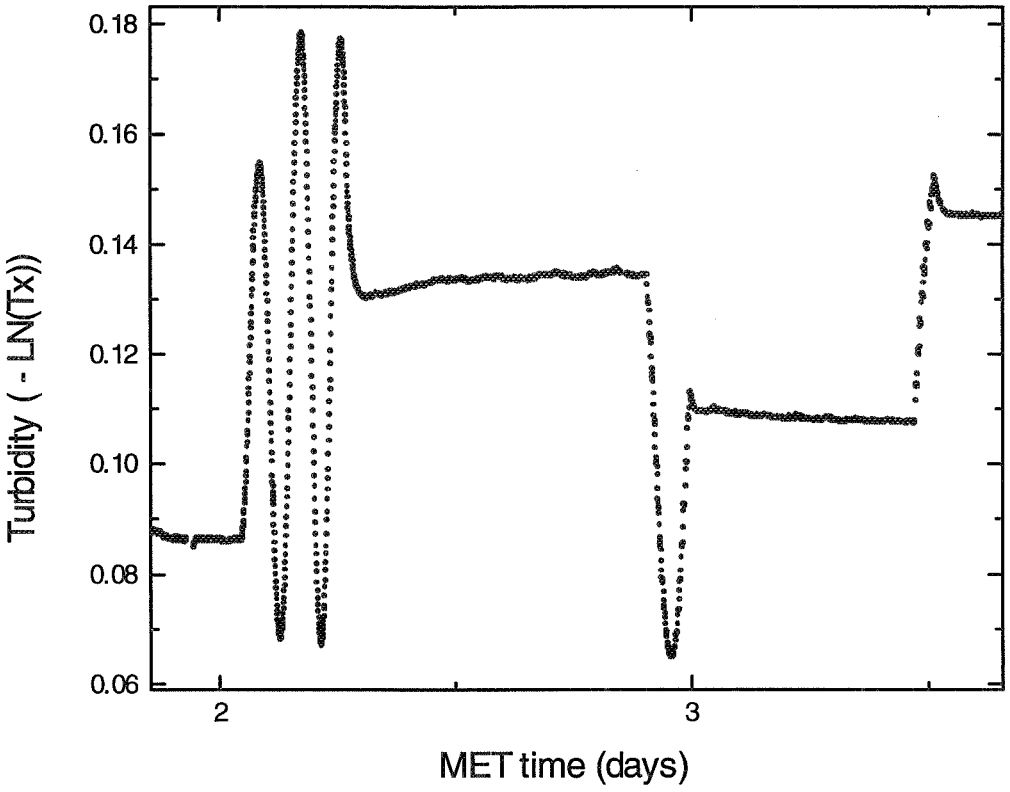

Fig. 6 Turbidity during large temperature scan, far from Tc, showing the interference fringes from the cell windows. By stopping the temperature scan near positions of maximum fringe slope, high sensitivity to local density changes could be realized. The horizontal sections are at times when the scanning was stopped to verify the equilibrium of the local density.

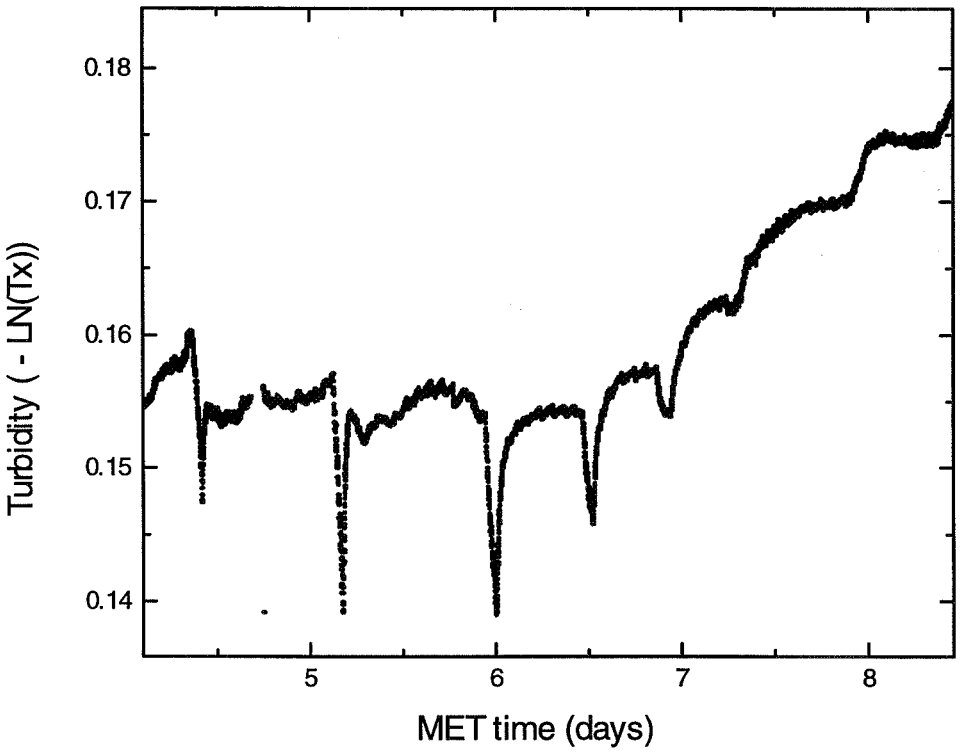

Fig. 7 Density transients during and following temperature step ramps during the mission. Approximately MET days 4 to 8.

We made a quantitative study of the density transients observed on some temperature changes during the mission. An example is shown in Fig. 8. Here the thermal expansion contribution has been subtracted and the residual phase interpreted as due to density changes. Thus we can plot $\delta\rho/\rho_c$ during and following a temperature change, in this case from 500 mK to 300 mK. This change was done with a sequence of 10 steps, 6 minutes apart. Notice that each step can be distinctly seen in the response of the fluid fluctuations. This is a striking demonstration of the effect of the surface film density changes occurring during the temperature changes; the laser beam crosses essentially only fluid which is in such a film. We were delighted to see the good agreement between the calculated density dynamics, modeled with numerical solutions of the adiabatic effect equations for a critical fluid.[3] The input to the model are the dimensions of the sample volume, the properties of critical xenon, and the measured temperature of the cell wall during the ramp. The comparison is absolute, without scaling. Attempts to model this effect for terrestial measurements have so far failed because of convective flows which quickly smear the wall induced density changes in the adiabatic expansion layers.

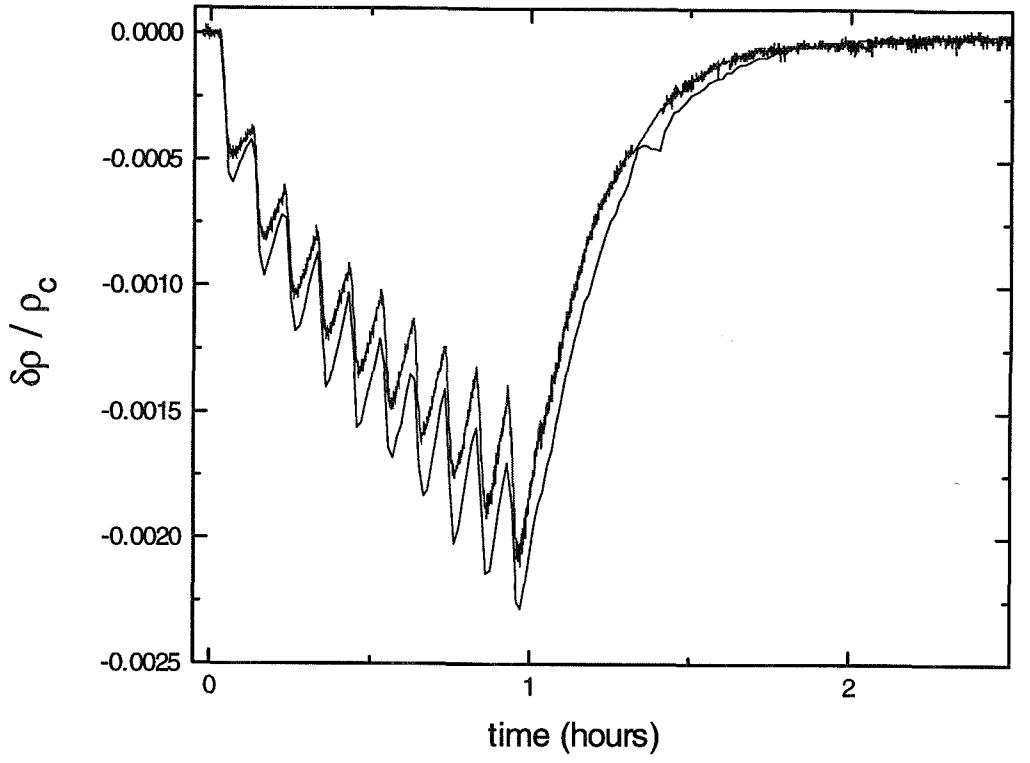

Fig. 8 Comparison of calculated and measured density perturbations due to a temperature ramp applied to sample cell wall. The ramp was from 500 mK to 300 mK from Tc, occurring at MET day 3, hour 11:22. This event appears in Fig. 6 as the last event and shows a large overshoot. The ramp consisted of 10 steps of 20 mK each over an hour interval. The comparison is absolute, without any scaling. The smooth curve is calculated based on the adiabatic equations for a hypercompressible fluid. The noisy curve gives the measurements.

With this background in using our "window-interferometer", we are certain of the interpretation of the drifting turbidity signals following dropping the laser power. We have looked carefully at our baseline data taken before and after the mission. There is no indication of this local heating. Thus we were surprised to see this strong effect during the mission. We believe that the build up of low density around the window hot spots is hidden on the ground by convective flows in the vertical sheet of the thin fluid sample. We estimate the temperature rise from the 48 ppm surface absorption from the two surfaces to be about 1.9 μK. Unfortunately, this small temperature change can produce more than 1.3 % local density error in the part of sample being probed by the laser scattering, when the temperature reaches 1 mK from Tc.

MEASURED CORRELATION FUNCTIONS

Precision measurements of the fluctuation decay rates, Γ, for two supplementary scattering angles were made. A total of 383 valid correlograms were recorded at 24 termperatures from 500 mK down to 2 mK. They were recorded in groups of 15 or more at each temperature point. They were recorded in the dual mode allowing both the forward and backward correlograms to be recorded simultaneously. An example of the correlograms produced by our flight adapted, ALV-digital correlator is shown in Fig. 9 The figure shows both forward and backward scattering correlograms which were computed and recorded simultaneously using 1.7 μW of laser power at a temperature of "2 mK" (see below) from Tc. Notice the clear presence of forward scattering dynamics in the backscattering correlogram. This is due to window reflections and is accounted for carefully in the fitting analysis. There is also a small amount of backscattering in the forward scattering correlogram which is also treated in the fitting functions. The signal-to-noise is good, even with this low laser power, due to the very strong scattering close to Tc.

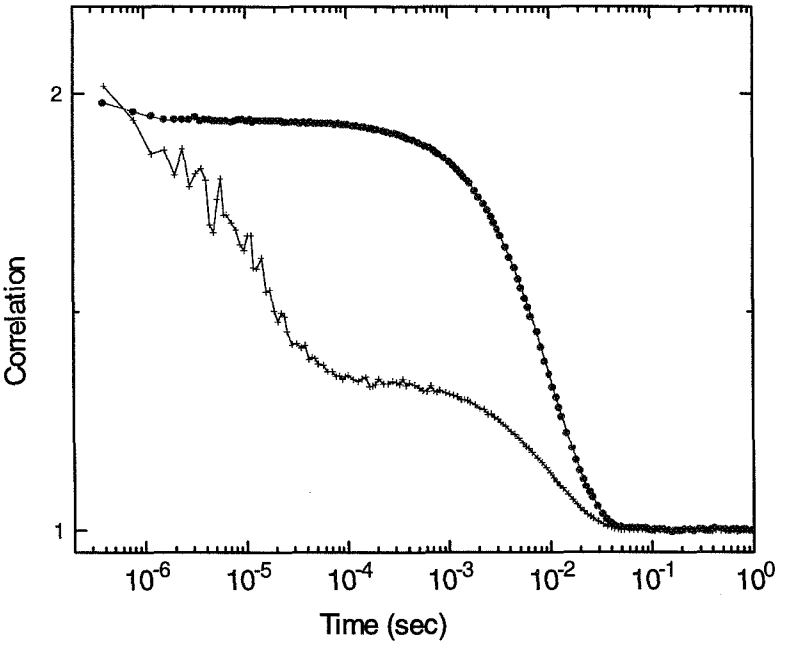

Fig. 9 Correlogram computed and recorded by the ALV correlator in the Zeno instrument during the second flight. Laser power 1.7 mW. The round point data symbols are from forward scattering and the + symbols are from back scattering. Temperature "2 mK" above Tc. The forward scattering has the slower decay rate so drops down to the background correlation at longer times. The "faster" fluctuations are seen in backscattering. Notice the clear presence of forward scattering dynamics in the backscattering correlogram from the window reflection.

Fig. 10 shows a set of forward scattering correlograms from the second flight covering the total range of temperatures. At temperatures above 100 mK the noise increases as expected due to shot-noise limitations at the 17 μW power used. The fluctuation lifetimes (inverse of the decay rates) are approximately at the time where the correlogram falls from 2 to 1. Notice the wide range of lifetimes covered in the experiment and shown in this semi-logarithmic plot.

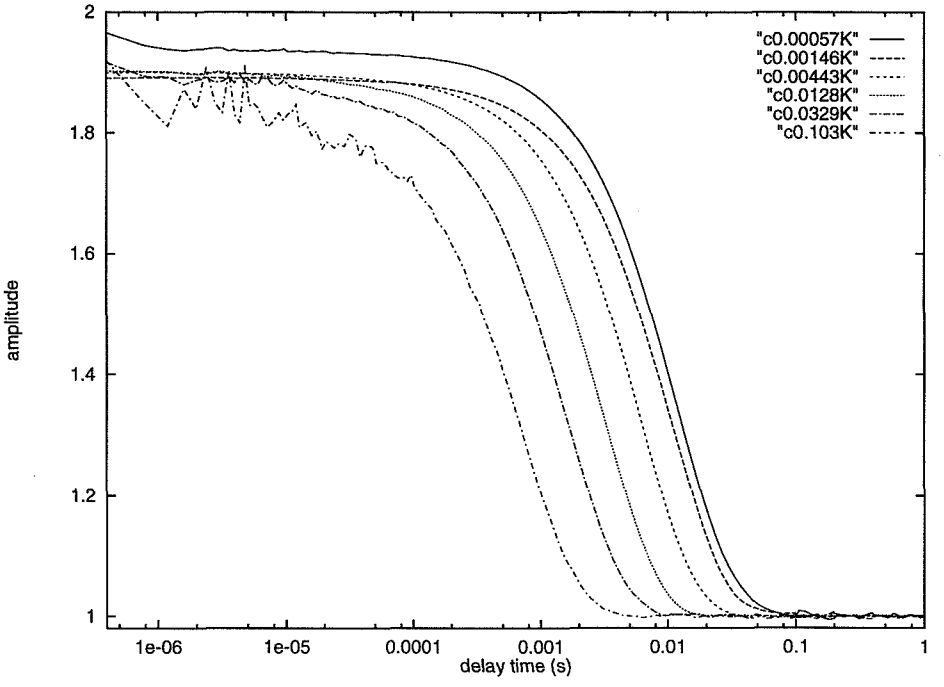

Fig. 10 Set of forward scattering correlograms recorded at temperatures from 2 mK to 100 mK during the second flight (USMP-3). The legend distinguishes the curves based on approach to Tc. The curves are correctly sorted but the labels are not accurate expressions of the approach to Tc (see discussion).

After least-squares fitting, the correlogram sets recorded at each temperature are used to produce an average fluid critical flucutation decay rate and its statistical error bar. The average decay rates are shown in Fig. 11 and Fig. 12 for forward and backward scattering angles (11.465 °and 169.546 ° angles, in the fluid) as plots versus temperature-distance from Tc. These are all from the second flight. The ground (1 g) points are from immediate post-flight testing at the Kennedy Space Center. The error bars are usually smaller than the plotting symbols here, except for the low power, backscattering correlograms.

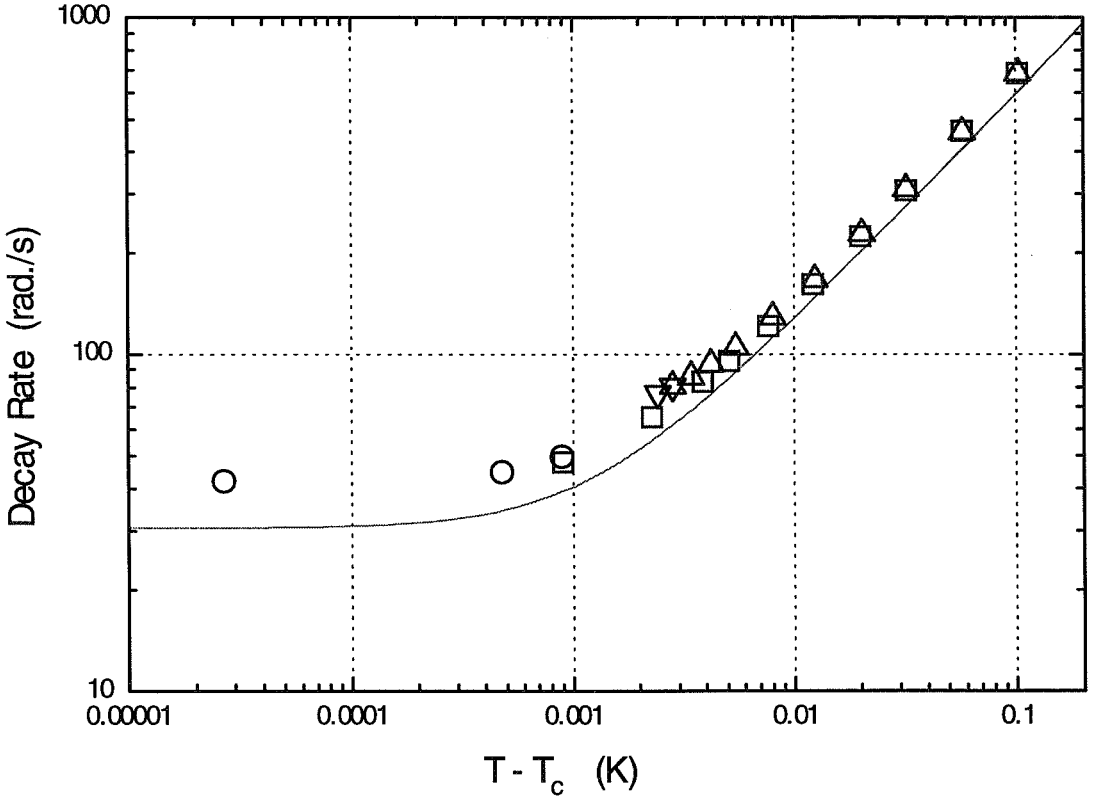

Fig. 11 Log-log plot of fluctuation decay rates for forward scattering (11.465 ° angle, in the fluid) versus temperature-distance to Tc. Symbols: squares, 17 μW scattering, flight 2; circles, 1.7 μW scattering, flight 2; triangles pointed up, 17 μW scattering, post-flight 2; triangles pointed down, 1.7 μW scattering, post-flight 2. The solid curve is a prediction based on equations of Burstyn, Sengers, Ferrell and Bhattacharjee.

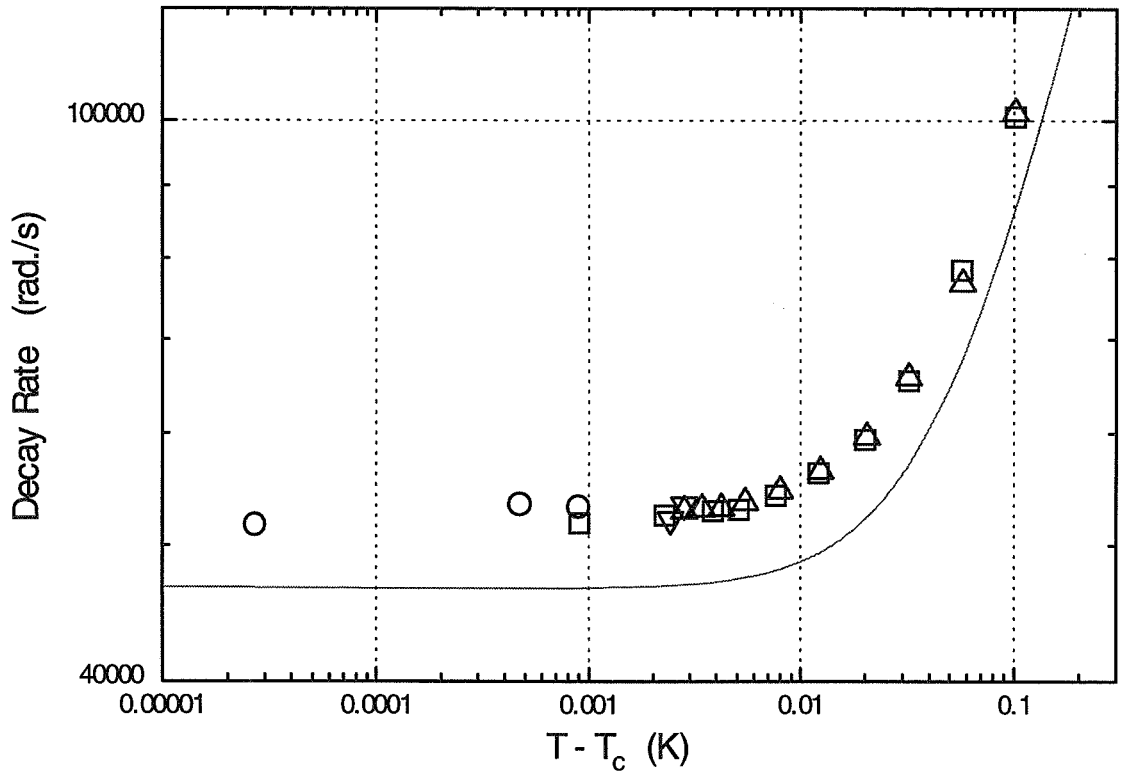

Fig. 12 Log-log plot of fluctuation decay rates for backscattering (169.546 ° angle, in the fluid) versus temperature-to Tc. Symbols: squares, 17 μW scattering, flight 2; circles, 1.7 μW scattering, flight 2; triangles pointed up, 17 μW scattering, post-flight 2; triangles pointed down, 1.7 μW scattering, post-flight 2. The solid curve is a prediction based on equations of Burstyn, Sengers, Ferrell and Bhattacharjee.

The solid curve is an estimate based on the work of Burstyn, Sengers, Ferrell and Bhattacharjee[4] for a sample of critical density. They showed that the critical part of the fluctuation decay rate for a fluctuation spatial wavevector q was given by

$$\Gamma(q,\xi) = R\frac{kT}{6\pi\nu\xi}\frac{\Omega(x)}{x^3}q^3(1+(B_1x)^2)^{x_\eta/2}, \qquad (1)$$

with R a dimensionless amplitude taken = 1.00, k Boltzman's constant, T the absolute temperature, ν the viscosity, ξ the correlation range, $x = q\xi$ the reduced wavevector, the Kawasaki function,

$$\Omega(x) = \tfrac{3}{4}(1 + x^2 + (x^3 - 1/x) \cdot \mathrm{atn}(x)), \qquad (2)$$

with B_1 a dimensionless constant taken as 0.5, and the viscosity exponent x_η anomaly taken as $x_\eta = 0.054$.[5] The viscosity function used is from refitting the data of Strump et al.[6] with the asymptotic-limit form from Burstyn, Sengers, Ferrell and Bhattacharjee[4] The curve is shown here before serious fitting is attempted to show that the data appear to be in reasonable agreement with expectations. There are greatly improved xenon viscosity measurements and a corrected and tested exponent x_η available from Berg and Moldover.[5] These cannot be used until they are refitted with the correct correlation range amplitude and exponent. The same calculated decay rate curve is used in all the figures, Figs. 11-15.

The post-flight, ground data are shown for comparison. The very strong effect of density stratification from earth's gravity gives a limiting-value of the decay rate almost 2x larger on the ground. On the ground we never saw decay rates smaller than 70 rad/s while the first flight saw rates down to 38 rad/s and the second, down to 42 rad/s for the forward angle. This was clearer in the first flight data[2] where there were more points close to Tc. Here the ground post-flight baseline data was taken as if Tc was the pre-flight value and so ended up with points too far from the critical point. Fig. 13 shows the data from the first flight for forward scattering fluctuation decay rates.

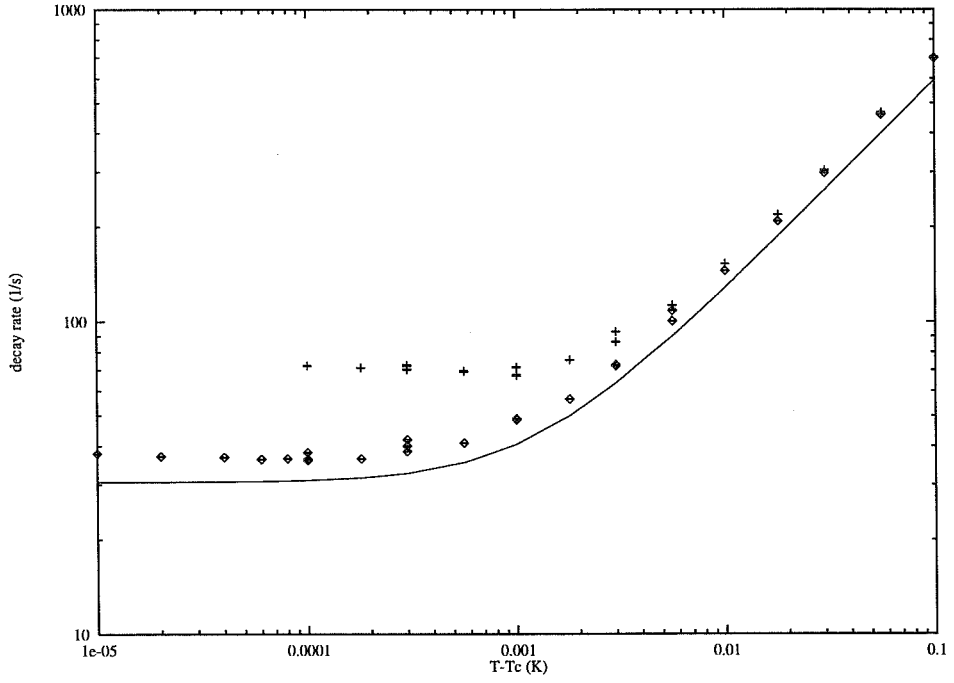

Fig. 13 Log-log plot of fluctuation decay rates for forward scattering from the first Zeno flight. Symbols: diamonds are the flight data, plusses are the ground data. The solid curve is a prediction based on equations of Burstyn, Sengers, Ferrell and Bhattacharjee. Notice that the flight data show limiting behavior almost 2x below the ground data.

We now know that the local density was slightly off critical due to local heating by the laser. Thus a better comparison to theory involves determining the correlation range ξ from the measured intensities, since the correlation range is directly related to the "distance" to the thermodynamic critical point. Eventually these will best be determined from some global least-squares fitting. For now we have estimated the correlation ranges by correcting for a 2.5% reflection in the forward/backward intensity ratios to arrive at simple Ornstein-Zernike ratios.[7] From these ratios and the known scattering wavevectors, we can estimate the correlation range of the fluctuations at each temperature-density point.

We can use the Cannell determination[7] of the correlation range, ξ, for xenon at the critical density,

$$\xi(\rho_c, T) = 1.78x10^{-8}(\frac{T - Tc}{Tc})^{-\nu} \quad \text{(cm)}, \tag{3}$$

refitted with a renormalization group exponent, $\nu = 0.63$, to convert the measured correlation ranges to equivalent (T-Tc) at the critical density and replot the decay rates in Fig. 14 and Fig. 15. The new temperature scale in these figures indicates the possibility that the density errors prevented a close approach to the critical in the second flight. The data plan called for measurements down to 100 μK while staying within 0.1% of critical density. This we now see was impossible with the sample used in the two Zeno flights. Though we did not reach the limiting behavior desired in the second flight, the experience gained with the "window density-interferometer" will allow a reanalysis of the first flight data using ξ. Many of the first-flight correlograms had lower decay rates and so were closer to the critical point and its limiting decay rate. Thus the data from the two flights should meet the goals of the Zeno experiment.

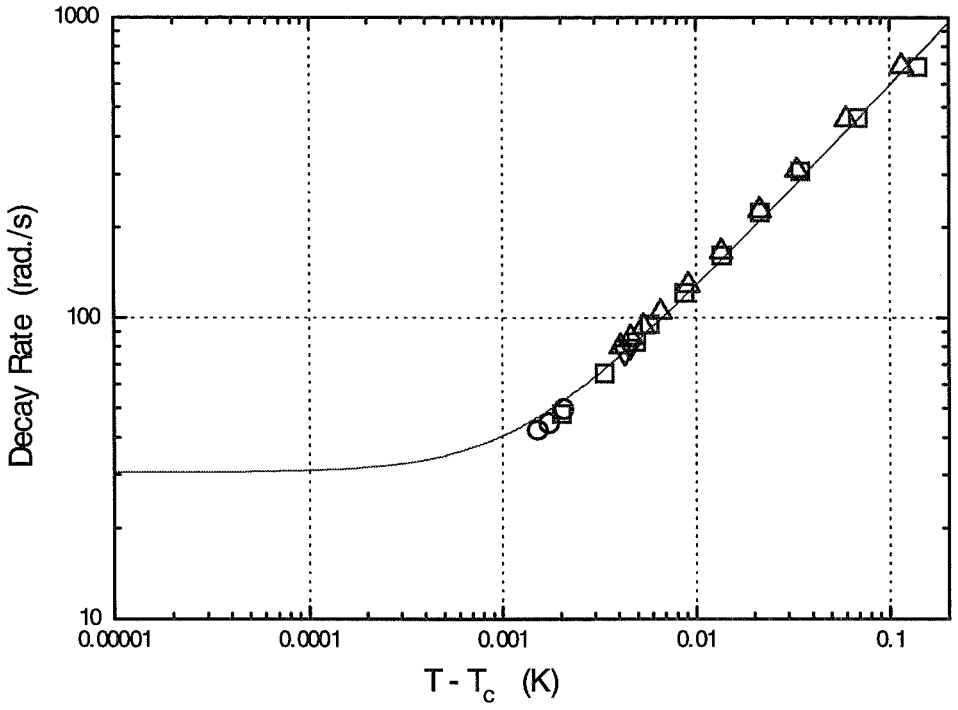

Fig. 14 Log-log plot of fluctuation decay rates for forward scattering (11.465 ° angle, in the fluid) versus a correlation-range corrected temperature distance to Tc. Symbols: squares, 17 μW scattering, flight 2; circles, 1.7 μW scattering, flight 2; triangles pointed up, 17 μW scattering, post-flight 2; triangles pointed down, 1.7 μw scattering, post-flight 2. The solid curve is a prediction based on equations of Burstyn, Sengers, Ferrell and Bhattacharjee.

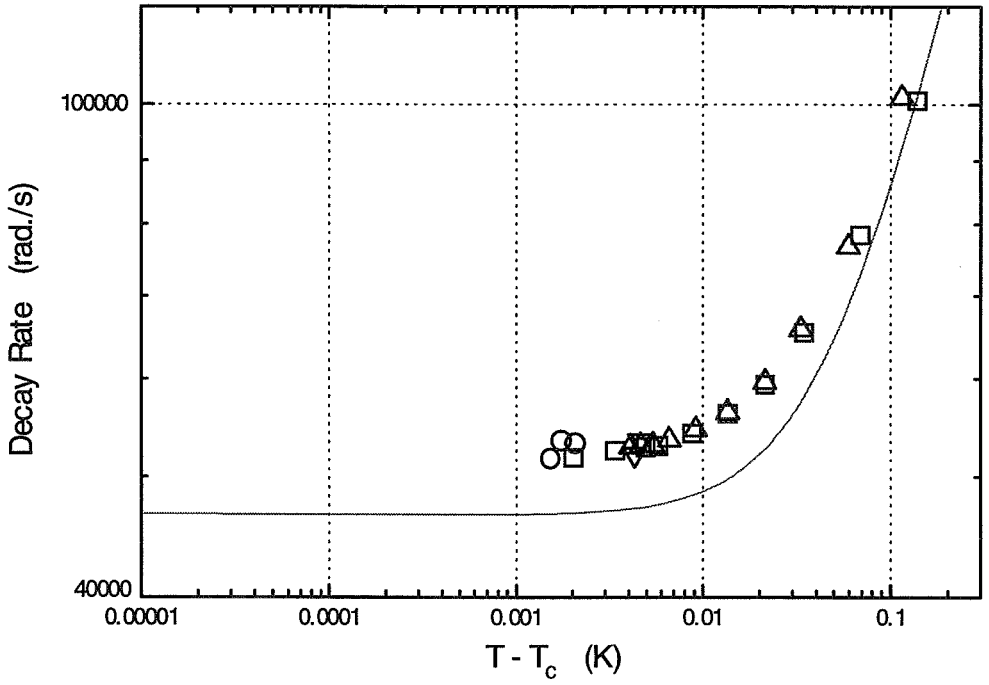

Fig. 15 Log-log plot of fluctuation decay rates for backscattering (169.546 ° angle, in the fluid) versus a correlation-range corrected temperature distance to Tc. Symbols: squares, 17 μW scattering, flight 2; circles, 1.7 μW scattering, flight 2; triangles pointed up, 17 μW scattering, post-flight 2; triangles pointed down, 1.7 μW scattering, post-flight 2. The solid curve is a prediction based on equations of Burstyn, Sengers, Ferrell and Bhattacharjee.

LOCATING THE PHASE BOUNDARY NEAR TC

It is a common experience for critical point experiments that have been carried on the Shuttle to experience a shift in temperature calibration from the launch stresses. Zeno has also seen this. Even though the drift rate of the repeated measurement of Tc over 3 years has shown the drift to be < 1 mK/year, the USMP-3 launch caused a −2.2 mK shift in the location of Tc on the instrument temperature scale. Thus we needed to adjust our estimate of the location of Tc during the data collection. Then based on our last estimate we set up the final scanned search for the phase boundary. The forward scattering intensity seen by the photomultiplier PMT-1 is plotted versus temperature in Fig. 16. This data was fitted as two straight lines with the intersection at To. This To we take as the phase separation temperature at the local density probed. The fit gave a best fit value for To with error estimate of ± 10 μK. The backscattering data was fitted in the same way. The two fit parameters for To agreed to within ± 20 μK. For comparison, Fig. 17 shows the post-flight search done in 1 g with all instrument settings the

same as flight.

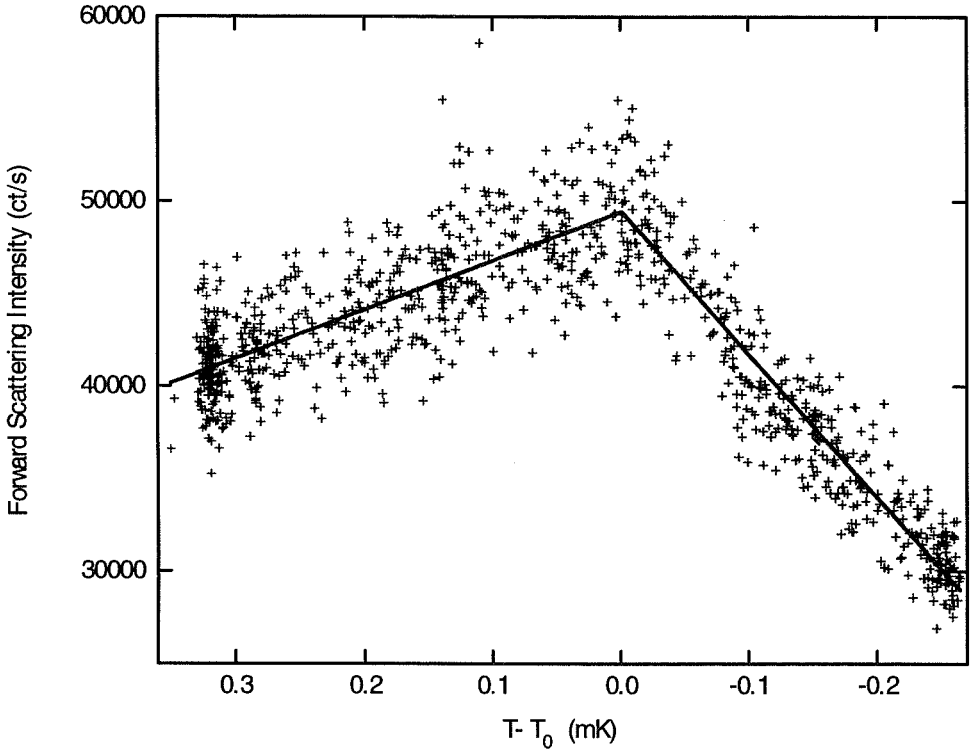

Fig. 16 Microgravity slow-scan search for the liquid-vapor phase-coexistence phase-boundary. Scan rate was -100 μK/hr. This was done in the last day of the mission. Data are marked with the + symbol while the straight lines were least-squares fitted to the data with the intersection a fitting parameter, To. The transition observed is much sharper than observed on earth.

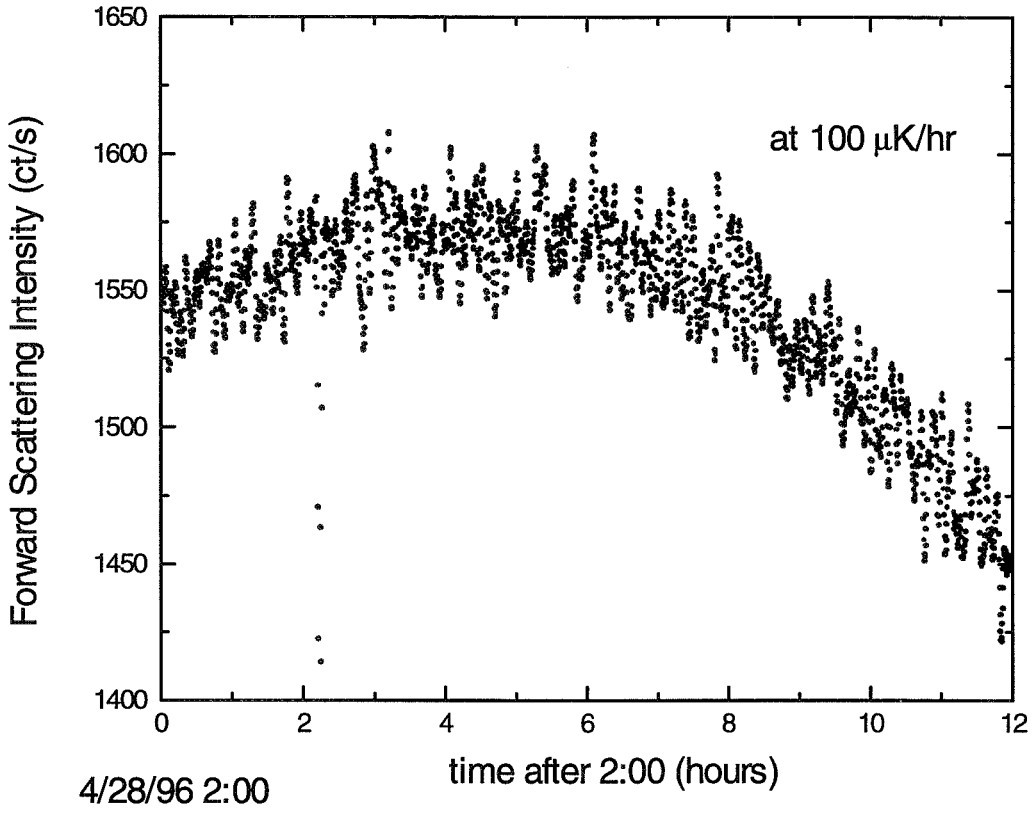

Fig. 17 Post-flight (1 g), slow-scan search for the liquid-vapor phase-boundary. Scan rate was -100 μK/hr, as in Fig. 16. Data are marked with a dot symbol.

One can see that the maximum intensity reached is 30x lower on earth and the peak is broader. The plot in Fig. 17 covers twice the time span as that in Fig. 16. The precision found in locating the phase boundary (about 0.6 mK below the Tc) in low gravity is almost a decade better than the best terrestrial measurements. The transition is much sharper in microgravity, probably due to the lack of convection and sedimentation, which smear the transition. We believe this to be the sharpest critical transition ever seen except for the helium lambda transition.

CONCLUSIONS

The second flight of the Zeno experiment provided a surprise in the discovery of detectable laser local heating even though the laser power was only 17 μW. We took time to characterize the "window interferometer" during the flight. Thus it was possible to use the interferometer to insure good local density stability until late in the mission when the laser power was changed. We have illustrated how the intensity ratios, corrected for window reflections, can determine the

correlation range, ξ, at each correlogram collection point. This method will enable calculation of the limiting decay rates close to the critical point from the combined flight data sets.

This experiment has reached the limits of the particular sample flown. The only way to lower the amount of local heating is to use a cell with all sapphire windows (14x higher conduction makes the local temperature rise 14x smaller). We have produced a flight qualified version of such a cell but it was made too late to be integrated into the Zeno experiment. One could lower the laser power, but only if detectors with much higher quantum efficiency were used: the laser powers used in the Zeno flights were at the shot-noise limits for recording precise correlograms in the time available. Finally, it would be good to know why the window surface absorption was 24x higher than the expected losses from superpolished surfaces (1 ppm). It seems that the greatest challenge turns out to be, not the approach to equilibrium, but rather the tiny temperature non-uniformities in the sample fluid, which make themselves strongly felt only in microgravity.

Finally, we have found the best, detailed confirmation of the adiabatic effects occurring in critical fluids in response to wall temperature changes. The successful modeling of the temperature-step-induced density changes during the second mission was only possible because of the data from the low gravity measurements in the unique Zeno sample cell.

ACKNOWLEDGEMENTS

This work was sponsored by the Microgravity Applications and Science Division of NASA through NASA-Lewis under contract NAG3-25370. We wish to acknowledge the tireless efforts of our project managers, John Borden at the University of Maryland, Richard Lauver at Lewis Research Center, NASA, and Richard Reinker at Ball Aerospace, who kept all the parts of this project moving to the end. Robert Stack of Ball Aerospace worked energetically to get the instrument checked out and tested for the reflight, and prepared himself to be an expert at commanding. Mark Sienkiewicz got the flight software modified so that we could run under all TFL's and added a new calculated turbidity function that corrected an old offset problem. Robert Berg and Michael Moldover were always sympathetic and helpful as they helped us and worked to get their related experiment on the viscosity of xenon, CVX, designed and built. Richard Ferrell and Jan Sengers have offered much stimulation and guidance over many years on the importance and subtle issues of critical transport coefficients. Finally, thanks go to the rest of our POCC team for working so hard to avoid making a false move or missing any data during the rather risky timeline of the second flight. They were: Greg Zimmerli, Andrew Peddie, and Klaus Gumpto.

REFERENCES

1. R.W. Gammon and J.N. Shaumeyer, "Science Requirements Document for Zeno," (NASA, Microgravity Science and Applications Division (MSAD), Washington, D.C.,1988).
2. R.W. Gammon, J.N. Shaumeyer, M.E. Briggs, H. Boukari, D.A. Gent, R.A. Wilkinson, "Highlights of the Zeno Results from the USMP-2 Mission," *NASA Technical Memorandum 4737*, (NASA, Marshall Space Flight Center, Huntsville, AL, 1996), p. 5-135.
3. H. Boukari, J. N. Shaumeyer, M. E. Briggs, and R. W. Gammon, "Critical Speeding Up in Pure Fluids", Phys. Rev. A 41, 2260-2263 (1990); H. Boukari, J. N. Shaumeyer, M. E. Briggs, and R. W. Gammon, "Critical Speeding Up Observed," Phys. Rev. Letters **65**, 2654-2657 (1990); and references therein.
4. H.C. Burstyn, J.V. Sengers, J.K. Bhattacharjee, and R.A. Ferrell, "Dynamic scaling function for critical fluctuations in classical fluids," Phys. Rev., **A28**, 1567, (1983).
5. R.F. Berg and M.R. Moldover, "Critical exponent for the viscosity of carbon dioxide and xenon," *J. Chem. Phys.* **93,** 1926 (1991).
6 . H.J. Strumpf, A.F. Collings and C.J. Pings, J. Chem. Phys. **60**, 3109 (1974).
7. David S. Cannell, "Experimental study of the liquid phase of SF_6 neat its critical point," Phys. Rev. A, **15**, 2053, (1977); H. Gütter and D.S. Cannell, "Correlation range and Rayleigh linewidths of xenon near the critical point," Phys. Rev A **22**, 285 (1980).

Page intentionally left blank

THE ISOTHERMAL DENDRITIC GROWTH EXPERIMENT

M.E. Glicksman & M.B. Koss
Materials Science & Engineering Department
Rensselaer Polytechnic Institute
Troy, NY 12180-3590
USA
(518)276-6721
glickm@rpi.edu
&
(518)276-2844
kossm@rpi.edu

D.C. Malarik
Microgravity Science Division
NASA Lewis Research Center
Cleveland, OH 44135
USA
(216)433-3203
diane.malarik@lerc.nasa.gov

Introduction

The growth of dendrites is one of the commonly observed forms of solidification encountered when metals and alloys freeze under low thermal gradients, as occurs in most casting and welding processes. In engineering alloys, the details of the dendritic morphology directly relates to important material responses and properties. Of more generic interest, dendritic growth is also an archetypical problem in morphogenesis, where a complex pattern evolves from simple starting conditions. Thus, the physical understanding and mathematical description of how dendritic patterns emerge during the growth process are of interest to both scientists and engineers [1].

The Isothermal Dendritic Growth Experiment (IDGE) is a basic science experiment designed to measure, for a fundamental test of theory, the kinetics and morphology of dendritic growth without complications induced by gravity-driven convection. The IDGE, a collaboration between Rensselaer Polytechnic Institute, in Troy NY, and NASA's Lewis Research Center (LeRC), in Cleveland OH, was developed over a ten year period from a ground-based research program into a space flight experiment [2,3]. Important to the success of this flight experiment was provision of *in situ* near-real-time teleoperations during the spaceflight experiment [4].

Background on Dendritic Growth Theory and Experiment

A number of theories of dendritic crystal growth, based on various transport mechanisms, physical

assumptions, and mathematical approximations, have been developed over the last fifty years. These theories attempt to predict a dendrite's tip velocity, V, and radius of curvature, R, as a function of the supercooling, ΔT (see the review by one of the authors [1]). The growth of dendrites in pure melts is known to be controlled by the transport of latent heat from the moving crystal-melt interface as it advances into its supercooled melt. Ivantsov, in 1947, provided the first mathematical solution to the dendritic heat conduction problem [5], and modeled the steady-state dendrite as a paraboloidal body of revolution, growing at a constant velocity, V. The resultant thermal conduction field can be expressed exactly in paraboloidal coordinates moving with the dendritic tip. The temperature field solution is known as the Ivantsov, or "diffusion-limited" transport solution. This solution is, however, incomplete, insofar as it only specifies the dendritic tip growth Péclet number, $Pe=VR/2\alpha$, (here Pe is the growth Péclet number, and α is the thermal diffusivity of the molten phase) as a function of the initial supercooling, and not the unique dynamic operating state; V and R. The Péclet number obtained from the Ivantsov solution for each supercooling yields instead an *infinite* range of V and R values that satisfy the diffusion-limited solution at that particular value of ΔT.

In the early 70's, succinonitrile (SCN), a BCC organic plastic crystal, was developed as a model metal analog system for studying dendritic growth [6]. SCN solidifies like the cubic metals, i.e., with an atomically "rough" solid-liquid interface, yet retains advantages because SCN displays convenient properties for solidification experiments, such as a low melting temperature, optical transparency, and accurate characterization of its thermophysical properties. The use of SCN greatly facilitated dendritic growth studies over the past twenty years, where because of its use, dendritic tip velocities could be accurately measured and used as a critical test of theory [6,7].

Theoretical efforts have concentrated on trying to discover an additional equation or length scale, which when combined with the Ivantsov conduction solution, "selects" the observed operating states (see references within ref. [1]). Although the underlying physical mechanisms for these "theories of the second length scale" are quite different, their results are invariably expressed through a scaling constant, $\sigma^*=2\alpha d_o/(VR^2)$, where d_o is the capillary length scale, a materials parameter defined from the equilibrium temperature of the crystal-melt interface, the solid-liquid interface energy, and the specific and latent heats. Although some theories predict the value of this scaling constant, in practice the scaling constant is used as an adjustable parameter to describe dendritic growth data in various materials.

Subsequent experiments with SCN showed that gravity-induced convection *dominates* dendritic growth in the lower supercooling range typical of metal alloy castings [8]. Convection, unfortunately confounds any straightforward analysis of dendritic solidification based on conductive heat transfer. There have been a few attempts to estimate the affect of natural or forced convection on dendritic growth [9], but these calculations are themselves based on yet unproven elements of dendritic growth theory, and, consequently, can not provide an independent test of the theory. In the higher supercooling range, where thermal convective influences diminish in comparison to thermal conduction, the morphological scale of dendrites becomes too small to be resolved optically at the high growth speeds encountered. The experimental situation prior to the microgravity experiment reported here, was that there appeared to be too narrow a range of supercoolings in any crystal-melt system studied terrestrially that remains both free of convection effects, and also permits an accurate determination of the dendrite tip radius of curvature.

The Isothermal Dendritic Growth Experiment

The Isothermal Dendritic Growth Experiment (IDGE) a NASA sponsored series of Space Shuttle microgravity experiments, was designed to grow and photograph dendrites in the absence of convective heat transfer for a fundamental test of dendritic growth theories. The data and subsequent analysis on the dendritic tip growth speed and size from the first flight of the IDGE, in March of 1994 (USMP-2/STS-62), has demonstrated that although the theory can make predictions that are in reasonable agreement with the results of the experiment, there are several important areas of disagreement [10-13].

Review of Results from the IDGE on USMP-2

We measured the dendritic growth velocities and tip radii of curvature of succinonitrile in microgravity using the IDGE instrument flown on the USMP-2 platform in the payload bay of the space shuttle Columbia (STS-62). The on-orbit microgravity data, when compared to terrestrial dendritic growth data, demonstrate that: (1) convective effects under terrestrial conditions remain significant even up to values as high as ΔT =1.7 K supercooling. (2) In the supercooling range from 0.47 K to 1.7 K, the data remain virtually free of convective or non-Ivantsov conditions, and may be used reliably for examining diffusion-limited, infinite boundary dendritic growth theories. (3) A diffusion solution to the dendrite problem, combined with a unique (measured) scaling constant, σ^*, does not yield individual growth velocity and radius predictions consistent with the observed dendritic growth velocities and radii as a function of supercooling. (4) The failure of this conventional formulation is currently attributed to small departures from the Ivantsov thermal diffusion solution, which is formulated for *paraboloidal* dendrites. Ivantsov's theory describes the overall dependence of Péclet number on supercooling, but predicts a value higher (5% - 15%) than the data we observed in microgravity in the diffusion-limited regime. (5) The scaling parameter σ^* does not appear to be a constant over a range of supercoolings. Finally, (6) the average σ^* measurements from the terrestrial and microgravity data are in good agreement, despite a difference of over six orders of magnitude in the quasi-static acceleration environment of low-earth orbit and terrestrial conditions [10-13].

Before the IDGE, it was not possible to test separately the Ivantsov transport solution and the interface scaling hypothesis. To our knowledge, the IDGE provides the first solid evidence that Ivantsov's formulation for paraboloidal dendritic growth does not accurately describe dendritic growth in SCN. The approximate agreement achieved between the transport theory and the microgravity data indicates that dendritic growth is indeed most likely governed by the conduction of latent heat from the crystal-melt interface, but the detailed Ivantsov formulation to describe that conduction process is in need of some modification.

One of the key assumptions in the Ivantsov model that we are actively investigating is whether a dendrite can be modeled as a parabolic body of revolution. Early observations of dendrite morphologies lead researchers to approximate the tip shape with a paraboloid. The notion that dendrites are actually *not* paraboloids of revolution was first demonstrated by the data of Huang and

Glicksman [7], and more recently by other researchers [14-18] including LaCombe et al. [19]. By assuming the form of a 4th-order polynomial, rather than a 2nd-order parabola, it is possible to characterize more realistically the shape of dendrite tips. Such a fourth-order equation describing a dendritic profile is $Y=X^2/2 + Q(\phi)X^4$, where X and Y are dimensionless coordinates, normalized with the radius of curvature at the tip of the dendrite. $Q(\phi)$ will vary with the azimuthal direction, and is generally assumed to be proportional to $\cos(4\phi)$ [14-18]. However, the recent work of LaCombe et al. [19,20] has shown that the $\cos(4\phi)$ form does not adequately describe the axial asymmetry. This is seen most readily seen in Fig. 10 of [19] and Fig. 4 of [20] where the $\cos(4\phi)$ functional form is superimposed upon the experimentally observed data describing the actual shape. Furthermore, for terrestrial data, this shape is seen to be independent of supercooling, i.e., the three dimensional shape scales with the size of the dendrite.

At the lower supercoolings ($\Delta T < 0.4$ K), variations in the growth speed beyond that due to measurement uncertainties, and a significant deviation of the heat transfer from that predicted from diffusive transport theory with boundary conditions at infinity. Recently, two models, both based on Cantor and Vogel's confocal parabola modification to Ivantsov [21], described in the *Journal of Crystal Growth* have suggested mechanisms for the heat transfer of a dendrite growing into a supercooled melt. One model, by Sekerka et al. [22], describes how convection resulting from the residual micro-accelerations present on orbit could enhance the heat transfer. Another, by Pines et al. [23], describes the observed speed enhancement as a thermal boundary layer effect arising from the proximity of the growth chamber wall.

Both models, by the adjustment of one parameter, describe the trends in the IDGE microgravity data, and the Stagnant Film Model of Sekerka et al. also describes the terrestrial data. However, when examined in precise detail [24,25], we have shown that neither model is correct. The chief reason being that both models rely, and are thereby "handcuffed", by the Ivantsov solution, which we have already shown is incorrect. In addition, since both models are, in part, based on the same formulation, we could not discriminate between the two of them based on the IDGE data from USMP-2 alone.

Thus, in the higher supercooling range investigated, both the heat transfer and the crystal growth physics components of current dendritic growth theories are in need of modification. In the lower supercooling range, the data are inconsistent with several models of dendritic growth that attempt to modify the basic diffusion-limited theory with the boundaries at infinity to include convection or container effects.

The IDGE on USMP-3

The scientific objectives of the second flight of the IDGE was to: characterize the three-dimensional shape of a dendrite tip; accumulate a dense data set on dendritic velocities and radii in the diffusion-limited infinite boundary regime; and to form dendritic velocity data sets to clarify current issues in the literature about whether convection or near-field boundary conditions affect the dendritic growth measurements in microgravity in the lower supercooling range.

The second flight of the IDGE took place on USMP-3 in February and March of 1996. The growth chamber filled with succinonitrile and the temperature control system were identical to those used for USMP-2. In addition to the high-resolution film data collected after the shuttle landed, growth velocities were measured in near-real time by downlinked, binary CCD images. Because only a limited supply of film could be carried on the shuttle, many growths were measured from CCD images alone. These steady-state velocity measurements were accurate to 2%.

Results from the IDGE on USMP-3 at Landing Plus One-Year

The microgravity environment on the space shuttle varied throughout the mission. Shuttle maneuvers, changes in attitude, motions of equipment or astronauts, all changed the amplitudes and directions of the micro-acceleration vectors. The Tethered Satellite System deployed on the same mission as USMP-3 also had profound effects on the microgravity environment. While the tether was reeled out and the massive (1 tonne) satellite moved away from the shuttle, the mass centroid gradually moved in the direction of the satellite. This caused the acceleration at the IDGE location to rise by a factor of about 80 in approximately twenty hours. When the tether broke, in an unfortunate accident, the microgravity suddenly returned to its initial low level.

Quasistatic microgravity levels were measured by the Orbital Acceleration Research Experiment (OARE) throughout the USMP-3 mission [26, and submission to this volume]. These measurements were corrected for the gravity gradient from IDGE to the shuttle's center of gravity. Although each measurement is accurate to about 5%, any time average of the microgravity level reveals significant variations in the quasi-static accelerations

The telemetry data obtained during flight, Figure 1, indicates that we accumulated sufficient data to meet our objectives. Currently, we are conducting data reduction and analysis to further our analysis in the diffusion-limited infinite boundary regime, and to characterize and compare the three-dimensional shape of a dendrite tip at both terrestrial and microgravity conditions. However, we have already aquired enough data, and performed analysis, to make conclusions about whether convection or near-field boundary conditions affect the dendritic growth measurements in microgravity in the lower supercooling range.

Dendrite tip velocity measurements at low supercoolings showed more run-to-run variation and proved to be much larger than diffusion-controlled models would predict. We sought to correlate the variation in growth velocities with the microgravity level. Data sets taken at supercoolings of 0.18 K, 0.26 K, and 0.36 K all show these effects. At the time of this report, our most complete analysis is for data obtained at a supercooling of 0.26 K.

The variation in growth velocity among the various repeated experiments is much larger than the measurement uncertainty (2%) of an individual run. Each growth cycle included in the data set had a tip growing with constant angle (relative to the growth chamber) and velocity for at least 15 minutes. We anticipated that both the magnitude of the microgravity level and the growth angle with respect to the quasi-static microgravity vector would affect the results. Figure 2 shows observed dendritic velocities plotted in a space representing the growth axis angle and the magnitude of the

quasi-static microgravity vector. Reading along any horizontal or vertical set of data, we could not detect any clear trend. However, the fluctuations occuring in microgravity level during each 15-minute period could obscure any correlations among growth cycles. Adding uncertainty measurments to the plot (Figure 3) makes it apparant that these data are not conclusive.

A more detailed examination of each growth cycle should reveal any correlations occuring on a shorter time scale. Specifically, we plotted the instantaneous dendrite tip positions relative to the regressed tip position calculated from the average steady state velocity. A typical example is shown in figure 4. Again, we could not detect a correlation of the growth speed with the magnitude or direction of the quasi-static microgravity level for any of the 30 cycles for which data are available. Even for the cycle during which the tether broke (figure 5), and a large change occured in the microgravity level, the dendrite that was growing still appeared to grow at the same constant velocity. Aside from a possible brief transient, the growth rate is neither faster nor slower than that observed before the break.

The variation in steady-state dendritic growth velocity does not appear to correlate with the measured changes in the quasi-static microgravity environment. This result suggests that changes in the microgravity level (10^{-7} to 10^{-5} g_o) do not significantly affect dendritic growth rates in SCN in the supercooling range above 0.18 K in the IDGE growth chamber.

Conclusions about Remote Telescience from the IDGE on USMP-3

In the investigation of dendritic growth phenomena, the IDGE team members were the experimenters, manipulating parameters and conditions in near-real time, making measurements, and analyzing data, and changing the subsequent experimental parameters. However, with respect to the operations of the flight hardware from a terrestrial laboratory, the IDGE was part of a larger experiment in remote teleoperations, paving the way to the microgravity science operations on the future International Space Station (ISS). NASA headquarters and the Telescience Support Center (TSC) at LeRC, with the goal of developing the experience and expertise to set up remote, non-NASA locations from which to control ISS experiments, used our recent IDGE space shuttle experiment as a proof-of-concept of remote operations. During the flight of IDGE on STS-75 in February and March of 1996, team members monitored this experiment from at a remote laboratory set up at Rensselaer rather than at the Payload Operations and Control Center (POCC) at the Marshall Space Flight Center, in Huntsville, AL, where all such operations usually originate. During the last four days of the mission, we expanded the team at Rensselaer and uplinked commands to the experiment. During the entire 14 day mission we had graduate and undergraduate students, whom we had trained, present at the Rensselaer facility.

Some details of this test of remote telescience has been published elsewhere [27]. Our brief experience at operating a microgravity space-flight experiment from a remote non-NASA location successfully identified some of the scientific advantages and many of the issues and challenges of remote teleoperations. Naturally, not all the potential issues of remote teleoperations could be identified based on one experiment's experience on one shuttle flight. For example, several issues of facility security and room access need to be better examined. Furthermore, only one experiment,

the IDGE, and one instrument, SAMS, was operating from remote sites. How several similar experiments would operate simultaneously from different remotes sites has not been examined or tested.

We have avoided any discussion of solutions and improvements to what was done at Rensselaer during USMP-3/STS-75, although in many cases solutions and improvements are self evident. However, in some cases solutions and improvements are not the province of a single project but that of a larger more encompassing organization. Nevertheless, the experience we gained operating the IDGE on USMP-3/STS-75 from Rensselaer, and our discussions with some of the experimenters who operated remote sites during USML-2 allows us to make some general suggestions on how to proceed to more robust remote teleoperation facilities.

First is merely to recognize the different modes of operations between how space shuttle microgravity experiments are conducted, and how a future space station microgravity experiment will most likely be conducted. For shuttle experiments, the limited time from launch to landing dictates many of the operational elements. One must be fully prepared well before launch, and there is little or no time to change plans or recover from mistakes. This requires both the Principal Investigator/Development teams and the POCC cadre be on-line fully for the duration of the mission. In addition, the short duration of space shuttle flights makes traveling and operating from the POCC eminently reasonable and practical.

The entire constraint for space station experiments changes because time is not the limiting variable. One does not need to operate around the clock for every minute the experiment in on-orbit. In fact for the space station this would be precluded by other constraints. Thus, time becomes a resource to be used liberally to think, replan, and even if necessary, set up supplemental ground-based tests, and only then take the appropriate action. Under those circumstances, traveling to the POCC is not the best use of the experimental teams time or resources with respect to how to best operate a microgravity experiment. Thus, for space shuttle experiments, the POCC is the best place to be, and remote sites only need be developed and implemented in support of testing for longer duration International Space Station experiments where we expect most PI's would better operate from their home facilities.

In consideration of the previous observation, it is counter-productive to tax the experiment teams, the POCC, and the TSC to set up *complete* remote teleoperations facilities with the near 100% guaranteed reliability demanded for a space shuttle experiment. Rather, the larger decision making bodies need to determine what are the crucial elements of the future space station experiment operations, and what elements of the current space shuttle experiments are similar to them. Then, various experiment teams like IDGE can operate *limited* remote teleoperation sites with the express purpose to conduct their science while simultaneously testing specific elements of remote teleoperations for the further development of space station remote facilities.

The remote teleoperation activities during USMP-3 performed as we had hoped, and based on this experience we understand the advantages and benefits versus the costs and challenges of such endeavors for the overall enhancement of the scientific return from on orbit. Remotely operating the IDGE aboard USMP-3 greatly enhanced our in-flight analytical capabilities, and served as a technical

"shakedown" of hardware and procedures that are destined to become commonplace in future microgravity research. In the course of this we learned that it is very important to have reliability in the data and command path. Until the technology is thoroughly tested and fine-tuned, it is advisable that appropriate backup data sources are maintained during the flight. Our approach to this was handled by maintaining the ability for these functions to be performed at the POCC if needed. The absence of some of the telemetry was restricting, but the additional space, equipment and manpower available at the university site were significant assets.

The experience gained in operating a microgravity experiment during USMP-3 is proving to be invaluable for planning future IDGE activities as well as other Space Shuttle and Space Station experiments. Once technical and reliability issues are resolved, the benefits obtained from university-based experiment operation such as: operational efficiency, cost savings, public exposure, and educational opportunities, will further improve the yield from microgravity research.

The microgravity community is poised to prepare for the coming space station era by learning from the experiences of remote teleoperations like those performed on USMP-3, and before that on USML-2. In this way, the development of each new teleoperation facility can build toward the ISS having learned from the evolution of such facilities from the recent past. In this way the promise of remote teleoperations as verified by this proof-of-concept can be brought to fruition. To prepare for the ISS era, we plan to do additional tests of remote telescience during IDGE third flight on USMP-4/STS-87.

Plans for the IDGE on USMP-4

The third flight, scheduled for launch in October 1997, will repeat the experimental protocols of the first two flights, but with a different sample material. This second test material, pivalic acid (PVA), is similar to SCN, but with a ten times higher surface energy anisotropy [28,29]. The surface energy, and the surface energy anisotropy are important parameters in the crystal growth physics of dendritic growth [1,29], and may be related to the three-dimensional anisotropy observed in the dendritic tip shape. In addition, we want to develop the data and analytical tools to characterize the non steady-state dynamic parameters, which lead to side branching and, we believe, will be another key in explaining the differences between the IDGE data and predictions from current steady-state dendritic growth models.

Acknowledgments

We thank, for the continuing interest, and financial support, the NASA Life and Microgravity Sciences and Application Division, (Code U), Washington, DC, under Contract NAS3-25368, with liaison provided NASA Lewis Research Center, Cleveland, OH. We also thank the flight crews of STS-62 and STS-75, the payload cadres for USMP-2 and USMP-3, the Rensselaer Operations and Control Center (ROCC) cadre, the IDGE engineeering team at or associated with the Microgravity Science Division at NASA Lewis, Rensselaer Administrative Sectretary T. Geren, graduate students L.A. Tennenhouse and J.C. LaCombe, and Post-Doctoral Research Associate A. Lupulescu.

References

1. M.E. Glicksman and S.P. Marsh, "The Dendrite", in Handbook of Crystal Growth, ed. D.J.T. Hurle, (ElsevierScience Publishers B.V., Amsterdam, 1993), Vol **1b**, p.1077.
2. M.E. Glicksman, et al., Met. Trans. A, **19A**, 1945, (1988).
3. M.E. Glicksman, M.B. Koss, and E.A. Winsa, JOM, **47**(8), 49, (1995).
4. M.E. Glicksman, M.B. Koss, L.T. Bushnell, J.C. LaCombe, and E.A. Winsa, 6th International Symposium on Experimental Methods for Microgravity Science, ed. Robert J. Schiffman, (The TMS, 1995, p. 51).
5. Ivantsov, Dokl. Akad. Nauk SSSR **58**, 56 (1947)
6. M.E. Glicksman, R.J. Schaefer, and J.D. Ayers, Met. Trans. A, **7A**, 1747, (1976).
7. S.C. Huang and M.E. Glicksman, Acta Metall., **29**, 701, (1981).
8. M.E. Glicksman and S.C. Huang, Convective Transport and Instability Phenomena, ed. Zierep and Ortel, Karlsruhe, (1982), 557.
9. R. Ananth and W.N. Gill, J. Crystal Growth, **91**, 587, (1988), and **108**, 173, (1991).
10. M.E. Glicksman, M.B. Koss, and E.A. Winsa, Phys. Rev. Lett., **73**, 573, (1994).
11. M.E. Glicksman, M.B. Koss, L.T. Bushnell, J.C. LaCombe, and E.A. Winsa, ISIJ International, **35**, 604 (1995).
12. M.E. Glicksman, M.B. Koss, L.T. Bushnell, and J.C. LaCombe, Modeling of Casting, Welding, and Advanced solidification Processes VII, eds. M. Cross and J. Campbell (The Minerals, Metals, and Materials Society, Warrendale, PA, 1995).
13. M.B Koss., L.T. Bushnell, J.C. LaCombe, and M.E. Glicksman, Chem. Eng. Comm., **152-153,** 351, (1996).
14. J. Maurer, B. Perrin, and P. Tabeling, Europhys. Lett. **14**, 575 (1991).
15. D. Kessler and H. Levine, Phys. Rev. A **36**, 4123 (1987).
16. D. Kessler and H. Levine, Acta Metall. **36**, 2693 (1988).
17. M. Ben Amar and E. Brener, Phys. Rev. Lett. **71**, 589 (1993).
18. E. Brener, Phys. Rev. Lett. **71**, 3653 (1993).
19. J.C. LaCombe, M.B. Koss, V.E. Fradkov, and M.E. Glicksman, Phys. Rev. E, **52** 2778 (1995).
20. J.C. LaCombe, M.B. Koss, M.E. Glicksman, L.T. Bushnell, and K.D. Hamly, Thermodynamics and Kinetics of Phase Transformations, Mat. Res. Soc. Symp. Proc. **398**, eds. J.S. Im, B. Park, A.L. Greer, and G.B. Stephenson, (Materials Research Society, Pittsburgh, 1996).
21. B. Cantor and A. Vogel, J Crystal Growth, **41**, 109, (1977).
22. R.F.Sekerka, S.N. Coriell, G.B. McFadden, J. Crystal Growth, **154**, 370, (1995).
23. V. Pines, A.Chait, and M. Zlatkowski, J. Crystal Growth, (in press, 1996).
24. M.E. Glicksman, M.B. Koss, L.T. Bushnell, J.C. LaCombe, and E.A. Winsa, Reprint # AIAA 96-0251, (1996).
25. L.T. Bushnell, M.B. Koss, J.C. LaCombe, and M.E. Glicksman, J. Crystal Growth (in press, 1997).
26. M.J.B. Rogers, R. Delombard, Summary Report of Mission Acceleration Measurements for STS-75 (1996).

27. M.B. Koss, J.C. LaCombe, M.E. Glicksman, L.T. Bushnell, D.C. Malarik, and E.A. Winsa, 8th International Symposium on Experimental Methods for Microgravity Science, ed. Robert J. Schiffman (The TMS, in press, 1996).
28. N.B. Singh and M.E. Glicksman, J. Crystal Growth, **98**, 573, (1989).
29. M. Muschol, D. Liu, and H.Z. Cummins, Phys. Rev. A, **46**(2), 1038, (1992).

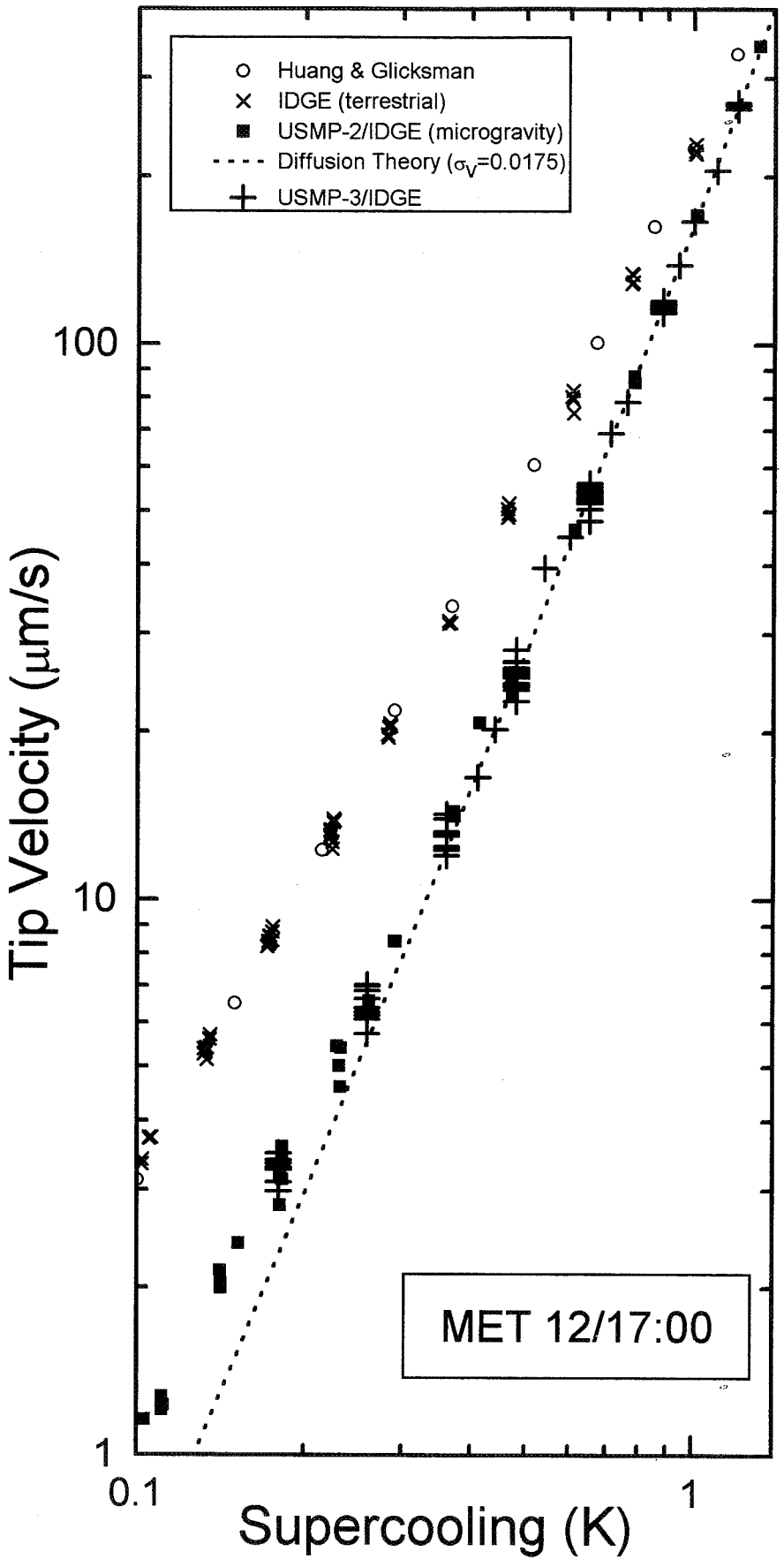

Figure 1: In situ dendritic growth velocity measurements from IDGE on USMP-3 during STS-75.

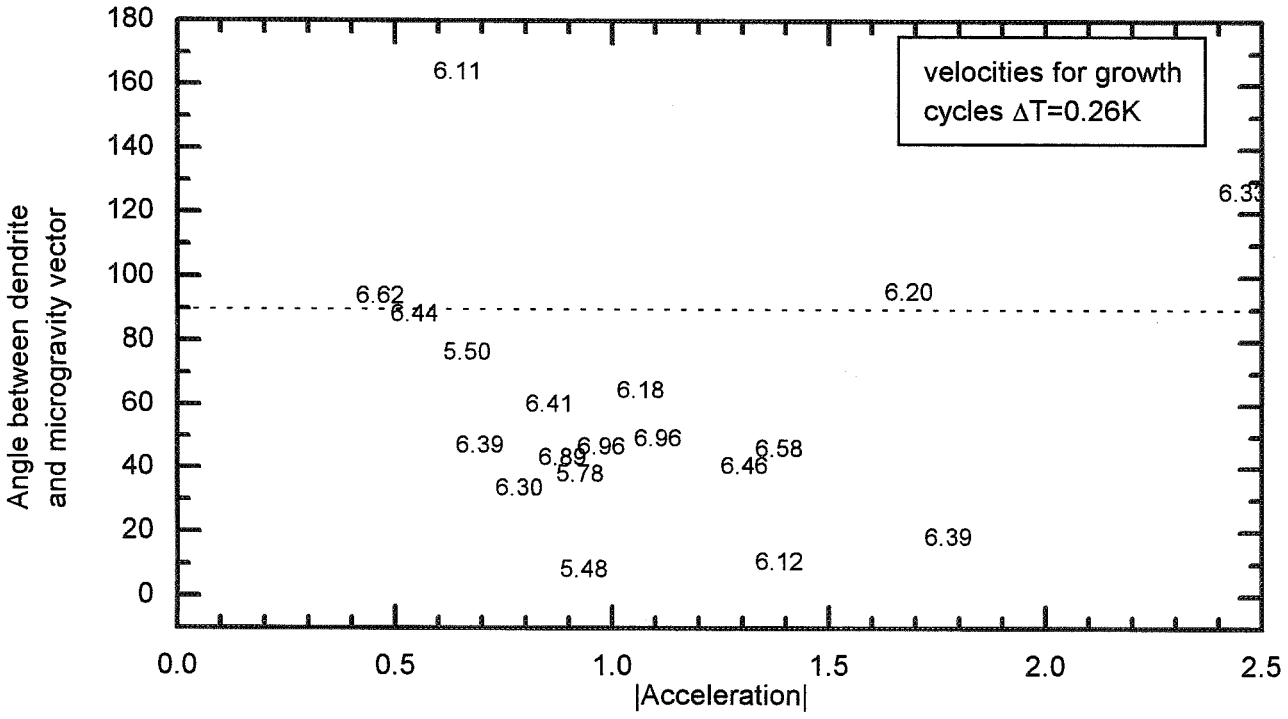

Figure 2: There is no clear correlation between steady-state dendrite velocity and the microgravity vector.

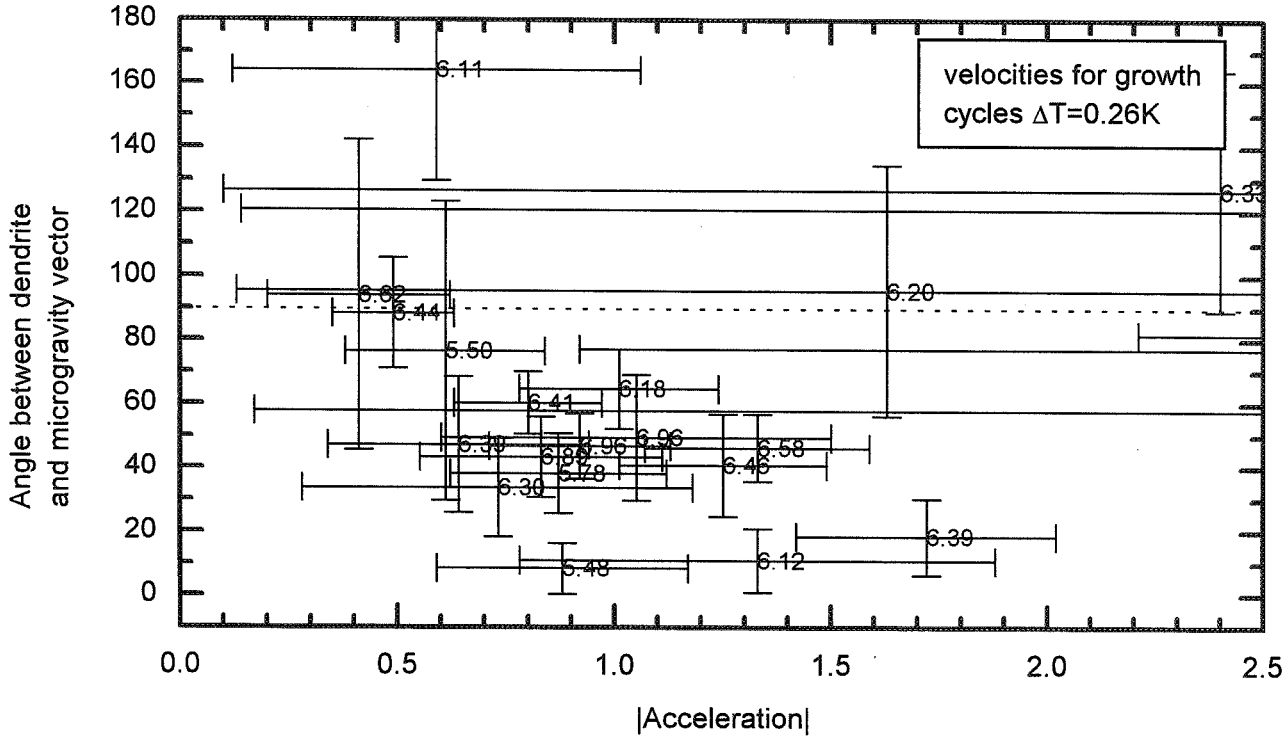

Figure 3: Variation in the quasi-static microgravity vector obscures any possible correlation with dendrite velocity.

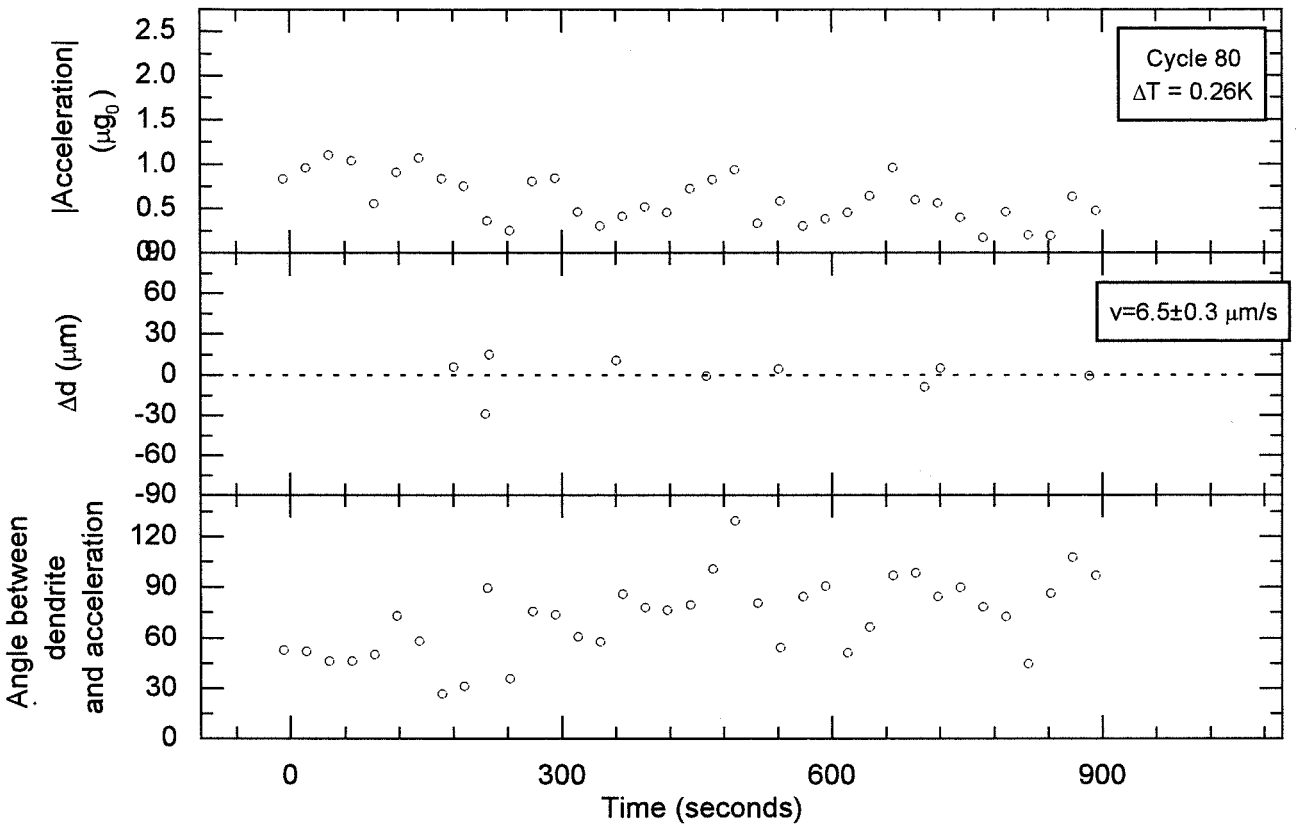

Figure 4: Noise in the dendritic growth does not appear to correlate with noise in the microgravity vector.

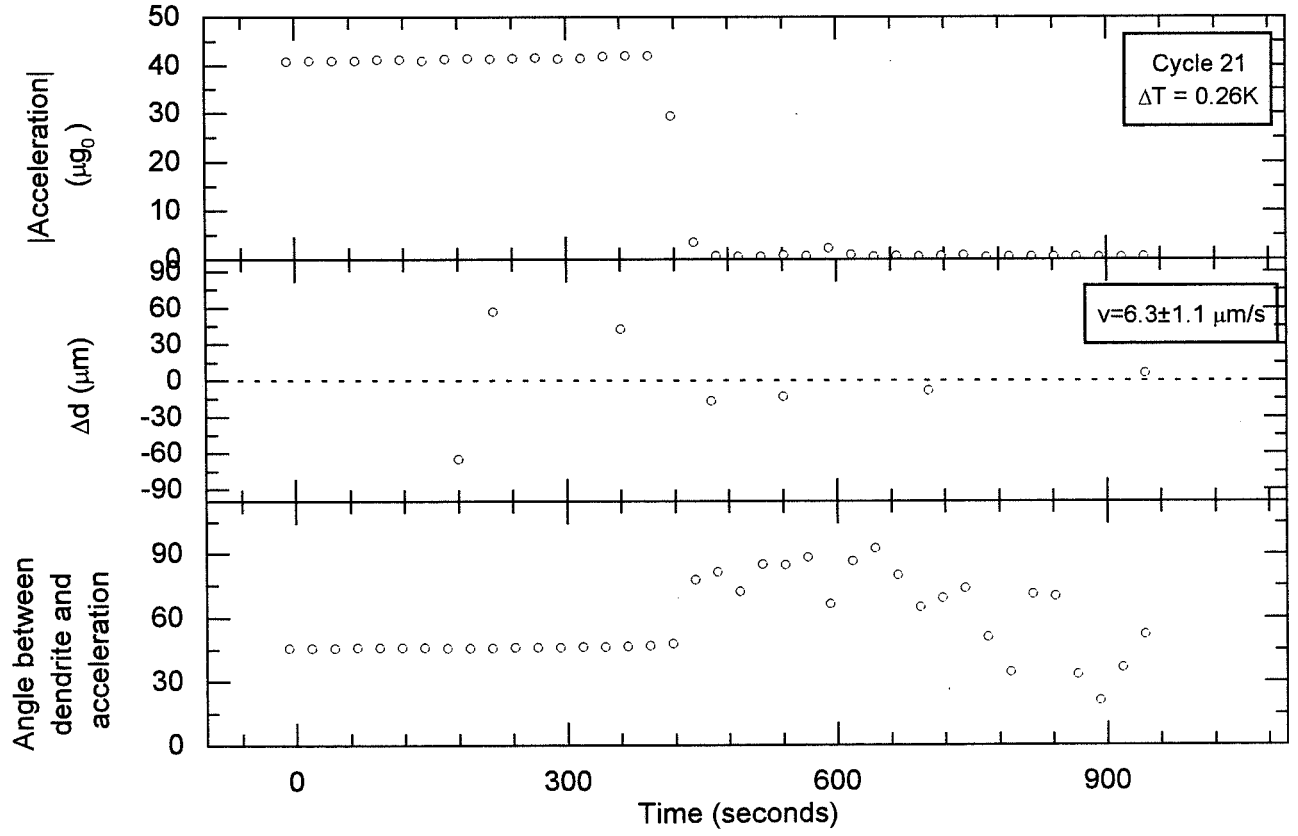

Figure 5: An abrupt change in the microgravity vector does not seem to affect the dendrite.

Page intentionally left blank

The Effect of Microgravity Direction on the Growth of PbSnTe

A.L. Fripp, and W.J. Debnam
NASA Langley Research Center
Hampton, VA 23681
Phone: 757-864-1503
FAX: 757-864-7891
email: a.l.fripp@larc.nasa.gov

W.R. Rosch
National Research Council
NASA Langley Research Center
Hampton, VA 23681-0001
Voice: 757 864-1534
Fax: 757 864-7891
E-mail: w.r.rosch@larc.nasa.gov

R. Narayanan
Department of Chemical Engineering
University of Florida
Gainesville, FL 32611
Voice: 352 392-9103
Fax: 352 392-9513
E-mail: ranga@pine.circa.ufl.edu

Introduction

The Space Shuttle *Columbia* was launched as STS-75 at 2018 GMT (Greenwich Mean Time) on February 22, 1996. One of the two major experiment packages was the Third United States Microgravity Payload (USMP-3), and one of the principal instruments on the USMP was the Advanced Automated Directional Solidification Furnace (AADSF). The AADSF is a multizone directional solidification furnace, and at the time of the USMP-3 flight was capable of processing only one sample per Shuttle mission which, for that flight, was a lead tin telluride (PbSnTe) crystal growth experiment. Archibald L. Fripp of the NASA Langley Research Center was the Principal Investigator.

In the one year since the flight experiment the sample has been retrieved from the spacecraft and analysis has begun. After presenting introductory material on why PbSnTe was chosen as a test material, why microgravity processing was expected to produce desired results, and what we expected to find in conducting these tests, this report will discuss the results to date which are far from complete.

Lead Tin Telluride:

Lead tin telluride is an alloy of PbTe and SnTe. The technological importance of PbSnTe lies in its band gap versus composition diagram which has a zero energy crossing at approximately 40% SnTe. This facilitates the construction of long wavelength (>6 μm) infrared detectors and lasers. The properties and utilization of PbSnTe are the subject of other papers.[1,2]

PbSnTe is amenable to study because it is easily compounded, it has a relatively low vapor pressure, and it is miscible with the same crystal structure for all compositions. There is also existing, though limited, literature on its growth and properties. The nominal composition for this work is 20% SnTe and 80% PbTe that produces a bandgap to match the long wavelength atmospheric window.

PbSnTe is also interesting from a purely scientific point of view. It is, potentially, both solutally and thermally unstable due to the temperature and density gradients present during growth. Density gradients, through thermal expansion, are imposed in directional solidification because temperature gradients are required to extract heat. Solutal gradients occur in directional solidification of alloys due to segregation at the interface. The gradients vary with both experiment design and inherent materials properties.

In a simplified one-dimensional analysis with the growth axis parallel to the gravity vector, only one of the two instabilities works at a time. During growth, the temperature in the liquid increases ahead of the interface. Therefore the density, due to thermal expansion, is decreasing in that direction. However, the phase diagram shows that the lighter SnTe is preferentially rejected at the interface. This causes the liquid density to increase with distance away from the interface, which is opposite from the density change due to the furnace temperature profile. Figure 1 is a plot of the composition vs. axial position of a typical Earth-grown crystal. The data points are plotted along with the analytical solution for the totally mixed case.

Coriell *et al.*[3] have shown that the two opposing density gradients cannot be readily balanced to stabilize the flow. Moreover, both experiments[4,5,6,7] and numerical analyses[5,8] have demonstrated that radial thermal gradients will start fluid motion long before the onset of convection predicted by a one-dimensional model. Hence, there will always be convection in the liquid.

Computational fluid dynamics was utilized to predict the extent of convection in microgravity. The CFD calculations were based on a finite volume technique.[9] The computational code allowed the calculations of time dependent three-dimensional flows and associated temperature and concentration profiles. The method behind the calculations involves the division of the calculation domain into a number of cells and then the field equations for mass, momentum and energy conservation are integrated over the volume of the cell. The calculation routine then involves the prediction of the field variables of temperature, concentration, velocity components and pressure at the various cell faces.

In practice the finite volume technique is used iteratively. Temperature and concentration fields are first guessed; they affect the body force through their effect on buoyancy. The corresponding velocity and pressure fields are then calculated. The computed velocity field is used to correct the earlier estimate of the temperature and solutal concentration field and the process continues until a desired convergence is reached.

This procedure is best explained by considering Figure 2. The ampoule liquid region is assumed to be constant as the solidification rates are normally very small. The boundary conditions indicate hot and cold zones as well as insulating zones. The far field concentration is assumed to be constant and the interface condition respects mass conservation along with solutal segregation. The effect of the magnitude of the gravity vector is seen in Figures 3 and 4, and we immediately conclude that the flow at low frequency low amplitude accelerations (10^{-5} g_e) will be of a weak toroid. Higher amplitude forces will cause solutal convection to come into play, but such high amplitude acceleration vectors were not present at the low frequency levels during USMP-3 and were mainly associated with high frequency activities such as booster firings and water dumps. While

we do not presently have any predictions on the effects of high frequency g-jitter it is clear from the order of magnitude of the calculated velocity vectors for the case of low frequency with 10^{-5} g_e that very little mixing should take place. The velocity is no greater than 10^{-5} cm/sec. Given an initial liquid region size of 5 cm, this small velocity amounts to an initial mixing time of 10^6 seconds. Meanwhile the solidification is at the rate of 1 cm/hour. When the liquid region size is about 1 cm the mixing time is about 2×10^5 seconds. Clearly this is insignificant because the entire growth period is about 2×10^4 seconds. In other words we predict that only diffusion controlled growth ought to prevail at $10^{-5}g_e$ and this is even more true at the lower gravitational levels experienced during the USMP-3 mission.

The effect of a five degree offset with respect to the vertical orientation was calculated and the results are graphically shown in Figure 3(c). What is seen from this figure is that small tilts give rise to swirling flow and this flow contains the solutal boundary layer to the depleting surface. This may be contrasted with toroidal flow in Figure 3(a) (for the vertical orientation) that sweeps the solute out of the solutal boundary layer. The solutal boundary layer contains most of the rejected SnTe and so swirling flow if anything should help by making diffusive growth more probable. In other words one might conclude that a constant off axis arrangement is better than if the acceleration vector were perfectly aligned along the ampoule. Figure 4 is a depiction of the mixing patterns that are seen when the ampoule is subjected to a time dependent tilt. It must be noted that the velocities are still very small and so even in the case when the tilt is a periodic function of time the growth is expected to be diffusion controlled.

In summary, we have concluded that diffusive growth was predicted under low frequency g-jitter conditions. The high frequency was not studied but we did conclude that the time constant for the fastest transporting mechanism (heat transfer) was much larger than the corresponding period for high frequency (5 Hz) g-jitter.

Bridgman Growth:

Bridgman crystal growth offers the opportunity to independently fix the temperature gradient and interface position with respect to the furnace. However, these parameters cannot be varied without bound. There are temperature limits on the furnace and ampoule as well as limits imposed by the growth process. An excellent review of recent advances in Bridgman growth has been given by Favier.[10]

The limits imposed by the growth process are primarily concerned with maintaining an initial solutal translation zone of reasonable length and preventing interfacial instability. Second order problems are the maintenance of interface shape control and thermal strain in the solid.

Due to the size of the AADSF, a sufficiently high growth rate is required to achieve steady state composition within 20 to 30 millimeters of the start of growth. The furnace must then be controlled to produce an axial thermal gradient in the melt that is sufficient to maintain a stable interface. If the growth is diffusion controlled, the growth distance needed to get within 1% of compositional steady state (i.e. uniform) growth is[11]

$$z_{ss} = 5D/kR \ . \qquad (1)$$

However, the permissible growth rate is limited by the fundamental phenomena of interface breakdown. The short form of the equation for preventing breakdown is

$$\frac{G_T}{R} > \frac{C_s}{D}\frac{(1-k)}{k}|m|. \qquad (2)$$

Equation (1) shows that a short initial transition zone requires a high growth rate while Equation (2) shows that a high growth rate requires a large thermal gradient to avoid interfacial breakdown. Increasing either the axial thermal gradient or the growth rate increases the density gradient and the mixing in the liquid. Consequently, it can be seen that there is a trade-off between growth rate, temperature gradient and the degree of mixing for a given acceleration level.

The PbSnTe growth experiment on USMP-3 was launched in February 1996. During the flight, three separate crystals were grown in a single, segmented ampoule. The crystals were grown in series, each in one of the three primary orientations with respect to the residual acceleration vector. The growths were roughly analogous to hot-on-top, cold-on-top, and horizontal growth.

While the immediate objective of that experiment was to grow PbSnTe and establish its fundamental growth properties, another, more important objective was to gain a better understanding of the mechanisms involved in generalized crystal growth, particularly those affected by gravity. This information will not only help produce better quality materials on Earth, but also help define future efforts of crystal growth in space and lead the way to more extensive materials science research.

Segmented Ampoule:

As mentioned before, the USMP-3 AADSF experiment used a single segmented ampoule to grow three separate PbSnTe crystals in series. The ampoule, represented in Figure 5, allows each of the three crystals to grow with different conditions without affecting the outcome of the others. For USMP-3, each crystal was grown identically except for the orientation of the ampoule with respect to the residual acceleration[12] vector.

Even though the use of a three cell ampoule decreases the total crystal length, and the percentage of crystal grown where the growth rate nearly matches the translation rate, it allows each of the cells to be grown under nearly identical conditions. A long crystal will obtain a nearly thermal steady state growth region sandwiched between two end effect thermal and compositional transient regions. Using the three cell sample decreases the length of any steady state region; however, it provides growth conditions that are nearly thermally equivalent for each of the three cells. Most important, it keeps the composition for the three different regions separated, so that each crystal will have identical starting compositions. Each cell is long enough to reach compositional steady state before the liquid diffusion tail reaches the end of the ampoule.

Results

Flight Operations

Space Shuttle *Columbia* (STS-75) was launched at 2018 GMT on February 22, 1996. The launch time defined Mission Elapse Time (MET) as 00 days/00 hours:00 minutes. This nomenclature, MET xx/yy:zz, without units, will be used to identify the relative time of events throughout the text of this report.

With the sample withdrawn 35 mm from its fully inserted launch position, the AADSF started heating at MET 06/10:07. Ampoule positions will be given by a translation position measurement, tpm, taken as the distance the ampoule is extracted, in mm, from full insertion, hence the present position is tpm = 35. The furnace was at temperature, hot zone 1150 °C and cold zone 525 °C, at MET 06/14. After a four hour thermal stabilization period the sample was repositioned to tpm = 37 where tc 1, in the base of cell #1, read 930 °C, which was the so called "start condition." Translation, at 10 mm/hr, to nucleate a seed in cell #1 started at MET 06/20:50. As deep undercooling[13] is not anticipated and the recalescence event is clearly obvious, at least on Earth, nucleation was expected within 15 cm (1 hr 30 min) after the start of translation. As of MET 06/22:55 no recalescence had been noted, and the translation was reversed to remelt, assuming nucleation had occurred, the solidified portion of the sample and reexamine the small temperature rise in tc 1 observed at 06/21:55. The sample was taken back to tpm = 37 and extraction translation resumed at MET 07/03:14, and the same perturbation in tc 1 occurred approximately 1 hr 5 min into the translation as it had done so the first time around (see Figure 6). This was taken as confirmation of recalescence and translation was stopped at MET 07/04:23. This remelting and re-nucleation procedure did not leave sufficient time for solutal diffusion before our "microgravity time" ended for day seven. An extra day for AADSF operations was requested and received.

At 08/02:14 the Shuttle was put into attitude pitch = 184.5°, yaw = 0°, and roll = 7° which had been calculated[12] to produce a nominal hot on top growth with respect to the microgravity acceleration vector. Dedicated microgravity time for cell #1 began at MET 08/03:00, and translation to grow the crystal in cell #1 started one hour later.

At MET 08/06:11, approximately 20 mm into the crystal growth, the Shuttle was put into an unscheduled free drift to help warm up a cold thruster nozzle. During a loss of signal (LOS) period the drift extended past expectations and at 08/06:41 had reached pitch = 187.6°, yaw = 5.2°, and roll = 27.9°. The Shuttle attitude was back to nominal settings by MET 08/06:48, but during the free drift time the acceleration vector alignment with respect to the furnace axis went from approximately 2° to approximately 45°. Figure 7 shows the three axis acceleration measurements, at the AADSF position during this period.

Translation was to continue until recalescence in cell #2. Both thermocouples in cell #2 were inoperable by this time so this step had to depend on knowledge of prior furnace calibration and tpm position rather than the observation of recalescence temperature changes. Translation continued to tpm = 120 which is well past the anticipated recalescence position and then reversed to tpm = 114.75 to remelt excess seed material. At this time all furnace translation stopped until the next dedicated microgravity time.

The Shuttle was positioned in attitude pitch = 90°, yaw = -17°, and roll = 0° at MET 09/02:19. Microgravity time begin at MET 09/03:00, and translation commenced one hour later to grow the crystal in cell #2. The cell #2 growth proceeded without any observed perturbations; however, the anticipated advent of recalescence in cell #3 looked as if it would occur in the midst of a forthcoming LOS period starting at approximately MET 09/11:12. As described previously, the plan had been to pause the furnace before the LOS, wait until re-acquisition of signal, and then continue translation. However, the diminution of the recalescence signal received from space as compared to that observed on Earth made reading the event amongst the stopping and starting of ampoule translation unlikely. It was decided to maintain the translation during the LOS, continue looking for the recalescence after the LOS until such tpm position where translation would have been stopped if both thermocouples had failed as with cell #2, and then to patch in the delayed transmission temperature data onto the curve as soon as it was available.

Translation was stopped at MET 09/11:36. The playback of LOS temperature data came in at 09/11:56 and showed that the recalescence in cell #3 occurred at about 09/11:17, the middle of the LOS. The translation was reversed for 2.5 mm to remelt part of the seed and then was stopped at tpm = 184.7 at MET 09/13:49 to await the next microgravity period to grow the crystal in cell #3.

The Shuttle went into the prescribed attitude pitch = 123°, yaw = 0°, and roll = 0° at MET 10/02:03. Microgravity time started at 10/03:00, and translation started at 10/04:00. The sample processed without major incident, and translation ceased at MET 10/10:36:48 at tpm = 250.28. A controlled furnace cool down started at MET 10/11:40:55. The ampoule was stored in the cold furnace at MET 10/20:02.

Acceleration Magnitudes and Directions

Calculation of the acceleration vectors at the insulation zone of the AADSF as a function of the Space Shuttle attitude produces a transcendental equation as the resultant transformation matrix is dependent on time and attitude varying drag, orbit shape and altitude, and the distance and direction of the AADSF from the center of gravity of the Shuttle. See references 14, 15, 16, and 17 for more information on this topic. As the attitude to produce what is essentially hot on top, hot on bottom, and horizontal growths could not be obtained from minimization of the transformation equation a study[18] was undertaken to try to zero in on the preferred attitudes. This and a subsequent, unpublished, study determined the Shuttle attitudes for the three different growth orientations with the following acceleration vectors and concomitant angles.

Note: The following values are nominal. They vary with, among other things, Shuttle drift, orbit position, and sun angle. Also, directions are given in body coordinates for the direction an object would travel in a less massive fluid. In this system an object, at the AADSF location, in attitude #1 would travel away from the center ofthe Shuttle through the cargo bay doors. This direction is from the hot zone of the AADSF toward the cold zone which is analogous to hot on top furnace orientation on Earth.

Attitude #1, Hot on top growth.

Pitch = 185°, Yaw = 0°, Roll = 7°
Acceleration along the Z axis = -0.75 micro g
Acceleration along the X axis = 0.01 micro g
Acceleration along the Y axis = 0.02 micro g
Approximate angle of acceleration vector with respect to AADSF center bore is approximately 2°. The desired angle is 0°.

Attitude #2, Hot on top bottom.

Pitch = 90°, Yaw = -17°, Roll = 0°
Acceleration along the Z axis = 0.2 to 0.4 micro g Acceleration along the X axis = -0.01 micro g
Acceleration along the Y axis = 0.1 micro g
Approximate angle of acceleration vector with respect to AADSF center bore is 140° to 160°. The desired angle is 180°.

Attitude #3, Horizontal growth.

Pitch = 123°, Yaw = 0°, Roll = 0°

Acceleration along the Z axis = 0.1 to 0.1 micro g Acceleration along the X axis = -0.4 micro g
Acceleration along the Y axis = 0.15 micro g
Approximate angle of acceleration vector with respect to AADSF center bore is -76° to 76°. The desired angle is 90°.

None ofthese attitudes are ideal. Attitude #1 is closest to that desired, and attitude #3 averages to the desired value of 90°, but the 14° variation is not desirable.

In addition to the drag and position effects of the low frequency accelerations on the sample the drag deceleration and the tendency for the orbiter to get into an aerodynamically stable mode necessitated the need for vernier booster firings. The forces associated with these corrective measures were of high magnitude (roughly $10^{-3}g_e$ - $10^{-4}g_e$) but were of a high frequency (5-10 Hz).

Comparison of these calculations to the measurements made in flight will be the subject of a subsequent paper.

Results, Post-Flight

X- and Gamma Ray Radiography

The flight sample was retrieved from the AADSF at the Kennedy Space Center in April 1996. Microfocus x-ray was used to examine the quartz ampoule for cracks before removal of the Inconel cartridge. No cracks in the fused quartz ampoule were observed, but the shadow outline of the crystals appeared much longer than expected.

The samples were further examined, still in the Inconel cartridge, with the 420 KV computer aided tomography (CAT) unit also available in the KSC non-destructive test laboratory. These high voltage x-rays are capable of penetrating the PbSnTe samples and exposing any voids, large pits, and bubbles. The results shown by this examination were totally unexpected; the crystals are cratered with large voids and riddled with meandering channels. Figure 8 shows a selected vertical slice of each crystal. This figure was made by reconstructing the transverse slices gathered in the normal CAT fashion. The CAT slices of each crystal are shown in Figures 9 to 11.

Similarities among the three crystals are that the initial formation, in the cold end of each of their respective cells, is a complete solid crystal that completely filled the base of that cell. (This solidarity of structure in the base did not hold upon microscopic examine. This topic will be discussed more fully in a later section.) After the formation of the base section, which is longer than the anomalous compositional distribution due to recalescence, each crystal then necked down almost to the point of discontinuity. The channels and cavities emanate from the upper (terms such as base and upper, of course, have their etymology in references to Earth gravity; here they are merely convenient terms to refer to positions relative to the coldest part of each experimental growth cell) ends of the voids that formed the necked down region. Finally, the last to freeze ends of the crystals become solid again.

The primary difference in x-ray appearance is the way a double set of cavities formed in cell #1 as opposed to the surface channels in the other two crystals.

These results were totally unexpected. Large pores or voids have been found in other space-grown crystals[19,20], but no large pores or other voids were found in the PbSnTe

crystal grown on the 1985 STS 61-A mission, and although Kinoshita[23] reported some porosity, his photographs showed monolithic crystals compared to these.

Sample Composition

The primary objective of this flight experiment was to examine the effect of the direction of the microgravity vector on the convective mixing of the liquid during directional solid)fication. The measurable physical parameter that is the most sensitive monitor of mixing in the liquid is the compositional profile in the solidified crystal. The difference in the analytical solutions for the profiles for both fully mixed and mixing via diffusion alone is shown in Figure 12.

Figures 13 to 15 are axial compositional profiles for cells #1 to #3, respectively. Each cell shows evidence of considerable mixing. With one minor exception, the free drift period already discussed, the Space Shuttle performed the pre-determined maneuvers for the growth periods as required, but the presence of voids creates the condition for surface driven (Marangoni) convection.[22] The problem now becomes that of separating Marangoni convection from density driven convection.

Figure 13 shows the axial compositional distribution of cell #1. The anticipated spike of SnTe shows the recalescence area at the left side of the plot, then the data flattens for what may be growth during thermal stabilization after the release of the latent heat. At 5 mm of growth, approximately the length of the produced seed after the solutal diffusion time, the composition shows signs of trying to go to diffusion growth but not making it. At approximately 25 mm of growth the curve closely approximates the fully mixed case. The following deserves further study, but the melt-solid interface would have been 25 mm from the base of cell #1 at approximately MET 08/06:30, the time of the Shuttle free drift which would have essentially turned the AADSF on its side for a few minutes.

After recalescence the axial compositional profile of the crystal in cell #2, the nominally hot on bottom orientation, follows the completely mixed curve for the first 45 mm of growth and then exhibits deviations (see Figure 14) that are, as yet, unexplained. Similar deviations occur in the axial compositional profile of the crystal grown in cell #3, but over a longer section (see Figure 15). As yet no acceleration perturbations have been related to these compositional variations. These crystals will be examined to try to correlate these compositional deviations with crystalline microstructure and the defect formation.

Microporosity

Figures 16 to 18 are photomicrographs of the first to freeze regions of cells #1 to #3 respectively. The first to freeze regions of the crystals grown in cells #1 and #3 clearly show random patterns of sub-millimeter pores which were not visible on the CAT scans. A few pores were seen at the very base of the crystal from cell #2, but the defects are not clearly visible in the attached figure. The volume of the pores in cells #1 and #3 were estimated using a retinex[23] technique to be approximately 4% of total in the base region. This value is the same as the volume reduction upon the phase change from liquid to solid state.

Summary

This paper is a work in progress for we are far from finishing the analysis of these fascinating and tantalizing samples. We started the flight experiment to determine the small, but predictable, differences in convective mixing due to the alignment of the acceleration vector. We are still trying to extract data on that topic, but such information is buried in the myriad observations of the large pore, void, and channel formations.

We have been able to show a few things within this time frame that are useful to the microgravity materials science community, and we believe that we will deliver a complete story when we complete the evaluation and analysis of the USMP-3 experiment, especially when we couple the results with the upcoming USMP-4 crystal growth experiments and the experiments of others in this area.

Acknowledgments

Many thanks to the many people the made this exciting work possible. To acknowledge everyone who contributed to the years of effort that went into this work would exceed the page limit of this paper. The Investigators are truly humbled by the effort, dedication, sacrifice, and brilliance offered by so many program, project, and support staff that make these esoteric space projects possible. They are the people who do all of the work while we get the glory. Thank you.

A precious few must be mentioned by name which in no way detracts from all the rest. We offer special thanks to Bob Rhome who guided the program and encouraged us to stay with it during internal reorganizations; Mike Wargo who shepherded the science and kept us on our toes; Roger Crouch, the sparkplug so vital to us in the earlier days; Fred Reeves, Jim Sledd, and Linda Jeter who kept nuts, bolts, and schedules together; Kent Pendergrass and Wayne Gandy who helped us learn what the furnace could do; Sandor (Alex) Lehoczky, Don Gillies, Peter Curreri, and Sherwood Anderson who guided us to flight; Bob Berry, Dick Simchick, Ned Baker, Glenn Woodell, and Jim Wells who have done so much for us at Langley; and Peter Engel at KSC for his expertise with the CAT unit. To one and all of them I say a very sincere and heartfelt, "Thank you."

References

1. T.C. Harman. "Control and Imperfections in Crystals of PbSnTe, PbSnSe and PbSSe." *J. Nonmetals I*, p 183 (1973).

2. S.G. Parker and R.W. Johnson. "Preparation and Properties of PbSnTe." in Preparation and Properties of Solid State Materials, vol. 6, W.R. Wilcox, ed., Marcel Dekker, Inc., New York, p 1 (1981).

3. S.R. Coriell, M.R. Cordes, W.J. Boettinger, and R.F. Sekerka. "Convective and Interfacial Instabilities During Unidirectional Solidification of a Binary Alloy." *J Crystal Growth*, vol. 49, p 13 (1980).

4. J.H. Hurst. "Electrochemical Visualization of Convection in Liquid Metals." Ph.D. Dissertation, The University of Florida, Chemical Engincering (1990).

5. B. Sears, R. Narayanan, T.J. Anderson, and A.L. Fripp. "Convection of Tin in a Bridgman System: I. Flow Characterization by Effective Diffusivity Measurements." *J. Crystal Growth*, vol. 125, p 404 (1992).

6. B. Sears, A.L. Fripp, W.J. Debnam, G.A. Woodell, T.J. Anderson, and R. Narayanan. "Convection of Tin in a Bridgman System: II. An Electrochemical Method for Detecting Flow Regimes." *J. Crystal Growth*, vol. 125, p 415 (1992).

7. B. Sears, T.J. Anderson, R. Narayanan, and A.L. Fripp. "The Detection of Solutal Convection During Electrochemical Measurement of the Oxygen Diffusivity in Liquid Tin." *Metallurgical Transactions B*, vol 24B, p 91 (1993).

8. F.M. Carlson, A.L. Fripp, and R.K. Crouch. "Thermal Convection During Bridgman Crystal Growth." *J. Crystal Growth*, vol. 68, p 747 (1984).

9. S. Patankar. "Numerical Heat Transfer and Fluid Flow." Taylor and Francis, Bristol, Pennsylvannia (1980).

10. J.J. Favier. "Recent Advances in Bridgman Growth Modelling and Fluid Flow." *J Crystal Growth*, vol. 9, p 18 (1990).

11. W.A. Tiller, K.A. Jackson, J.W. Rutter, and B. Chalmers. "The Redistribution of Solute Atoms During the Solidification of Metals." *Acta Met. I*, p 428 (1953).

12. B.P. Matisak, A.X. Zhao, R. Narayanan, and A.L. Fripp. The Microgravity Environment: Its Prediction, Measurement, and Importance to Materials Processing. Presented at The Tenth American Conference on Crystal Growth, August 4-9, 1996, Vail, Colorado and accepted for publication in the *Journal of Crystal Growth.*

13. A.L. Fripp, R.K. Crouch, W.J. Debnam, I.O. Clark, and J.B. Wagner. "Effects of Supercooling in the Initial Solidification of PbTe-SnTe Solid Solutions." *J. Crystal Growth*, vol. 73, p 304 (1985).

14. R.C. Blanchard, M.K. Hendrix, J.C. Fox, D.J. Thomas, and J.Y. Nicholson. "Orbital Acceleration Research Experiment." *J. Spacecraft and Rockets*, vol. 24, p 504 (1987).

15. J.I.D. Alexander and C.A. Lundquist. "Motions in Fluids Caused by Microgravitational Acceleration and Their Modification by Relative Rotation." AIAA 25th Aerospace Sciences Meeting, January 12-15, 1987, Reno, Nevada, paper AIAA-87-0312.

16. B.P. Matisak, M.J.B. Rogers, and J.I.D. Alexander. "Analysis of the Passive Accelerometer System (PAS) Measurements During USMI-1." AIAA 32nd Aerospace Sciences Meeting, January 10-13, 1994, Reno, Nevada. paper AIAA-94-0434.

17. R. DeLombard. "Compendium of Information for Interperting the Microgravity Environment of the Orbiter Spacecraft." NASA Technical Memorandum 107032, August 1996, NASA Lewis Research Center, Cleveland, Ohio.

18. B.P. Matisak. "Update to USMP-3/STS-75 AADSF Attitude Design Study." #410RPT0736, Teledyne Brown Engineering, Huntsville, Alabama, August 31, 1995.

19. D.H. Matthiesen and J.A. Majewski. "The Study of Dopant Segregation Behavior During the Growth of GaAs in Microgravity." NASA Conference Publication

3272, vol. 1, p 223, May 1994. Joint Launch + One Year Review of USML-1 and USMP-1 with the Microgravity Measurement Group.

20. J.B. Andrews, L.J. Hayes, Y. Arikawa, and S.R. Coriell. "Microgravity Solidifcation of Al-In Alloys." 35th Aerospace Sciences Meeting, AIAA, Reno, Nevada, January 6-10, 1997.

21. K. Kinoshita and T. Yamada. "PbSnTe Crystal Growth in Space." *J. Crystal Growth*, vol. 147, p 91 (1995).

22. R.J. Naumann. "Marangoni Convection Around Voids in Bridgman Growth." *J. Crystal Growth*, vol. 154, p 156 (1995).

23. D.J. Jobson, Z. Rahman, and G.A. Woodell. "Properties and Performance of a Center/Surround Retinex." IEEE Transactions on Image Processing, vol. 6, p 451 (1997).

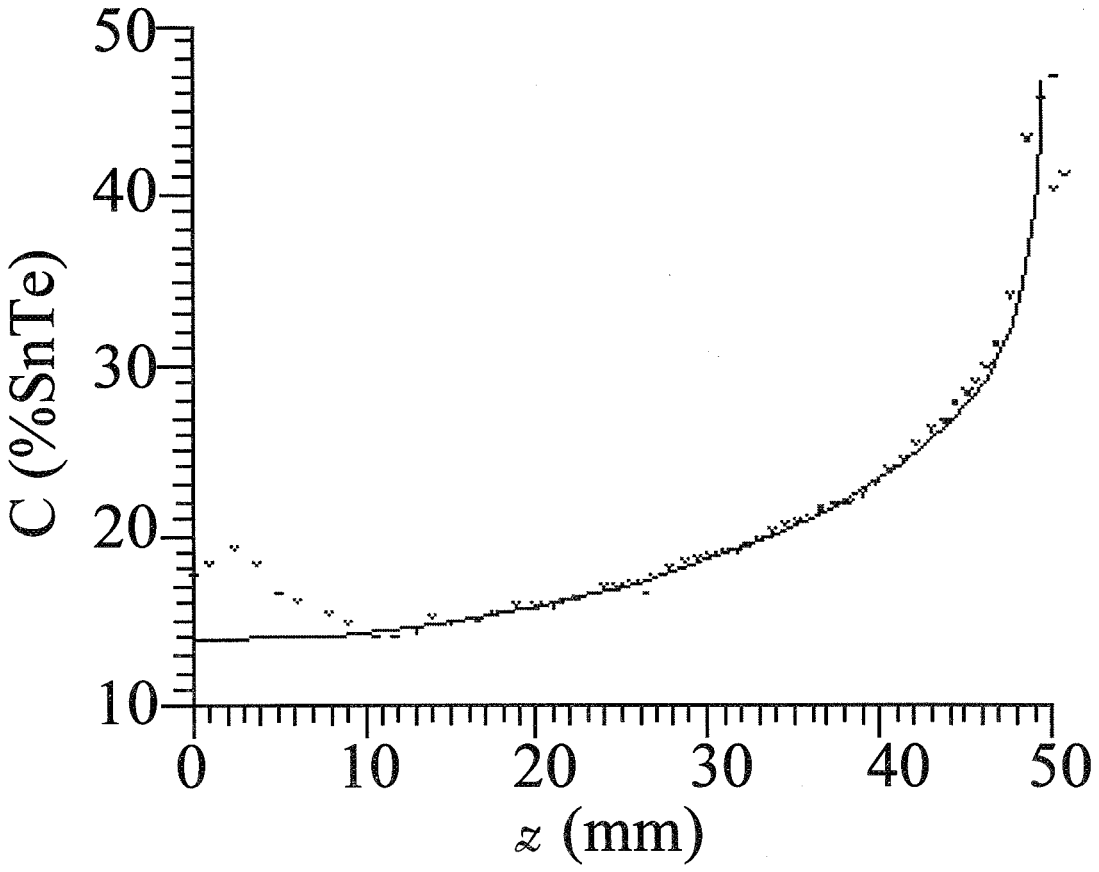

Figure 1. Axial composition of Earth grown PbSnTe crystal. The solid line is from the analytical equation for totally mixed melt. This crystal was grown in a low gradient furnace, hence the first to freeze region is larger than that of crystals grown in the AADSF.

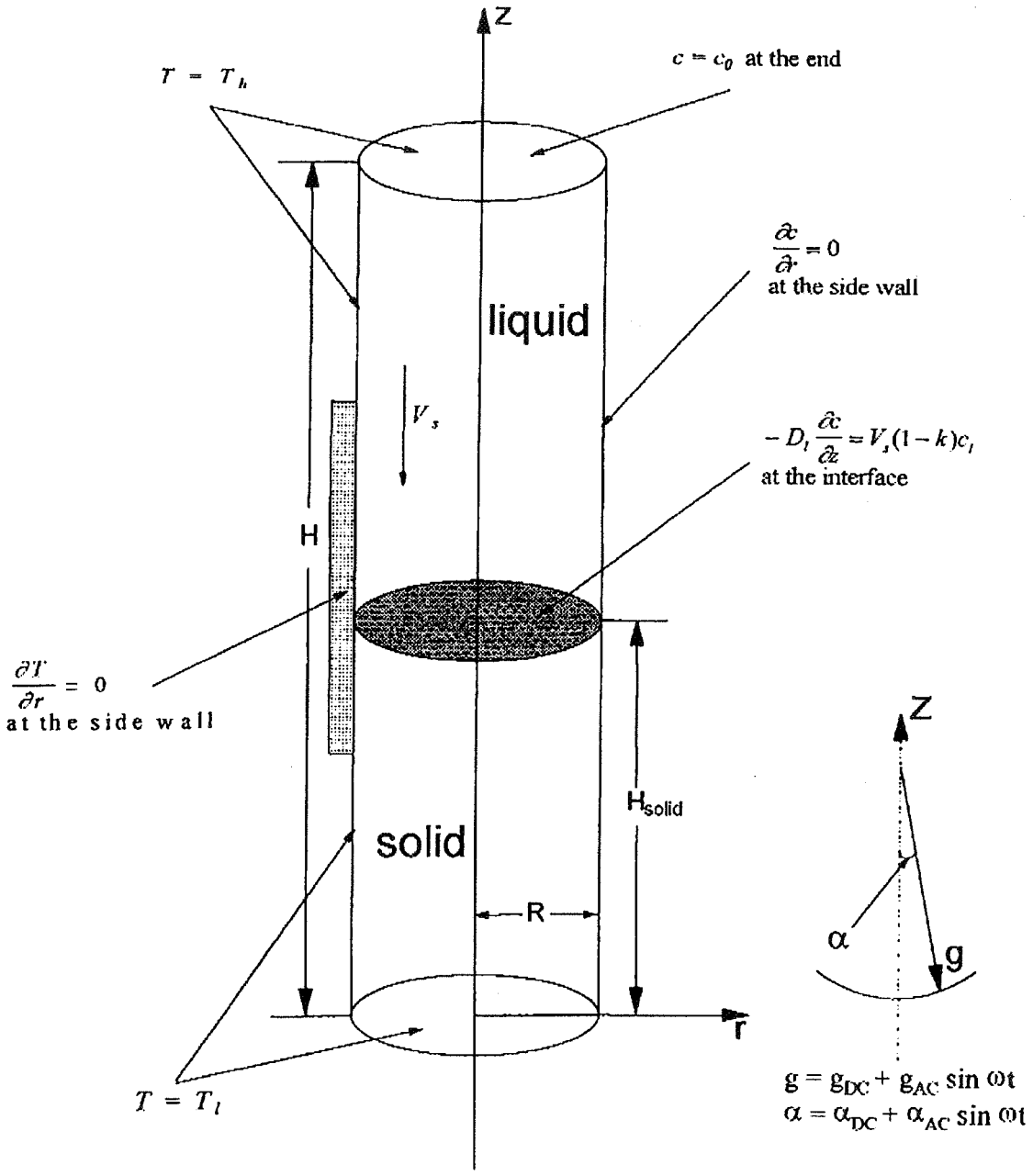

Figure 2. Schematic of the geometric, thermal, and concentration boundary conditions used in the computational fluid dynamical calculations in this study.

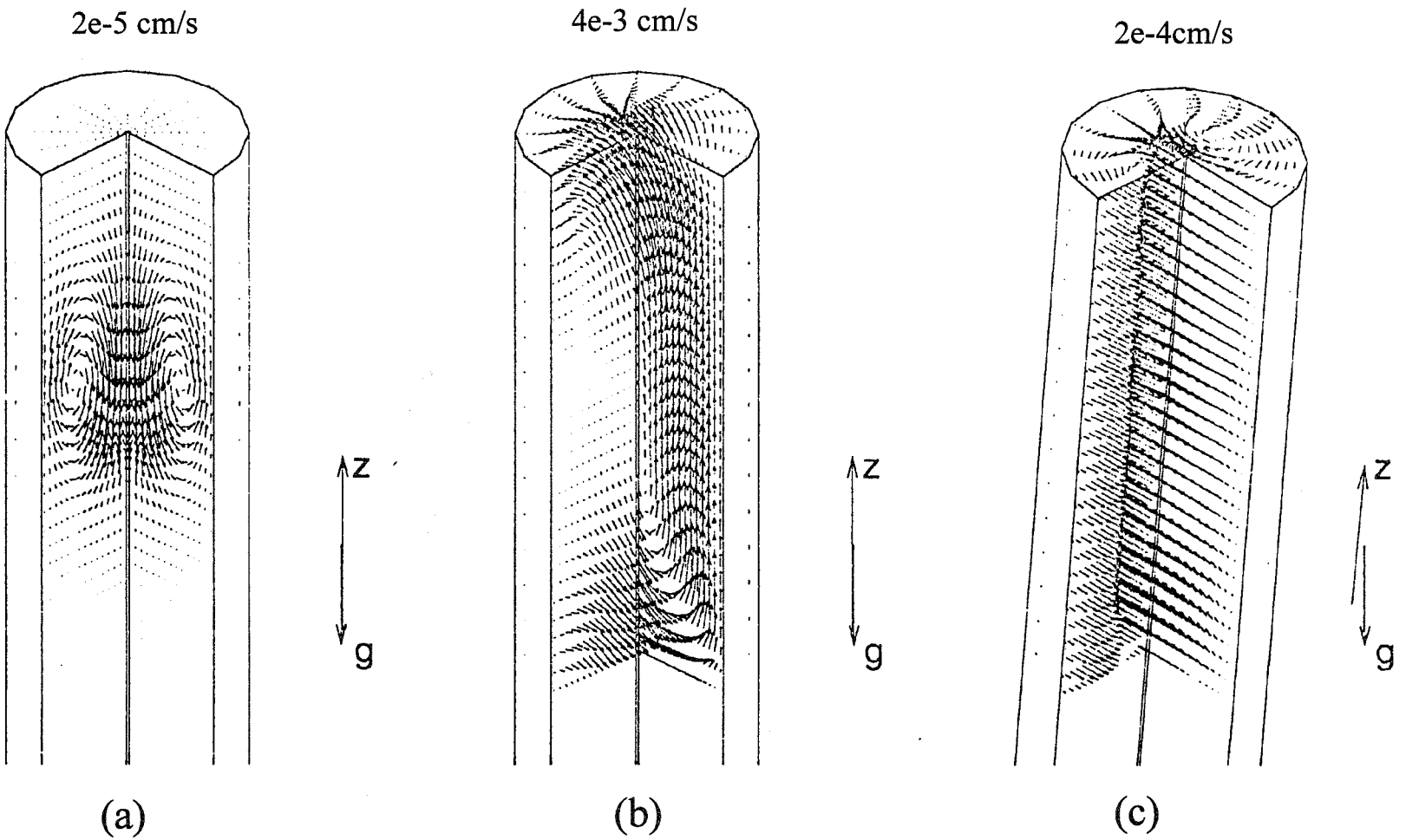

Figure 3. The three-dimensional flow field in the liquid region with constant acceleration magnitude and direction. (a) Acceleration is aligned with ampoule axis at 10-5 Earth gravity. (b) Acceleration is aligned with ampoule axis at 10-4 Earth gravity. (c) Acceleration is misaligned with ampoule axis by 5°with magnitude of 10-5 Earth gravity.

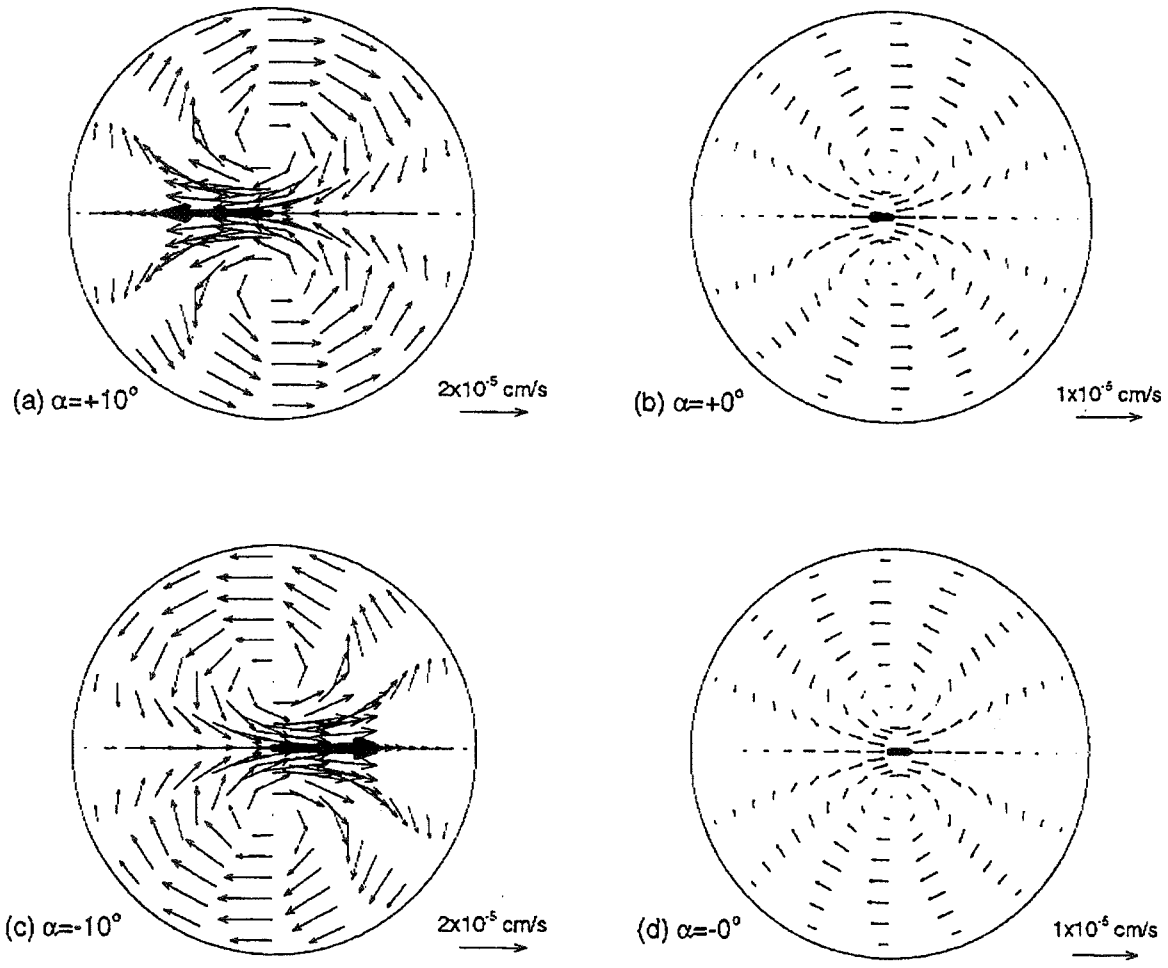

Figure 4. The two dimensional flow field near the melt solid interface when the acceleration vector (magnitude of 10-5 Earth gravity) is undergoing a 10°time dependent tilt variation at a frequency of one cycle per hour.

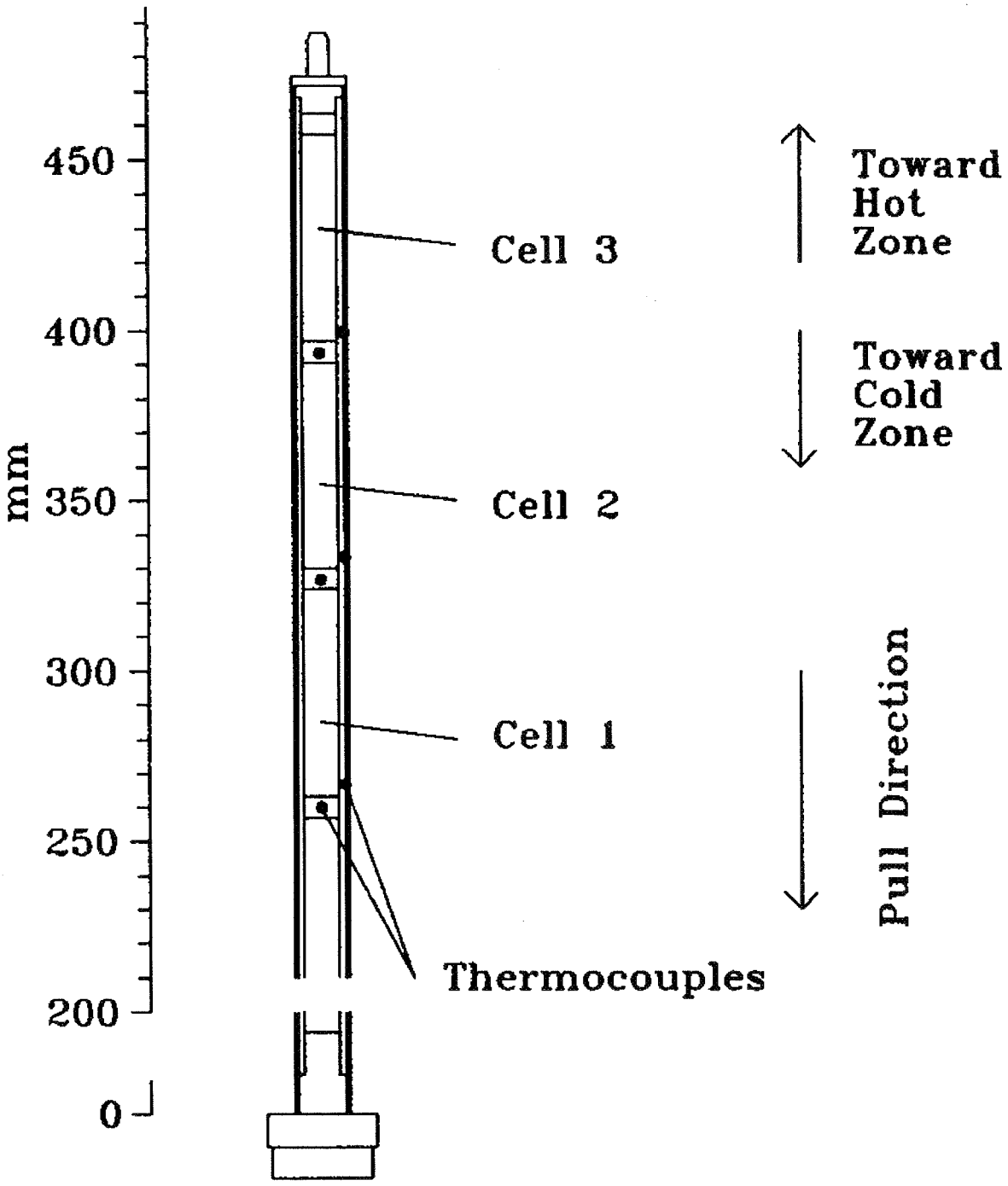

Figure 5. A typical segmented ampoule showing the three cells, and the location of the sample thermocouples.

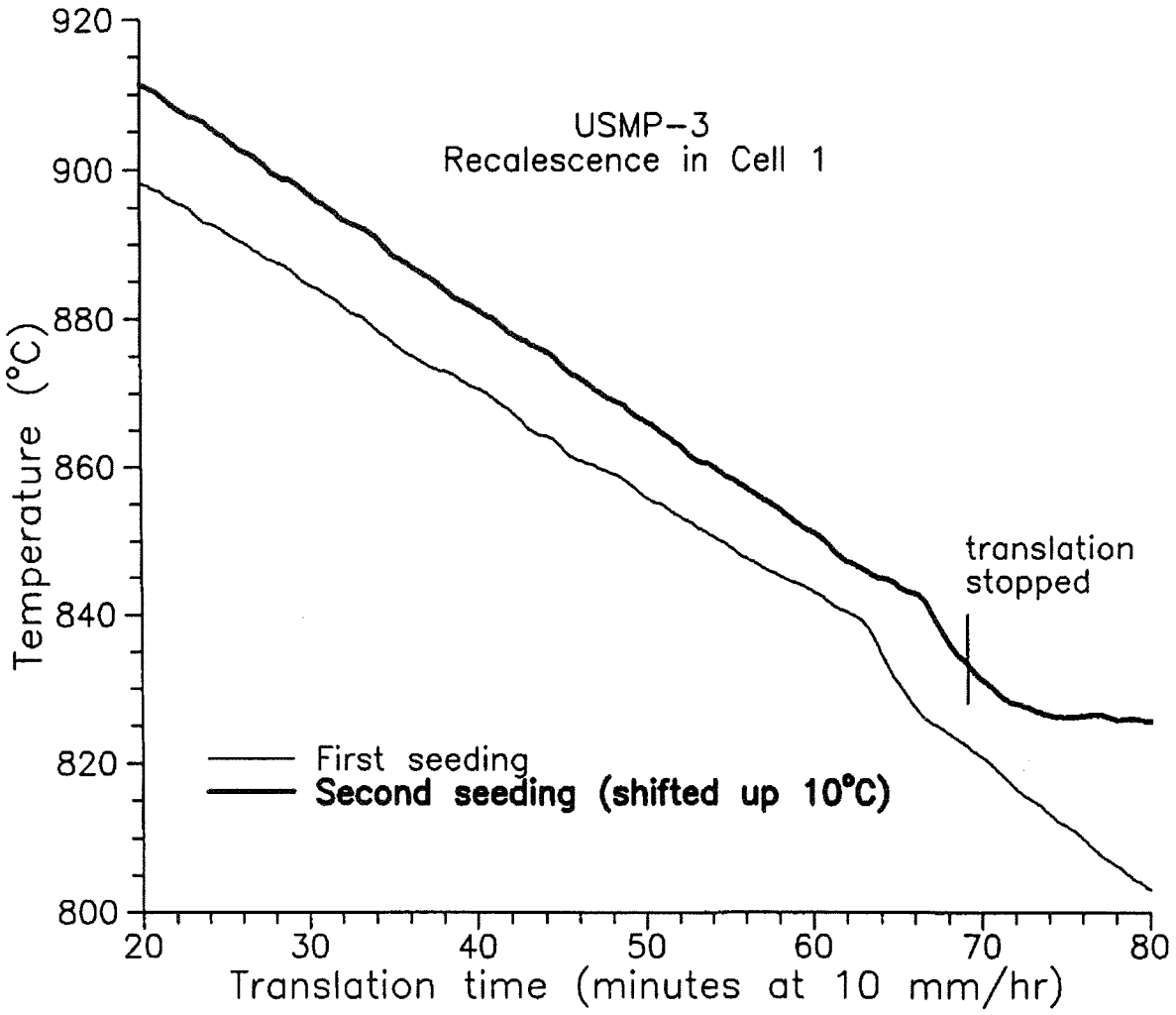

Figure 6. Temperature response the recalescence in cell #1. The response did not show a sharp peak as in Earth grown events, but showed a rounded temperature change. The event was repeated (upper curve displaced by 10 oC for clarity) to verify the observation.

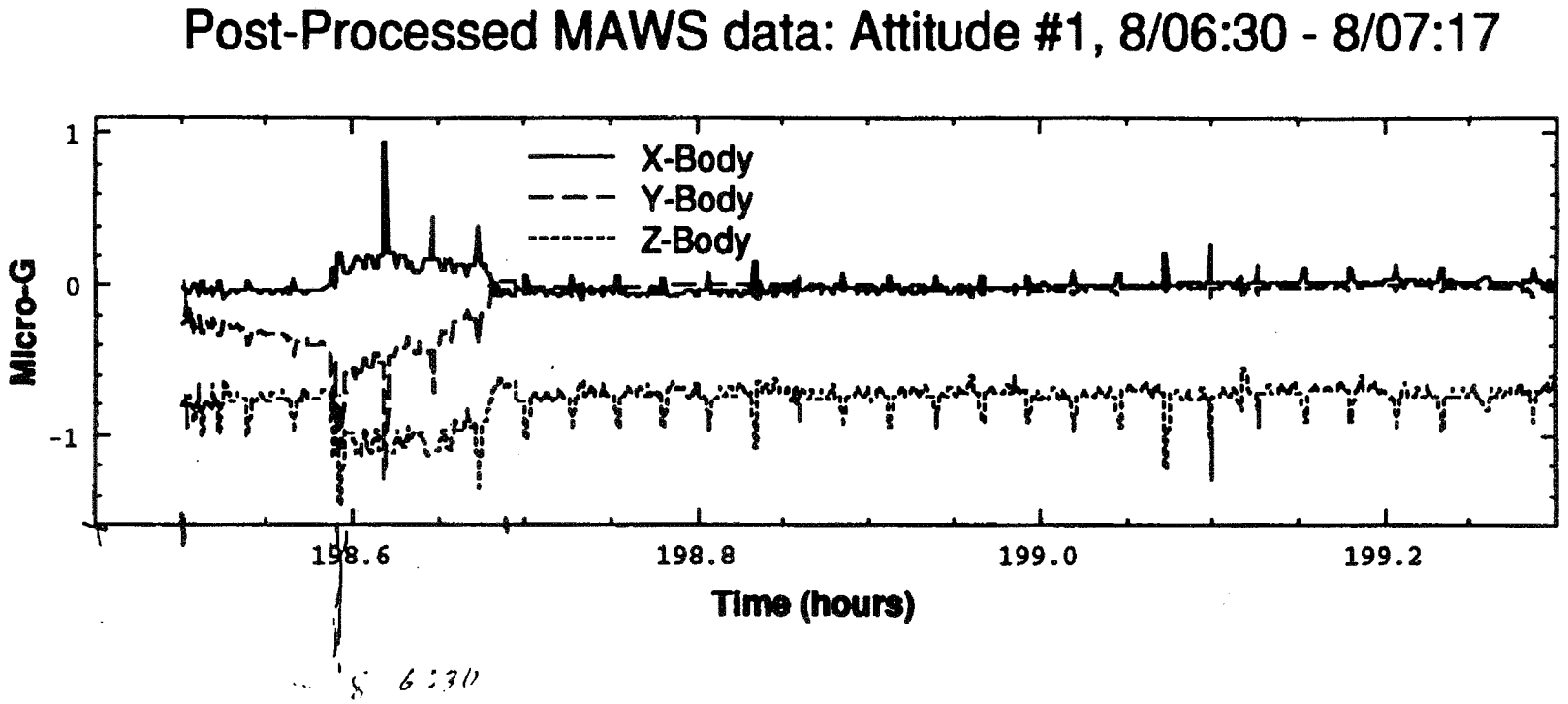

Figure 7. The acceleration magnitudes, at the AADSF freeze zone, for each of the three primary directions. The Z acceleration is along the AADSF furnace bore and in such direction that more dense fluid would move from the hot zone toward the cold zone. This time slice shows the acceleration during the free drift period that occurred at approximately MET 8/06:30 (198.6 hours on the graph).

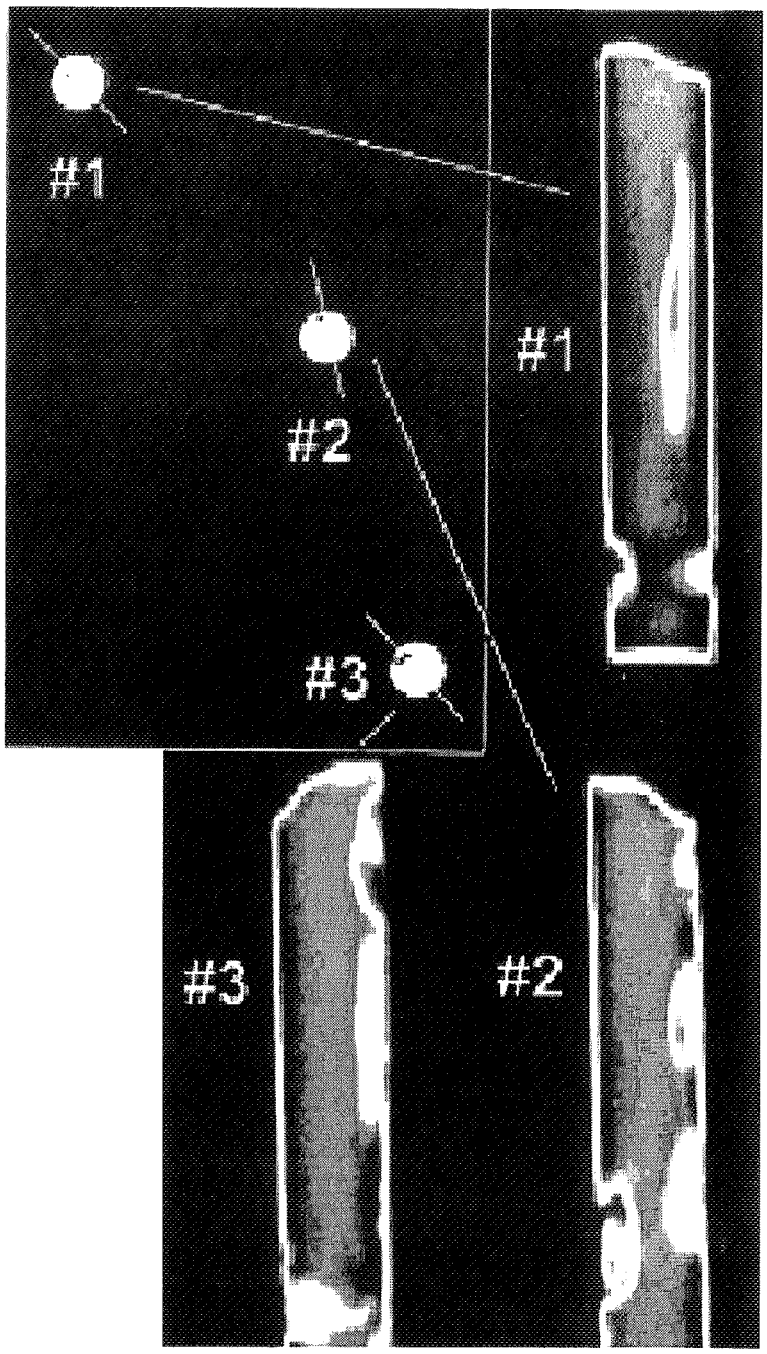

Figure 8. Vertical slices of the three USMP-3 PbSnTe crystals. These scans were made from the integrated results of CAT scans. Each crystal is positioned with the first to freeze end down. The insert at the upper left shows the position of the vertical slice for each crystal.

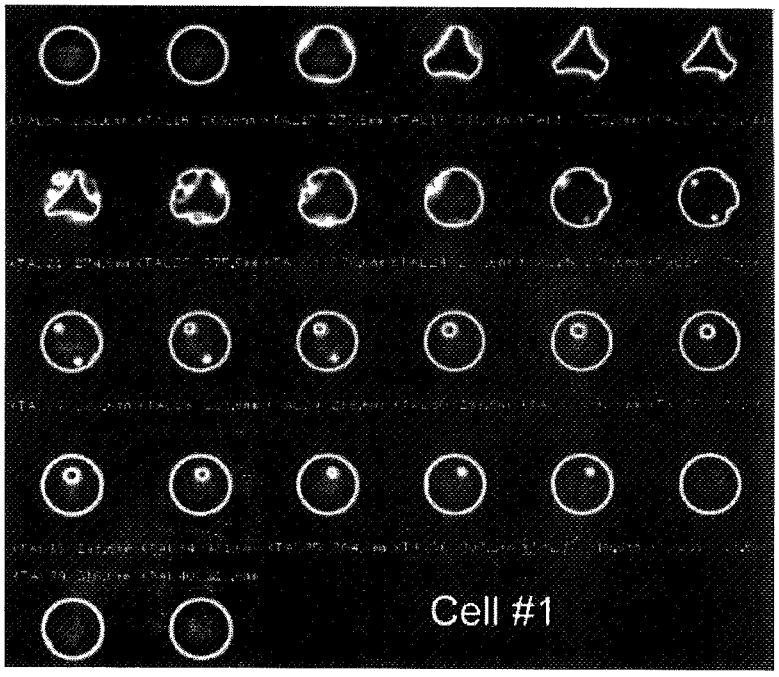

Figure 9. Successive CAT, horozontal, slices of Cell #1. The first to freeze end is at upper left. The first thirteen slices were taken at 1 mm steps and the remaining slices at 3 mm steps. Images were made with 420 KV x-rays.

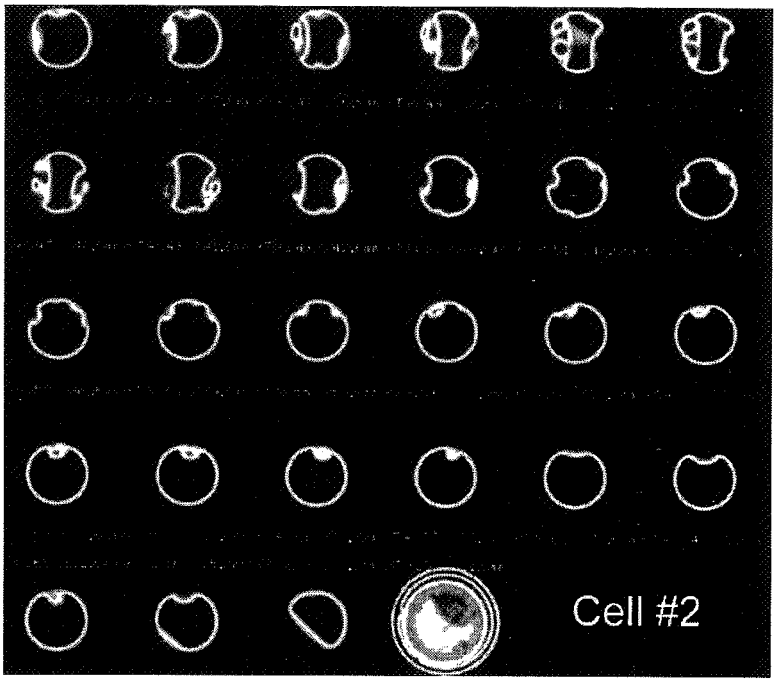

Figure 10. Successive CAT, horozontal, slices of Cell #2. The first to freeze end is at upper left. The first thirteen slices were taken at 1 mm steps and the remaining slices at 3 mm steps. Images were made with 420 KV x-rays. The first scan was taken approximately 8 mm above the base of the crystal hence it shows the beginning of the void formation.

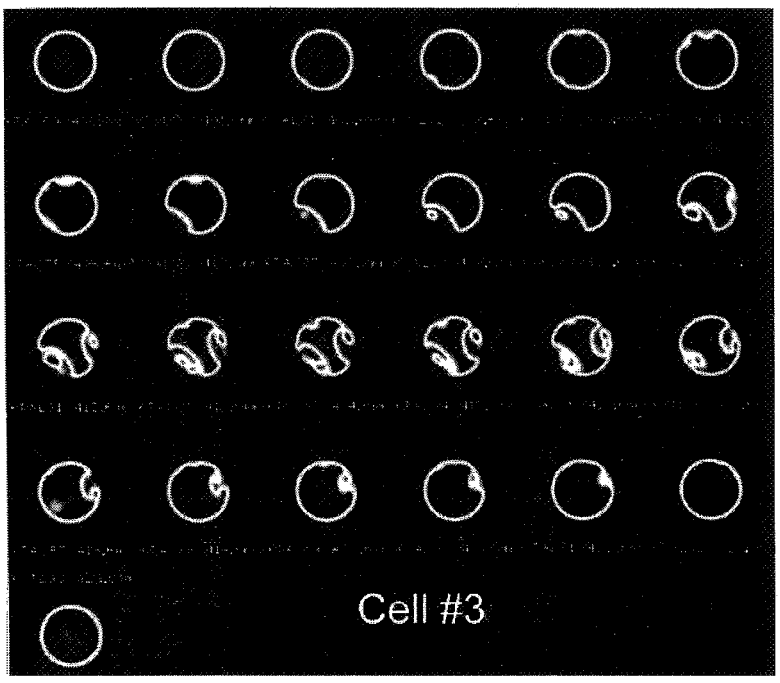

Figure 11. Successive CAT, horozontal, slices of Cell #3. The first to freeze end is at upper left. The first twenty six slices were taken at 1 mm steps and the remaining slices at 3 mm steps. Images were made with 420 KV x-rays.

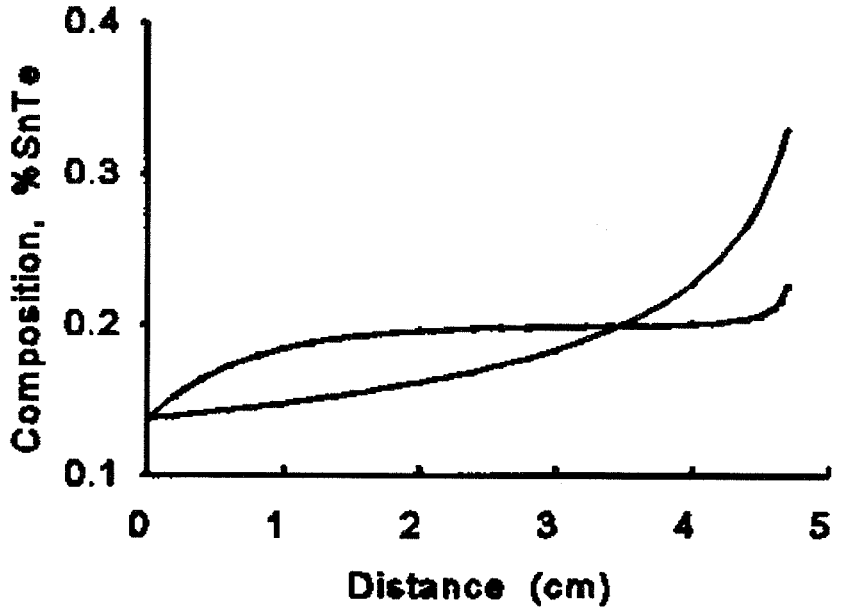

Figure 12. Graphs of the one dimensional analytical solutions for the profiles for both fully mixed and mixing via diffusion only during the directional solidification of PbSnTe.

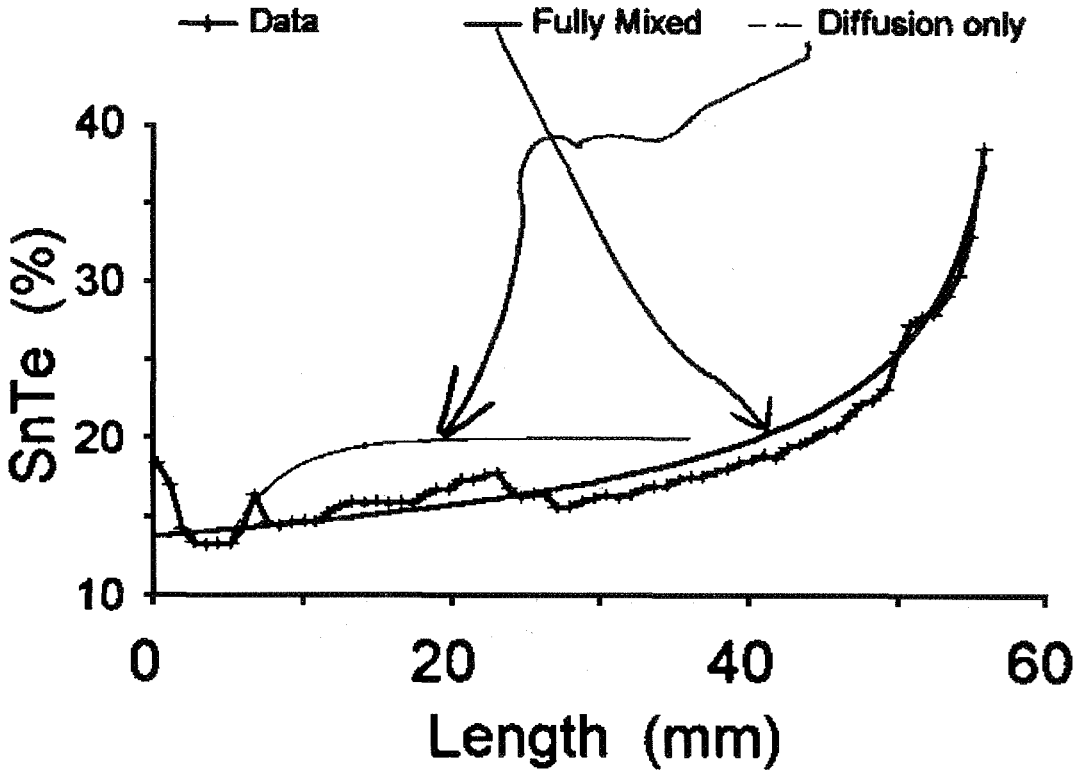

Figure 13. Axial composition scan of cell #1. The data scan was made 2 mm from the center line. Also shown are the analytical curves for a totally mixed sample and the start of one grown with diffusion mixing only. The anticipated composition spike of SnTe shows at the recalescence area at the left side of the plot, then the data flattens for what may be growth during thermal stabilization after the release of the latent heat. At 5 mm of growth the composition shows signs of trying to go to diffusion controlled growth. At approximately 25 mm of growth the curve closely approximates the fully mixed case.

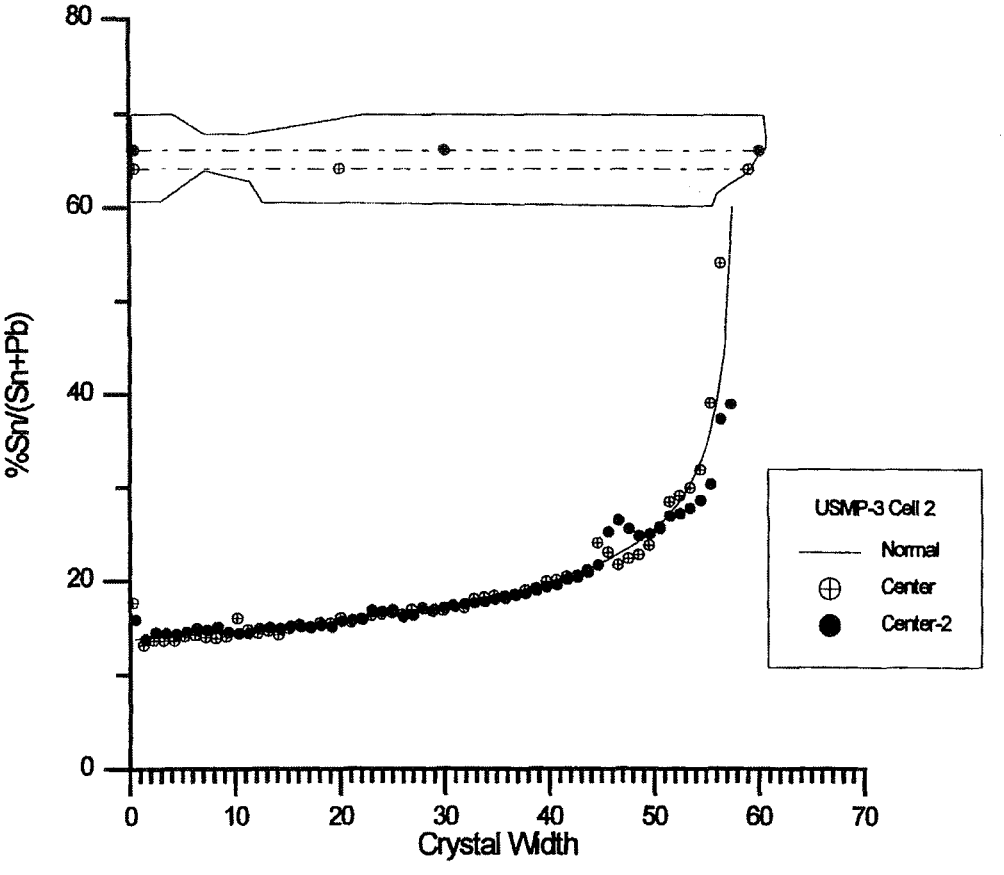

Figure 14. Axial compositional profile of the crystal in cell #2, the nominally hot on bottom orientation, follows the completely mixed curve for the first 45 mm of growth and then exhibits deviations that are, as yet, unexplained.

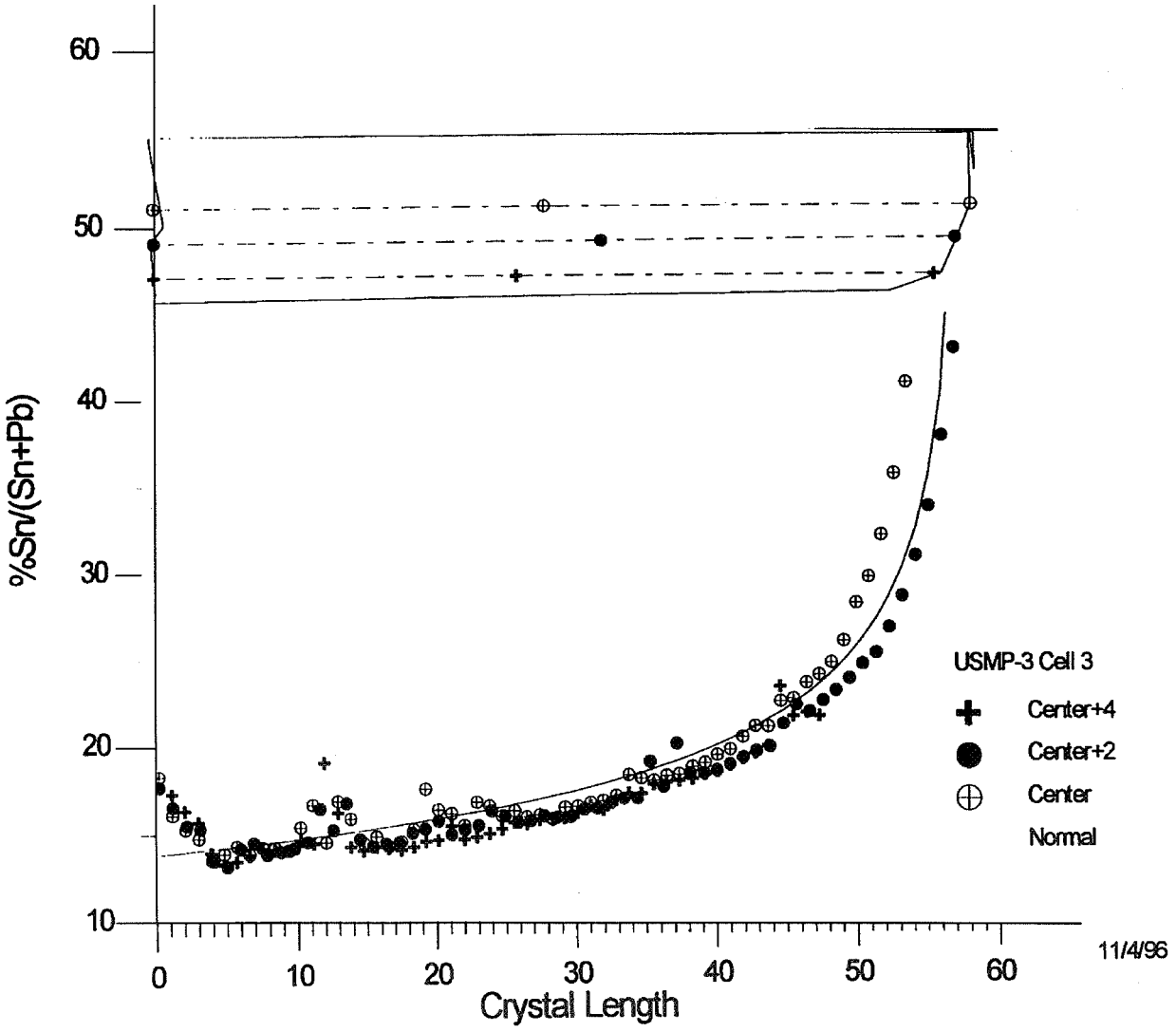

Figure 15. Axial compositional profile of the crystal grown in cell #3. This crystal shows similar deviations from totally mixed as the crystal in cell #2 but over a longer section.

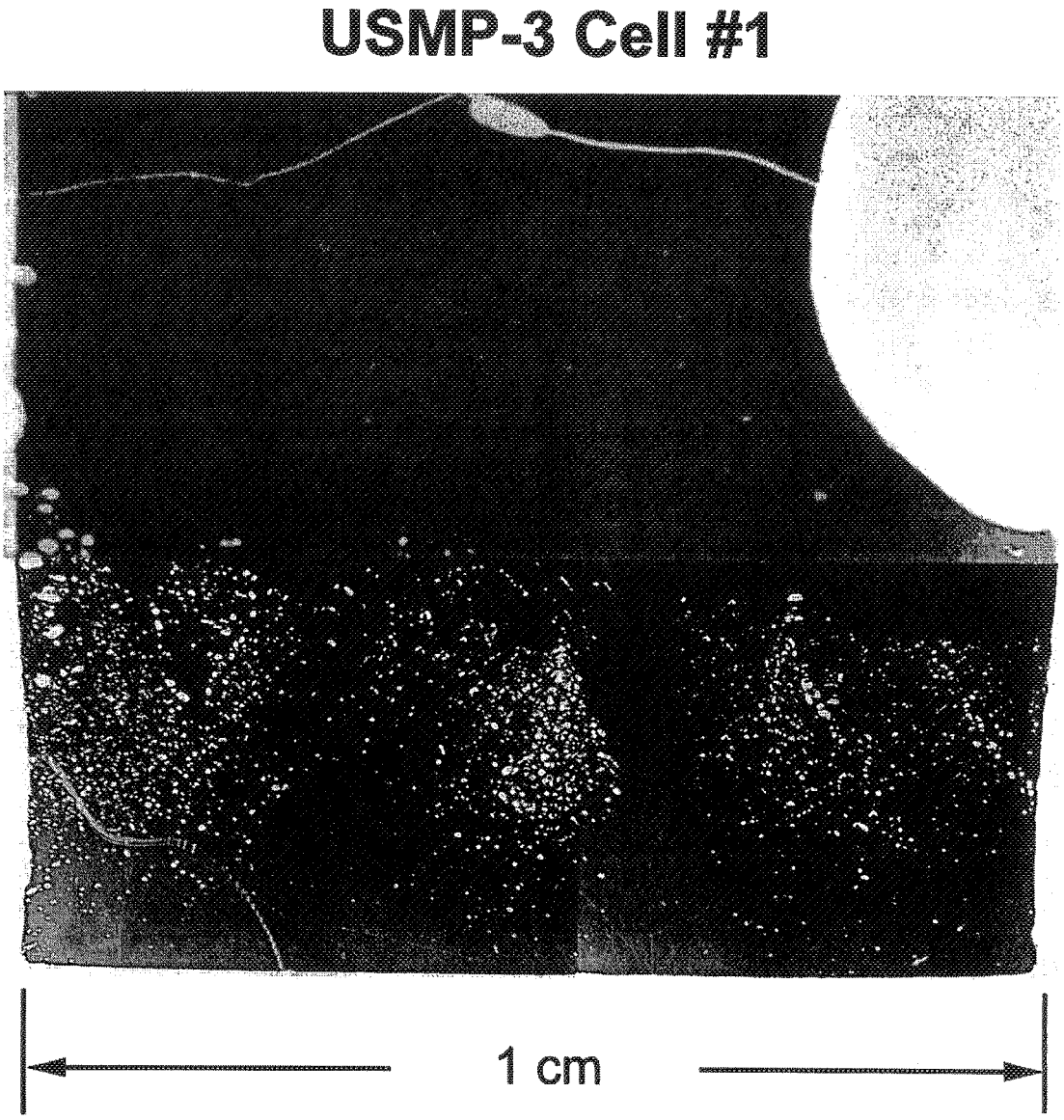

Figure 16. Photomicrograph of the first to freeze region of cells #1. The first to freeze region clearly shows random patterns of sub millimeter pores which were not visible on the CAT scans.

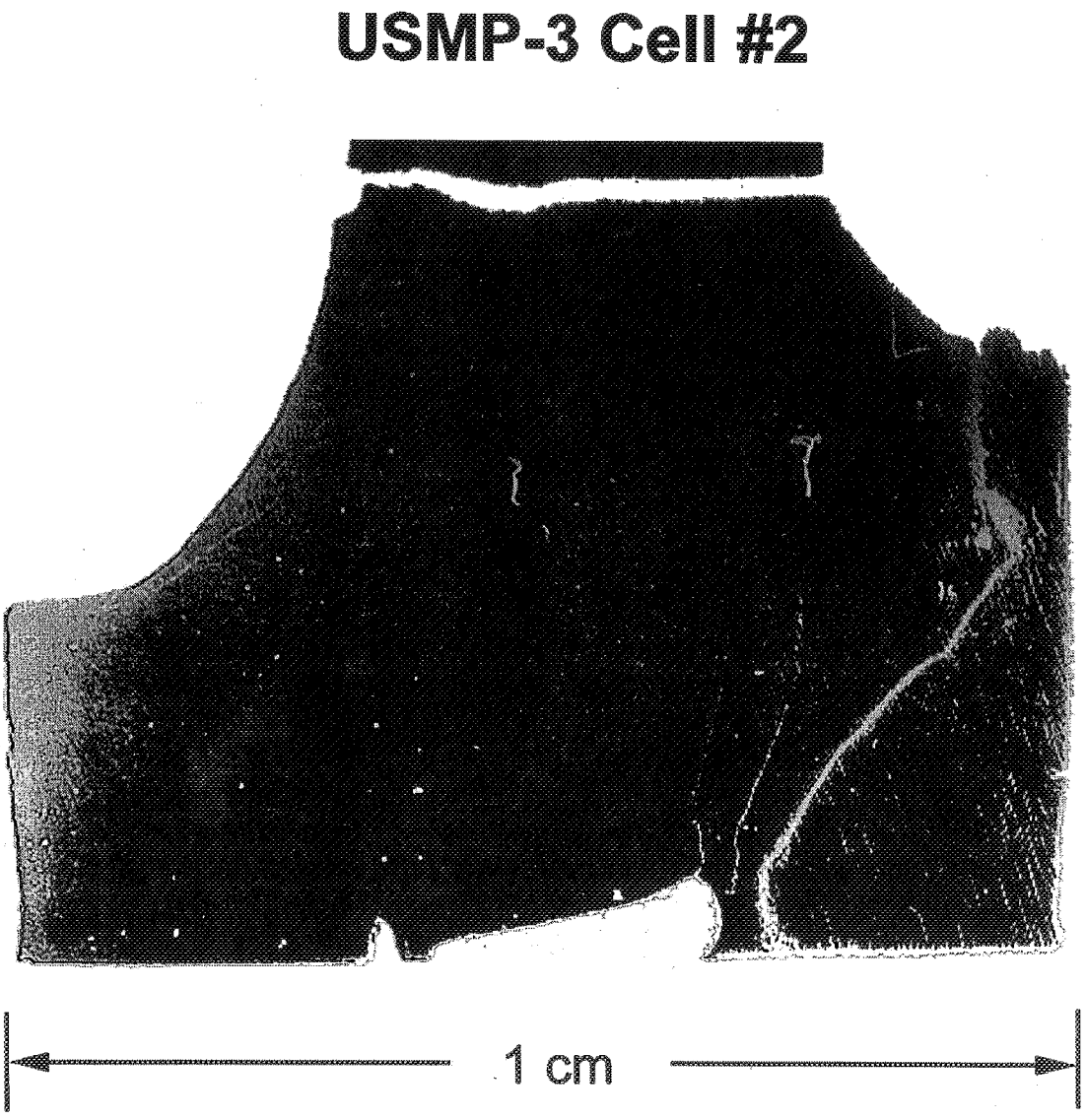

Figure 17. A few pores were seen at the very base of the crystal from cell #2, but the defects are not clearly visible in the photograph.

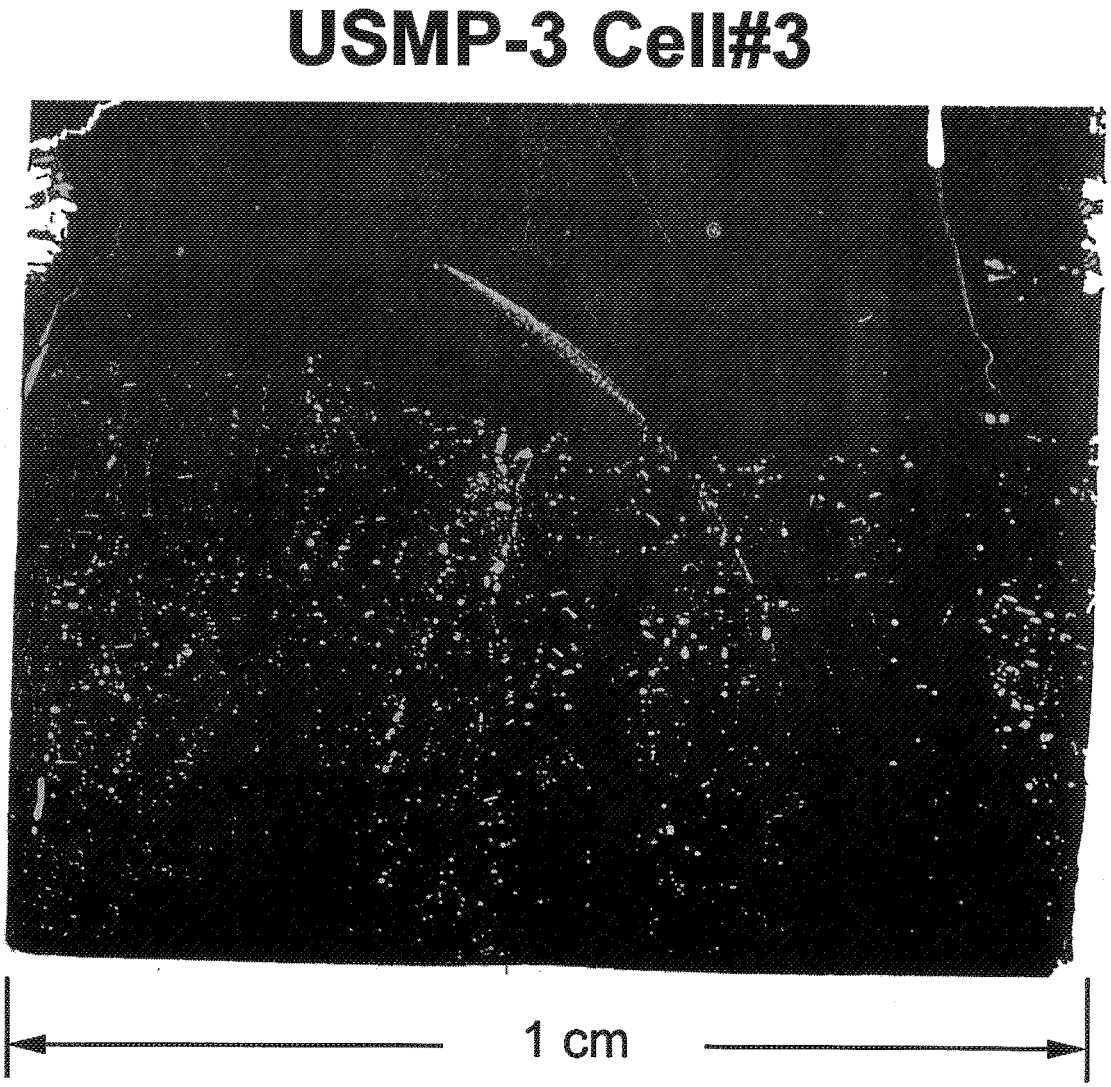

Figure 18. Photomicrograph of the first to freeze region of cell #3. The first to freeze region clearly shows random patterns of sub millimeter pores which were not visible on the CAT scans.

Page intentionally left blank

FORCED FLOW FLAME SPREADING TEST: PRELIMINARY FINDINGS FROM THE USMP-3 SHUTTLE MISSION

Kurt R. Sacksteder
Microgravity Combustion Science Branch
MS 500-115, NASA Lewis Research Center
Cleveland, Ohio, 44135
Phone: 216-433-2857
Kurt.Sacksteder@lerc.nasa.gov

James S. T'ien
Mechanical and Aerospace Engineering
Case Western Reserve University,
Cleveland, Ohio, 44106
Phone: 216-368-4581
jst2@po.cwru.edu

Paul S. Greenberg
Microgravity Combustion Science Branch
MS 110-3, NASA Lewis Research Center
Cleveland, Ohio, 44135
Phone: 216-433-3621
Paul.Greenberg@lerc.nasa.gov

Paul V. Ferkul
National Center for Microgravity Research
MS 110-3, NASA Lewis Research Center,
Cleveland, Ohio, 44135
216-433-8107
Paul.Ferkul@lerc.nasa.gov

Richard D. Pettegrew
National Center for Microgravity Research
MS 500-115, NASA Lewis Research Center
Cleveland, Ohio, 44135
Phone: 216-433-8321
Richard.Pettegrew@lerc.nasa.gov

Hsin-Yi Shih
Mechanical and Aerospace Engineering
Case Western Reserve University
Cleveland, Ohio, 44106

Abstract

The Forced Flow Flame spreading Test (FFFT) is a study of flame spreading over solid fuels in very low-speed air flows. The FFFT experiment is part of a peer-reviewed, NASA Research Announcement Award for a space-based experiment entitled, "Solid Inflammability Boundary at Low Speeds," (SIBAL) intended for operations on the Space Station. In the FFFT experiment, a series of 15 experiments conducted aboard the space shuttle during the USMP-3 mission provided information about the structure and spreading characteristics of flames in low-speed, concurrent flows. The test samples included flat sheets of cellulose and cast cylinders of cellulose, burned in air at velocities of approximately 1 to 8 cm/sec. The test results have been successfully compared to theoretical predictions of the SIBAL program, a fundamentally based numerical simulation of concurrent flow flame spread. Additionally, some guidance for the design characteristics of the SIBAL flight experiment have been obtained including some verification of the theoretical predictions of flame size versus the required size of the SIBAL flow duct, and the effect of the presence of thermocouples in the vicinity of near-limit flames in microgravity.

Introduction

Flame spreading over solid fuels is a classical problem in combustion science. Over the past few decades, many workers have attempted to unravel the complex interaction of chemical and physical processes that control spread rates and flammability. Considerable progress has been made in understanding the mechanisms of spreading flames under certain conditions; nearly all under the influence of normal gravity. A more complete understanding of the spreading and flammability limit mechanisms can be obtained if the domain of experimental and modeling efforts is extended into sub-normal levels of gravitational acceleration because only in reduced gravity are low, controllable, oxidizer flow velocities in the flame zone obtainable.

In the study of flame spreading mechanisms, two broad classes are distinguished: flame spread in opposed flow, in which the direction of the oxygen flow is opposite to the direction of flame spread; and concurrent flow, in which the flame advances in the same direction as the oxygen flow.[1] In general, the magnitude of the relative velocity between the flame and the oxidizer affects flame spread and extinction because of the convection of heat, oxygen and products. In a natural convective environment in normal gravity, the gas phase is accelerated by body forces acting on density (temperature) gradients in and near the flame and velocities thus vary along the length of the flame. The minimum characteristic velocity near the bottom of the flame are estimated, for air at normal pressure, to be 20 to 90 cm/sec , depending upon the flame temperature associated with a particular fuel. This buoyant velocity is the minimum observable air velocity regardless of how the solid is oriented or whether or not an imposed flow (e.g. wind) is added in any direction. Thus, in the normal gravity environment, flame behavior and extinction mechanisms cannot be studied in relative flow velocities below approximately 20 cm/sec.

Flame spreading and flammability studies in flow velocities that are smaller than this, i.e., the same order as the diffusional velocities, provide additional insight into the mechanisms that control flame spread rates and the mechanisms that cause flame extinction. Already, the small amount of existing data on flow effects on flame spreading obtained in microgravity experiments and modeling has revealed the existence of an extinction mechanism that could not be anticipated by extrapolations from normal-gravity data. In low-speed flows, radiative emissions from the fuel surface and from the flame become sufficiently large compared to the rate of heat release from the flame that: 1) flames can achieve a steady length and spread rate in concurrent flows, rather than the acceleratory growth normally observed in normal gravity upward burning, and, 2) flames can be extinguished because of the radiative losses, rather than through diminished reactant residence time in the flame to which normal-gravity upward burning flammability limits are attributed.

We are developing a space experiment for flight aboard the International Space Station attempting to validate the theoretical prediction of the flammability boundary for a thin combusting solid in low-speed, forced-concurrent flow. In the Solid Fuel Inflammability

[1]Thus in normal gravity burning of vertical surfaces, buoyancy induces opposed flow in downward burning and concurrent flow in upward burning.

Boundary at Low Speed experiment, or SIBALS, a sequence of variations in atmospheric oxygen percentage and flow velocity will be used to determine the flammability boundary. In addition, diagnostic measurements of flow parameters, temperatures, gas phase chemical species and radiant emissions will be used to determine the structure of the spreading flame as it approaches the flammability boundary.

The typical way of determining the flammability boundary for a material is a tedious process involving a number of tests to map the go/no-go conditions. In light of the volume and stowage limitations of spacecraft, we have developed a novel flammability test device that facilitates the proposed experiment. A schematic of the SIBALS experiment is shown in Fig. 1 in which it is seen that by dispensing the thin solid fuel from a spooled source at a rate equal to the rate of fuel consumption in the flame, the flame can be rendered stationary with respect to the experiment apparatus and the array of diagnostic devices needed to record the flame structure. The fuel is guided through the length of a flow duct complete with appropriate flow conditioning devices. In a single run, several combinations of atmospheric oxygen content and flow velocity can be imposed upon an existing flame until one of these parameters falls outside the locus of flammable conditions.

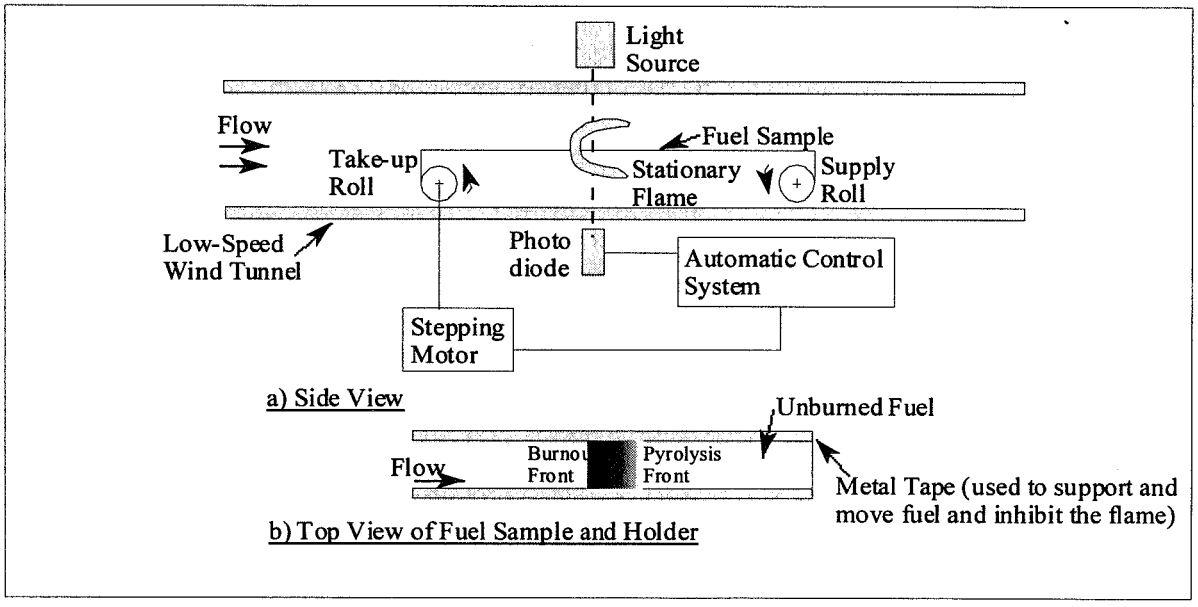

Figure 1 Schematic of the Solids Inflammability Boundary At Low Speed (SIBALS) experiment concept

Some important aspects in the design of such an experiment include the length of the flow duct needed to express entirely the flame length without interference from artificial heat losses either to the upstream flow conditioning devices or the downstream duct exit, where the incoming fuel begins heating. Additionally, establishing the existence of test conditions under which a steady flame length and propagation speed can be reached could provide added confidence that the required diagnostic devices can function sequentially yet observe an unchanging flame.

The Forced Flow Flame spreading Test (FFFT) was conceived as part of the SIBALS experiment for the purpose of providing preliminary observations of steady flame propagation in low speed flows, then, provided that quasi-steady flames could be achieved, provide some estimate of the flame size, luminosity and temperatures for use in the design of the SIBALS experiment. The FFFT was built to operate inside the Middeck Glovebox Facility, (MGBX) which was designed to provide electrical power, circulating air that is filtered and cooled, photographic capabilities, and a degree of isolation between the operating experiment and the crew member.

The FFFT glovebox experiment hardware, shown in Fig.2 consists primarily of 16 fuel-sample assemblies (two examples shown) and two low-speed wind tunnel modules. The modules have a flow cross section of 7cm x 10cm and a 17cm test section length, with the flow drawn (pulled) by a small fan through the test section at speeds of between approximately 1 and 8 cm/sec. Because the air flow velocity was considered such a crucial parameter in the data return from the FFFT, a special low-speed flow anemometer device was fashioned and installed upstream of the

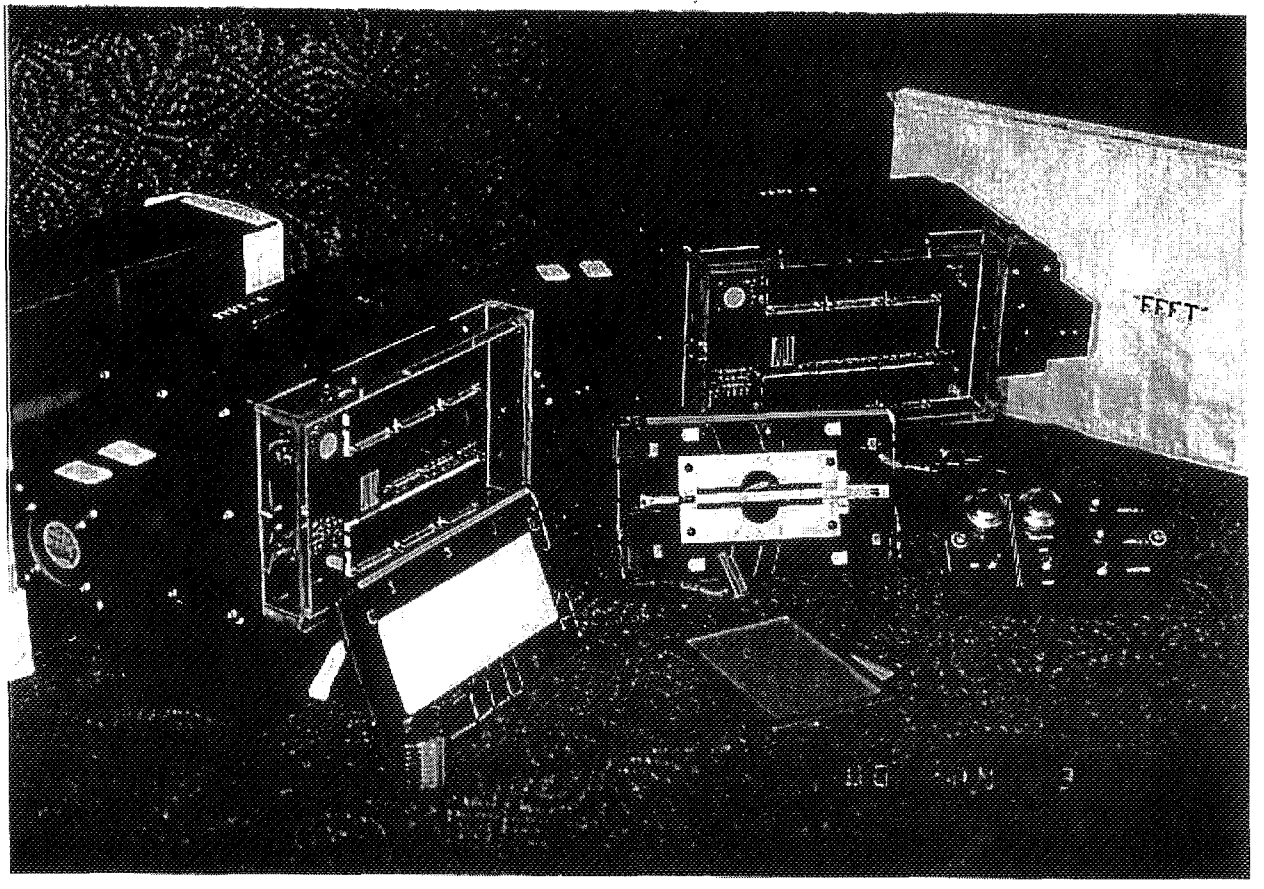

Figure 2 Forced Flow Flame Spread Test (FFFT) flight hardware including the two FFFT wind tunnel modules, one of eleven flat samples, one of the five cylindrical samples, two of the sixteen exit screens and the FFFT control box.

test section to measure the airflow directly and avoid relying upon a secondary measurement. The test section was isolated from the surroundings by metal walls with polycarbonate windows and small-mesh metallic screens at the inlet and outlet cross sections for flow conditioning, heat

absorption and particulate capture. The windows were arranged for imaging flames in each of two orthogonal directions, the front window also contained displays of thermocouple temperatures and an image of the low-speed flow anemometer.

The fuel sample assemblies consisted of steel cards to which the fuel was mounted, electrical wiring for the fuel ignitor, thermocouple wire pairs and, in some cases, a fuel heater element. A total of 16 fuel samples were flown. Of the 16 samples, 11 were flat samples of an ashless filter paper. The flat samples (an example is shown in figure 3) were taped to the steel cards using a kapton tape. Ignition was planned using an electrically heated wire. To explore the influence of thermocouples on flames in low-speed flows near the predicted flammability limit, thermocouples were arrayed in two different configurations in the flat samples and, as a reference, in some cases omitted entirely. The thermocouples were intentionally configured asymmetrically to avoid missing an influence of their presence due to a symmetrical interference.

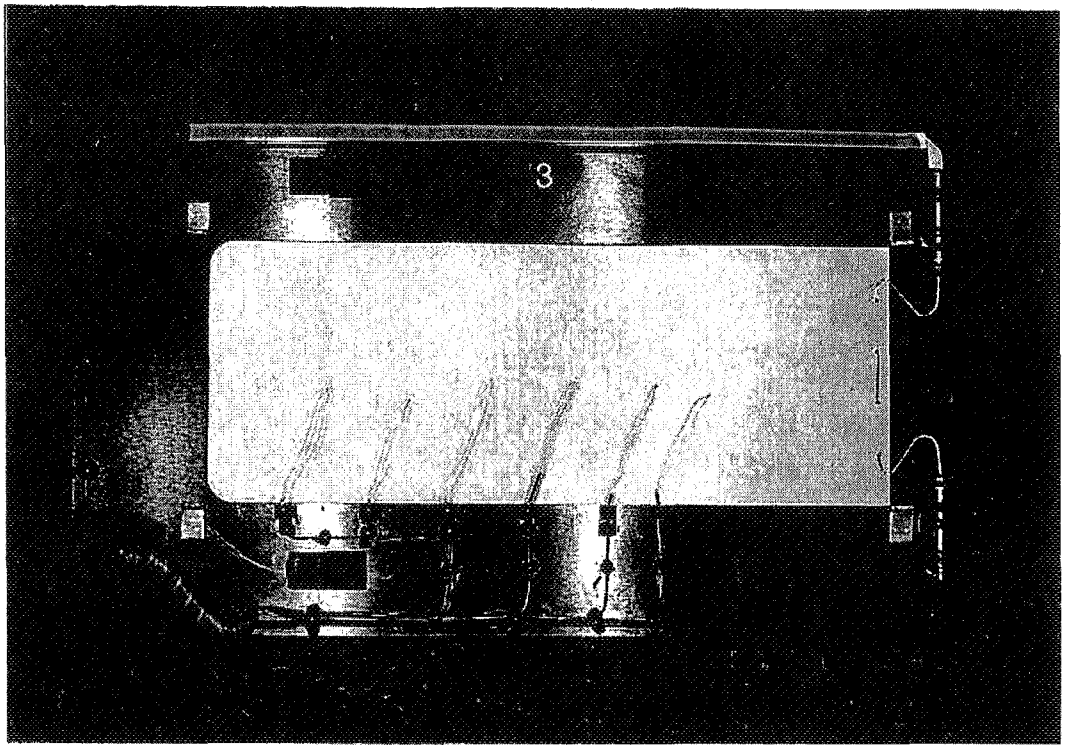

Figure 3 FFFT flat sample. Ignitor wire is shown on the right end of the sample and the thermocouple array is positioned along the sample centerline. During combustion the air flows from right to left to obtain concurrent- flow flame spreading.

The remaining 5 samples were cylinders of cast cellulose prepared from a slurry of ground paper. The cylinders were cast around small electrical heater rods (an example is shown in fig. 4) used to raise the initial fuel temperature in a controlled way just before ignition. Because thermocouples are less likely to influence the slowly spreading flames over thicker fuels, the cylindrical samples were each instrumented with nearly identical thermocouple arrays.

The test matrix for the samples was arranged to obtain redundant observations for a limited number of test conditions. The flat samples were all essentially the same except for the individual thermocouple array configurations and were grouped to obtain observations at each of three air flow velocities. At each flow velocity, the effect of the different thermocouple arrays would be observed. The cylindrical samples were to be burned at the same three flow velocities, and a single velocity to be chosen during the flight for varying the initial fuel temperature. The

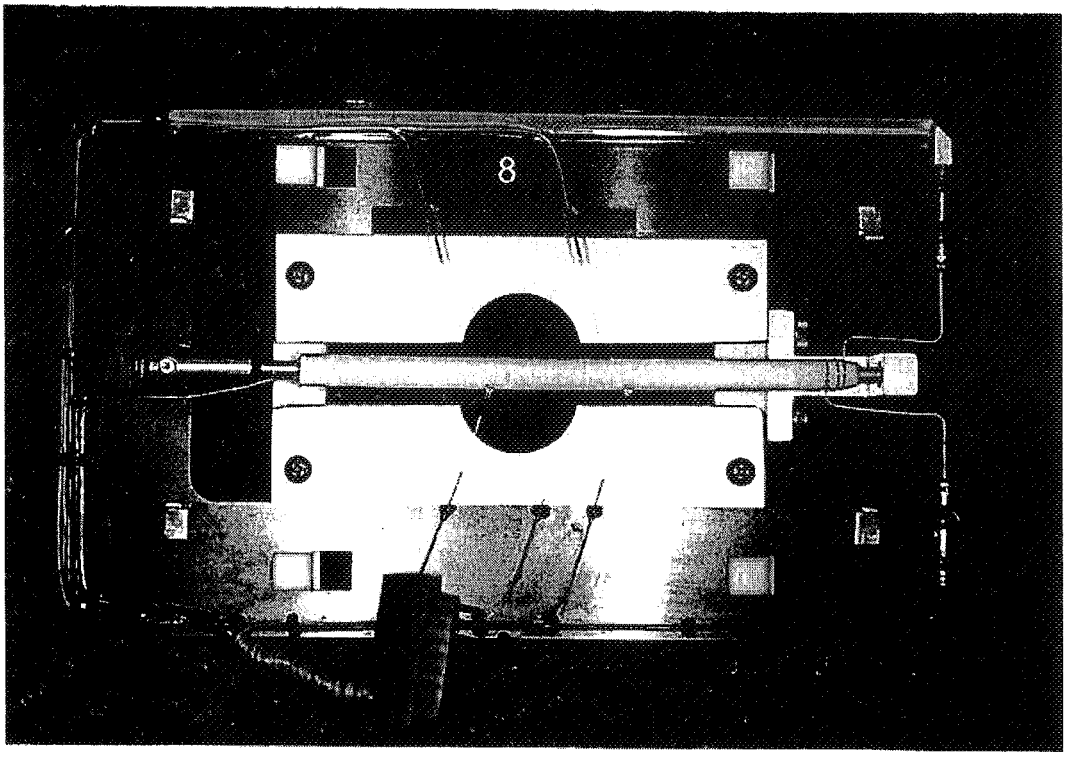

Figure 4 FFFT cylindrical sample. Fuel material is cast over a cylindrical heater rod. Ignitor wire is located on the right hand end of the fuel sample and thermocouple array positioned in the plane of the sample mounting card.

cylindrical samples were conceived as a method for controlling the temperature of a relatively thick fuel while keeping the amount of fuel to a minimum. From the standpoint of theory, the cylindrical samples also provide modelers a simplified fuel-surface and gas-phase radiation boundary condition, reducing their problem from three dimensions to two.

The flow anemometers in the two FFFT modules were each carefully calibrated. Mass flow controllers were used to measure total mass flow through the duct inlet and the indicated flow speed in the modules was set to the plug-flow velocity (i.e., uniform profile) corresponding to the reference mass-flow measurements and occurring at the entrance screen. Limited hot wire anemometry measurements were made at the test section centerline which measurements corresponded to the peak velocity calculated using a viscous flow code model of the flow duct. Considerable effort, including DC-9 reduced gravity tests were made to ensure that the flow calibrations were isolated from gravitational influences such as possible effects of the mass of the anemometer element.

The intent of this document is to provide a summary of the most important results of the FFFT experiment conducted during the USMP-3 mission and to discuss how these results can be used to better understand the flame spreading process and to improve the design concepts of the SIBALS project.

A Summary of the USMP-3 Mission Activity

During the USMP-3 mission, ten flat samples of ashless filter paper and five cylindrical samples of cast cellulose were burned using concurrent flow speeds of 2-8 cm/sec. One of the flat samples did not ignite even with several attempts by the crew to do so. The ignitor of the failed sample was seen to clearly function in the video recording, but the sample was finally handled enough that a determination of the cause of the ignition failure could not be made. We note that this sample was stowed next to the flight sample that was inadvertently given to and burned by the crew during ground training at the Johnson Space Center (JSC) shortly before launch. Although the repaired sample and its neighbor were inspected before they were turned over for the second time for flight, no faults were detected. The refurbished fuel sample assembly burned normally in flight, and the refurbished FFFT module, damaged in the training incident, worked without flaw.

The 16 samples were grouped together in sets of four, in most cases three flat samples and one cylindrical sample. The last group of four was reserved for test conditions to be determined during the flight. Each group of samples was to be burned in the same velocity airflow. Each group of three flat samples included one sample with no thermocouples, one with the six thermocouples each at a different distance from the fuel surface, and one with thermocouples arranged in a repeated pattern. After the first burns, the thermocouples were found to disrupt the progress of the flame and fuel-surface pyrolysis. With this clear demonstration made early, the astronaut crew were asked to bend most of the installed thermocouples away from the remaining flat samples, leaving one downstream near the end of each sample.

Before any samples were ignited the crew reported that the flow velocities indicated by the calibrated anemometers of both modules were quite high and independent of the FFFT fan control setting. The crew was asked to check, and reported that the glovebox air circulation was set to the lowest speed (or off) as specified in the procedures (since we were aware of the interaction between the air circulation system set at a high speed and the FFFT module anemometer). To compensate for the apparently high flow, the crew attached multiple sheets of first-aid gauze as a flow impedance over both module inlets where the anemometers are located, returning the anemometers to approximately nominal behavior. With testing after the mission both in the MGBX and with mass flow controllers used both in normal gravity and aboard the DC-9 aircraft, we determined that the high velocity indications were caused by flow from the glovebox air circulation fan impinging upon the FFFT inlet, and that the MGBX air circulation fan was working normally. Additional post-flight calibrations (in normal gravity and in reduced-gravity aircraft tests, with and without the gauze the crew added to the module inlets) have also shown that the calibrations of the flow anemometers were not changed during the mission. Hence, the flow speed indications recorded in-flight are still acceptable. The uncertainty

introduced into the flight data interpretation because of the gauze are a slight reduction in the absolute pressure in the vicinity of the sample burning and some unquantifiable disturbance to the velocity distribution apparent in the latter portions of some of the flame-image sequences.

Results: Flat Samples

Ten flat samples were burned successfully in concurrent flow air velocities of about 1 cm/sec to about 8 cm/sec. The detailed results of sample 6 are presented here as an example of the broader data set.

Figure 5 shows the data extracted from the video and film images of sample 6 in which the flame spread in the presence of approximately 1 cm/sec indicated air flow. The dark symbols are measurements taken from the video record of the fuel surface along a line parallel to the direction of flow and flame spreading, and show the behavior of the charring pyrolysis region of the fuel. This data provides some visualization of any transient response of the fuel to the flame and any thermal disturbances such as the thermocouples. These data begin about 13 seconds after the sample was ignited when the video image shows a distinct flame unaffected by the bright glare of the ignitor wire. By the time at which the pyrolysis region could be tracked, its length had reached about 1.5 cm from which it varied by +/- 0.1cm until about 30 seconds after ignition.

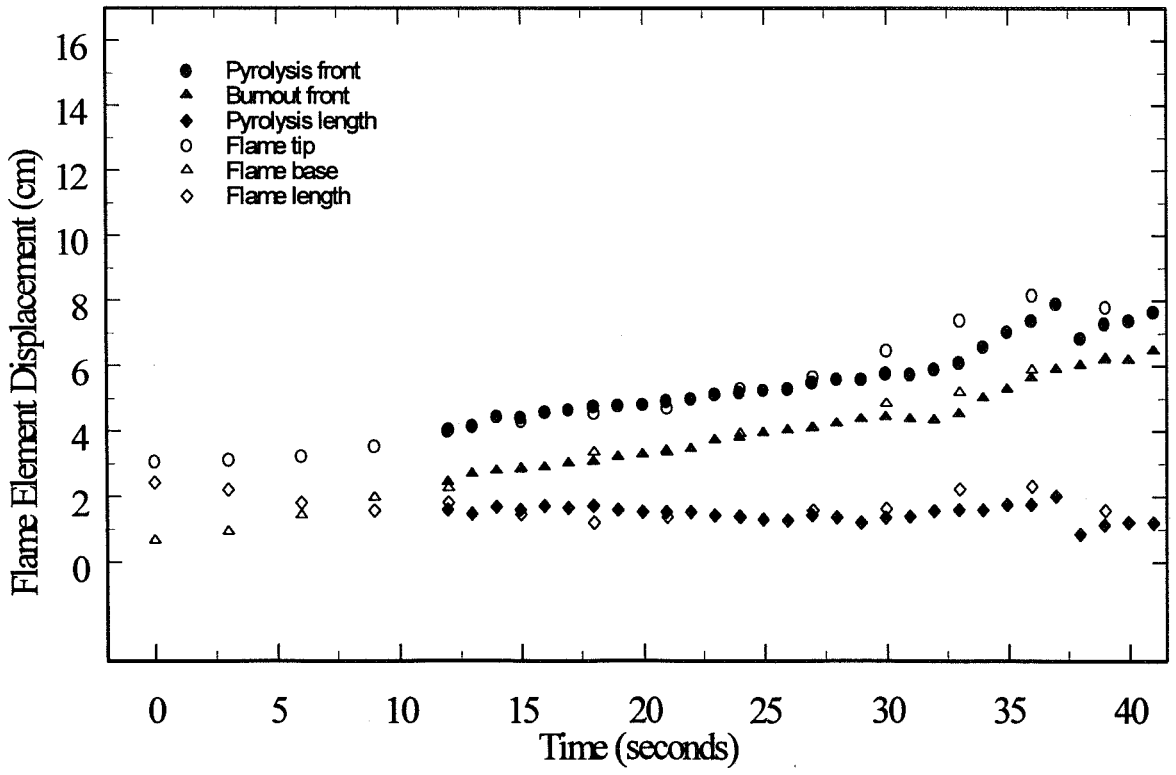

Figure 5 Position of flame features versus time of FFFT sample number 6, ashless filter paper, burning in air at normal atmospheric pressure at a flow velocity of approximately 1cm/sec.

The clear symbols in Fig. 5 indicate the progress of the visible flame measured from a series of still photographs made from the perspective of the edge view of the flat paper sample. The first of these photographs was taken shortly after ignition when the flame, enhanced by the energy of the ignitor, had a length of about 2.2 cm. When the ignitor was switched off, the flame decreased in size until reaching approximately the same length as the pyrolysis region of the fuel surface, at about 13 seconds. The change in flame length is associated with the energy deposition rate of the ignitor which is larger than the energy release from the flame. While the ignitor is energized, the fuel pyrolyzes at a greater rate than achievable by the flame alone. Hence, more vaporized fuel is available to the air stream and the resulting flame is longer.

Between about 13 and 30 seconds after ignition, the flame and pyrolysis lengths are approximately the same. At 30 seconds, the flame appears to accelerate. The video view of the fuel surface reveals that at that time, the fuel begins to burn asymmetrically. We have interpreted this asymmetry as being caused by a small flow disturbance caused, in turn, by the application of the medical gauze at the FFFT duct inlet. The apparent abrupt shortening of the flame and pyrolysis length, indicated at about 37 seconds, is an artifact of the asymmetry effect on the flame tracking algorithm and is not physical.

Figures 6 shows a comparison between an image of the flame in FFFT test 6 and the results of the numerical simulation of concurrent flow flame spreading developed as part of the SIBALS project. The numerical model includes full Navier Stokes equations for low-speed flows and detailed estimations of gas-phase radiation for a gray absorbing, emitting and non-scattering medium. The simulation was specially modified to model the conditions expected in the FFFT experiment, in particular, by altering the boundary conditions to simulate the duct dimensions of the FFFT modules. Figure 6 shows the results of the simulation with the free stream velocity of

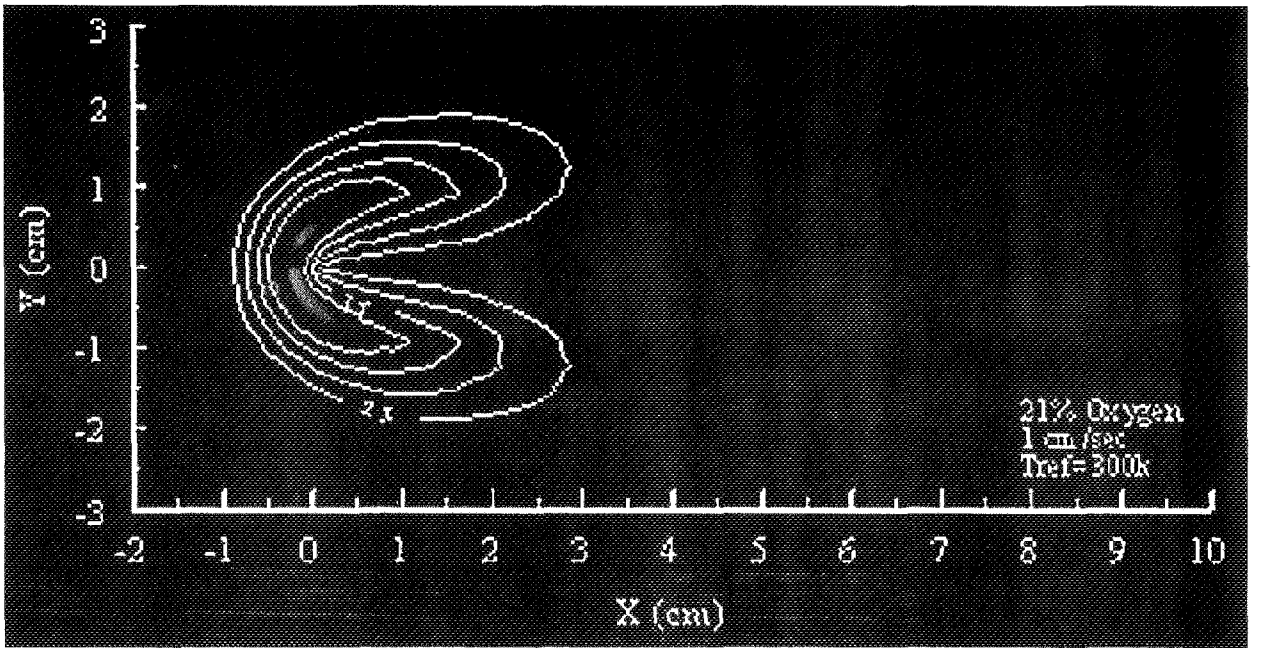

Figure 6 Comparison of a flame image from FFFT test 6 with reaction rate contours from the numerical simulation of concurrent-flow flame spreading.

1 cm/sec. Contours of the logarithm of the reaction rate, i.e., the disappearance rate of fuel mass, overlay the image from the FFFT test 6. The curvature of the blue region of the flame (the darker region in the monochrome image) matches that of the contour of 10^{-4} gm/cm^3/sec, particularly near the stagnation point or plane of symmetry of the flame. Reaction rate contours are sometimes used instead of temperatures for comparison with the visible flame because the blue emissions from the flame are related to the population of excited intermediate species in the flame, which only exist in regions of higher chemical reactivity.

Figure 7 shows the temperature history of the single thermocouple that was in contact with the fuel surface near the downstream end of the fuel sample in test 6. Between the time of ignition and approximately 53 seconds thereafter, the fuel is slowly heated. At approximately 53 seconds after ignition, the flame reaches the vicinity of the thermocouple raising the temperature in 3-4 seconds to the pyrolysis temperature of about 720K. While the fuel pyrolyzes and vaporizes the temperature is approximately constant. Upon the completion of the fuel vaporization (fuel burnout) the thermocouple experiences gas phase temperatures. As the fuel burnout point and flame continue to propagate downstream, the thermocouple passes through the flame, experiencing the peak flame temperature that occurs in the plane of symmetry previously occupied by the fuel.

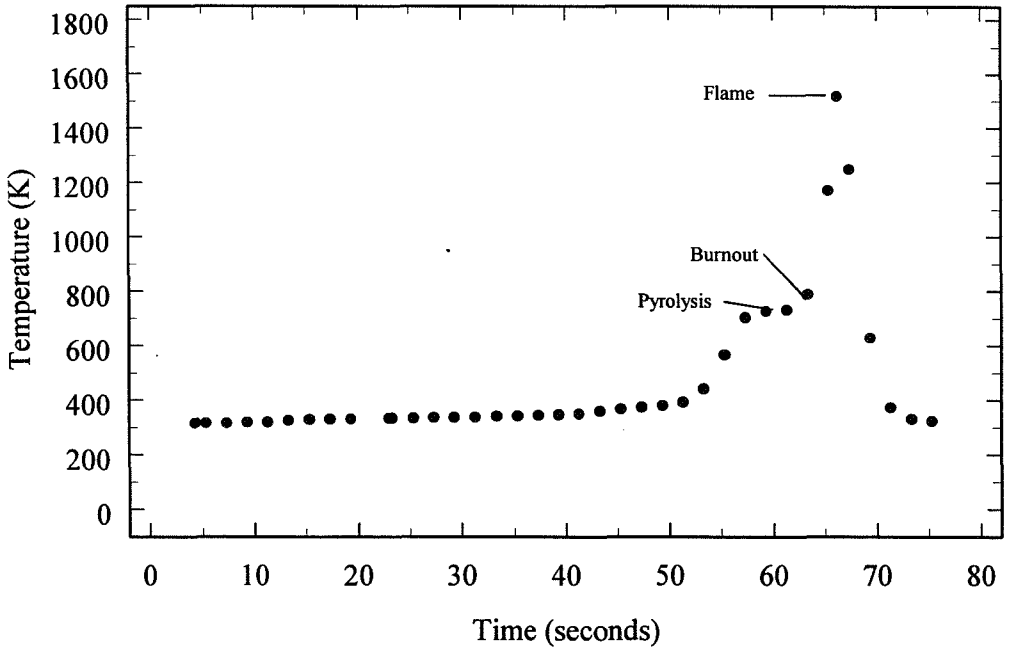

Figure 7 Time history of temperature at a point on the fuel surface for a flame spreading over ashless filter paper in a purely forced concurrent flow of 21% oxygen / 79 % nitrogen in an indicated free stream velocity of approximately 1 cm/sec.

The pyrolysis and flame temperature shown in figure 7 are quite similar to earlier measurements obtained in drop tower tests and to the results of the numerical modeling. However, since the flame spread was clearly affected by the thermocouple, the temporal distribution shown in figure 7 may not represent what would be predicted for unaffected spreading.

The flat samples burned in higher air velocities all seemed to grow throughout the test time or exhibited flame lengths that were as high as 8 cm. Because of the limitations in size imposed upon experiments in the glovebox facility we cannot be certain that the growing flames were approaching what might eventually have been a steady length as the theory predicts. The flames in the lower air velocities, i.e., about 1-3 cm/sec appear to have achieved a steady length in about 13 - 15 seconds. It is difficult to claim, however, that the entire flame/fuel system had reached a steady configuration because residual, and much slower, transients could still be possible in the fuel induced by the energetic ignition phenomena. We would require that the flame traverse at least two times the pyrolysis length after achieving a steady flame length in order to be confident that the solid fuel transients had been dissipated. However, we interpret the observed flame length, and its successful comparison to the theory, to be supportive of the theoretical results.

Results: Cylindrical Samples

Five cylindrical samples were burned successfully in concurrent flow air velocities of about 2 cm/sec to about 8 cm/sec. Figure 8 shows a summary of the lengths of the flames spreading over the samples in varying flow velocities at a fixed initial fuel temperature and varying initial fuel

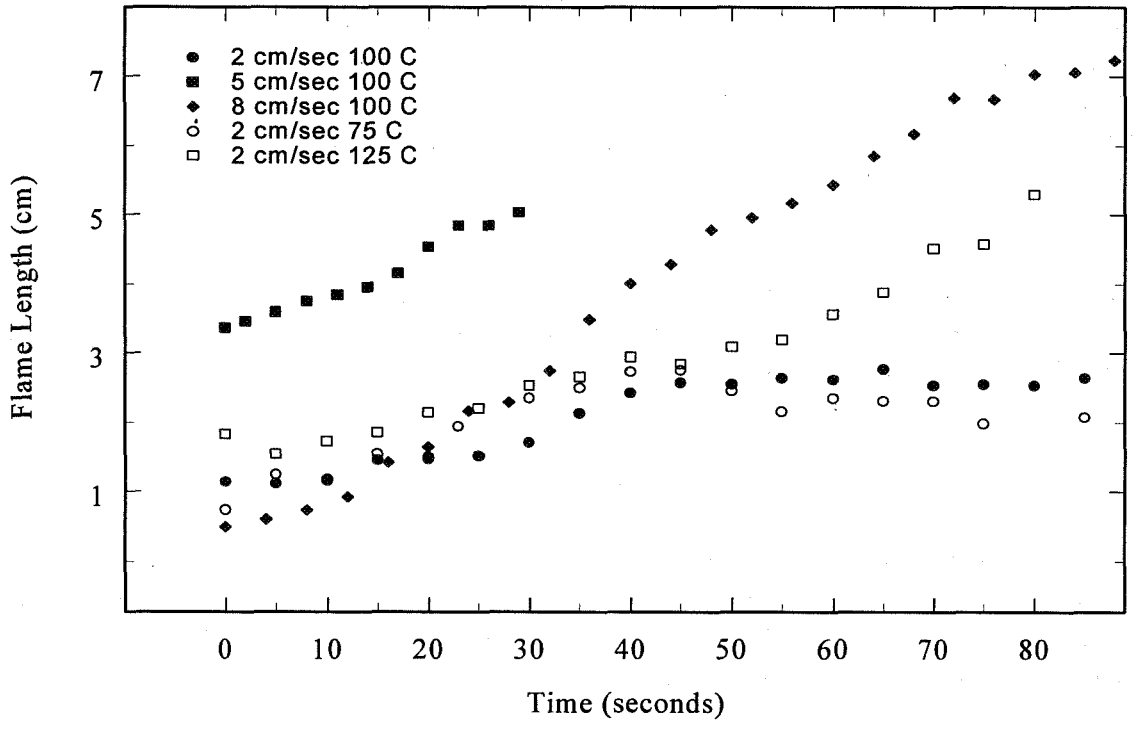

Figure 8 Comparison of flame lengths for FFFT cylindrical samples in various air flow velocities and initial fuel temperatures

temperature with a single fixed flow velocity. These data were obtained from the results of the 35mm film camera, the framing rate of which was adjusted to attempt to capture the flame over the duration of the experiment. The experiment conducted at 5 cm/sec and 100 C was the first FFFT cylinder burned and the framing rate was too high (based upon our pre-mission guess of

the spread rate) to capture the entire experiment. After the first experiment with cylindrical samples, the framing rates were adjusted, hence the data from other samples is more complete.

The solid plotting symbols show flame length variations with time for samples burned with an initial fuel temperature of 100C, but with varying flow velocity. During the observation time available, the flame grew for samples burning in air flow velocities of 5 and 8 cm/sec. However, in flow velocity of 2 cm/sec, the flame reached an approximately steady length after about 45-50 seconds, and maintained this length for the remainder of the observable test time.

The hollow plotting symbols show flame length variations with time for samples burned at a fixed air flow velocity of 2 cm/sec, but with variations in initial fuel temperature. For the sample preheated to an initial temperature of 125 C, the flame grew for the entire observable test time. The sample heated to only 75 C, rendered a flame that reached a peak length at about 40 seconds, then began to shrink. The sample at 100 C, as we have already observed, exhibited an apparently steady flame length.

These results are to be quite useful for the future development of theoretical simulations of cylindrical fuel sample burning. They include a possible spreading-regime transition, based on flow velocity, between large and growing flames at higher flow velocities and steady spreading at lower flow velocities. Similarly, a possible regime transition, based on the initial fuel temperature, may have been observed between growing, steady and shrinking flames. This interpretation of the data is subject to the limitation discussed earlier that steadiness is not assured until the flame has spread far from the ignition region because of transitory effects on the solid fuel.

In the final burning of cylindrical samples, the crew accepted our request to shut off the air flow in the FFFT module just before the flame reached the end of the fuel sample. Upon stopping the air flow, the flame very quickly shrank and quenched, providing a dramatic demonstration of the flow effects on fuel flammability in microgravity.

Conclusions

The FFFT experiment conducted aboard the USMP-3 mission was considered quite successful, providing some data that can be compared directly to the results of theoretical predictions. Perhaps more importantly, the results are quite useful for the preparations of the more complete experimental effort planned for the space station era.

For the flat fuel samples, the results indicate that the theoretical predictions of the flame structure, as evidenced by the observed flame length, are quite reasonable for the low velocity portion of the test matrix. The flames at higher flow velocities grew too large for a reasonable comparison because of the size limitations of the glovebox. Flame length is not nearly complete, however, in terms of the requirements for verifying the numerical simulation. More detailed diagnostics, such as gas-phase species measurements, are needed and are planned for the SIBALS experiment.

The FFFT module duct is too short to capture the behavior of flames spreading in air flow velocities above about 2-3 cm/sec. Together with the confidence obtained in the numerical simulation, this information will refine the design of the flow duct for the SIBALS experiment.

The obvious effect of the thermocouples on the progress of the flames spreading over the thin fuel samples provides a cautionary note to the design of thin fuel experiments. We believe that these effects are the most prominent for test conditions where the flame spreads quickly. Where the flame spreads more slowly, the transient influence of the thermocouples may not be so pronounced.

The cylindrical fuel sample data have provided benchmark data for the development of numerical simulations. This configuration might be a more fundamental configuration that the flat sample case because of the simplification in the radiation modeling that is obtained from the inherently two-dimensional axi-symmetric geometry. The apparent transition between growing, steady and shrinking flames that have been observed provide a challenge to the theory to reproduce.

Acknowledgments

The authors would like to acknowledge the herculean efforts put forth on our behalf by many people associated with the USMP-3 mission and the building of our experiment. In particular, we would like to thank Brian Quigley and Terry Rodgers, and the many technicians and fabrication specialists at the NASA Lewis Research Center for yet another excellent job. We would also like to express our gratitude to the members of the Teledyne Brown and NASA Marshall Space Flight Center Glovebox Team, who always found a way .

Bibliography

1. Frey, A.E. and T'ien, J.S., "Near-Limit Flame Spread Over Paper Samples," Combustion and Flame, Vol. 26, p.257-267, 1976.

2. Frey, A.E. and T'ien, J.S., "A Theory of Flame Spread over a Solid Fuel Including Finite-Rate Chemical Kinetics," Combustion and Flame, Vol, 36, p.263-289, 1979.

3. Altenkirch, R.A, Eichhorn, R., and Shang, P.C., "Buoyancy Effects on Flames Spreading Down Thermally-Thin Fuels," Combustion and Flame, Vol. 37, p.71, 1980.

4. T'ien, J.S., "Diffusion Flame Extinction at Small Stretch Rates: The Mechanism of Radiative Loss," Combustion and Flame, Vol. 65, pp. 31-34, 1986.

5. Olson, S.L., Ferkul, P.V., and T'ien, J.S., "Near-Limit Flame Spread over a Thin Solid Fuel in Microgravity," Twenty-Second Symposium (International) on Combustion, pp. 1213-1222, The Combustion Institute, 1988.

6. Vedha-Nayagam, M. and Altenkirch, R.A., "Gravitational Effects on Flames Spreading over Thick Solid Surfaces," Acta Astronautica, Vol. 12, no. 7/8, pp. 565-572, 1985.

7. Bhattacharjee, S., Altenkirch, R.A., and Sacksteder, K.R., "Implications of Spread Rate and Temperature Measurements in Flame Spread over a Thin Fuel in a Quiescent, Microgravity, Space-Based Environment," Combustion Science and Technology, Vol. 91, no. 4-6, pp. 225, 1993.

8. Bhattacharjee, S., Altenkirch, R.A., and Sacksteder, K.R., "The Effect of Ambient Pressure on Flame Spread over Thin Cellulosic Fuel in a Quiescent, Microgravity Environment," Journal of Heat transfer, Vol.118, pp.181-190, 1994.

9. Ramachandra, P.A., Altenkirch, R.A., Bhattacharjee, S., Tang, L., Sacksteder, K.R., and Wolverton, M.K., "The Behavior of Flames Spreading over Thin Solids in Microgravity," Twenty-Fifth Symposium (International) on Combustion, Combustion and Flame, Vol. 100, pp. 71-84, 1995.

10. West, J., Tang, L., Altenkirch, R.A., Bhattacharjee, S., Sacksteder, K.R.,and Delichatsios, M., "Quiescent Flame Spread Over Thick Fuels in Microgravity," Twenty-Sixth Symposium (International) on Combustion, The Combustion Institute, 1996.

11. Sacksteder, K.R. and T'ien, J.S., "Buoyant Downward Diffusion Flame Spread and Extinction in Partial-Gravity Accelerations," Twenty-Fifth Symposium (International) on Combustion, pp. 1685-1692, The Combustion Institute, 1994.

12. Sacksteder, K.R., "The Implications of Experimentally Controlled Gravitational Accelerations for Combustion Science", Twenty-Third Symposium (International) on Combustion, the Combustion Institute, pp. 1589-1596, 1990.

RADIATIVE IGNITION AND TRANSITION TO SPREAD INVESTIGATION (RITSI)

Takashi Kashiwagi
Building & Fire Research Laboratory
NIST
Gaithersburg, MD 20899

Phone: 301-975-6699
FAX: 301-975-4052
email: takashi.kashiwagi@nist.gov

Sandra L. Olson
Lewis Research Center
NASA
Cleveland, OH 44135

216-433-2859
216-433-8660
sandra.olson@lerc.nasa.gov

Abstract

A total of 25 experiments was conducted in the Glovebox Facility on the USMP-3 mission to study the behavior of both flaming and smoldering ignition events, the transition from ignition to flame/smoldering spread, and the flame/smoldering growth pattern in air. Twenty-one of the 25 experiments were flaming experiments and the remainder were smoldering experiments. Ignition was initiated by a heated wire across a thermally thin filter paper in the middle of the sample for the two-dimensional configuration and by a focused beam from a halogen/tungsten lamp at the center of the sample for the three-dimensional configuration. The external air flow velocity was varied from 0 cm/s to 6.5 cm/s. The ignition and subsequent flame spread events were recorded by a video camera, a 35 mm camera, and 6 thermocouples (2 in the gas phase and 4 in the sample). The results indicate that non-piloted radiative ignition of the paper by external thermal radiation tends to occur more easily than in normal gravity. In the two-dimensional configuration, the transition from ignition to downstream flame spread never occurred; only the transition to upstream spread took place. In the three-dimensional configuration, a char growth pattern emerged in the shape of a fan, with the ignited area as the center of the fan and the fan spreading in the upstream direction. The internal angle of the fan increased with an increase in external flow velocity (higher flow velocity gave a more opened fan pattern). At an external flow velocity of 5 cm/s, the flame was horseshoe-shaped and the char pattern became an elongated semicircle toward upstream. It appears that the peak upstream flame spread rate was reached at a higher external velocity than for the two-dimensional flame front. Flame spread much faster along open edges of the sample paper than along the sample face, presumably due to there being larger supply of oxygen and energy feedback at the open edges than at the surface. These results indicate the possible importance of the effect of the flame front shape such as the curvature of the flame front on spread rate and flame strength. A complex, unexpected finger-shaped char growth pattern was observed during the smoldering experiment. Higher external flow velocity increased the number of localized smoldering fronts, of the char fingers they left behind, and frequency of bifurcations from the fingers. At present, it is not clear what caused such a complex char growth pattern .

Introduction

Ignition of solid fuels by external thermal radiation and subsequent transition to flame spread are processes that not only are of considerable scientific interest but which also have fire safety applications. The fire safety strategy in a spacecraft is (1) to detect any fire as early as possible, (2) to keep any fire as small as possible, and (3) to extinguish any fire as quickly as possible [1,2]. This suggests that a material which undergoes a momentary ignition might be tolerable but a material which permits a transition to subsequent flame spread would significantly increase the fire hazard in a spacecraft. If the transition does not take place, then by definition flame spread does not occur. Therefore, the limiting condition under which flame cannot spread should be calculated from a model of the transition from ignition instead of by the traditional approach based on limits to a steady flame spread model. However, although the fundamental processes involved in ignition have been suggested [3,4,5,6], there have been no definitive experimental or modeling studies due to the flow motion generated by buoyancy near the heated sample surface. One must solve the time-dependent Navier-Stokes equations over an extended region to represent the highly unstable buoyant plume accurately. It is especially important to provide correct far-field boundary conditions, particularly velocities. This is also important during the transition period from ignition to flame spread but there has been hardly any previous work on this transition.

Almost all previous works have studied ignition and flame spreading separately [7,8]. In order to avoid the specification of the boundary conditions, previous detailed radiative ignition models were assumed to be one-dimensional [9,10,11] or were applied at a stagnation point [12]. The mismatch between experimental and calculated geometries in normal gravity means that theories cannot be compared directly with experimental results except for specific configurations under which the plume is not formed. In previous flame spread studies, time-dependent flame spread models are limited to upward flame spread over a vertically oriented material surface in normal gravity and is generally assumed to be two-dimensional. Almost all detailed flame spread models [7,8,13] were based on the steady-state flame spread rate and, as far as we are aware, there are no previous studies of three-dimensional time-dependent flame spread which is initiated from a small, localized ignited area. This scenario is most common in real fires. The mechanism of the transition from ignition to flame spread also controls the extinction limit of flame spread, which is affected by the flame history, starting at ignition. Since this is an inherently transient process, conventional approaches analyzing the steady-state flame spread near its extinction limit cannot truly reveal the dynamic aspects of the transition. Modeling of the transition from ignition to flame spread is extremely difficult in a normal gravity environment. Thus, the study of localized ignition and the subsequent transition to flame spread in a three-dimensional configuration in a microgravity environment is needed to obtain new information for understanding transition mechanisms.

Smoldering (non-flaming glowing combustion) is one of the common modes of initiation of fires; it might provide potentially hazardous conditions due to its high CO yield, but there are only a limited number of studies available. Therefore, its detailed mechanism is not fully understood. Although the heat release rate from smoldering is smaller than that from flaming, the temperature of the smoldering front is as high as 800 °C or more and the induced buoyant

flow from the high temperature smoldering front cannot be neglected in normal gravity. The induced buoyant flow makes it extremely difficult to quantify and control the supply rate of oxygen to the smoldering front in normal gravity. Since the supply of oxygen to the smoldering front is one of the critical parameters which control smoldering spread rate, it is extremely difficult to predict the effects of slow external flow on smoldering behavior and its spread rate over a cellulosic surface.

1. Experimental Objectives

The Radiative Ignition and Transition to Spread Investigation experiment (RITSI) was designed to obtain test data on the following phenomena:

(1) Observe and measure the effects of low external flow velocity similar to ventilation velocities in a spacecraft on flaming ignition, transition, and flame growth pattern over a thin cellulosic paper surface in the two-dimensional configuration and also in the three-dimensional configuration.

(2) Observe and measure flame spread along open edges and corner of thin paper at different external low flow velocities.

(3) Observe and measure the effects of low external flow velocity on the growth pattern of smoldering from localized smoldering ignition.

To make these observations, 15 experiments were planned with an additional 10 samples as extra if added experimental time became available. Fortunately, all 25 tests could be conducted over three days; the tests conditions are listed in Table 1. 15 tests were conducted for item (1), 6 tests were for item (2), and 4 tests were for item (3).

2.Experimental Hardware and Operations

RITSI USMP-3 Glovebox experiment hardware, shown in Figure 1, consists of two experimental modules, a control box, a display box, and two parts boxes, which house the fifteen individual sample boxes and other miscellaneous supplies, including 10 additional fuel samples. One sample box is shown opened to reveal the sample card, product filter, and cleaning supplies (not visible) stowed inside. The small external control box (which attaches to the outside of the Glovebox front door) include fan on/off and variable speed control, ignitor wire activation radiant heater activation and variable power adjustment, and chamber light on/off switch.

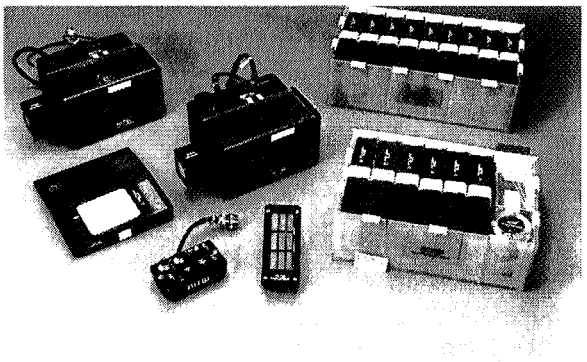

Figure 1 RITSI hardware picture (two modules, two sample/holder storage containers, one sample/holder, electronic control, and outputs desplay)

Each experimental module, shown schematically in Figure 2, uses a small fan to generate a low flow velocity of up to 6.5 cm/s through the test section. The test section was 85 mm wide x 95 mm high x 171 mm long. The transparent lid of the duct opens for access to change sample cards. A filter downstream of the combustion event collects particulates and other combustion

products.

A near-infrared tungsten/halogen radiant heater is used to ignite most samples, and is recessed into the back wall of the duct to minimize disturbances to the flow, as also shown schematically in Figure 2. The power to the lamp was measured during each test. The lamp automatically deactivated at a preset time. The emission spectrum of the lamp was measured from 2 to 20 μm using a FTIR.

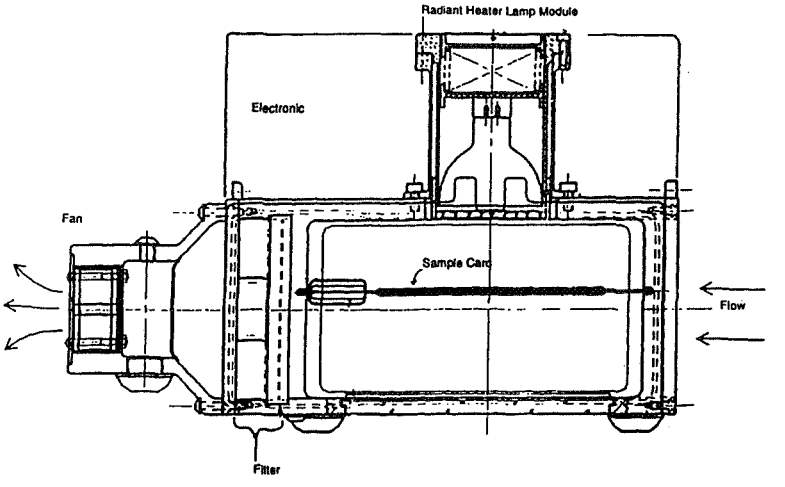

Figure 2 Schematic cross section view of hardware

A sample card is shown in Figure 3. A 10 cm x 8.7 cm sheet of Whatman 44[1] ashless filter paper was used as the sample. The center part of the sheet over the irradiated area was blackened to increase absorption of the incident beam from the lamp. The absorptivity of the blackened paper was measured by the NIST radiometric group between 1 and 20 μm. The samples were ignited at a central location either by the focused beam from the lamp (three-dimensional configuration) or along a line by a heated wire to observe planar flame growth (two-dimensional configuration). A few samples were doped with a smolder promoting agent, potassium acetate, to study smolder propagation from a central ignition point. Six 0.05 mm diameter type K thermocouples and an ignitor wire (30 gauge Kanthal wire) were pre-installed across the sample on each sample holder. Four thermocouples were installed in the sample at the center, 2 cm and 4 cm downstream from the center and at 2 cm upstream. Two thermocouples were installed at 2 mm above the sample surface at 2 cm upstream and also downstream locations from the center. The thermocouple data were recorded along with radiant

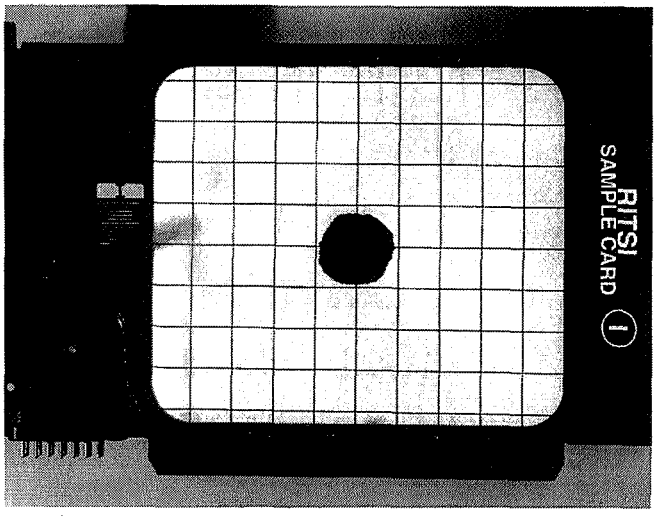

Figure 3 Sample card with 1 cm by 1 cm grid

[1]Certain company products are mentioned in the text in order to specify adequately the experimental procedure and equipment used. In no cases does such identification imply recommendation or endorsement by the National Institute of Standards and Technology and NASA, nor does it imply that the products are necessarily the best available for the purpose.

heater power, ignitor power, and flow velocity.

Color video pictures were taken in the direction normal to the sample surface to view changes in the flame shape and char pattern. Red diodes were used to illuminate the sample surface. Still color photographs were taken at an oblique angle to the sample by a motor-driven 35 mm camera. The flaming tests require the use of a blue transmitting/red blocking top window to observe the dim flame through the near-IR lamp light being scattered by the smoke, in addition to the red LED light being scattered. A window transmissive throughout the visible was used to image the smoke patterns for the smoldering tests.

The test matrix is given in Table 1. The first fifteen tests were instrumented with thermocouples; the last ten were assembled in orbit without thermocouples using the spare sample materials flown.

3. Test Results and Discussion

3.1 Ignition

Ignition was achieved in almost all tests using either a heated wire or a lamp. Since radiative ignition was not achieved with the same system in normal gravity, it was initially planned that a heated wire above the irradiated sample surface would be used as a pilot during the lamp irradiation if ignition was not achieved in the first radiative ignition test without the heated wire. Surprisingly, however, ignition was achieved without using a heated wire in the first test, and all tests in the three-dimensional configuration were ignited by the lamp alone. It appears that in normal gravity, hot combustible degradation products were cooled and swept away from the hot irradiated surface due to buoyancy-induced flow and non-piloted ignition was thus difficult to achieve in normal gravity. In microgravity, however, the hot combustible degradation products tended to stay near the irradiated surface (expansion and diffusion are the only mechanisms which cool and slowly move the products away from the irradiated area) and non-piloted ignition (self-induced pilot from the hot irradiated surface) tended to occur compared to the case in normal gravity. Radiative ignition by the lamp was quite reproducible and preliminary results show that the ignition delay time (a little over 4 s after the ignition switch was turned on) was nearly constant in the range of flow velocities used in this study. This ignition delay time included about 2.2 s from power on to a point where the output of the lamp reached the designated flux. Ignition by a heated wire was less reproducible than that by the lamp due to changes in wire contact with the sample caused by the expansion of the wire after it heated. Ignition tended to occur at one face of the sample surface at first followed by the second ignition on the other face of the sample surface.

3.2 Transition and Growth of Flame and Char Pattern

3.2.a Two-dimensional Configuration

Four tests were conducted at the external flow velocities of 0, 2, and 5 cm/s. The behavior of the flame from the side view parallel to the paper sample is shown in Figs 4 for the three different

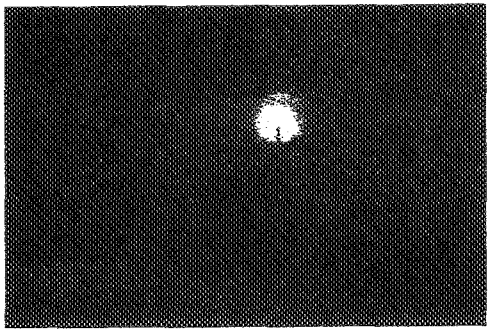

Figure 4a: quiescent ignition

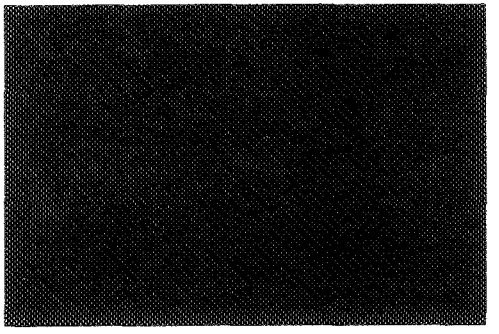

Figure 4b: quiescent transition

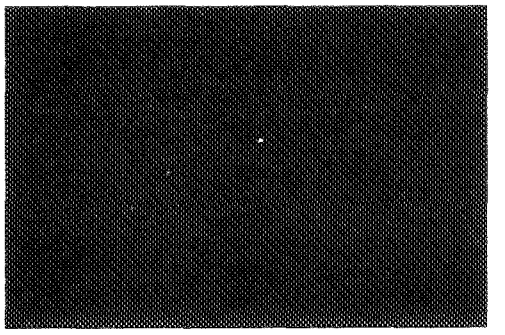

Figure 4c: quiescent extinction

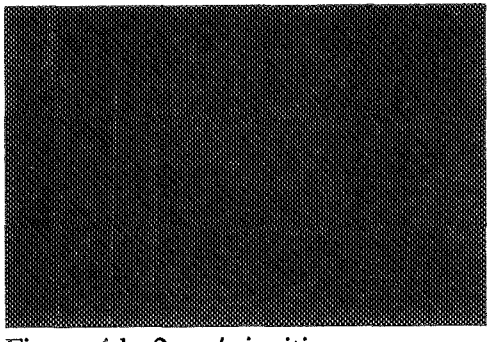

Figure 4d: 2 cm/s ignition

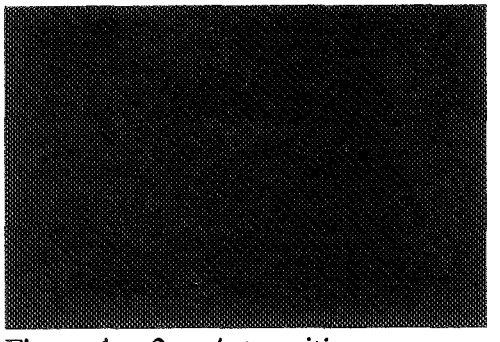

Figure 4e: 2 cm/s transition

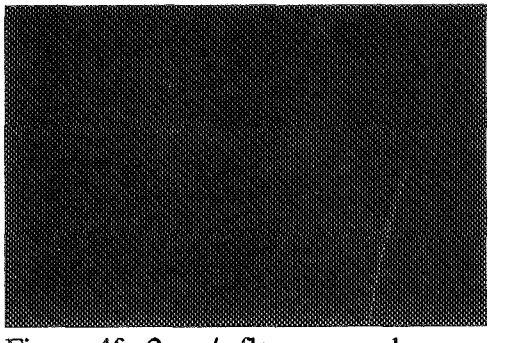

Figure 4f: 2 cm/s flame spread

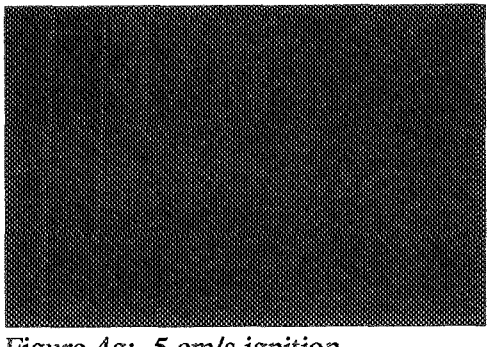

Figure 4g: 5 cm/s ignition

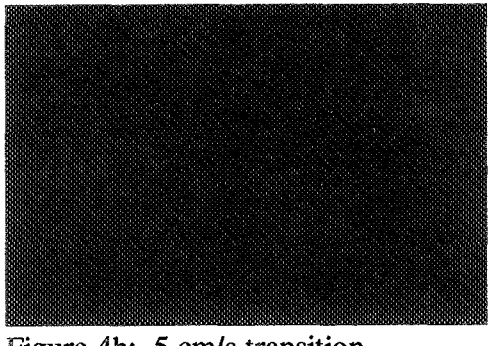

Figure 4h: 5 cm/s transition

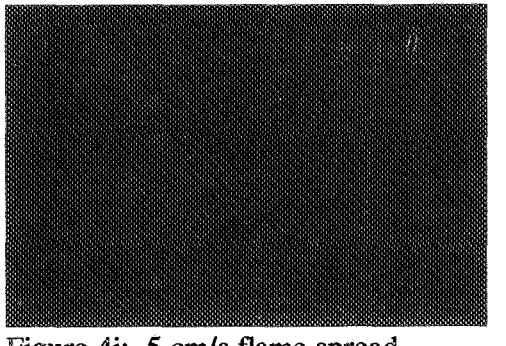

Figure 4i: 5 cm/s flame spread

Figure 4 Flame spread at three different flow velocities in two-dimensional configuration (Flow from right)

flow velocities at three different stages: ignition, transition to flame spread, and fully developed flame spread. At ignition, Figs. 4a, 4d, and 4g, a blue flame appeared only over one face of the sample surface due to the contact condition of the expanded heated wire with the sample as discussed above. In the quiescent condition, Fig. 4a, an orange glow appeared over the other face of the sample surface. This glow was caused by the scattered light from the glowing heated wire by degradation products from the paper sample; it was not flame. This glow died and only the bottom side of the flame persisted, as shown in Fig. 4b. Nevertheless, a much fainter scattered vapor cloud can still be seen in this figure. At the later stage , Fig. 4c, the bottom flame disappeared leaving a faint vapor cloud similar to the that over the other face of the sample surface; the transition from ignition to flame spread did not occur. These clouds indicate that there might be enough combustible degradation products in the gas phase close to the heated wire to ignite but it appears that oxygen supply was not sufficient to yield ignition. At 2 cm/s and 5 cm/s, flames appeared on both sides of the sample surface and the flames continued to spread upstream to the end of the sample. This observation suggests that flames over both sides of the sample surfaces might be needed for the transition to flame spread and the supply of oxygen appears to be the rate-controlling process to transition to flame spread. The observed upstream flame spread has been predicted in our theoretical calculation [14] and the overall shape of the spreading flame calculated in this reference is very similar to that seen in these figures. The flame became longer with an increase in the external flow velocity and the color of the flames remained blue in the range of the flow velocities used in this study.

Selected video pictures normal to the sample surface in the two-dimensional configuration are shown in Figs. 5. Since the blue color of the flames was faint, only the growth pattern of the char layers (faint dark color) can be seen in these figures. Careful observation reveals that a spreading blue flame front was several millimeters ahead of the char front. This is also confirmed by an earlier temperature increase 2 mm above the sample surface than the temperature increase in the sample at a location 2 cm upstream from the center of the irradiated area, as shown in Fig.6. The figure shows a rapid sample temperature increase at the center of the irradiated area up to about 450 °C; it stayed at this temperature even when the lamp was turned off at about 6 s. After about 8 s, this temperature started to increase gradually up to almost 700 °C, presumably due to glowing (smoldering) of the char. The increase in sample temperature at two downstream locations (2 cm and 4 cm from the irradiated center) occured at earlier time than that at 2 cm in the upstream but its rate of increase in the downstream location was much less than that in the upstream location. This indicates that hot combustion products were swept downstream shortly after the onset of ignition but the sample temperature at the 2 cm downstream location was not high enough, only up to about 200 °C till 10 s and later up to about 250 °C, to generate char. Even the gas phase temperature at 2 mm from the surface at the 2 cm downstream location went up to only about 400 °C compared to above 800 °C at the 2 cm upstream location. At the 4 cm downstream location, the sample temperature increases up to only about 150 °C. It is expected that at least 300 °C is needed to form char for this sample [15]. Therefore, the char layer growth was observed only in the upstream side at 2 and 5 cm/s flow velocities. With the measured sample temperature history during the approaching flame front (fitting with a linear temperature increase with time), the net energy feedback rate (total feedback rate minus radiative/convective losses from the sample surface) from the upstream spreading flame front to the sample at the 2 cm upstream position and also those from hot combustion

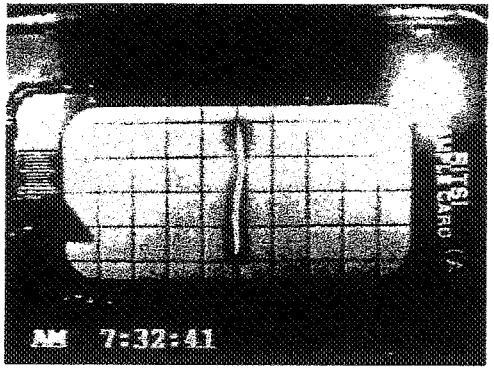

Figure 5a: quiescent igition

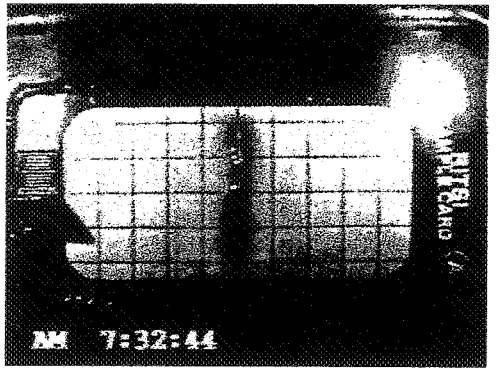

Figure 5b: quiescent transition

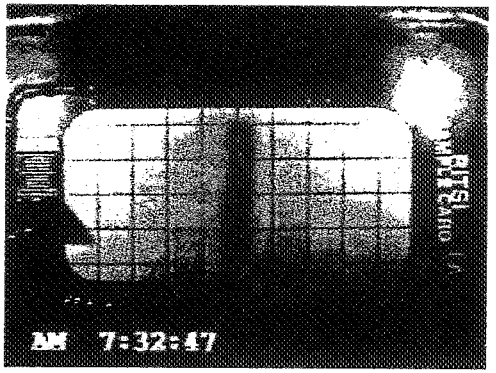

Figure 5c: quiescent extinction

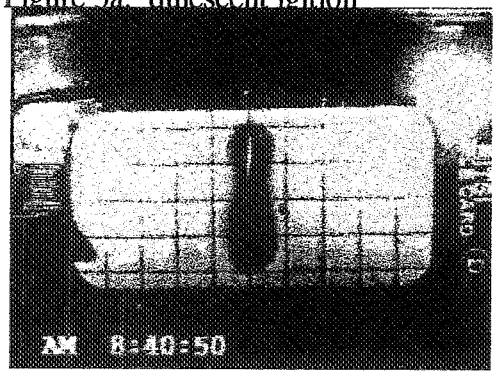

Figure 5d: 2 cm/s after ignition

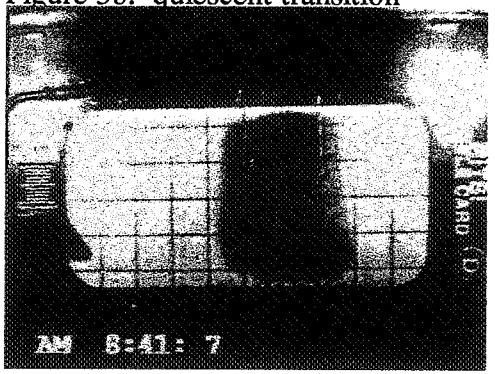

Figure 5e: 2 cm/s spread

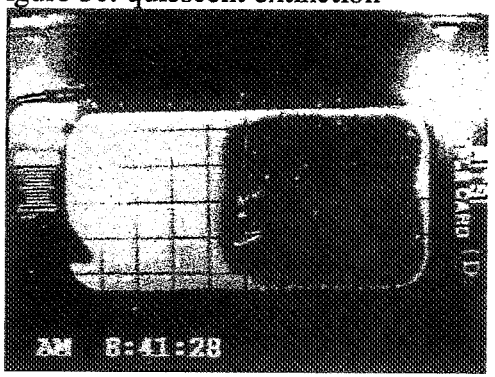

Figure 5f: 2 cm/s fully spread

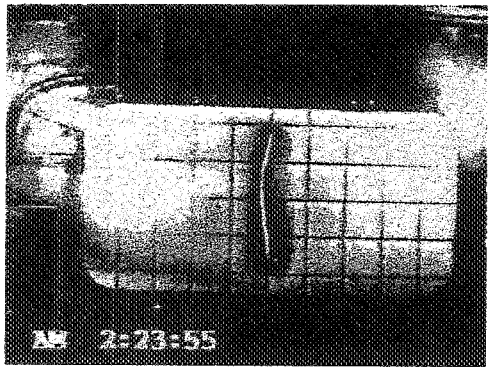

Figure 5g: 5 cm/s after ignition

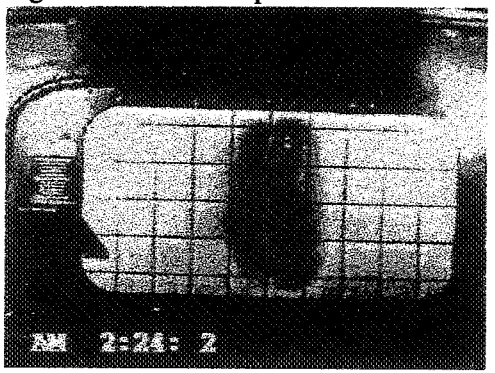

Figure 5h: 5 cm/s spread

Figure 5i: 5 cm/s nearly fully spread

Figure 5 Char growth patterns at three different flow velocities in two-dimensional configuration (Flow from right).

products flow at 2 cm and 4 cm downstream locations were calculated. In the calculation it was assumed that the sample was thermally thin and the flame and the flow were symmetric about the sample; the net energy feedback rate from the upstream flame is 3.3 W/cm^2 ± 10% for each surface (top and bottom), that from the hot products flow at the 2 cm downstream location is 0.6 W/cm^2 ± 10% for each surface and that at the 4 cm downstream location is 0.2 W/cm^2 ± 10% for each surface.

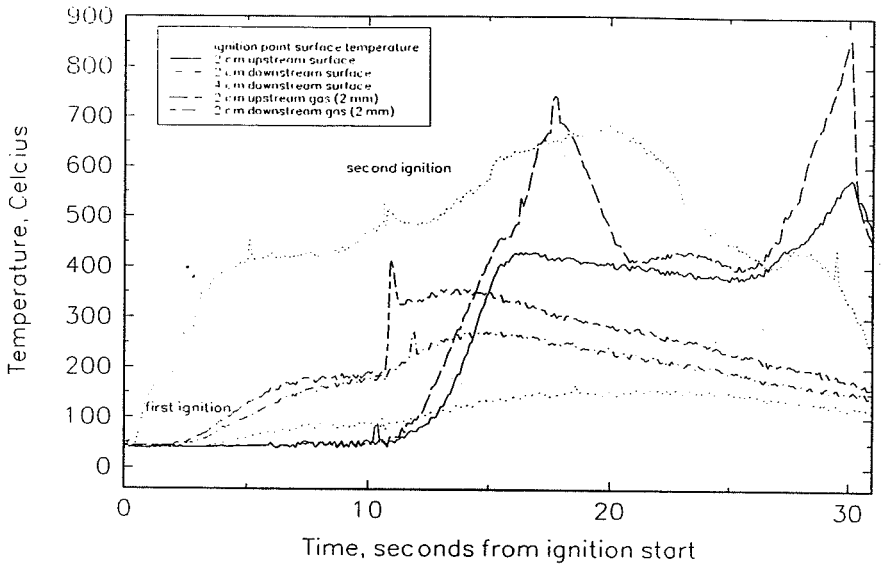

Figure 6 Temperature histories in two-dimensional configuration, 5 cm/s

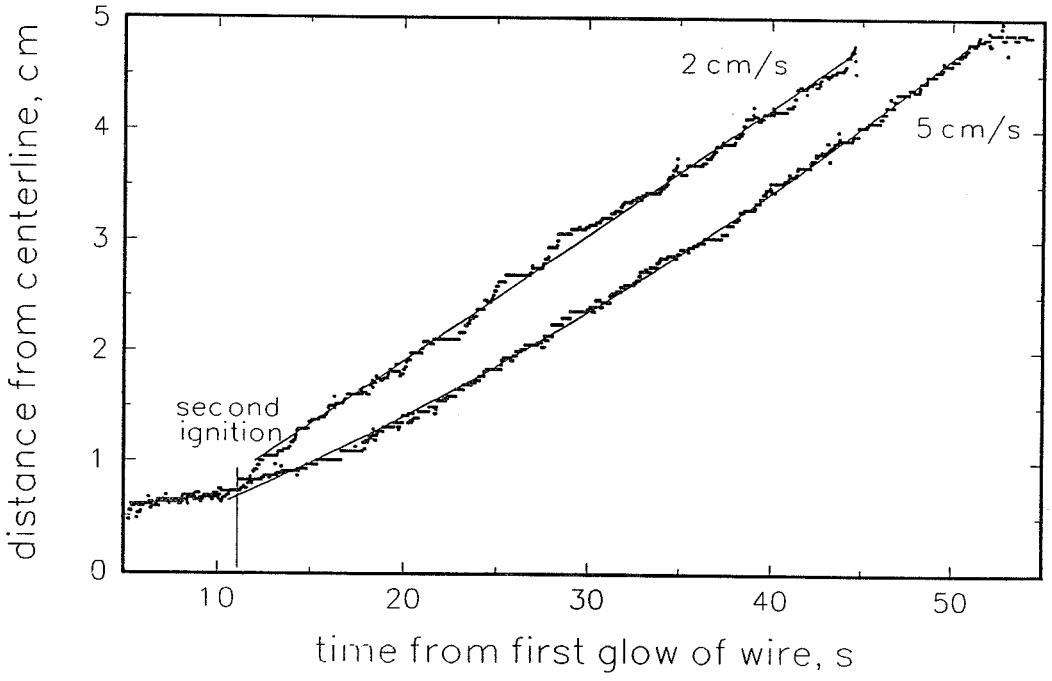

Fig. 7 Upstream char-front location histories in two-dimensional configuration.

Since the flame was faint and hard to see clearly in the recorded videos, the growth of the char patterns shown in Figs. 5 was used to calculate char spread rate. As the distance between the spreading char front and traveling flame front appeared to be nearly constant, it was assumed that

the char spread rate was the same as flame spread rate. The position of the char front spreading toward upstream was measured at different times for the external flow velocities of 2 cm/s and 5 cm/s; the results are plotted in Fig.7. As shown in this figure and discussed above, the flame hardly spread when only one side of the sample was ignited. After the second ignition at the side opposite from the first ignition, the flames started to spread. At 2 cm/s, it appears that char spread at an apparently steady rate shortly after the second ignition but at 5 cm/s, initially char spread slowly and then reached the apparently steady rate. Both apparently steady char spread rates are about the same; they were 0.11 ± 0.01 cm/s. Since the char spread rate for the case of 5 cm/s appears to increase with an increase in distance from the ignited area, as shown in Fig.7, some caution is needed for the spread value at an external flow velocity of 5 cm/s.

3.2 b Three-dimensional Configuration

Although flaming ignition was observed in the quiescent condition, transition to flame spread did not occur. However, that transition did occur at external flow velocities of 0.5 cm/s, 1 cm/s, 2 cm/s, 3.5 cm/s, 5 cm/s and 6.5 cm/s. The growth patterns of flame for the 0.5 cm/s, 2 cm/s, and 6.5 cm/s cases are shown in Figs. 8. These pictures were taken by a 35 mm camera looking downward at an oblique angle. The color of the flames was blue during the experiments, similar to the above cases for the two-dimensional configuration. At 0.5 cm/s, a small flame spread only upstream maintaining the initial flame shape from shortly after ignition. The flame never grew laterally from the initial width and this is also clearly seen in the growth pattern of char in Figs. 9a-c. However, the flame and char growth patterns did grow laterally outward with an increase in the external velocity, as shown in Figs. 8 and 9. At 2 cm/s, the flame had a crescent shape and the char growth pattern was initially an elongated circle pointing upstream; at later times, it became fan-shaped. At 6.5 cm/s, the shape of the flame became like a horseshoe with the tails of the horseshoe flame extending downstream. The char pattern became an elongated circle in the upstream direction with a relatively flat downstream side. A similar shape was also observed in 35% and 50% oxygen concentrations at 5 cm/s external flow velocity [16], although the color of these flames was orange. Our theoretical calculations predicted a similar shape of flame at 5 cm/s [16]. A major difference in flame shape between air in this study and 50% oxygen concentration is that a spreading spherical flame was observed in a quiescent condition in 50% oxygen concentration compared with no transition to flame spread in the air case. Therefore, at low external velocities, the char patterns were more or less spherical in 50% oxygen concentration instead of the narrow strip char pattern observed in the air case. The observed trend of opening the angle of the char pattern in the upstream direction with an increase in external flow velocity of air in microgravity is quite different from the narrowing angle trend of the down stream flame with an increase in external flow velocity in normal gravity. However, it is expected that further increase in external velocity in microgravity would eventually reduce upstream flame spread rate and be sufficient to promote downstream flame spread. Thus, this observed trend of the char pattern is unique and should occur only at low external flow velocities and low oxygen concentrations, such as in air, in microgravity.

The sample temperatures were measured along the center line at four locations; one was at the center of the irradiated area, one was at the 2 cm upstream location, and two were at 2 cm and 4 cm downstream locations. The gas-phase temperatures were measured 2 mm above the sample surface at the 2 cm downstream location and at the 2 cm upstream location. The results for an

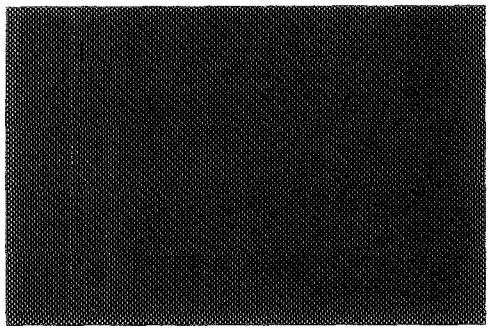

Figure 8a: 0.5 cm/s after ignition

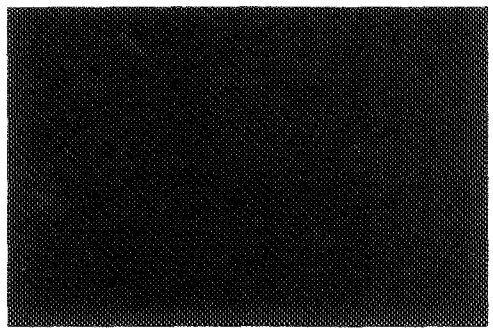

Figure 8b: 0.5 cm/s spread

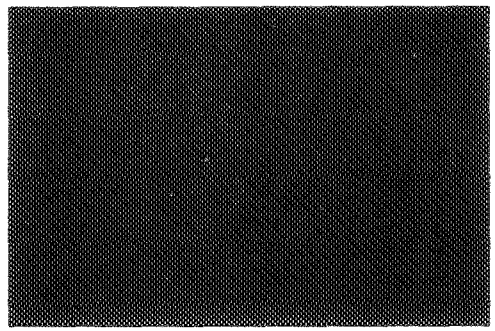

Figure 8c: 0.5 cm/s full spread

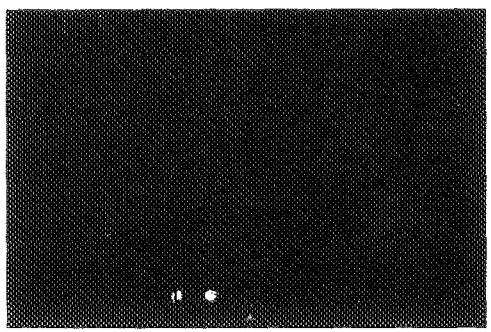

Figure 8d: 2 cm/s after ignition

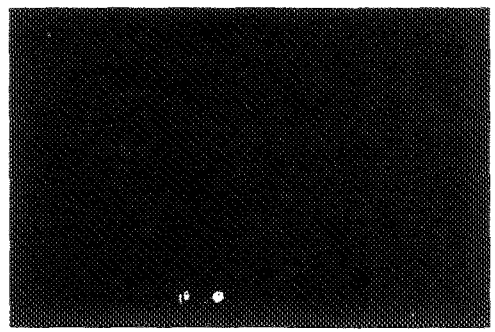

Figure 8e: 2 cm/s spread

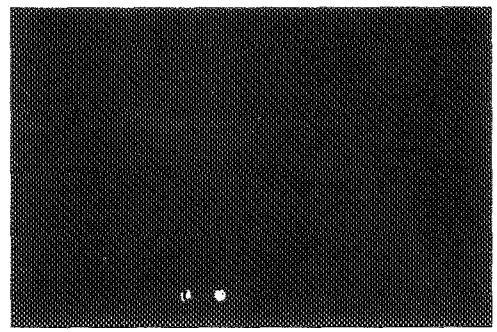

Figure 8f: 2 cm/s full spread

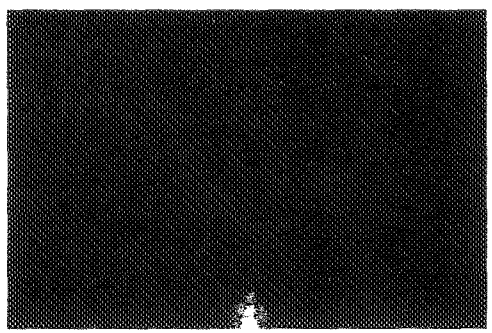

Figure 8g: 6.5 cm/s after ignition

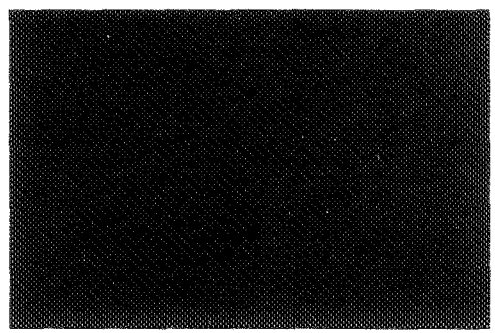

Figure 8h: 6.5 cm/s spread

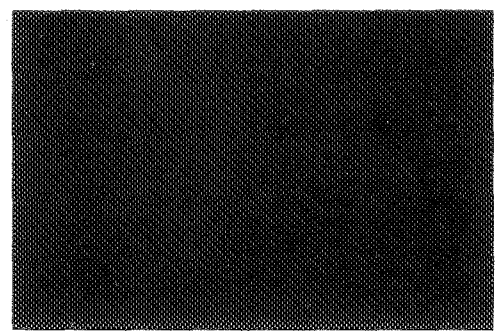

Figure 8i: 6.5 cm/s full spread

Figure 8 Flame spread patterns at three different flow velocities in three-dimensional configuration (Flow from right)

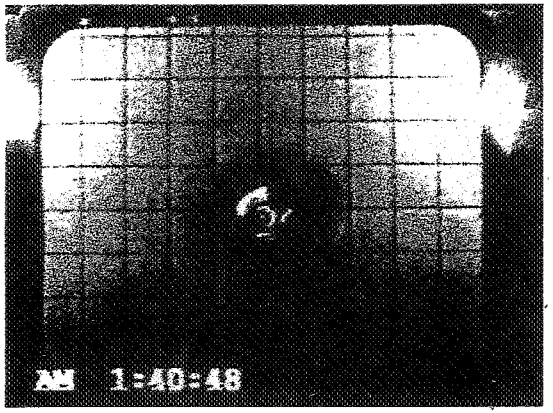

Figure 9a: 0.5 cm/s after ignition

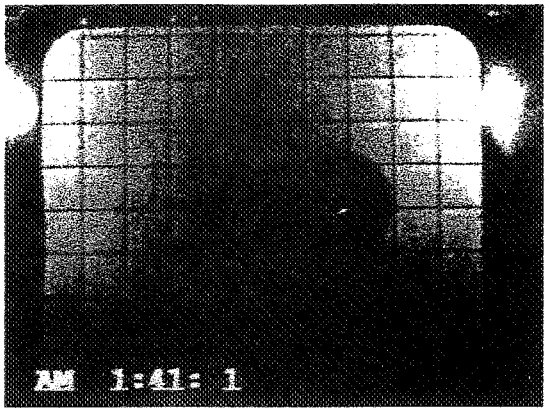

Figure 9b: 0.5 cm/s spread

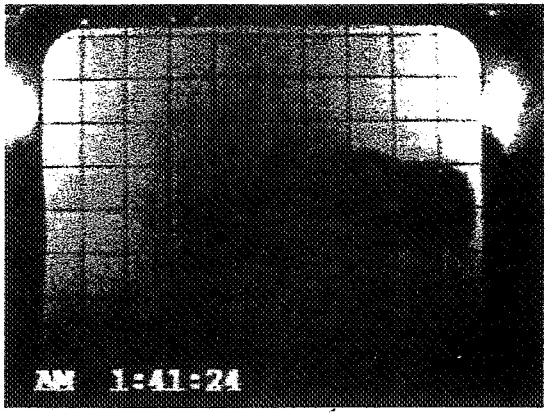

Figure 9c: 0.5 cm/s fully spread upstream

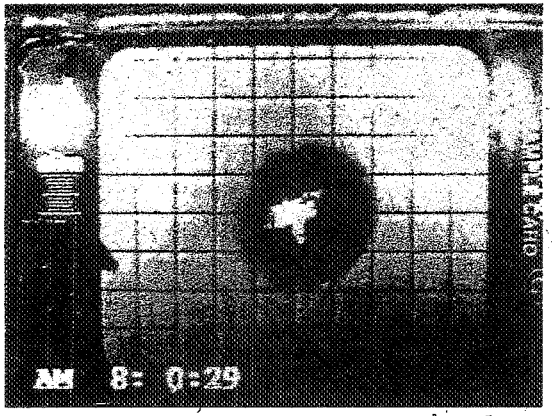

Figure 9d: 2 cm/s after ignition

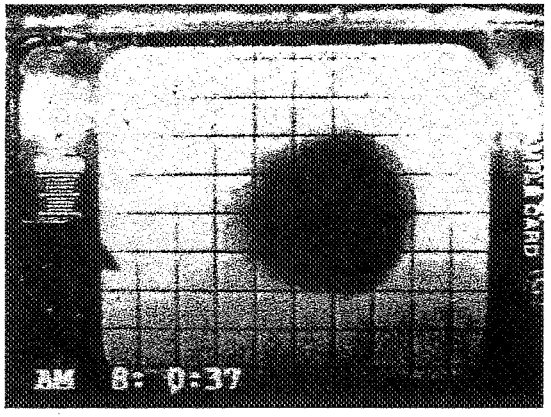

Figure 9e: 2 cm/s spread

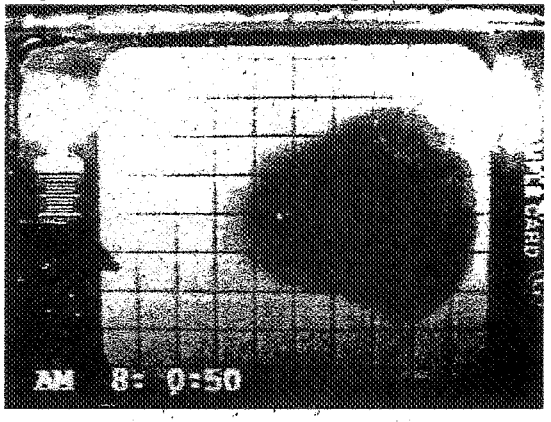

Figure 9f: 2 cm/s fully spread upstream

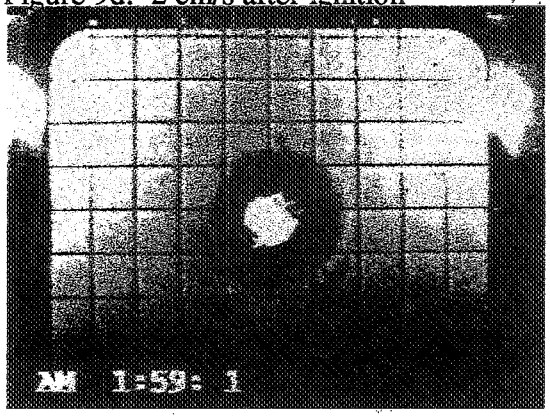

Figure 9g: 6.5 cm/s after ignition

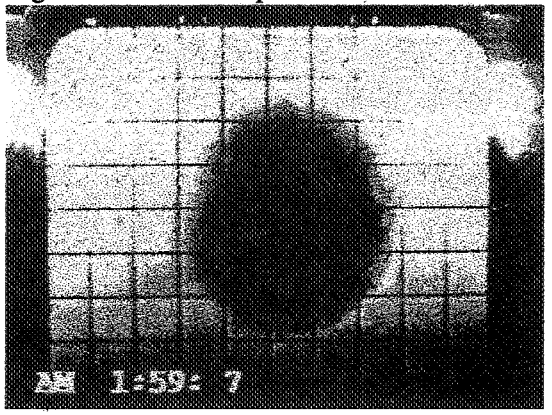

Figure 9h: 6.5 cm/s spread

Figure 9i: 6.5 cm/s fully spread upstream

Figure 9 Char growth Patterns in the three-dimensional configuration (Flow from right)

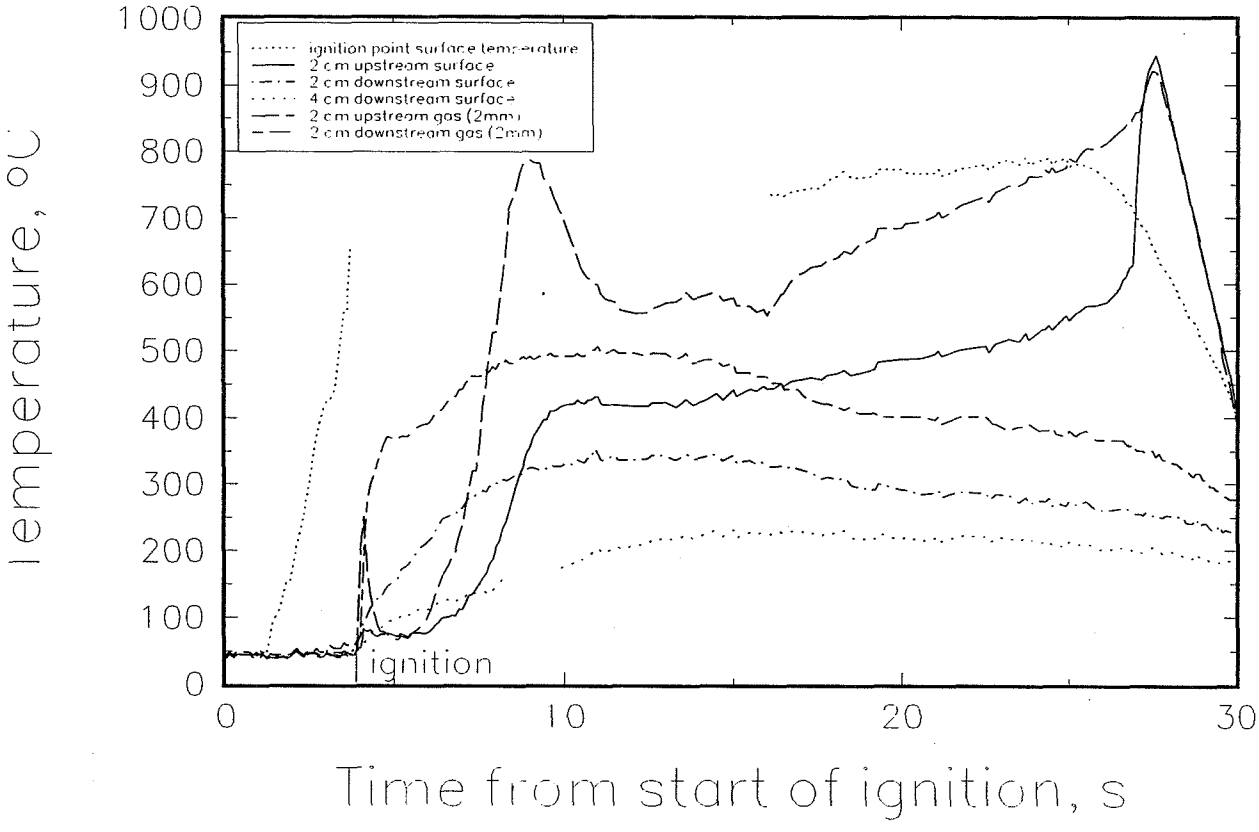

Fig. 10 Temperature histories in three-dimensional configuration, 5 cm/s.

external flow velocity of 5 cm/s are shown in Fig. 10. Time zero was defined as the moment when the power to the lamp was turned on. The delay of temperature increase at the center of the irradiated area was due to the lamp's heat-up time, as discussed above. Unfortunately, the LED display for the center thermocouple was obscured by the reflection of the lamp light and its output could net be read shortly after ignition until the lamp was turned off. A high center temperature indicates that there might be some additional increase in the thermocouple temperature due to the absorption of external radiation from the lamp by the thermocouple bead. Ignition can be recognized as the sudden jumps in the two gas phase temperatures at the locations 2 cm from the center of the irradiated area. The downstream gas phase temperature continued to increase after the ignition due to the flow of hot combustion products but the upstream gas phase temperature dropped rapidly. However, the downstream gas phase temperature went up only to about 500 °C which is much lower than a realistic flame temperature. The behavior of the upstream gas phase temperature indicates that a sudden expansion of flame at ignition momentarily reached to this location but the gas there contracted and the external flow quickly cooled down the local gas temperature. The downstream sample temperatures at the 2 cm and 4 cm locations increased earlier than that at the 2 cm upstream location due to the convecting heating from the hot combustion products flow. However, the downstream sample temperature increased up to only about 350 °C at 2 cm and to about 220 °C at 4 cm. The upstream temperature at 2 cm increased rapidly to about 430 °C and further increase appears to be caused by movement of the thermocouple bead into the gas phase. The first peak of the downstream gas

phase temperature 2 mm above the sample surface at 2 cm was due to the traveling flame front and the second peak was due to the approach of the tail end of the flame. The net energy feedback rate from the traveling downstream flame to the sample surface was calculated with the temperature plot at 2 cm upstream location using the same assumptions described in the two-dimensional configuration. The value is 4.1 W/cm^2 ± 10% for each face of the sample surface (two flames along the two faces of the sample); this is about 25% higher than that in the two-dimensional configuration discussed above. The net energy feedback rates at the two downstream locations are 1.6 W/cm^2 ± 10% and 0.5 W/cm^2 ± 10%. These values are also significantly larger than those in the two-dimensional configuration: about 30% and 100%, respectively.

The histories of the char front spreading upstream along the centerline are plotted in Fig.11 using the results shown in Fig.9 to determine the relationship between the location of the char front and

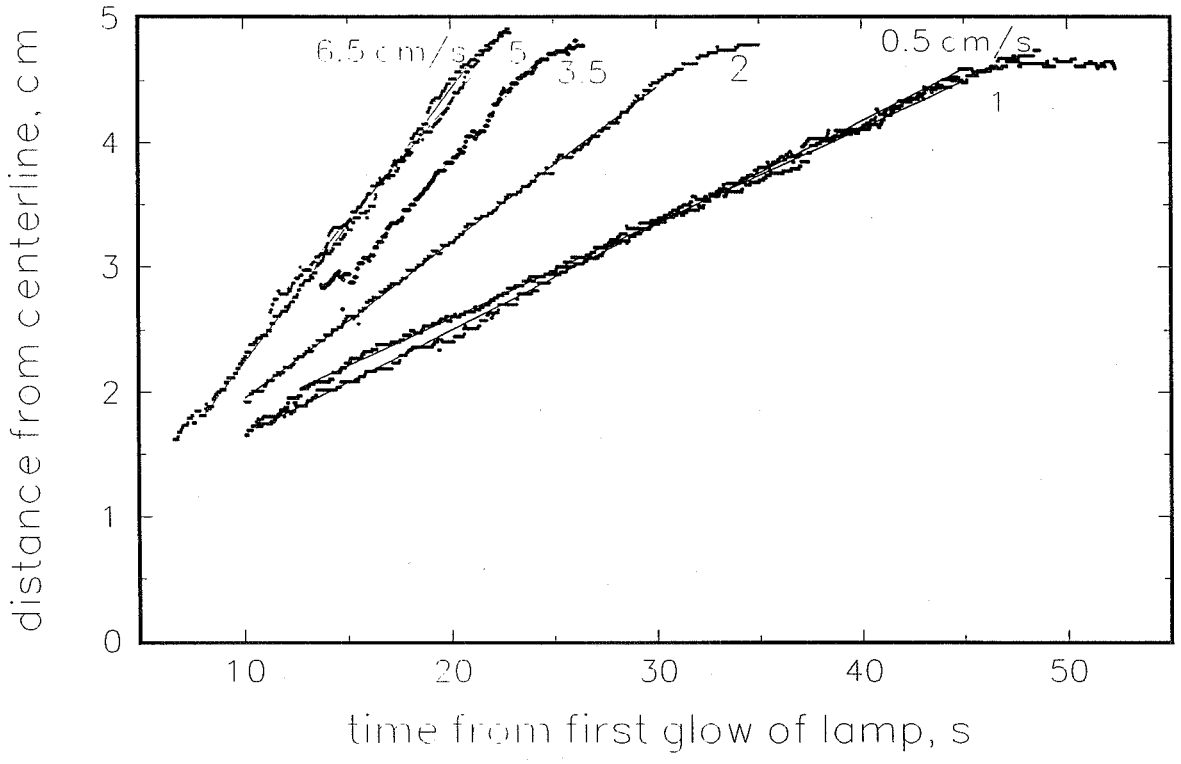

Fig. 11 Upstream char-front location histories in three-dimensional configuration.

time after the initial glow of the ignitor wire. Although the shape of the flame and the curvature of the flame front changed with time, the relationships can be reasonably well fitted by linear equations except when the char front came close to the sample edge. Thus, apparent steady-state-like char front spread rates along the centerline are obtained for each external flow velocity. These apparent steady-state char spread rates are plotted against the external flow velocity in the two- and three-dimensional configurations. The results are shown in Fig.12. Some caution is needed in comparing the results between the two-dimensional configuration and the three-

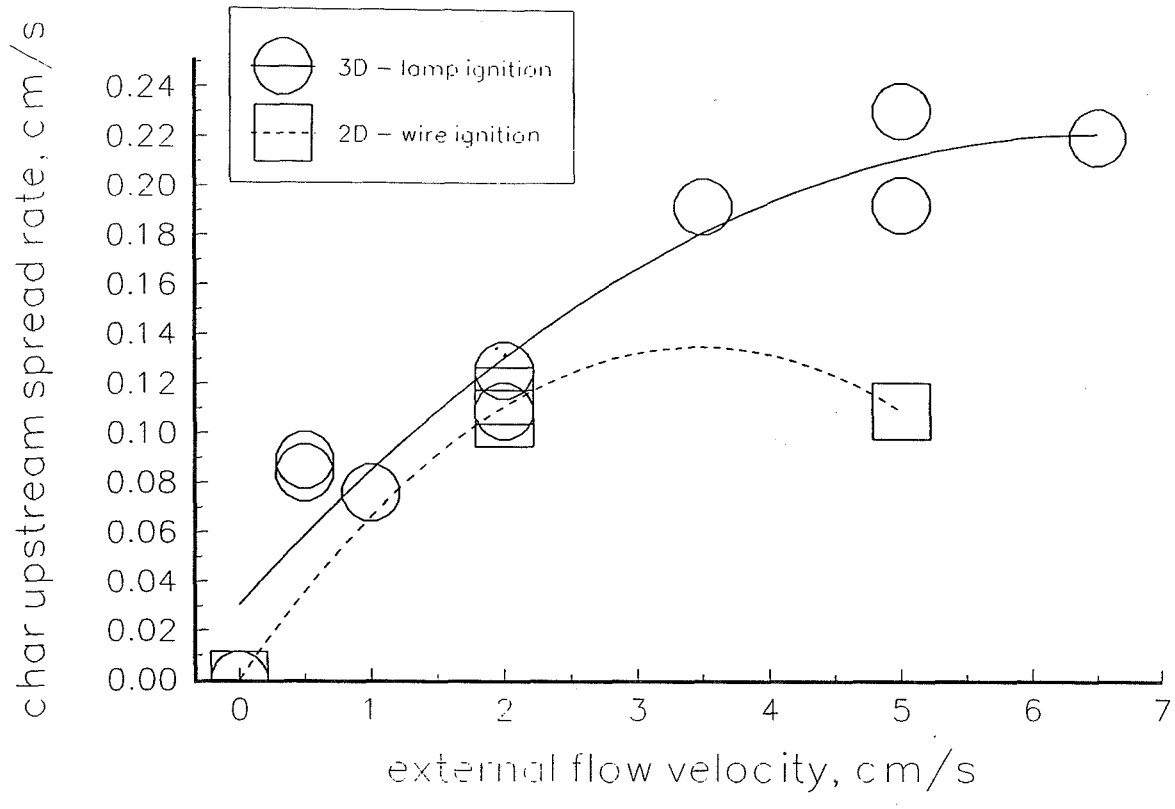

Fig. 12 Char upstream spread rate versus external flow velocity.

dimensional configuration due to the transient nature of the three-dimensional flame and the fact that there is only one data point at 5 cm/s in the two-dimensional configuration. However, it is interesting to note that in the three-dimensional configuration the char spread rate continues to increase with an increase in external velocity and it appears that the maximum spread rate might not have been reached. On the other hand, it appears that the maximum flame might already be reached in the two-dimensional configuration. (The existence of a maximum flame spread with respect to external flow velocity was first demonstrated by Olson. [17]) Since only four experiments were conducted in the two-dimensional configuration and also since there is some unsteady nature of the char spread rate for the case of 5 cm/s, further experiments are needed to determine the relationship between the spread rate and external flow velocity. If this trend is true, the above discussed higher net energy feedback rate from the flame to the sample surface in the three-dimensional configuration indicates that the three-dimensional flame front might be more intense due possibly to a larger oxygen supply at the curved flame front. In the regime where oxygen supply is a critical rate-controlling process, a curved flame front has a larger area for incoming oxygen to reach. A similar trend of a higher maximum flame spread rate in the three-dimensional configuration versus that in the two-dimensional configuration was also observed in 35% and 50% oxygen concentrations in our drop tower experiments. However, if our explanation is correct, the flame spread rate in the three-dimensional configuration should decrease as the curvature of the flame decreases with an increase in the distance from the ignition area. Although a slow down of spread rate beyond 4 cm from the center is observed, as shown in Fig.11, it is not clear that this was caused by a more planar flame front or by the flame front moving at a higher flow velocity when the flame got close to the leading edge of the boundary

layer. In order to confirm this trend further, we need to conduct more tests in the two-dimensional configuration, with larger size samples in the three-dimensional configuration, and also at higher external flows.

3.2c Flame spread along the open edges of samples

The flame spread behavior along the open edges of the paper sample was studied using a narrow sample, 4 cm in width, in the same sample holder. Ignition was achieved by the lamp illuminating the center of the sample; initially, the flame spread radially upstream. This behavior is shown in Figs. 13. Once the flame reached the open edges of the sample, the flames at each edge spread much more rapidly than the flame along the center line, as shown in Figs. 13b, 13c, 13e, and 13f. At the open edges of the sample, oxygen supply to the flame (almost 360°) and energy feedback from the flame to the sample (from three sides) are much larger than that for the flame along the center of the sample (about 180° for oxygen supply and only two sides for energy feedback). However, under an external flow velocity of 2 cm/s, it appears that oxygen concentration along the downstream edges was not sufficient due to dilution from the combustion products of upstream flame; flame spread along only the upstream edges. Above an external flow velocity of 3.5 cm/s, oxygen supply to the downstream edges was sufficient and flames spread downstream as well as upstream along the open edges of the sample as shown in Figs.13e and 13f.

3.3 Smoldering

In RITSI, four smoldering experiments were conducted with ignition initiated at the center of the sample by the lamp. The sample was doped with potassium ions to enhance char formation and char oxidation (4.2 weight % ±5% in spatial non-uniformity). Although a ring-shaped smoldering front was initially observed in normal gravity (the-ring shaped front gradually deformed due to induced buoyant flow from the hot smoldering surface), unexpected, very complex finger-shaped char patterns with localized smoldering fronts at the finger tips were observed in microgravity; such patterns are seen in Figs.14. In these pictures, the white spots are the localized smoldering fronts. The direction of growth of the char pattern was mainly upstream; higher external flow velocity tends to increase the number of localized smoldering fronts, the number of fingers, and also the frequency of bifurcations from each finger. At present it is not clear what caused this complex pattern. One possible explanation is that there is some non-uniformity in sample thickness and the concentration of potassium ions (doped to the sample to enhance smoldering) in the filter paper. Since potassium ions were heavily doped into the samples (more than needed to make sure that smoldering rate does not depend on the ion concentration), we believe that this phenomenon was not caused by a non-uniformity (± 5%) in ion concentration in the sample. Since smoldering induces roughly 20 cm/s buoyancy induced flow in normal gravity, it might be that any non-uniformity of the sample tends to be suppressed in normal gravity. In microgravity, however, it appears that a flow velocity up to 6.5 cm/s does not suppress it. Another possible explanation is that this is a unique instability phenomenon which could occur only at low flow velocities below the buoyancy induced flow velocity such as is the case under microgravity conditions.

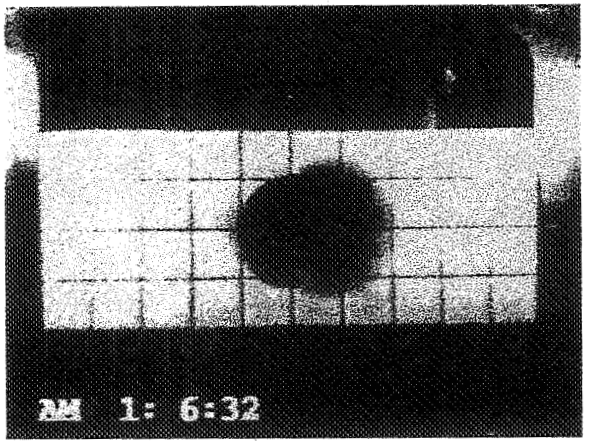

Figure 13a: 2 cm/s post ignition

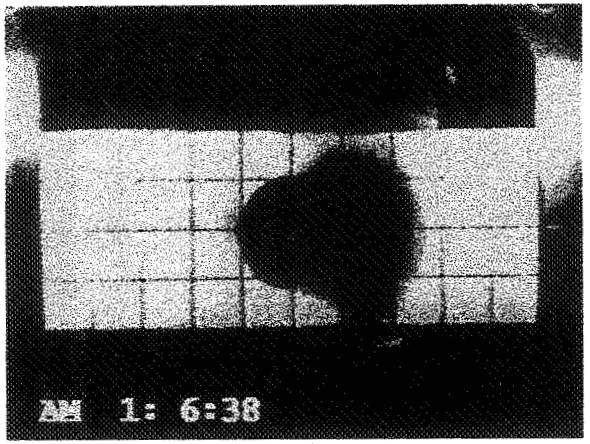

Figure 13b: 2 cm/s enhanced edge spreading

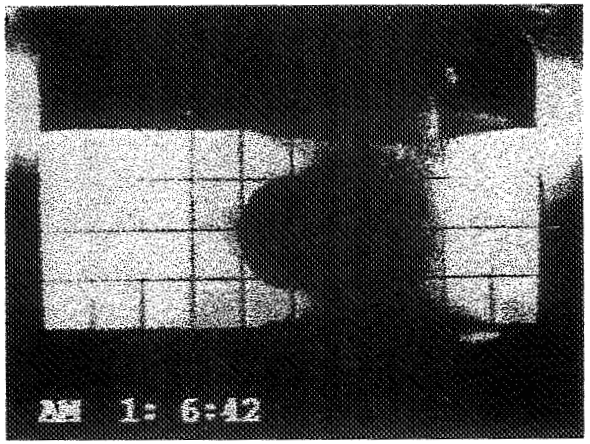

Figure 13c: 2 cm/s upstream spread only

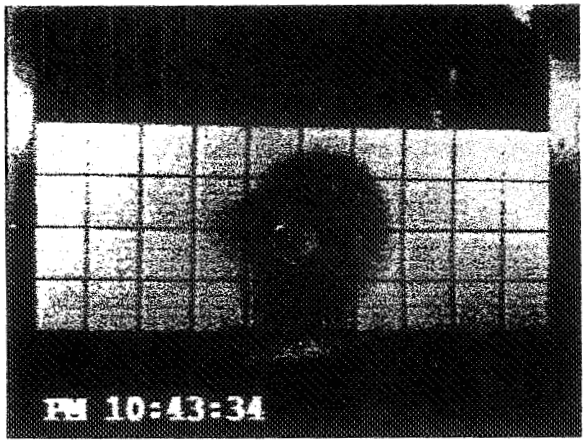

Figure 13d:5 cm/s post ignition

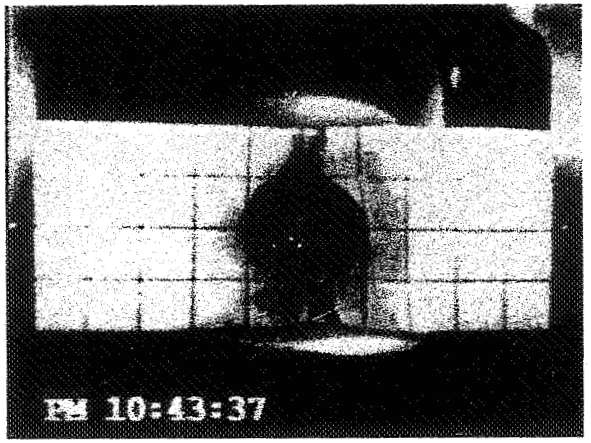

Figure 13e: 5 cm/s enhanced edge spreading

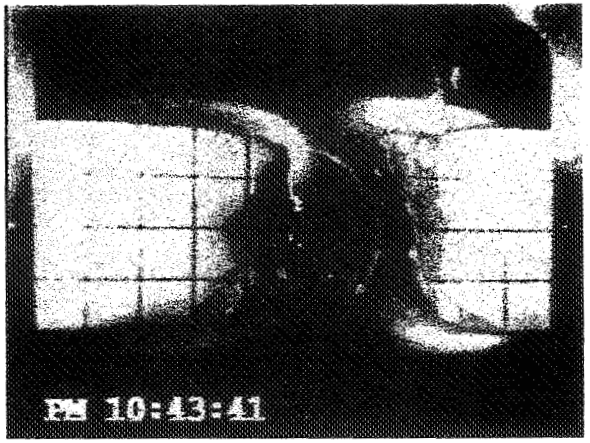

Figure 13f: 5 cm/s bidirectional edge spread

Figure 13 Flame spread patterns along open edges (Ignition was initiated at the center, Flow from right).

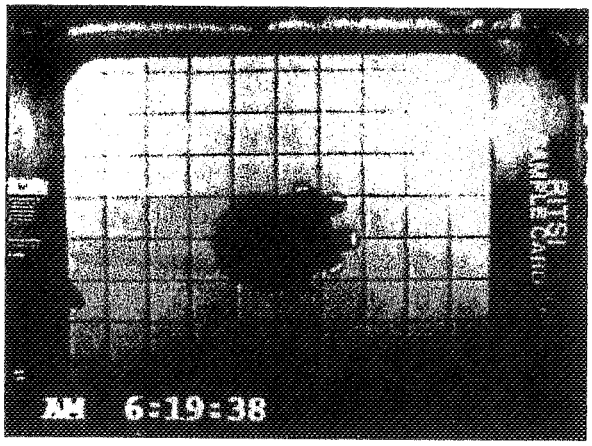

Figure 14a: 0.5 cm/s flow test, just after ignition

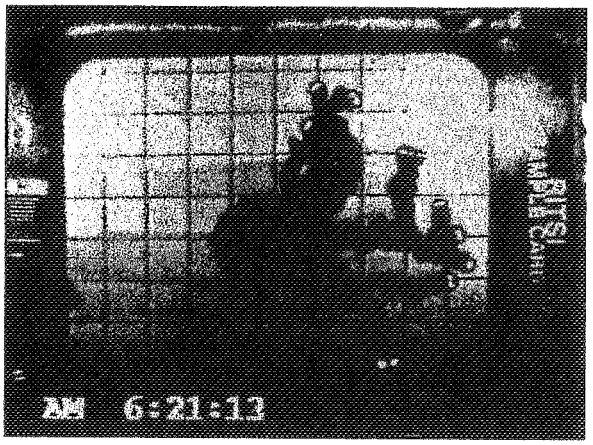

Figure 14b: 0.5 cm/s flow test, later in the burn

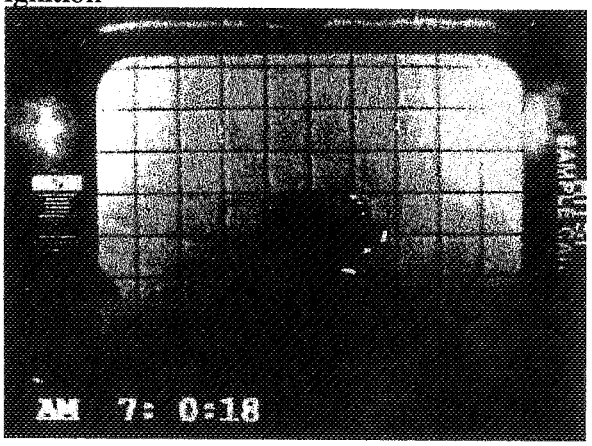

Figure 14c: 2 cm/s flow test, just after ignition

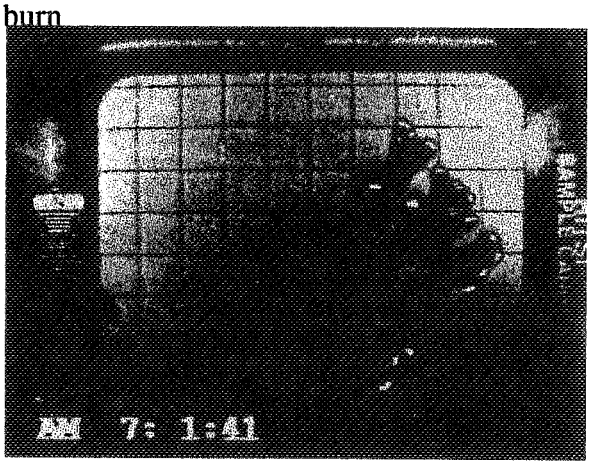

Figure 14d: 2 cm/s flow test, later in the burn

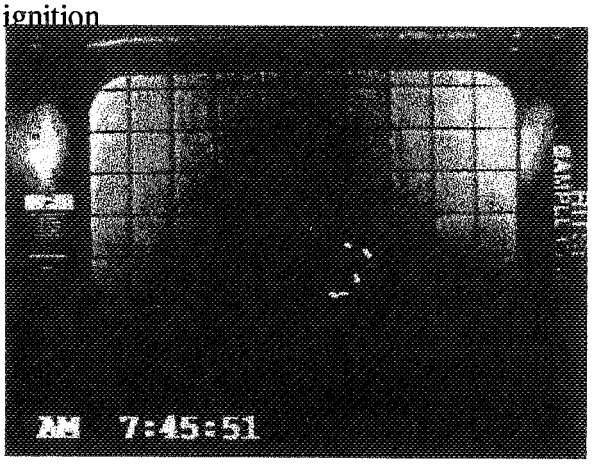

Figure 14e: 6.5 cm/s flow test, just after ignition

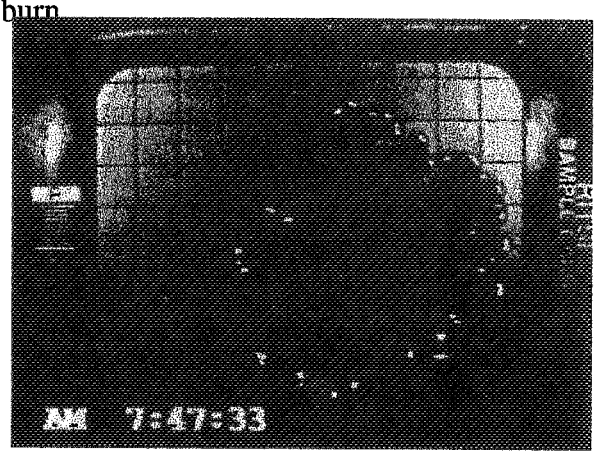

Figure 6: 6.5 cm/s flow test, later in the burn

Figure 14 Smoldering char growth patterns at different flow velocities. (Flow from right)

4. Summary

Non-piloted ignition by external thermal radiation of a cellulosic paper tends to occur more easily in microgravity than in normal gravity. Downstream flame spread was never observed in the two-dimensional configuration exposed to external flow velocity of up to 5 cm/s, when ignition was initiated locally in the middle part of a thin paper. This was presumably due to lack of oxygen due to the dilution of combustion products from the upstream flame (oxygen shadow effect). In the three-dimensional configuration, when ignition was initiated locally in a small circle in the center of the sample, flame spread was again mainly upstream. At the lowest flow (0.5 cm/s) for sustained spread, the flame remained a very small hemisphere that propagated directly upstream without any lateral spread. At 1 cm/s, the flame fanned out slightly as it propagated upstream. The fan angle increased with flow velocity. At 6.5 cm/s, the flame became horseshoe- shaped. It appears that the three-dimensional flame front (i.e., curved flame front) might be more intense than that in the two-dimensional flame front (planar flame) due to larger oxygen supply to the curved flame front. The peak upstream flame spread rate in the two-dimensional configuration tends to occur at lower external flow velocity than that in the three-dimensional configuration. The shape of the upstream flame front might have important effects on the strength of the flame front and upstream flame spread rate.

Flame spread much faster along open edges of a thin paper sample than along the sample surface. At the external flow velocity of 2 cm/s, flame spread along open edges only upstream while, above 3.5 cm/s, flame spread along open edges downstream as well as upstream.

An unexpected, complex surface smoldering char growth pattern was observed when localized smoldering was initiated at the center of the sample by a lamp. Instead of a ring-like smoldering front as is observed in normal gravity, finger-shaped char growth pattern with several localized smoldering fronts was observed. Generally, the char growth pattern was mainly upstream. The number of localized smoldering fronts, the number of fingers, and the frequency of bifurcations of the finger increased with an increase in external flow velocity. At present, it is not clear what causes this complex char growth pattern.

Acknowledgment

This work is funded by the NASA Microgravity Science Program under the Inter-Agency Agreement No. C-32001-R.

References

1. Friedman, R. and Sacksteder, K.r. "Fire Behavior and Risk Analysis in Spacecraft" NASA TM100944, December 1988.

2. Smith, R. and Kashiwagi, T. *J. Applied Fire Sci.* 1-2: 103-113(1990-91).

3. Kashiwagi, T. *Fire Safety J.* 3: 185-200(1981).

4. Kashiwagi, T. *Combust. Flame* 34: 231-244(1979).

5. Muto, N., Hirano, T. and Akita, K. *Seventeenth Symposium (International) on Combustion*, The Combustion Institute, Pittsburgh, 1183-1190(1978).

6. Akita, K. in "Aspects of Degradation and Stabilization of Polymers" (H.H.G. Jellinek, Ed.), Elsevier Scientific, 1978, Chapt.10.

7. Bhattacharjee, S and Altenkirch, R.A. *Twenty-Third Symposium (International) on Combustion*, The Combustion Institute, Pittsburgh, 1627-1633(1990).

8. Frey, A.E. and Tien, J.S., *Combust. Flame*, 36: 263 289(1979).

9. Kashiwagi, T. *Combust. Sci. Tech.* 8: 225-236(1974).

10. Kindelan, M. and Williams, F. *Combust. Sci. Tech.* 16: 47-58(1977).

11. Krishnamurthy, L. *Acta Astronaut.* 3: 935 (1976).

12. Amos, B. and Fernandez-Pello, A.C. *Combust. Sci. Tech.* 62: 331-343(1988)

13. Di Blasi, C., Crescitelli, S. and Russo, G. *Fire Safety Science- Proceedings of the Second International Symposium*, p119-128(1989).

14. McGrattan, K.B., Kashiwagi, T., Baum, H.R., and Olson, S.L., *Combust. Flame*, 106: 377-391(1996).

15. Kashiwagi, T., and Nambu, H., *Combust. Flame*, 88: 345-368(1992).

16. Kashiwagi, T., McGrattan, K.B., Olson, S.L., Fujita, O., Kikuchi, M., and Ito, K. "Effects of Slow Wind on Localized Radiative Ignition and Transition to Flame Spread in Microgravity", to appear in *Twenty-Six Symposium (International) on Combustion*, The Combustion Institute.

17. Olson, S.L., *Combust. Sci. Technol.*, 76: 233-249(1991).

Table 1 Test Matrix

Test No.	Configuration	Flow cm/s	Ignitor	Notes
1	Flaming 2D	5	Wire	
2	Flaming 3D	5	Lamp	
3	Flaming 3D	5	Lamp	
4	Flaming 2D	2	Wire	
5	Flaming 2D	0	Wire	No transition
6	Flaming 3D	2	Lamp	
7	Flaming 3D	0.5	Lamp	
8	Flaming 3D	2	Lamp	Spread along open edges
9	Smolder 3D	5	Lamp	Smoldering
10	Smolder 3D	0.5	Lamp	Smoldering
11	Flaming 3D	3.5	Lamp	
12	Flaming 2D	2	Wire	
13	Flaming 3D	1	Lamp	
14	Smolder 3D	2	Lamp	Smoldering
15	Smolder 3D	6.5	Lamp	Smoldering
16	Flaming 3D	2	Lamp	
17	Flaming 3D	5	Lamp	Spread along open edges
18	Flaming 3D	0	Lamp	No transition
19	Flaming 3D	2	Lamp	Spread along open edges
20	Flaming 3D	1	Lamp	No 35 mm camera
21	Flaming 3D	0.5	Lamp	No 35 mm camera
22	Flaming 3D	6.5	Lamp	
23	Flaming 3D	5	Lamp	Spread along corner
24	Flaming 3D	3.5	Lamp	Spread along open edges
25	Flaming 3D	5	Lamp	Spread along corner

Page intentionally left blank

COMPARATIVE SOOT DIAGNOSTICS: 1 YEAR REPORT

David L. Urban

DeVon W. Griffin
Microgravity Science Division
NASA Lewis Research Center

Melissa Y. Gard
NASA Marshall Space Flight Center

Introduction

Even though combustion is commonly thought of as a process that consumes solid and liquid fuels via a gas phase flame, combustion of most materials produces a variety of condensed phase (solid and liquid) products. The structure and composition of these products are functions of the materials being burned and the details (environment, size, intensity) of the combustion process itself. These condensed products comprise "smoke" and can be divided into a few general groups: 1. droplets or particles of the original polymer or its monomer, 2. Incompletely oxidized pyrolysis (thermal decomposition) products of the fuel, 3. inorganic compounds (e.g. metal oxides and ash from fossil fuels) and 4. hydrocarbon soot (the major constituent of soot is carbon). Particulate from the first 2 groups can be either liquid or solid at room temperature, depending upon the composition.

The motivation for the CSD experiment lies in the broad practical importance of understanding combustion generated particulate. Depending upon the circumstances, particulate matter can affect the durability and performance of combustion equipment, can be a pollutant, can be used to detect fires and, in the form of soot, can be the dominant source of radiant energy from flames. Bright sooty fires are desirable for efficient energy extraction in furnaces and power equipment. In contrast, soot-enhanced radiation is undesirable in many propulsion systems (e.g. jet engines). The non-buoyant structure of most flames of practical interest (turbulent) makes understanding of soot processes in low gravity flames important to our ability to predict fire behavior on earth. These studies also have direct applications to fire safety in human-crew spacecraft, since smoke is the indicator used for automated detection in current spacecraft [3, 4].

In addition, recent tests conducted on MIR [1] showed that a candle in a truly quiescent spacecraft environment can burn for tens of minutes. Consequently, this test and many earlier tests have demonstrated that fires in spacecraft can be considered a credible risk [2,3,4]. In anticipation of this risk, NASA has included fire detectors on Skylab, smoke detectors on the Space Shuttle (STS), and smoke detectors in the design for the International Space Station (ISS). In the Comparative Soot Diagnostics (CSD) experiment, these smoke detectors were tested using, quasi-steady, low-gravity, particulate generating materials. Samples of the particulate were also obtained from these low-gravity sources. This experiment provides the first such measurements aimed toward understanding of soot processes here on earth and for the testing and design of advanced spacecraft smoke detection systems.

This paper describes the operation and preliminary results of the CSD, a project conceived and developed at NASA Lewis Research Center. The CSD flight experiment was conducted in the Middeck Glovebox Facility (MGBX) on USMP-3. The project is supported by NASA Headquarters Microgravity Science and Applications Division and Code Q.

In the earliest missions (Mercury, Gemini and Apollo), the crew quarters were so cramped that it was considered reasonable that the astronauts would rapidly detect any fire. The Skylab module, however, included approximately 20 UV-sensing fire detectors. The Space Shuttle has 9 particle-ionization smoke detectors in the mid-deck and flight deck and Spacelab has six additional particle-ionization smoke detectors. The designated detectors for the ISS are laser-diode, forward-scattering, smoke or particulate detectors. Current plans for the ISS call for two detectors in the open area of the module, and detectors in racks that have both cooling air flow and electrical power. Due to the complete absence of data concerning the nature of particulate and radiant emission from incipient and fully developed low-g fires, all three of these detector systems were designed based upon 1-g test data and experience. As planned mission durations and complexity increase and the volume of spacecraft increases, the need for and importance of effective, crew-independent, fire detection grows significantly. To provide this level of protection, more knowledge is needed concerning low-gravity fire phenomena and, in particular, how they might be detected and suppressed.

The objectives of CSD are to examine the particulate emission from a variety of pyrolyzing and combusting sources and to quantify the performance of several particulate-sensing diagnostic techniques. Prior to CSD, no combustion-generated particulate samples had been collected, near the flame zone, for well-developed microgravity flames. All of the extant data either came from drop tower tests and therefore only corresponded to the early stages of a fire or from the exit plenum in a Glovebox test in which case the sample was a time integral of the entire burn period. The fuel sources in the drop tower tests were restricted to laminar gas-jet diffusion flames and very rapidly overheated wire insulation [5, 6]. The gas-jet tests indicated, through thermophoretic sampling, [5] that soot primaries and aggregates (groups of primary particles) in low-gravity may be significantly larger than those in normal gravity (1-g). This raises new scientific questions about soot processes as well as practical issues for particulate size sensitivity and detection/alarm threshold levels used in on-orbit smoke detectors. Furthermore, it is has been suggested, but not shown, that the aggregates of individual particles may grow to very large sizes in a microgravity fire of longer duration than available on the ground. Preliminary tests in the 2.2 second drop tower suggest that particulate generated by overheated wire insulation may be larger in low-g than in 1-g [6]. Transmission Electron Microscope (TEM) grids downstream of the fire region in the Wire Insulation Flammability experiment [7] as well as visual observation of long string-like aggregates, further confirm this suggestion. The combined impact of these limited results and theoretical predictions is that, as opposed to extrapolation from 1-g data, direct knowledge of low-g combustion particulate is needed for more confident design of smoke detectors for spacecraft.

This paper presents the results of the microgravity portion of the CSD experiment. The results include the temporal response of the detectors and average sizes of the primary and aggregate particles captured on the thermophoretic probes. Complete assessment of the microgravity data and its combination with the normal-gravity data are still in process and will be reported later.

Background/Previous Work

Although optical detectors (responding to a fire's radiant emission rather than the presence of particulate) were used in the Skylab module and were considered for use on ISS, their implementation has been hampered by the facts that they require a line-of-sight to the area to be monitored and the lack of knowledge of radiant signatures for low-g fires. Consequently, smoke detection has been favored for newer spacecraft applications. As noted above low-g smoke detection has several challenges that make direct application of 1-g technology inappropriate. These issues include: dust discrimination, sampling in the absence of buoyant flows, lack of a knowledge base of low-g particulate size distributions, and lack of knowledge of appropriate alarm levels. Different portions of spacecraft raise unique design problems. Inside equipment racks, a more probable location for fires given the presence of power and heat-producing devices, free volume is limited and air flow paths may be tortuous, avionics air flow however is often present (serving both as an oxidant source and smoke gathering mechanism). Outside the racks, in the crew space, free volume is much less limited and potential ignition sources are less common but potential fuel is more abundant (e.g. paper, clothing, and trash materials). In addition, air residence times (and therefore detection times) in the inhabited space are long (tens of minutes in some portions of the shuttles). Future operation plans for the ISS suggest that modules will have electrical systems turned on but no human occupants present. In situations such as this, adequate fire/smoke detection systems for both the racks and the crew space are needed.

Well-established normal-gravity fires emit small particulate of the size range to which ionization detectors are more sensitive than optical detectors [8]. Less well-established or smoldering fires will produce larger particulate, owing to the large amount of condensed, unoxidized fuel pyrolysis products and the incomplete soot oxidation. For this type of fire, light scattering/obscuration detectors are more appropriate. However, for materials heated slowly as in the very early stages of some fires,

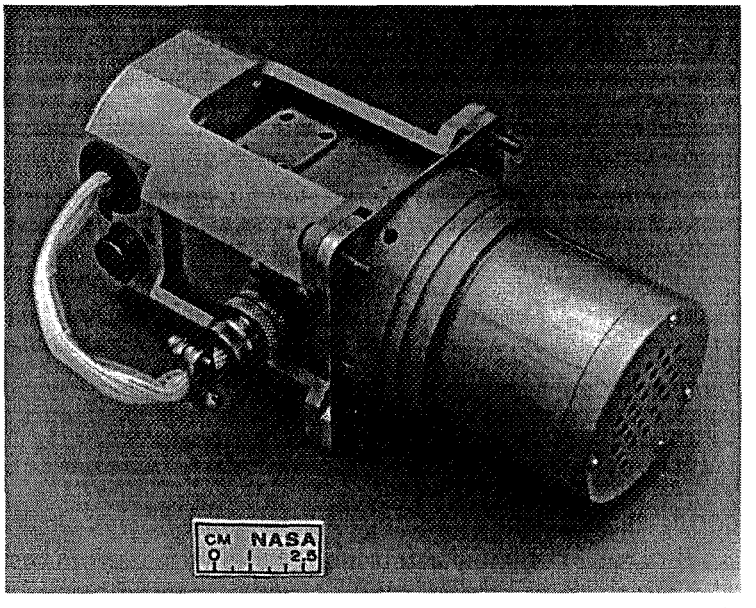

Figure 1. Photograph of the detector used in the Orbiter (STS) fleet and on SpaceLab. The air enters from the right and is exhausted out the port under the small plate on the top left.

the particulate can be very small, and therefore more easily sensed by ionization detectors [9]. This analysis was used by Brunswick Defense in their decision to pursue an ionization detector (Fig. 1) for the STS. The design consists of a dual-chamber ionization detector that is in the flow path created by a vane pump. This vane pump provides some active sampling capability and also the flow for an inertial separation system which is designed to make the detector insensitive to particulate larger than 1 to 2 microns, depending upon the particle mass.. These advantages are offset by a fairly large power consumption (9 Watts), fan noise, and limited life due to the moving parts. The detector produces a discrete alarm signal and two analog signals related to the detected smoke density. For the tests reported here, the analog voltage was measured. This voltage has a baseline of 11.4 for the detector used here and decreases in the presence of smoke. The alarm value is set at the factory using a fixed offset from the internal detector baseline and consequently the analog output voltage at alarm is different for each detector. The analog voltage at alarm for the detector used in this work was 10.6 volts.

The design developed for the ISS by Allied Signal (Fig 2) consists of a 2 pass laser diode obscuration system that also has a photo-diode positioned to sense forward scattered light (30 degrees) on the return path. The system is designed to alarm based on the magnitude of the scattered light signal. Dust discrimination is based on frequency analysis of the scattered light signal. The system is less sensitive to particles smaller than the wavelength of the laser (near IR) than it is to larger particles. The minimum reported sensitivity is 0.3 microns [10]. It draws relatively little power (1.5 W) and it has a long operational life. The current planned alarm value is 2 volts or 1% obscuration per foot.

The performance of these two detectors has been compared in normal gravity [10, 11]. Consistent with expectations, for cases where large particles were expected (punk smoke) the initial response of

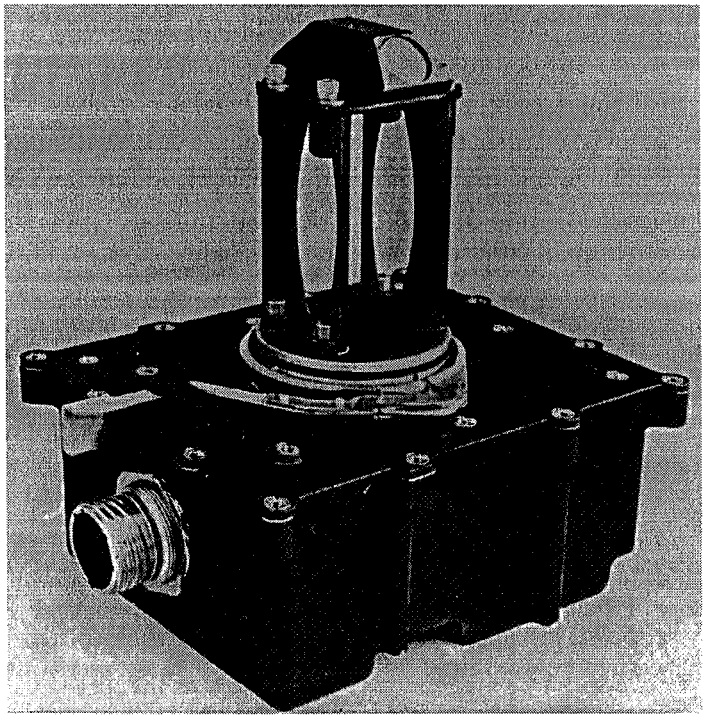

Figure 2. Photograph of an engineering model of the ISS smoke detector. The lasers and other electronics are in the black enclosure below and the laser beam passes through the space enclosed by the framework on the top, reflecting off of turning mirrors at the top.

both detectors was about the same but the ISS detector reached the alarm threshold more rapidly. For sources of smaller particle-size smoke (over heated wire) the STS detector was quicker both in initial response and in time to alarm. The implementation (alarm threshold selection) of both of these systems in microgravity is hampered by the lack of knowledge of their performance against low-gravity combustion generated particulate.

Objectives

The objectives of CSD are to examine the particulate formation from a variety of particulate-generating sources and to quantify the performance of several particulate-sensing diagnostic techniques. The sources include: a candle tested at three coflow air velocities and four overheated materials (paper, silicone rubber, and teflon and kapton coated wires) each tested at three heating rates. The paper, silicone rubber and wire insulations are materials found in spacecraft crew cabins and candles produce hydrocarbon soot typical of many practical 1-g flames.

Four diagnostic techniques were employed: thermophoretic sampling to provide samples of the particulate for size analysis, laser-light extinction measurements near the source to provide total smoke production data, and laser light scattering and ionization detector measurements to provide data concerning the performance of the detectors for these particulate sources.

Hardware Description

The CSD experimental hardware consists of two modules named the Near-Field Module and Far-

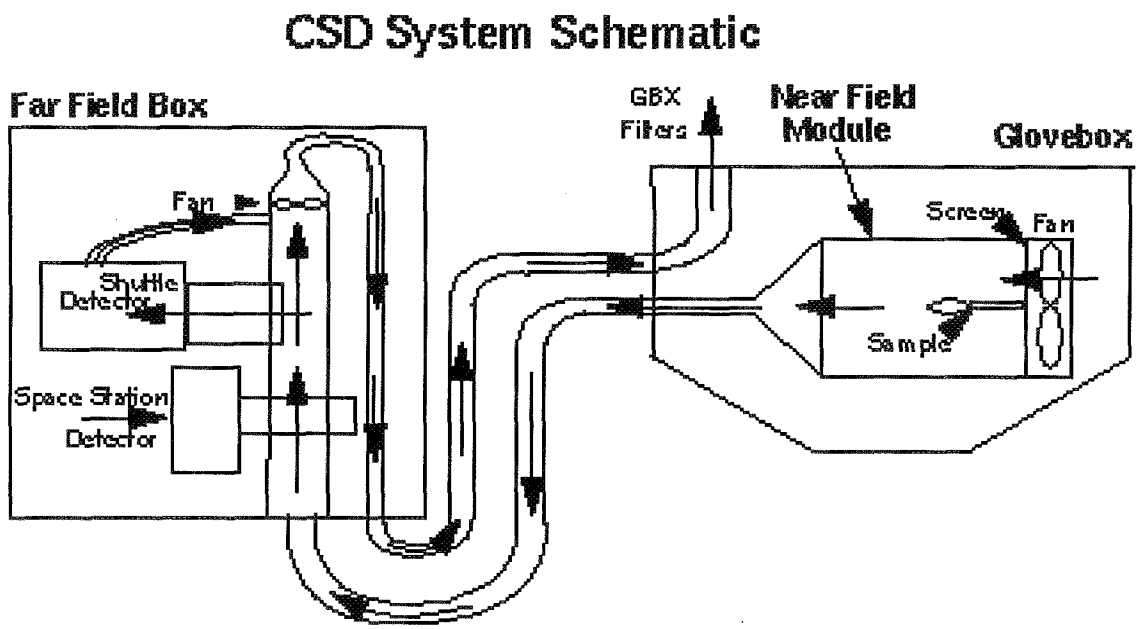

Figure 3. Schematic showing installation of the CSD Near Field Module inside the Glovebox and Far Field Module outside of the Glovebox.

Field Box as shown in the figure 3.The Near-Field Module is installed inside the Glovebox and contains the sample and the near field diagnostics. The Far-Field Box is external to the Glovebox and contains two spacecraft smoke detectors. Products from the near field tests are transported to the Far-Field Box and subsequently back into the Glovebox via teflon hoses which enter the Glovebox through ports in the airlock door. All of the combustion products are contained in either the Glovebox or the Far Field Box; by the time the experiment is completed, all of the products are returned to the Glovebox.

A photograph of the Near-Field Module is shown in figure 4. It consists of a small test chamber fitted with a sample carrier that holds the sample being tested. A small fan blows air from the glovebox into the right side of the chamber past the sample and out the left side where it enters the hose to the Far-Field Module. The sample is ignited or overheated by a resistively heated Kanthal wire. The

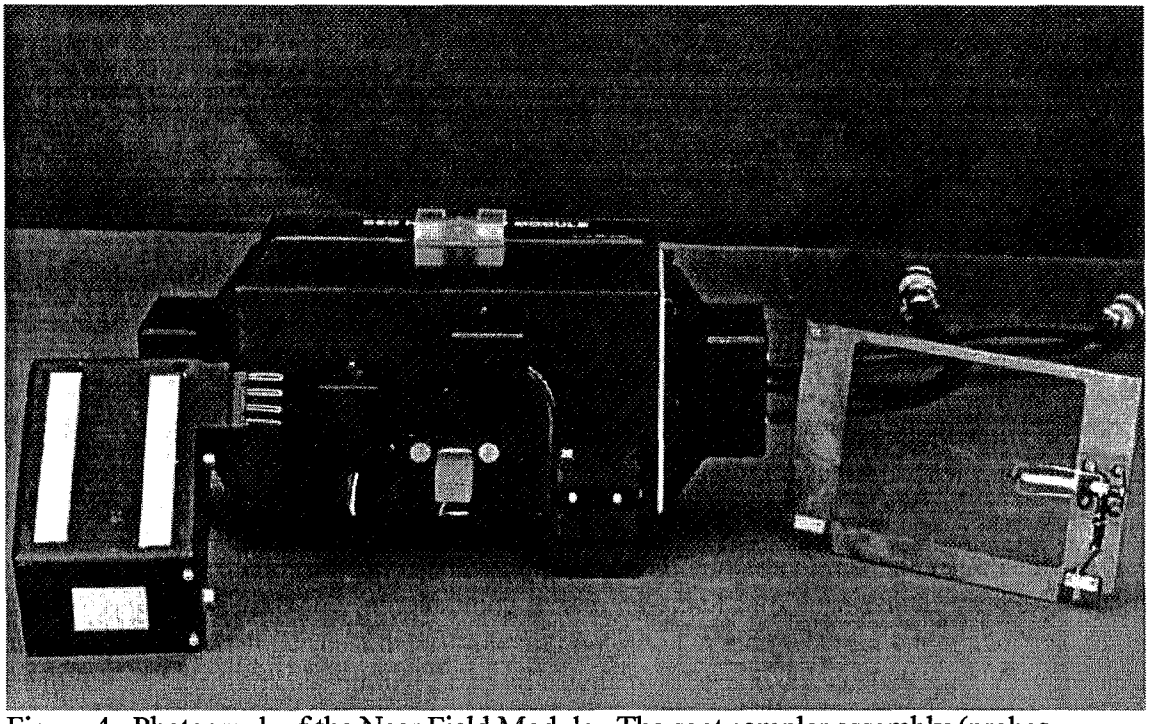

Figure 4. Photograph of the Near Field Module. The soot sampler assembly (probes extended) is on the left, and is installed in the hole in the center of the near field Module. A sample card with a candle installed is on the right.

smoke particulate is sampled by a rake of thermophoretic probes and smoke production is detected by a laser light extinction system.

The Far Field Box (Fig. 5) contains a duct and a fan to transport the smoke from the Near Field Module to two spacecraft smoke detectors, one matching the STS detector (Fig. 1) and the other (Fig. 2) is identical to the ISS detector with the exception that its signal is amplified by a factor of 6.6 over the ISS standard. This amplification was added because the engineering model of the ISS detector that was used for developing the test matrix displayed very low signal levels. Since the tests were intended more as a test of each technology rather than specific designs or alarm levels, the signal was amplified in the model used in the flight tests. Post flight calibration of both units by Allied Signal revealed that the engineering model was operating below specification by a factor of 5, voiding the

reason for the amplification. However, despite the amplification, sufficient dynamic range exists on the measurement that it is possible to predict when an unamplified unit would show significant detection. The analog signals from the various instruments are displayed by digital readouts on the Far Field Box where they are recorded by a video camera for later transcription.

Procedure and Operational Sequence

The crew installed the near field hardware in the Glovebox, attached the Far Field Box to the Glovebox, and positioned the video cameras. The operator then ran the self diagnostic procedures on the two smoke detectors and activated the video cameras, turned on the ignitor for a predefined period of time (15 to 60 seconds), and initiated the thermophoretic soot samplers to sample the smoke. The actual duration of each combustion event was typically 2 minutes. After the experiment, the operator stowed and reloaded the soot samplers, the test sample, and the filters at the end of the return line from the Far Field Box. At this point the operator either stowed the modules or initiated another run. The tests ran very efficiently and after the first two sessions, typically ran ahead of schedule. The sessions consisted of 2 to 7 runs each. The majority of the tests were run with predefined igniter power levels , however, to examine the response threshold, some of the tests in the final session were conducted repeatedly on the same samples at small increases of power level for each retest.

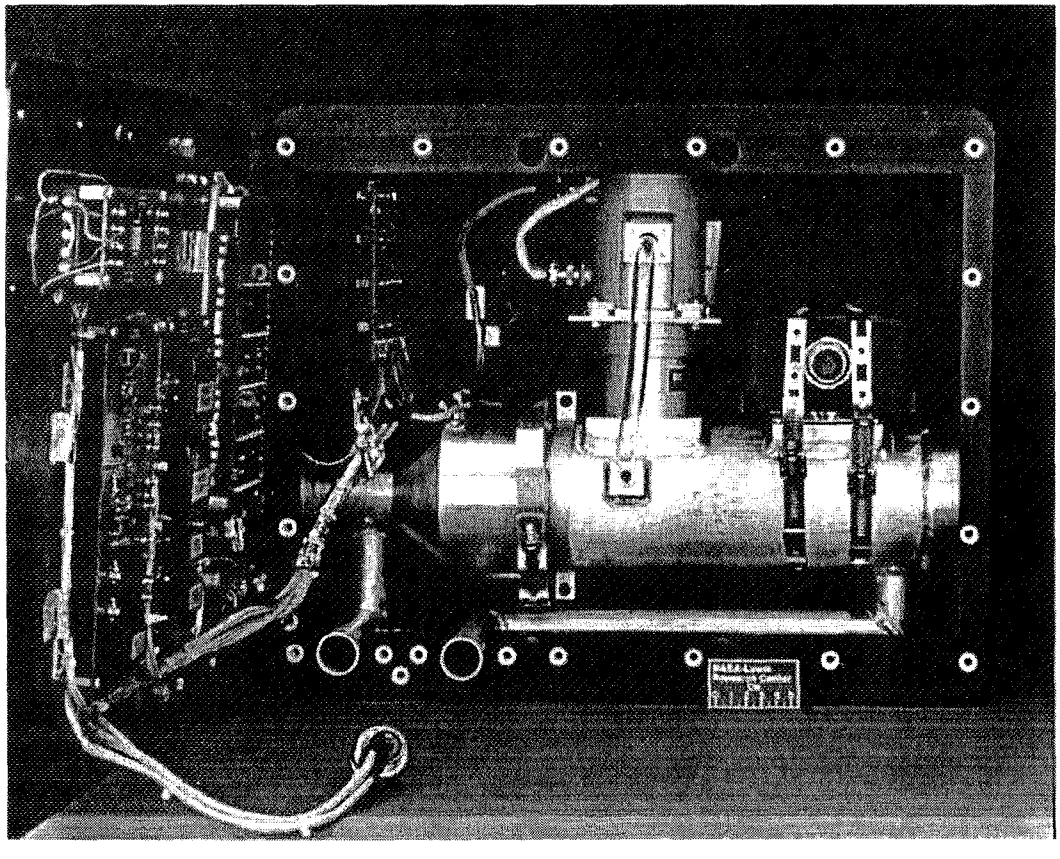

Figure 5: Photograph of the inside of the Far Field Box. The STS detector is the aluminum module in the center of the duct and the ISS detector is the black module on the right.

Data Reduction

After flight, the particulate collected on the thermophoretic probes were analyzed using a Transmission Electron microscope (TEM) to determine primary and aggregate particle dimensions. The remains of the samples were weighed to determine their mass loss. The digital data was transcribed from the video record and analyzed to determine the response of the detectors. Once the flight mass loss rates were determined, 1-g operation conditions to produce the same loss were determined. These conditions are being used to produce a 1-g comparison data set.

Results

In all, 25 tests were performed and the data from the runs are summarized in table 1, which lists the mass loss rate of the sample, the time it took for the signal to reach a value of 20% of the operating range of the detector and the time and value of the peak signal for both detectors. Since these tests were designed to function as a test of the detection technologies rather than the detectors themselves

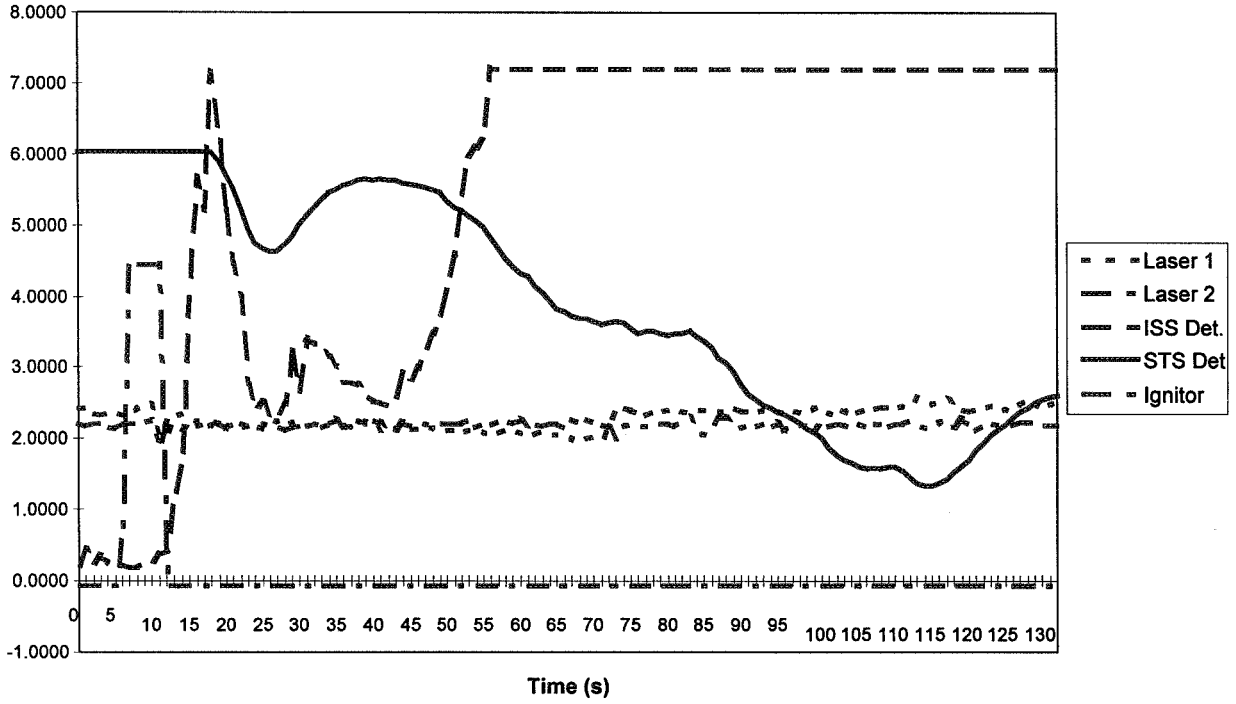

Figure 6: Traces of smoke detector signals as a function of time for a candle test (#16). Initial peak on both detectors is wax vapor released by the ignition process. The units on the vertical axis are arbitrary, the smoke detector data have been scaled so their dynamic ranges have similar vertical extent.

(or their alarm setpoints), 20% of the dynamic range was selected to tabulate as a consistent detection point for both detection technologies. The selection of the actual alarm level for each detector is more

Table 1 Detector Signals from CSD Flight tests (ISS values are scaled to flight detector sensitivity)

	ISS Detector				STS Detector				
Test Point	Time to 20% (s)	Time to Maximum (s)	Voltage at maximum	% FS at Maximum	Time to 20% (s)	Time to Maximum (s)	Voltage at Maximum	% FS at Maximum	mass loss rate (micro-gm/s)
10 (Paper)	31	33	7.22	29.6	—	—	—	—	43.4
15 (Paper)	20	21	7.21	29.5	54	61	9.2	91.7	consumed
20 (Paper)	—	24	1.56	6.1	—	18	11.27	5.8	consumed
25e (Paper)	—	73	0.75	0.2	—	89	11.34	4.1	multiple tests
5g (Paper)	—	71	0.74	2.1	—	70	11.37	1.3	multiple tests
1 (Candle)	61	62	7.2	29.6	—	82	9.65	73.4	consumed
6 (Candle)	—	70	2.3	9.2	—	67	10.55	36.0	consumed
11 (Candle)	69	69	6.88	28.3	35	75	9.9	9.9	consumed
16 (Candle)	45	49	7.21	29.2	47	108	9.53	9.5	consumed
2 (Silicone Rubber)	20	20	7.22	30.1	—	82	11.14	11.6	107
7 (Silicone Rubber)	18	19	7.22	30.1	—	44	11.24	7.4	58.7
12 (Silicone Rubber)	21	23	7.23	30.1	—	31	11.39	1.2	130
17 (Silicone Rubber)	16	17	7.22	30.1	—	39	11.21	8.7	128
22(Silicone Rubber)	32	34	7.24	30.2	—	52	11.28	6.9	15.2
3 (Teflon)	55	62	7.23	34.5	72	76	10.88	22.6	86.2
8 (Teflon)	—	61	4.18	16.9	—	67	11.27	6.6	141
13 (Teflon)	27	27	7.21	29.6	—	35	11.17	10.0	155
18 (Teflon)	31	32	7.22	29.6	39	42	10.92	20.3	143
21 (Teflon)	—	78	0.29	0.8	—	81	11.29	6.5	47.9
23a (Teflon)	—	46	0.51	1.7	—	59	11.36	2.5	multiple tests
4 (Kapton)	14	15	7.21	29.6	25	37	10.1	54.4	37.5
9 (Kapton)	14	23	7.23	29.7	28	37	10.64	32.5	56.5
14 (Kapton)	13	14	7.21	29.6	24	33	10.19	50.8	106
19 (Kapton)	10	10	7.21	29.6	25	30	10.36	43.6	99.4
24 (Kapton)	—	28	0.88	3.3	—	74	11.09	14.3	4.29

complex than mere detection as false alarm rejection and other issues must be considered. The bulk of the tests were overheated material tests in which the heating level was established to produce a target weight loss rate without causing the sample to develop a sustaining combustion reaction. The intent of these tests was to produce smoke typical of an incipient fire where much of the material is being heated but has not yet ignited. The candle tests and one of the paper tests were combustion tests where the samples were ignited so the combustion products could be observed. Figures 6-9 contain the signal data from two typical candle, one Kapton and one silicone rubber tests respectively. The response of the smoke detectors, the ignitor voltage and the signal for the lasers in the near field module are plotted with respect to time. As plotted, the data for the ISS detector overstates the sensitivity of the flight unit since the unit used here is 6.6 times more sensitive than the flight model. These tests were neither designed nor expected to reach specific alarm levels. Instead the tests were planned to provide a measure of the relative sensitivity of the two detector types to low gravity smoke particulate by providing sufficient particulate to achieve adequate signal levels on the detectors. To explore the effect of heating rate on particle size, the different tests with each material were conducted at different ignitor power levels. The results of the tests are discussed below by sample type.

Candle Tests

In all tests the detector's signals showed an immediate peak that is attributed to the wax vapor released by the ignition process. This peak was detected more quickly by the ISS detector. Once the candle was ignited, the STS detector showed strong signals for all tests while the ISS detector showed strong signals for tests 1 and 16 (e.g. Fig. 6) and very weak signals (if unamplified) for tests 6 and 11 (e.g. Fig. 7). The cause of this is still under investigation.

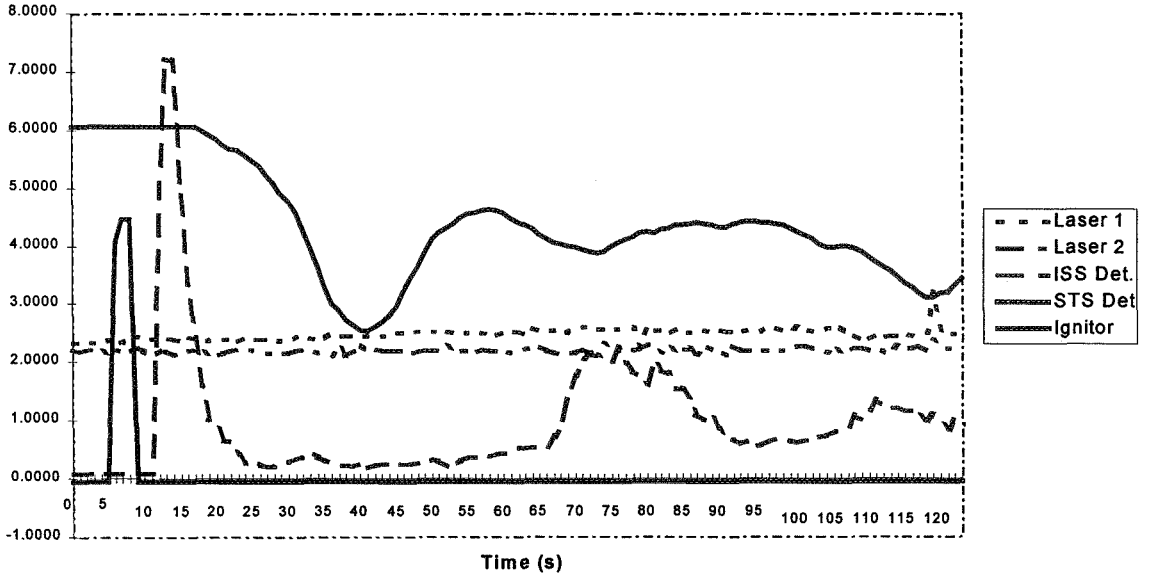

Figure 7: Traces of smoke detector signals as a function of time for a candle test (#6). Initial peak on both detectors is wax vapor released by the ignition process. The units on the vertical axis are arbitrary, the smoke detector data have been scaled so their dynamic ranges have similar vertical extent.

Paper Tests:

Runs 5g, 10 and 25e were pyrolysis runs i.e. they did not produce a flame but instead allowed the paper to degrade into pre-combustion or pyrolysis products. Of these, run 10 showed appreciable mass loss and was readily detected by the ISS detector while the STS detector produced marginal signal. In contrast, 1-g comparison tests show strong signals on both detectors. Runs 5g and 25e were the last runs in a series of tests aimed at finding the threshold detection level for the sample. These tests showed slightly higher signals for the ISS detector, however, if scaled to real detector performance (i.e. unamplified) neither detector showed distinct signal. Test 20 was a flaming test of a small paper sample and showed a marginal advantage for the STS detector. Test 15 was intended to be a pyrolysis test but self-heating caused the sample to develop a self-sustaining smolder reaction late in the test. The ISS detector detected both the pyrolysis and flaming intervals while the STS detector only detected the smoldering interval.

Teflon Wire Tests:

Both detectors showed strong signals for tests 3, 13, and 18 . On test 8, however, the STS detector showed minimal signal and the ISS had a weak signal (unamplified). For Test 21 the STS detector showed a weak signal compared to no signal (even amplified) for the ISS detector. Test 23b showed no signal for either detector.

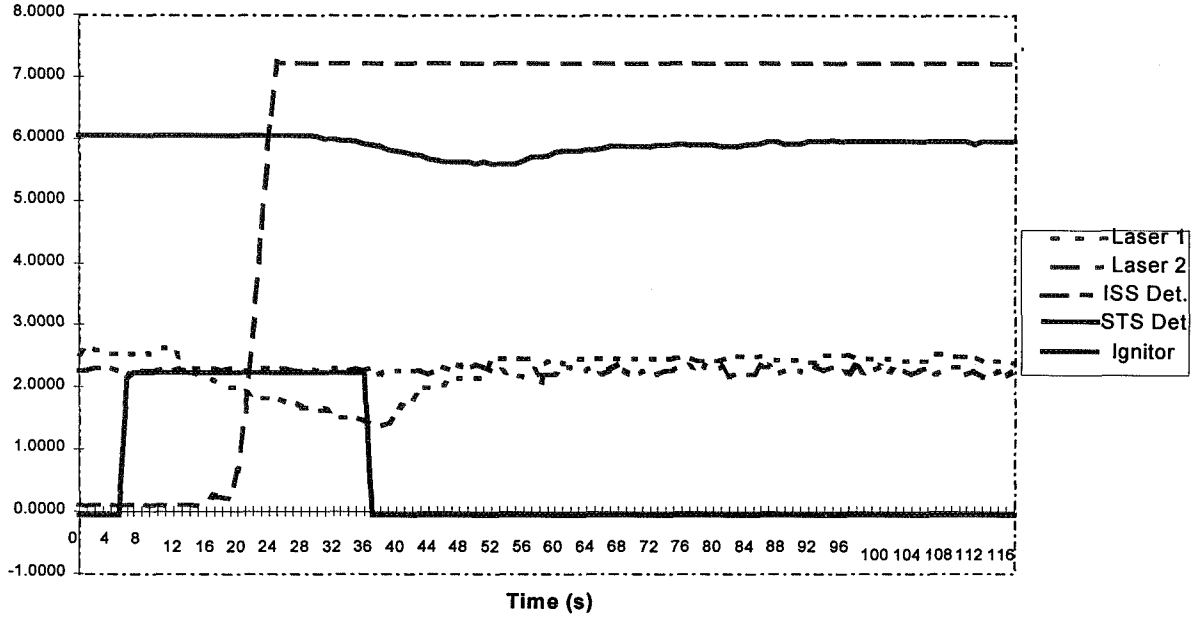

Figure 8: Traces of smoke detector signals as a function of time for a silicone rubber test (#7). The units on the vertical axis are arbitrary, the smoke detector data have been scaled so their dynamic ranges have similar vertical extent.

Silicone Rubber Tests

For all of the tests with silicone rubber, the ISS detector showed very strong signals while the STS detector showed at most a weak signal (Fig. 8). This is contrary to 1-g comparison test results where this material also shows a strong signal on the STS detector.

Kapton Wire Tests

Both detectors showed strong signals for 4, 9, 14 and 19 with both producing low signals (STS slightly higher) for test 24 which was a low mass loss test

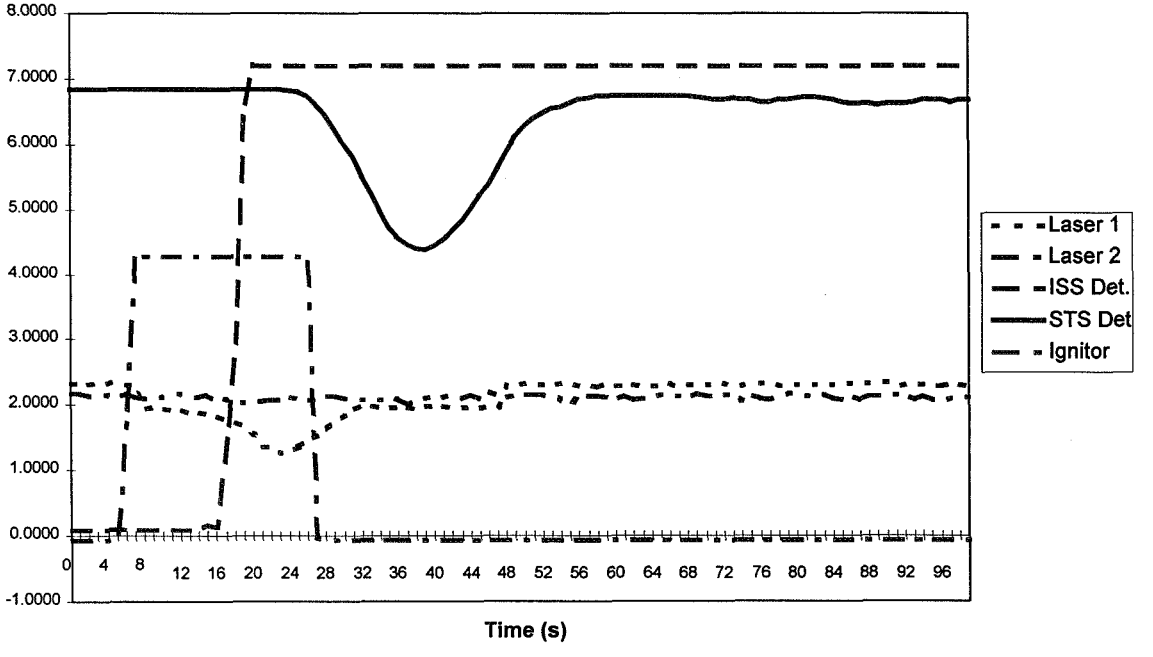

Figure 9: Traces of smoke detector signals as a function of time for a Kapton test (#14). The units on the vertical axis are arbitrary, the smoke detector data have been scaled so their dynamic ranges have similar vertical extent.

TEM Results

Thermophoretic sampling has been used previously in the drop tower for gas jet diffusion flames and for overheated wires [5, 6]. The technique takes advantage of the tendency of small particulate to move toward and attach to cool objects. For the overheated but not burning materials, a weak thermal gradient was expected and consequently the probe was left in place for 45 seconds while in the case of the much hotter candle flame the probe was left in for less than a second. When the probes were returned to earth, the grids were removed and analyzed in a TEM to determine the primary particle and aggregate size distribution. Timing of the deployment of the soot sampler required rapid subjective decisions by the crew member. Based upon our video record, they did an excellent job. We encountered less stable flow of the smoke plume than we anticipated and had a high rate of loss of

TEM grids due to failure of the adhesive. Consequently particulate samples were not obtained on all tests.

Figures 10 a-c contain TEM images of typical particulate from Teflon, Kapton and Candle tests. The three images are at the same magnification and show the significant variation in the particulate morphology for the three materials.

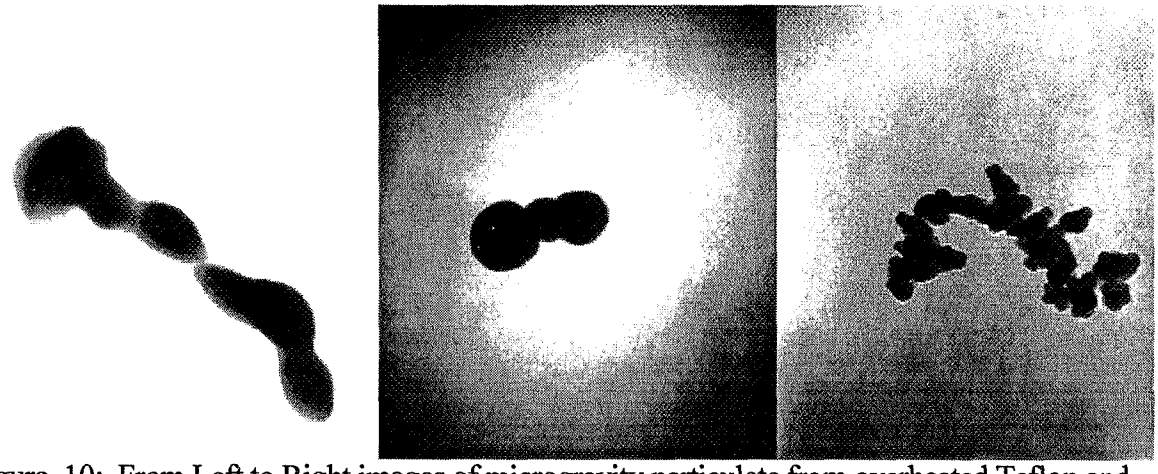

Figure 10: From Left to Right images of microgravity particulate from overheated Teflon and Kapton and Candle soot.

Table 2 summarizes the results for the tests for which good sampling was achieved. Significantly, despite strong smoke levels visible in the video record, no particulate material was found on the TEM grids for overheated paper and silicone rubber tests. The suspected cause of this is that the particulate for these materials is actually liquid droplets which later evaporate or spread out on the grids' surface, rendering them undetectable by the TEM. The primary particle dimensions range from 30 to 40 nm for soot to 60-100 nm for Kapton and 130 to 200 nm for Teflon. The aggregate soot dimensions grow with distance from the candle from 400 nm at 15 mm from the wick to 1200 nm at 35 mm from the wick. The Kapton aggregates range from 220 - 250 nm and the Teflon aggregates range from 600- 1100 nm. The dimensions reported in Table 2 are geometric averages (averages based upon a log-normal size distribution). The probe centerlines were 10 mm apart along the flow axis and are numbered sequentially beginning with the probe nearest to the sample. Each probe assembly inserted the 4 probes simultaneously. The size of the candle aggregates grew with distance from the candle, reaching 1.2 microns. The rejection criteria for the inertial separation in the STS detector is based upon a 1 to 2 micron particle mass. Since the soot from these tests was still very successfully detected, apparently soot particles of 1.2 microns have not reached the rejection mass level. The Teflon and Kapton samples produced large primaries with the largest occurring in Teflon test 13 (195 nm) the resultant aggregates were 1.1 microns.

Table 2 TEM results

Test Point	Probe Number	Primary Diameter (nm)	Aggregate diameter (nm)
1 (Candle)	1	44	417
	2	33	742
	3	39	1185
16(Candle)	2	38	710
	4	32	1252
8(Teflon)	1	136	608
	4	134	------
13(Teflon)	1	195	1084
	2	154	669
9 (Kapton)	1	79	234
	4	95	253
19(Kapton)	3	74	119
	4	85	184
20(Flaming Paper)	1	29	406
	2	26	425
	3	24	301

Discussion

Data analysis and interpretation are well underway but have not yet been completed. The companion 1-g test program is also underway but incomplete. However, the smoke produced in the low-g silicone rubber and paper tests was thick and clearly visible while in comparable1-g tests, it was only marginally visible for the same mass loss rate. This can be explained by the absence of buoyant flows which (in 1-g) dramatically accelerate the gas velocities in the vicinity of the source, reducing the

residence time of the particulate in regions of high concentration. Since particulate sizes for the smoke from these two materials could not be obtained with TEM analysis, the reasons for the lower signal levels from the STS detector can only be inferred. It is likely that these droplets had more opportunities to coalesce into droplets whose size exceeded the maximum size for which the STS detector is sensitive (1-2 microns). For very low mass loss tests for wire insulation materials, the STS detector showed more signal than the ISS model. Once the 1-g comparison tests are complete, further analysis of the results will be possible.

Conclusions

The CSD experiment successfully produced controlled quantities of smoke particulate from a variety of sources. The response of the STS and ISS detectors to these smoke sources was measured and samples of the smoke particulate were successfully obtained from many of the tests. The assembled data provide the first examination of the response of spacecraft smoke detectors to microgravity smoke particulate.

The most significant conclusion to be drawn, so far, from this work is that sensitivity to the smoke from an individual material in 1-g does not indicate strong sensitivity to the smoke from the same material in low-g. Despite the presence of a forced flow (provided by a fan) in the low-g tests the absence of buoyant flows apparently changed the particle size distribution. We have not yet determined if the change is sufficiently systematic that correlations can be obtained. Both detectors showed responsiveness for the majority of materials; the STS detector showed limited sensitivity to pyrolyzing materials that produce liquid particulate. The particle dimensions covered a wide range from 30 to 200 nm for primary particles and from 220 to 1200 nm for aggregates.

Acknowledgments

The assistance of D. Michael Hoy of NASA JSC in providing samples and in obtaining an Orbiter smoke detector is much appreciated. This program received financial support from NASA Codes UG and Q. The in-kind assistance provided by Boeing, Allied Signal and Brunswick Defense was necessary to allow testing of flight smoke detectors. Several students (D. Crouch, L.J. Dallaire and C. Lundquist)were instrumental in performing the tests needed to develop the flight apparatus and in post flight data analysis. The careful execution of these experiments, while on-orbit, by A. Allen and F. Chang-Diaz was critical to CSD's success and is much appreciated. Finally, J. Romanin and P. Howard were responsible for the bulk of the design, and the assistance of the MGBX team and the POCC Cadre were all critical to the success of this experiment.

References

1) Dietrich, D., personal communication, 1997.

2) Friedman, R., 1992. Fire Safety Practices and Needs in Human-Crew Spacecraft. Journal of Applied Fire Science, 2:243-259.

3) Friedman, R., K. Sacksteder and D. Urban. 1991. Risks, Designs and Research for Fire Safety in Spacecraft. NASA TM 105317.

4) Friedman, R., and D. Dietrich, 1991. Fire Suppression in Human-Crew Spacecraft. NASA TM 104334

5) Ku, J.C., D.W. Griffin, Greenberg, P. S., and J. Roma. 1995: Buoyancy-Induced Differences in Soot Morphology. Combustion and Flame, 102:216-218.

6) Paul, M., F. Issacci, G. E. Apostalakis and I. Catton. 1993. The Morphological Description of Particles Generated from Overheated Wire Insulations in Microgravity and Terrestrial Environments. Heat Transfer in Microgravity System-1993, S. S. Sadhal and A. Hashemi eds. ASME-HTD Vol. 235:59-66.

7) Greenberg, P. S., K. R. Sacksteder and T. Kashiwagi. 1995. Wire Insulation Flammability Experiment: USML-1 1 Year Post Mission Summary. Joint Launch + one Year science Review of USML-1 and USMP-1 with the Microgravity Measurement Group. NASA CP 3272 V II.

8) Bukowski, R.W. and G.W. Mulholland. 1978. Smoke Detector Design and Smoke Properties. NBS Technical Note 973.

9) Chuan, R. L. and H. D. Chen. 1986. Aerosol Characterization in an Incipient Fire. Second International Aerosol Conference, Berlin, Sept.

10) Steisslinger, H. R., D. M. Hoy, J. A. McLin and E. C. Thomas. 1993. Comparison Testing of the Space Shuttle Orbiter and Space Station Freedom Smoke Detectors. SAE Paper 932291,Warrendale, PA, 23rd Intl. Conference on Environmental Systems, Colorado Springs, CO, July.

11) McLin, J. 1993. Smoke Comparison Test Report Doc. # 93-05902, Allied Signal Aerospace.

PRINCIPAL INVESTIGATOR MICROGRAVITY SERVICES—USMP-3

Melissa J. B. Rogers, Kenneth Hrovat, Milton E. Moskowitz, Timothy Reckart
Tal-Cut Company
North Olmsted, Ohio

Kevin M. McPherson and Richard DeLombard
NASA Lewis Research Center
Cleveland, Ohio

Abstract

Two accelerometers provided acceleration data during the STS-75 mission in support of the third United States Microgravity Payload (USMP-3) experiments. The Orbital Acceleration Research Experiment (OARE) and the Space Acceleration Measurement System (SAMS) provided a measure of the microgravity environment of the Space Shuttle Columbia. The OARE provided investigators with quasi-steady acceleration measurements after about a six hour time lag dictated by downlink constraints. SAMS data were downlinked in near-real-time and recorded on-board for post-mission analysis. These two accelerometer systems are briefly described.

Using a combination of data analysis techniques, the microgravity environment related to several different Orbiter, crew, and experiment operations is presented and interpreted. The microgravity environment represented by SAMS and OARE data is comparable to the environments measured by these instruments on earlier microgravity science missions. Thruster activity on this mission seen in the SAMS data appear to be more frequent than on other microgravity missions with the combined firings of the F5L and F5R jets producing significant acceleration transients. Of the events studied, the crew activities performed in the middeck and flight deck, SPREE table rotations, a waste collection system compaction, and a fuel cell purge had negligible effects on the microgravity environment of the USMP-3 carriers. The Ku band antenna repositioning activity resulted in a brief interruption of the ubiquitous 17 Hz signal in the SAMS data. In addition, the auxiliary power unit operations during the Flight Control System checkout appeared to have a significant impact on the microgravity environment.

Acknowledgments

Alan Bachik, Code DF at NASA Johnson Space Center (JSC), provided information about the Flight Control System Checkout procedure. Quinn Carelock, Code DF82 at JSC, provided information about the waste collection system and timing for compaction operations during STS-75. Kenneth J. Welzyn and Edward Litkenhaus of NASA Marshall Space Flight Center, Jeffrey Zelicksen of CAS Inc., and Nestor Voronka of the University of Michigan provided information and data pertinent to operations of the Tethered Satellite System. Michael Moses, Code DFG with Rockwell

Space Operations Co. at JSC, provided thruster firing information. Ku band antenna information was provided by Richard La Brode, Code DF, Rockwell International at JSC. Brenda Eliason, with Rockwell International at JSC, provided the STS-75 Green Book which summarized the as-run mission activities.

1. Introduction

Microgravity science experiments are conducted on the NASA Space Shuttle Orbiters to take advantage of the reduced gravity environment available in low earth orbit. Accelerometer systems are flown in conjunction with these experiments to record the microgravity environment to which they are subjected. The third United States Microgravity Payload (USMP-3) and the Tethered Satellite System (TSS-1R) flew on the Orbiter Columbia on mission STS-75 from 22 February to 9 March 1996. Two accelerometer systems managed by the NASA Lewis Research Center (LeRC) flew to support the USMP-3 experiments: the Orbital Acceleration Research Experiment (OARE) and the Space Acceleration Measurement System (SAMS).

The Principal Investigator Microgravity Services (PIMS) project at NASA LeRC supports principal investigators of microgravity experiments as they evaluate the effects of varying acceleration levels on their experiments. During the STS-75 mission, PIMS provided real-time displays of the SAMS data to the investigator teams, enabling them to make appropriate parameter adjustment decisions pertaining to their experiments. PIMS also provided OARE data plots to users as the data became available. The data were delayed due to downlink constraints. PIMS performed specific processing of archived SAMS and OARE data for USMP-3 and TSS-1R investigators so that they could perform in-depth analyses of their experiment results during the mission.

This report summarizes the microgravity environment of Columbia during the STS-75 mission. The following sections gives some details about the accelerometer systems, including the real-time data acquisition, processing, and display operations PIMS performed during the mission. Finally, the effects of specific mission and payload activities on the microgravity environment are detailed.

2. Orbital Acceleration Research Experiment

The OARE measures quasi-steady accelerations from below 1×10^{-8}g up to 2.5×10^{-3}g, where $1g = 9.81 m/s^2$. The OARE consists of an electrostatically suspended proof mass sensor, an in-flight calibration subsystem, and a microprocessor which is used for in-flight experiment control, processing, and storage of flight data [1-4]. The acceleration sensor's output signal is filtered using a Bessel filter with a cut off frequency of 1 Hz. The output signal is digitized at 10 samples per second and is then processed and digitally filtered with an adaptive trimmean filter prior to electronic storage on-board. During STS-75, a system write fault resulted in the corruption of the data stored electronically within OARE. The unprocessed data are recorded on the Orbiter payload tape recorder. At regular intervals during the STS-75 mission, the unprocessed OARE data were downlinked from the Orbiter to the MSFC Payload Operations Control Center (POCC). The POCC Data Reduction team transferred files of downlinked data to PIMS computers in the POCC. The

PIMS computers processed the OARE data and displayed data for the PIs using the World Wide Web and the POCC video matrix.

The OARE was mounted to the floor of Columbia's cargo bay on a keel bridge, close to the Orbiter center of gravity. The approximate location and orientation of the sensors are given in Table 1 and Fig. 1. In this report, the OARE data are presented in terms of the Orbiter body coordinate system. Fig. 2 indicates the difference between the Orbiter body and structural coordinate systems. The subscript b represents the Orbiter body coordinate system. The subscript o is used to indicate the Orbiter structural coordinate system. The OARE data sign convention used here is such that when there is a forward thrust of the Orbiter, it is reported as a negative X_b acceleration. We refer to this convention as being consistent with a frame of reference fixed to the Orbiter. OARE data are available from MET 000/00:10 to 015/21:03.

3. Space Acceleration Measurement System

The SAMS is used to measure the low-gravity environment of Orbiters in support of microgravity science payloads [5-10]. STS-75 was the fourteenth SAMS flight on an Orbiter. Two SAMS units flew on STS-75. One SAMS unit was located on each MPESS carrier in support of USMP-3 experiments. The unit designated SAMS-1 (also called Unit F) was located on the forward carrier and used two triaxial sensor heads to support the AADSF and MEPHISTO experiments. The signals from these two triaxial sensor heads were filtered by low pass filters with cutoff frequencies of 10 Hz (TSH 1A) and 25 Hz (TSH 1B). These signals were then sampled at 50 and 125 samples per second, respectively. TSH 1A data were downlinked in near real-time during the mission and data from TSH 1B were recorded onboard using SAMS optical disks.

The unit designated SAMS-2 (also called Unit G) was located on the aft carrier and used three triaxial sensor heads to support the IDGE and Zeno experiments. The signals from these three triaxial sensor heads were filtered by low pass filters with cutoff frequencies of 5 Hz (TSH 2A), 10 Hz (TSH 2B), and 25 Hz (TSH 2C). These signals were then sampled at 50, 50, and 125 samples per second, respectively. Data from TSH 2A and TSH 2C were alternately downlinked or recorded on optical disks onboard. Data from TSH 2B were recorded on optical disks. In general, TSH 2C data were downlinked early in the mission, while TSH 2A data were downlinked later in the mission. In this report, the SAMS data are presented in terms of the Orbiter structural coordinate system. The SAMS data sign convention used here is such that when there is a forward thrust of the Orbiter it is recorded as a negative X_o acceleration. We refer to this convention as an inertial frame of reference fixed to a point in space. The orientations and locations of the SAMS heads, with respect to the Orbiter structural coordinate system, are given in Table 2 and Fig. 3. For STS-75, a total of approximately 3.5 gigabytes of SAMS data are available between MET 000/02:57 and 014/11:13.

The SAMS data that were downlinked were routed to PIMS computers in the POCC. The PIMS computers processed the SAMS data from both units and displayed data for investigators using the World Wide Web and the POCC video matrix. Additionally, Teledyne Brown Engineering personnel modified SAMS data display software so that the crew could capture the SAMS data stream and

display it on a laptop computer. The display was a scrolling plot of ten seconds of the three axes of one unit of SAMS data, with a delay of about 20 seconds. This was the first time an Orbiter crew was able to use SAMS data to get real-time feedback on the effects of their activities and Orbiter operations on the microgravity environment.

4. SAMS and OARE Data Analysis

The data recorded by SAMS on STS-75 were processed to correct for pre-mission bias calibration offsets and to compensate for temperature and gain related errors of bias, scale factor, and axis misalignment. The resulting units of acceleration are g's where 1 g = 9.8 m/s^2. The data were orthogonally transformed from the five SAMS TSH coordinate systems to the Orbiter structural coordinate system. The OARE data recorded during STS-75 and presented here have been compensated for temperature, bias, and scale factors [11] and orthogonally transformed to the Orbiter body coordinate system.

After this initial data correction phase, data analyses were applied to the SAMS and OARE data to characterize the acceleration environment of the mission. Because of the inherent differences between OARE (frequency range 10^{-5} Hz to 1 Hz, sampling rate 10 samples per second) and SAMS (frequency range 0.01 Hz to 25 Hz, sampling rate 50 to 125 samples per second on STS-75) data, some data analysis techniques are more applicable to data from one system than the other. The particular processing technique used also depends on the type of information desired [15].

5. Columbia Microgravity Environment—STS-75

This section discusses the microgravity environment of the Orbiter Columbia during the STS-75 mission as recorded during a specific crew activity that was performed for environment characterization, during several thruster firing events, during SPREE rotary table operations, during a Ku band antenna repositioning, during the Flight Control System checkout, during the Tethered Satellite System deploy and tether separation, during a waste collection system compaction operation, during a fuel cell purge, and while the Orbiter was positioned in different attitudes.

5.1. Crew Quiet Time Test

Prior to the mission, the crew members were interested in performing specific activities to demonstrate how they can operate quietly to minimize crew induced disturbances to the microgravity environment. Conversations with STS-75 crew members and mission planners resulted in a suite of activities that were performed during a block of time between TSS-1R operations and the USMP-3 microgravity science operations. After the mission, correlation between the SAMS data and the activities performed by the crew were determined using video tape and crew notations of the activities.

The activities were conducted from MET 006/15:00 to 006/15:37. and included normal crew ac-

tions involving the middeck lockers, galley equipment, crew equipment (bunks, footloops, and cameras), the waste collection system, crew motions, cabin air fans, and thruster operations. The crew members were basically quiet during this demonstration time. Analyses of SAMS data collected during this period indicate no apparent correlation between the crew activities and the acceleration levels. Note, however, that with the SAMS sensors located on the MPESS carriers, these data indicate how the activities of the crew in the middeck and flight deck of the Orbiter affected the microgravity environment at the location of the sensitive USMP-3 experiments. The data do not represent what the environment was at the site of the activity and we can draw no conclusions about the effects of these same activities on the acceleration environment of the middeck, flight deck, or of a Spacelab module that may house sensitive experiments while such activities are occurring in the Orbiter.

5.2. Attitude Adjustment and Maintenance

Orbiter attitude adjustment and maintenance is performed using the Reaction Control System (RCS) and the Orbital Maneuvering System (OMS). STS-75 provided several opportunities to investigate the effects of these systems on the microgravity environment.

Examination of the ten second interval average plots of SAMS data reveals a somewhat regular train of short-duration, high-magnitude disturbances most notable in the Orbiter Z_o-axis data and, to a lesser extent, in the X_o-axis data. Correlation of SAMS data from MET 010/04 with Orbiter downlink data confirmed that these disturbances were induced when two Vernier Reaction Control System (VRCS) thrusters (F5L and F5R) were fired simultaneously as required for attitude maintenance with a 1° deadband. See reference [12] for identification of individual RCS jets. Fig. 4 shows SAMS Unit F TSH 1B data with a ten second interval average calculation applied. In Fig. 4 the simultaneous firing of the two thrusters is indicated by the + markers. Note from the o markers that firing either of these thrusters individually leaves little or no evidence in the interval average data. However, when fired in tandem there is an appreciable momentary shift in the DC acceleration levels as evidenced on the X_o- and Z_o-axes.

The USMP-3 MEPHISTO experiment focused on mass transport in directionally solidifying Sn-Bi alloys. Part of their experiment was a benchmark study to correlate well-defined acceleration conditions with well-controlled solidification conditions. The acceleration sources used for this study were nine Primary RCS (PRCS) firings, one OMS firing, and one Orbiter roll maneuver. SAMS Unit F TSH 1B data from three of the PRCS firings are shown in Figs. 5-7. Note that because the sign convention for the X and Z axes are opposite for the Orbiter structural and body coordinate systems, the $-Z_b$ burn of Fig. 5 causes a shift in the $+Z_o$ direction. Reference 13 discusses several PRCS and OMS firings that occurred during STS-75, some of which are the MEPHISTO activities. Table 3 compares acceleration level shifts as seen in the SAMS data to dV/dt values obtained from Reference 13. While the exact provenance of the dV/dt values are unclear, the correlation shown in the table is significant.

Figure 8 is provided as a more detailed view of the accelerations associated with one of the MEPHISTO PRCS events. The fifteen second $-Z_b$ axis PRCS 5D maneuver was performed at MET

012/12:25 using the PRCS thrusters L2D, L3D, R2D, R3D, F3D, and F4D [13]. As seen by the six discretes at the top of Fig. 8, two of the forward thrusters (F3D, F4D) were fired for the entire fifteen second burn. The Y-axis components of these two jets negated each other and the Z-axis components were additive. This action translated the nose of the Orbiter in the $-Z_b$ direction, while the tail was translated in the $-Z_b$ direction by firing 4 aft jets (L2D, L3D, R2D, R3D). Note that the aft jets were not fired continuously and these transients are clearly seen in the SAMS Z_o data in Fig. 8.

5.3. SPREE Rotary Table Operations

The TSS-1R Shuttle Potential and Return Electron Experiment (SPREE) was designed to measure the charged particle populations around the Orbiter. SPREE was mounted on the port side of the TSS-1R MPESS. The sensors for SPREE were two pairs of electrostatic analyzers, each pair mounted on a motor-driven rotary table. These tables were configured to rotate at one revolution per minute. During STS-75, the SPREE experiment team requested rotations during USMP-3 microgravity periods. A series of tests were performed to determine whether or not the rotations had a deleterious effect on the microgravity environment. During an Orbiter free drift period, the two rotating tables were parked and rotated at 1 rpm. The table rotation rate translates to a frequency of ~0.02 Hz. No notable accelerations are seen in the SAMS data, nor are there any evident transients in the data when the table rotations were initiated or ceased. This was analyzed by PIMS during the mission and because there were no evident accelerations related to the SPREE rotations, the USMP-3 Mission Scientist permitted SPREE operations as needed during the microgravity periods. OARE data are not available for this time period because of OARE instrument calibrations operations.

5.4. Ku band Antenna Repositioning

The Ku band antenna on the Orbiters is used to transmit data and voice communications between the Orbiters and ground stations via the Tracking and Data Relay Satellite System satellites [14]. The Ku band deployed assembly is mounted on the starboard sill of the payload bay. It is deployed and activated after the payload bay doors are opened. The antenna dish is edge-mounted on a two-axis gimbal. The alpha gimbal provides a 360° roll movement around the pole of the gimbal. The beta gimbal provides a 162° pitch movement around its axis. The alpha gimbal has a stop at the lower part of its movement to prevent wraparound of the beta gimbal control cable. Periodically, the Ku band antenna beta cabling requires positioning to ensure that it does not become twisted in a way that could cause the antenna to bind. This gimbal flip is achieved by a fast slew of the antenna dish in the direction needed to unwrap the cable.

Figure 9 shows a spectrogram generated from SAMS Unit F TSH 1B data for a period in which the Ku band antenna was repositioned. In this figure, the 17 Hz acceleration signal characteristic of the antenna's dither frequency stops at MET 007/13:05:25, and resumes approximately 17 seconds later. This break in the usually continuous 17 Hz signal is related to the repositioning activity. During fast slew operations, the 17 Hz dither is disabled.

5.5. Flight Control System Checkout

Approximately one day before scheduled re-entry, a two-part checkout procedure is performed to verify operations of the Orbiter Flight Control System (FCS). The first part of this checkout uses one of the three Auxiliary Power Units (APUs) to circulate hydraulic fluid in order to move the rudder, elevons, and ailerons of the Orbiter. As an APU is activated, exhaust gas is vented in the $-Z_b$ direction. The result of this venting is similar in nature to a VRCS jet firing, ranging from nearly 0 to 30 pounds of force. The exhaust does not vent as a steady stream, but cycles at approximately 1 to 1.5 Hz.

Part one of the FCS checkout on STS-75 lasted for approximately 25 minutes. Fig. 10 is a SAMS Unit G TSH 2A spectrogram showing the extent of the first part of the FCS checkout. The activation of APU1 occurred at about 013/15:03, note the sudden change in acceleration characteristics. Of particular note is the appearance of a 1.3 Hz signal and several upper harmonics. These signals remain in the data throughout the checkout period, with slight shifts in the frequencies about 13 and 18 minutes into the plot. Broadband excitation of the microgravity environment about four minutes into the plot appear to be correlated with changes in APU1 turbine activity as are shorter excitations between 013/15:20 and 013/15:27. Part two of the FCS checkout procedure tests various Orbiter electronics systems and did not cause a measurable disturbance to the microgravity environment.

5.6. TSS-1R Operations

The USMP-3 investigators were very interested in how the deployment of the TSS-1R satellite would affect the quasi-steady environment of Columbia. OARE data shown in Fig. 11 depict the quasi-steady environment of the Orbiter at the OARE location for a six hour period encompassing TSS deploy operations. This plot indicates the microgravity levels prior to TSS Satellite deploy, during the flyaway and deploy phases, at the time of the tether break, and after the tether separation.

From an average acceleration level of $X_b=8\times10^{-8}$g, $Y_b=-1.8\times10^{-7}$g, $Z_b=6.7\times10^{-7}$g in the Orbiter deploy attitude, PYR=(210°, 10°, 188°), the environment changed to $X_b=-1.8\times10^{-5}$g, $Y_b=-1\times10^{-7}$g, $Z_b=3.7\times10^{-5}$g at the time of the tether separation. The shift in acceleration levels indicated here is consistent with predictions of the quasi-steady environment with the satellite deployed to 20 km.

Figs. 12 and 13 are two different representations of SAMS data collected during the satellite deploy activities. Fig. 12 shows SAMS Unit F TSH 1A data with the signal processed using a thirty second interval average. Fig. 13 is a spectrogram of SAMS Unit F TSH 1A data for the deploy time. Transient accelerations at about 003/01:40 and between 003/02:00 and 003/03:00 appear in Figs. 11-13. These are related to Orbiter maneuvers during the TSS deploy operations. A series of transients at about 003/01:20 is caused by RCS activity, activated to compensate for TSS dynamics. In the spectrogram there is a band of disturbances that starts between 5 and 10 Hz and ranges up to about 20 Hz. These disturbances appear to correspond to the speed of the deploying TSS cable. The speed of the cable was varied during deployment for experimental investigations and because of coupled TSS and Orbiter dynamics. Frequencies of about 6 Hz are consistent with calculations of disturbance frequencies using nominal values for the size of pulleys and the cable speed. Mul-

tiple pulleys of various sizes could correspond to the multiple traces in the SAMS spectrogram of Fig. 13. Figure 14 shows the response of SAMS Unit F TSH 1A to the break of the TSS tether. The initial response to the break is a ringing at about 9 Hz.

5.7. Waste Collection System Compaction

The Waste Collection System is a multifunctional system used primarily to collect and process biological waste from crew members. This system is located in the Orbiter middeck. Within the waste collection system is a compactor device which is used to increase the commode capacity. Compaction is typically performed once per flight. The compactor is manually driven using a ratchet wrench. A mobile vane is rotated around on the radius of the commode. Because the compactor only collects and compacts what is already collected in the commode, compaction should not affect venting from the waste collection system vacuum vent. The waste compaction operation was performed at approximately 009/01:32 during STS-75. Analysis of SAMS data indicate that the compaction did not disturb the acceleration environment on the MPESS carriers. OARE data from that time frame indicate no apparent venting forces are associated with the compaction operation.

5.8. Fuel Cell Purge

The three fuel cell power plants, through chemical reactions, generate all of the 28-volt direct-current electrical power for the Orbiters from launch through landing [14]. The fuel cells are located under the payload bay area in the forward portion of the Orbiter's midfuselage. The fuel cell power plants generate heat and water as by-products of electrical power generation. The water is directed to the potable water storage subsystem. If the water tanks are full or there is line blockage, the water is vented overboard through the water relief line and nozzle. This vent is indicated in Fig. 15 (FCP water relief) which is an overview of the Orbiter onboard venting locations.

During normal fuel cell operation, it is necessary to cleanse the cells at least twice daily to purge contaminants. H_2 and O_2 purging occurs concurrently, and the venting is directed so that the only non-compensated thrust is in the Orbiter Y-axis direction. There were no apparent disturbances seen in the OARE or SAMS data associated with a fuel cell purge at 011/02:54.

5.9. Orbiter Attitude

The STS-75 mission had several primary attitudes defined for the TSS-1R and USMP-3 payloads. There were a variety of attitudes and Orbiter maneuvers before the tethered satellite deployment and after the tether separation during the first five days of the mission. The as-flown attitude timeline should be consulted for detailed times and attitude parameters [13].

The attitude flown for the USMP-3 payload during the majority of the last eight days of the mission (MET 005/00:15 to 013/14:00) was a gravity gradient attitude -XLV/+ZVV (PYR~95°,5°,0°). This

USMP-3 default attitude was chosen to minimize attitude changes, the number of thruster firings, and to reduce the possibility of Orbiter debris damage. Variations in the microgravity environment due to Orbiter attitudes are best seen in the OARE data. Fig. 16 is a plot of OARE data for the entire STS-75 mission. Fig. 17 is an example of the quasi-steady environment related to the nominal USMP-3 attitude.

Three different attitudes were flown during processing of the three AADSF samples on MET days 008, 009, and 010. These AADSF attitudes were designed to result in a quasi-steady vector in line with, against, and transverse to the crystal growth direction. The resulting quasi-steady environment associated with each of these attitudes is represented in Figs. 18-23.

6. Summary

The microgravity environment of the Space Shuttle Columbia was measured during the STS-75 mission using accelerometers from two different instruments, OARE and SAMS. The OARE provided USMP-3 investigators with quasi-steady acceleration measurements after about a six hour time lag dictated by downlink constraints. SAMS data were downlinked in near real-time in support of the USMP-3 investigators and recorded on-board for post-mission analysis.

Using a combination of data analysis techniques, the microgravity environment related to several different Orbiter, crew, and experiment operations is presented and interpreted. SAMS data are analyzed to determine the effects of specific crew activities, Reaction Control System jet firings, SPREE experiment table rotations, a Ku band antenna repositioning, the Flight Control System checkout, Tethered Satellite System deploy activities, a waste collection system compaction, and a fuel cell purge. OARE data are analyzed for the same TSS-1R, WCS, and fuel cell purge operations and for times with different Orbiter attitudes.

The specific crew activities performed in the middeck and flight deck, the SPREE table rotations, the WCS compaction, and the fuel cell purge had negligible effects on the microgravity environment of the USMP-3 MPESS carriers. Of particular note in the analysis of VRCS data is that the F5L and F5R jets when fired in tandem caused appreciably higher magnitude accelerations than expected based on the magnitudes of single firings. The Ku band repositioning activity resulted in a brief interruption of the ubiquitous 17 Hz signal in the SAMS data.

The STS-75 microgravity environment represented by SAMS and OARE data is comparable to the environments measured by the instruments on earlier microgravity science missions. VRCS activity on this mission appears to be somewhat more frequent than on other microgravity missions with the combined firings of the F5L and F5R jets producing significant acceleration transients. Orbiter structural modes and crew exercise frequencies are typically the same among Orbiters, missions, and crew members. The main differences among missions are the specific frequencies of equipment oscillations. Better coordination between PIMS and experiment and Orbiter systems designers and engineers is needed to help identify the sources of all distinct characteristics of the Orbiter microgravity environment. For STS-75, we have expanded our understanding of the effects of Orbiter operations on the environment by investigating the Ku band antenna repositioning, WCS

compaction, fuel cell purges, and FCS checkout activities. Of these, only the APU operations during the FCS checkout appeared to have a significant impact on the microgravity environment.

7. References

[1] Blanchard, R. C., M. K. Hendrix, J. C. Fox, D. J. Thomas, and J. Y. Nicholson, Orbital Acceleration Research Experiment. J. Spacecraft and Rockets, Vol. 24, No. 6, (1987) 504 - 511.

[2] Blanchard, R. C., J. Y. Nicholson, and J. R. Ritter, STS-40 Orbital Acceleration Research Experiment Flight Results During a Typical Sleep Period. NASA Technical Memorandum 104209, January 1992.

[3] Blanchard, R. C., J. Y. Nicholson, J. R. Ritter, Preliminary OARE Absolute Acceleration Measurements on STS-50. NASA Technical Memorandum 107724, February 1993.

[4] Blanchard, R. C., J. Y. Nicholson, J. R. Ritter, and K. T. Larman, OARE Flight Maneuvers and Calibration Measurements on STS-58. NASA Technical Memorandum 109093, April 1994.

[5] DeLombard, R., B. D. Finley, Space Acceleration Measurement System description and operations on the First Spacelab Life Sciences Mission. NASA Technical Memorandum 105301, November 1991.

[6] DeLombard, R., B. D. Finley, and C. R. Baugher, Development of and flight results from the Space Acceleration Measurement System (SAMS). NASA Technical Memorandum 105652, January 1992.

[7] Baugher, C. R., G. L. Martin, and R. DeLombard, Low-frequency vibration environment for five shuttle missions, NASA Technical Memorandum 106059, March 1993.

[8] Rogers, M. J. B., C. R. Baugher, R. C. Blanchard, R. DeLombard, W. W. Durgin, D. H. Matthiesen, W. Neupert, and P. Roussel, A Comparison of low-gravity measurements onboard Columbia during STS-40. Microgravity Science and Technology VI/3 (1993) 207 - 216.

[9] Finley, B. D., C. Grodsinsky, and R. DeLombard, Summary report of mission acceleration measurements for SPACEHAB-01, STS-57. NASA Technical Memorandum 106514, March 1994.

[10] Summary report of mission acceleration measurements for STS-73. NASA Technical Memorandum 107269, July 1996.

[11] Rice, J.E., OARE Technical Report #148, OARE STS-75 (USMP-3) Final Report, CSI-9603, June 1996.

[12] DeLombard, R., Compendium of information for interpreting the microgravity environment of the orbiter spacecraft, NASA Technical Memorandum 107032, August 1996.

[13] STS-75 Space Shuttle Mission Report, NSTS-37406, Johnson Space Center, April 1996

[14] Shuttle Operational Data Book, Volume 1, JSC-08934, Rev. E, Johnson Space Center, Houston, TX, January 1988.

[15] Rogers, M. J. B., K. Hrovat, M. Moskowitz, K. McPherson and R. DeLombard, Summary report of mission acceleration measurements for STS-75. NASA Technical Memorandum 107359, November 1996.

OARE Sensor		Sample Rate: 10 samples/second
Location: Orbiter Cargo Bay Keel Bridge		Frequency: 0 to 1 Hz
ORIENTATION		**LOCATION**
Orbiter Structural Axis	**Sensor Axis**	**Structural Axis**
X_O	$-X_{OARE}$	$X_O = 1153.3$ in
Y_O	Z_{OARE}	$Y_O = -1.3$ in
Z_O	Y_{OARE}	$Z_O = 317.8$ in

Table 1. STS-75 OARE Head Location and Orientation

Unit F Head 1A (TSH-1A)		Sample Rate: 50 samples/second
Serial no.: 821-19		
Location: Forward MPESS, Forward rail		Frequency: 10 Hz
ORIENTATION		**LOCATION**
Orbiter Structural Axis	**Sensor Axis**	**Structural Axis**
X_O	$-Y_H$	$X_O = 1048.37$ in
Y_O	$+Z_H$	$Y_O = 4.82$ in
Z_O	$-X_H$	$Z_O = 418.13$ in

Unit F Head 1B (TSH-1B)		Sample Rate: 125 samples/second
Serial no.: 821-21		
Location: Forward MPESS, Forward rail		Frequency: 25 Hz
ORIENTATION		**LOCATION**
Orbiter Structural Axis	**Sensor Axis**	**Structural Axis**
X_O	$-Y_H$	$X_O = 1048.37$ in
Y_O	$+Z_H$	$Y_O = -4.73$ in
Z_O	$-X_H$	$Z_O = 418.13$ in

Unit G Head 2A (TSH-2A)		Sample Rate: 50 samples/second
Serial no.: 821-4		
Location: Inside IDGE, (aft MPESS)		Frequency: 5 Hz
ORIENTATION		**LOCATION**
Orbiter Structural Axis	**Sensor Axis**	**Structural Axis**
X_O	$-X_H$	X_O = 1135.42 in
Y_O	$+Y_H$	Y_O = -45.24 in
Z_O	$-Z_H$	Z_O = 433.96 in

Unit G Head 2B (TSH-2B)		Sample Rate: 50 samples/second
Serial no.: 821-29		
Location: Aft MPESS, Aft rail		Frequency: 10 Hz
ORIENTATION		**LOCATION**
Orbiter Structural Axis	**Sensor Axis**	**Structural Axis**
X_O	$+Y_H$	X_O = 1136.82 in
Y_O	$-Z_H$	Y_O = -4.82 in
Z_O	$-X_H$	Z_O = 418.13 in

Unit G Head 2C (TSH-2C)		Sample Rate: 125 samples/second
Serial no.: 821-20		
Location: Aft MPESS, Aft rail		Frequency: 25 Hz
ORIENTATION		**LOCATION**
Orbiter Structural Axis	**Sensor Axis**	**Structural Axis**
X_O	$+Y_H$	X_O = 1136.82 in
Y_O	$-Z_H$	Y_O = 4.73 in
Z_O	$-X_H$	Z_O = 418.13 in

Table 2. STS-75 SAMS Head Location and Orientation

Firing	Average acceleration (from plot)	dV/dt [12]
OMS-3	46 mg	50 mg
PRCS 5D	11 mg	14 mg
PRCS 5C1	6 mg	6 mg
PRCS 5C2	7 mg	6 mg

Table 3. Accelerations Associated with PRCS Activity

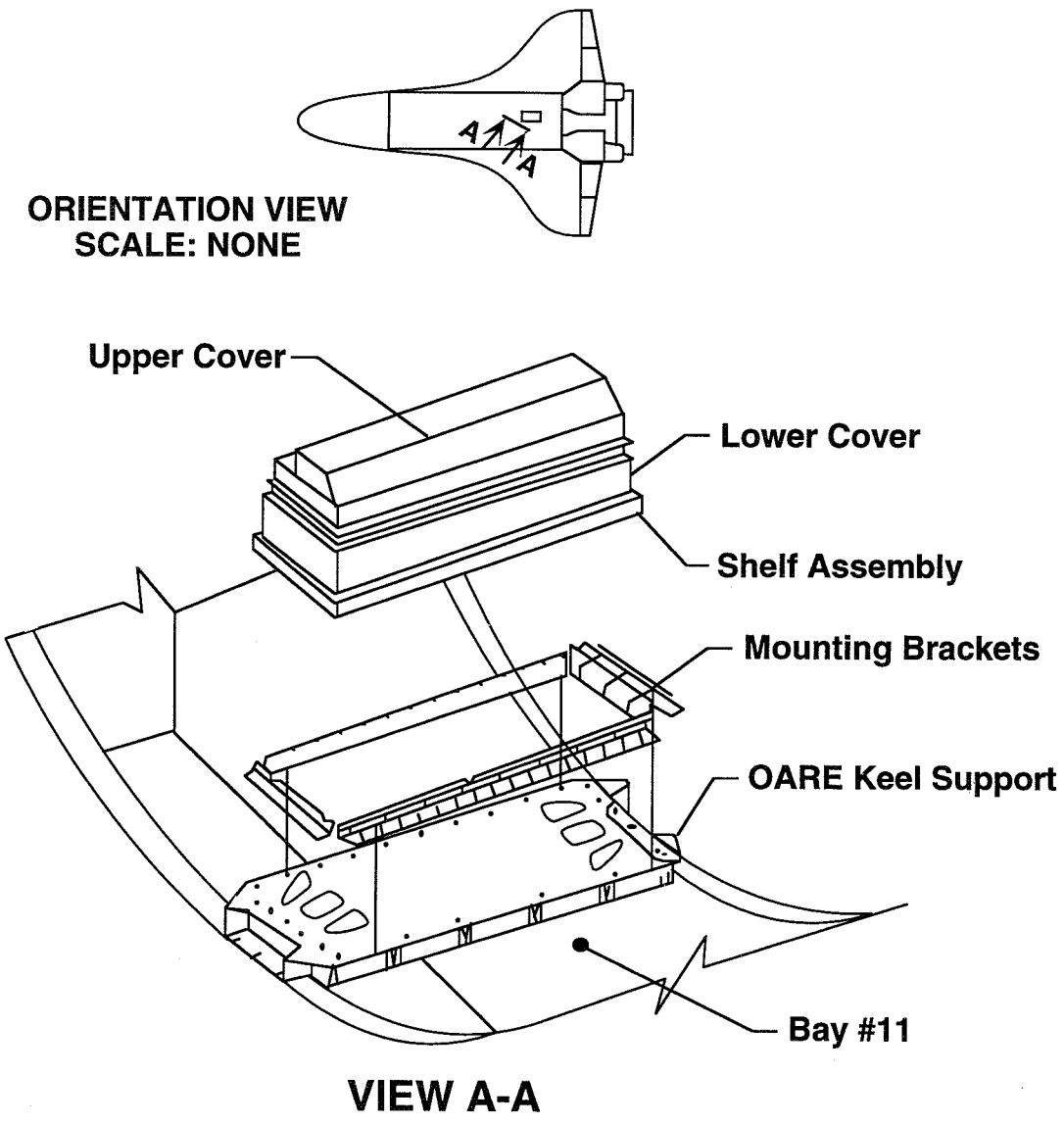

Figure 1. Approximate OARE instrument location on STS-75

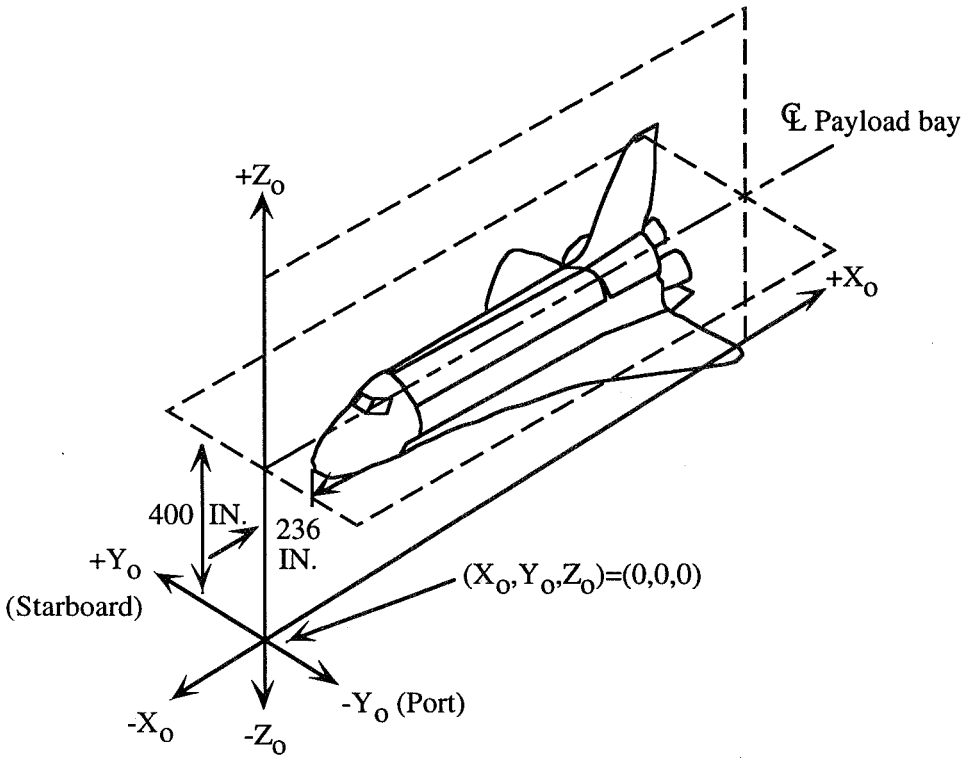

Orbiter structural coordinate system.

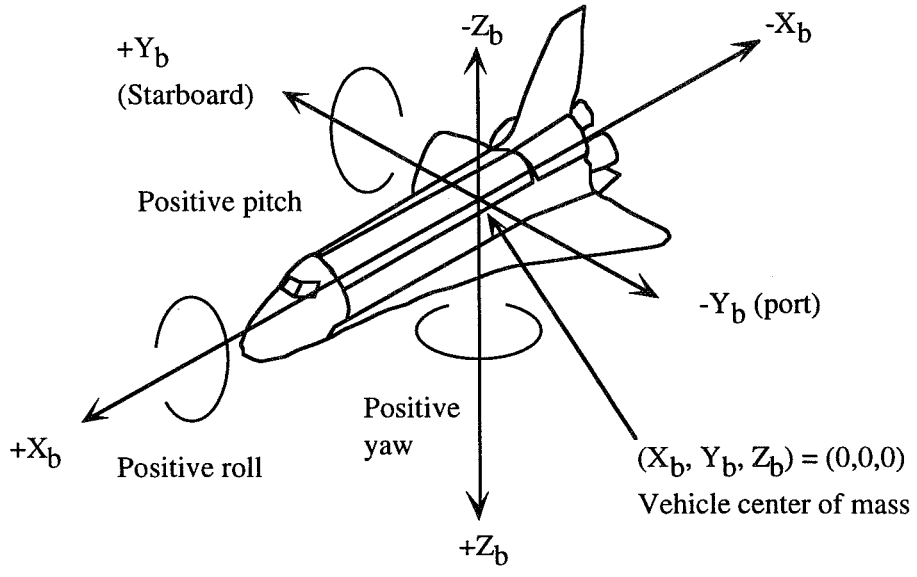

Orbiter body coordinate system.

Figure 2. Orbiter body and structural coordinate systems

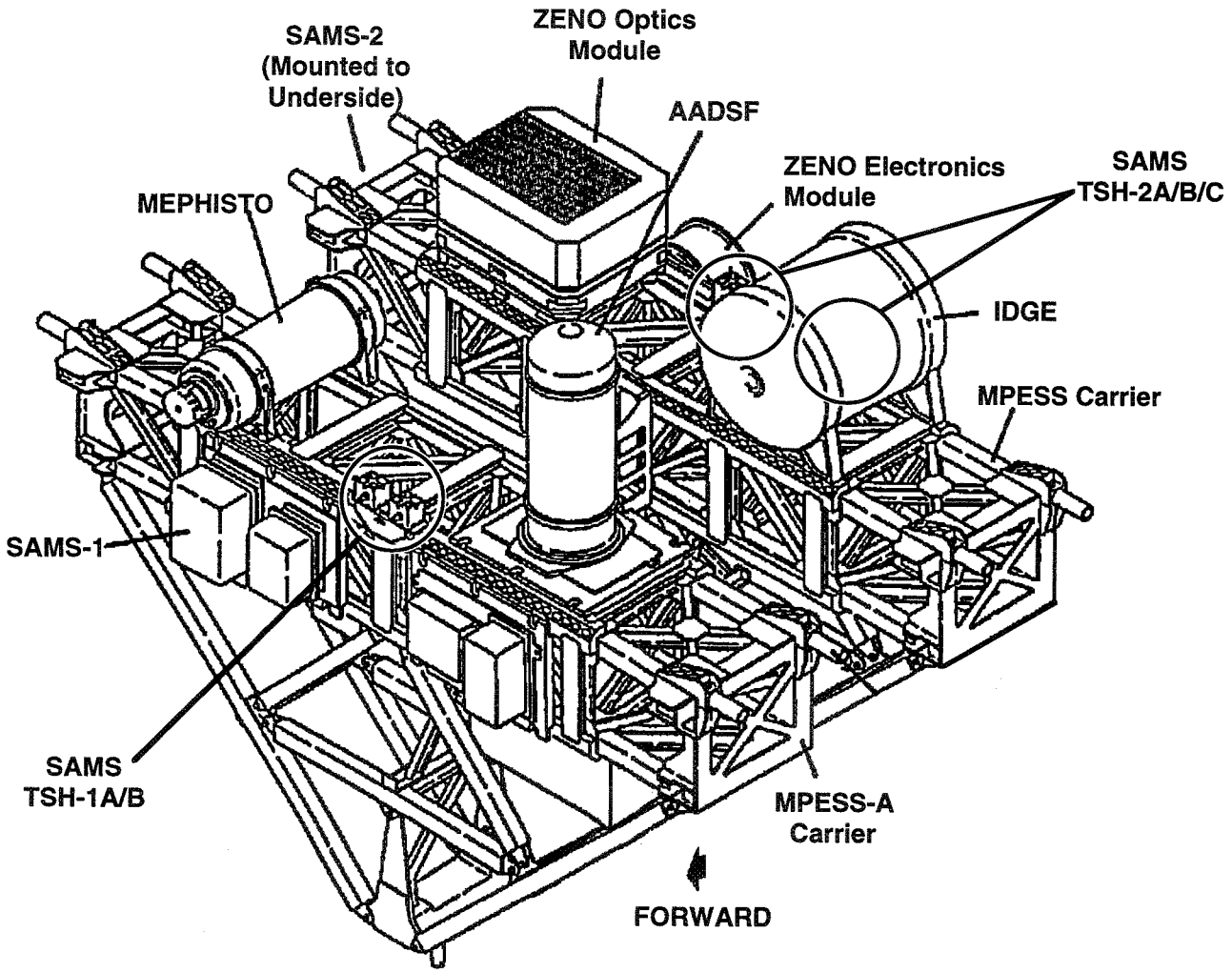

Figure 3. Approximate location of SAMS sensors on the USMP-3 MPESS carriers, STS-75

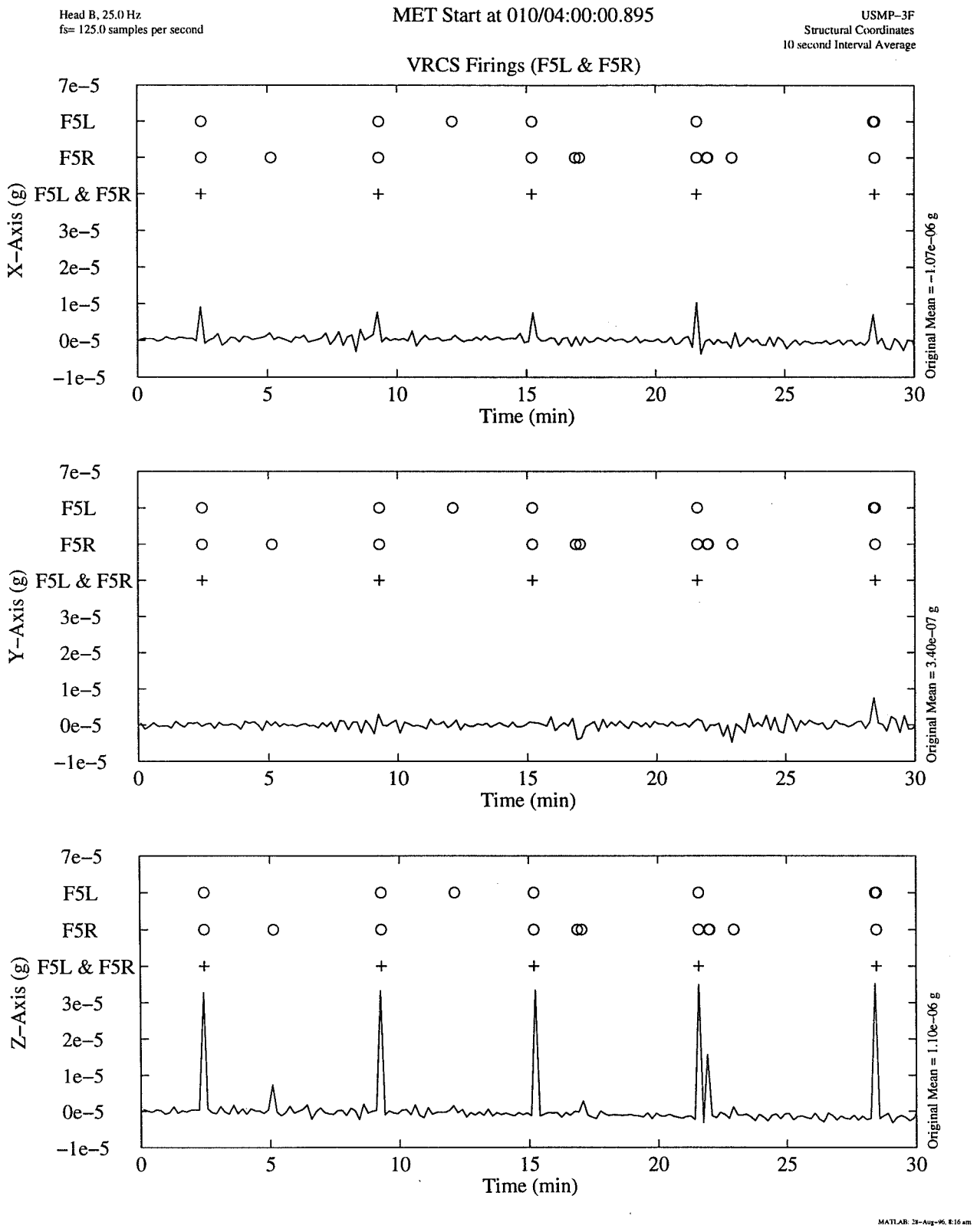

Figure 4. SAMS Unit F TSH 1B data, ten second interval average, showing use of F5L and F5R VRCS jets for attitude maintenance. Simultaneous F5L and F5R jet firings indicated by + markers, individual events indicated by o markers. MET start 010/04:00.

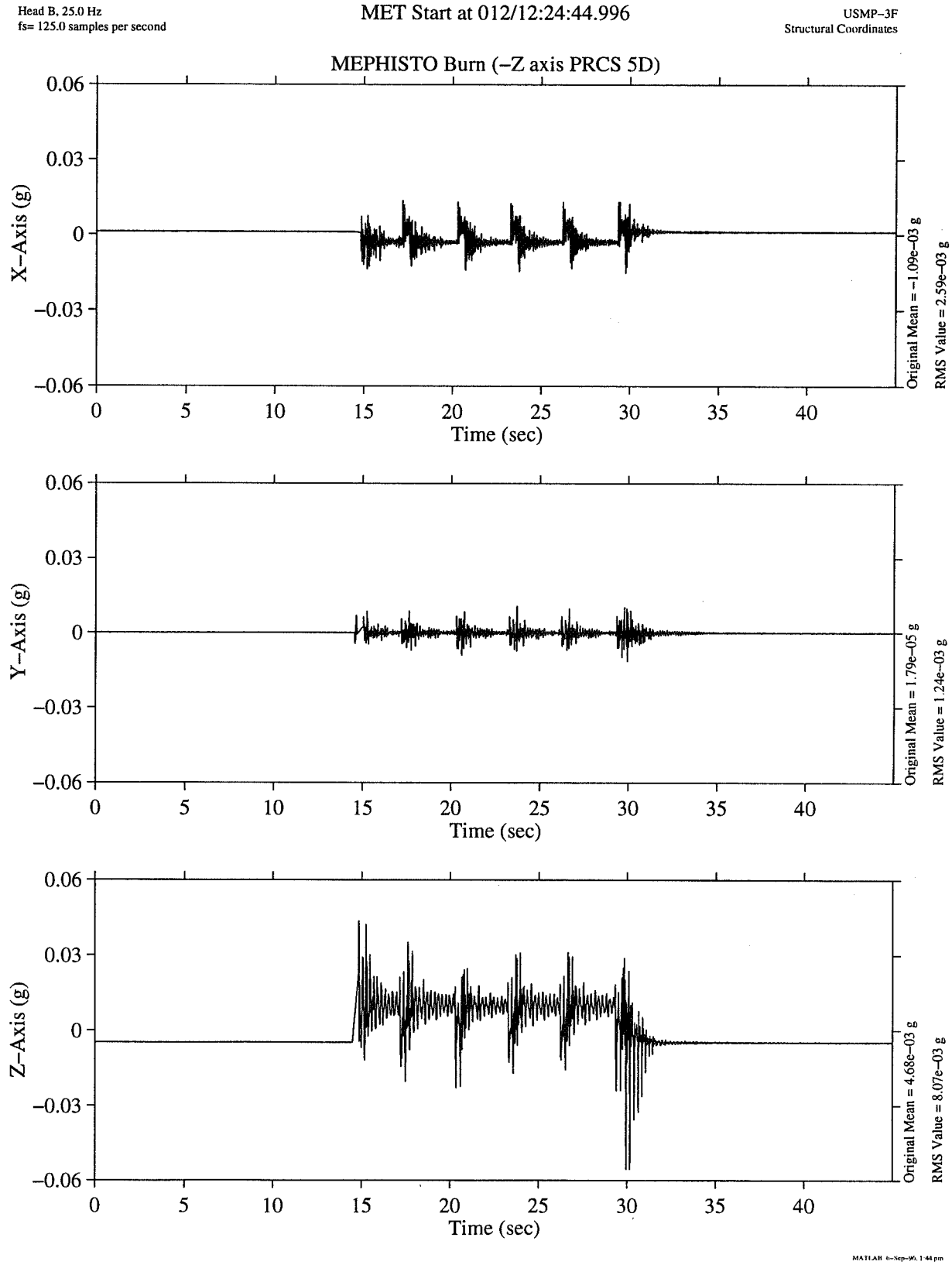

Figure 5. SAMS Unit F TSH 1B data from MEPHISTO PRCS 5D ($-Z_b$) event. MET start 012/ 12:24:45.

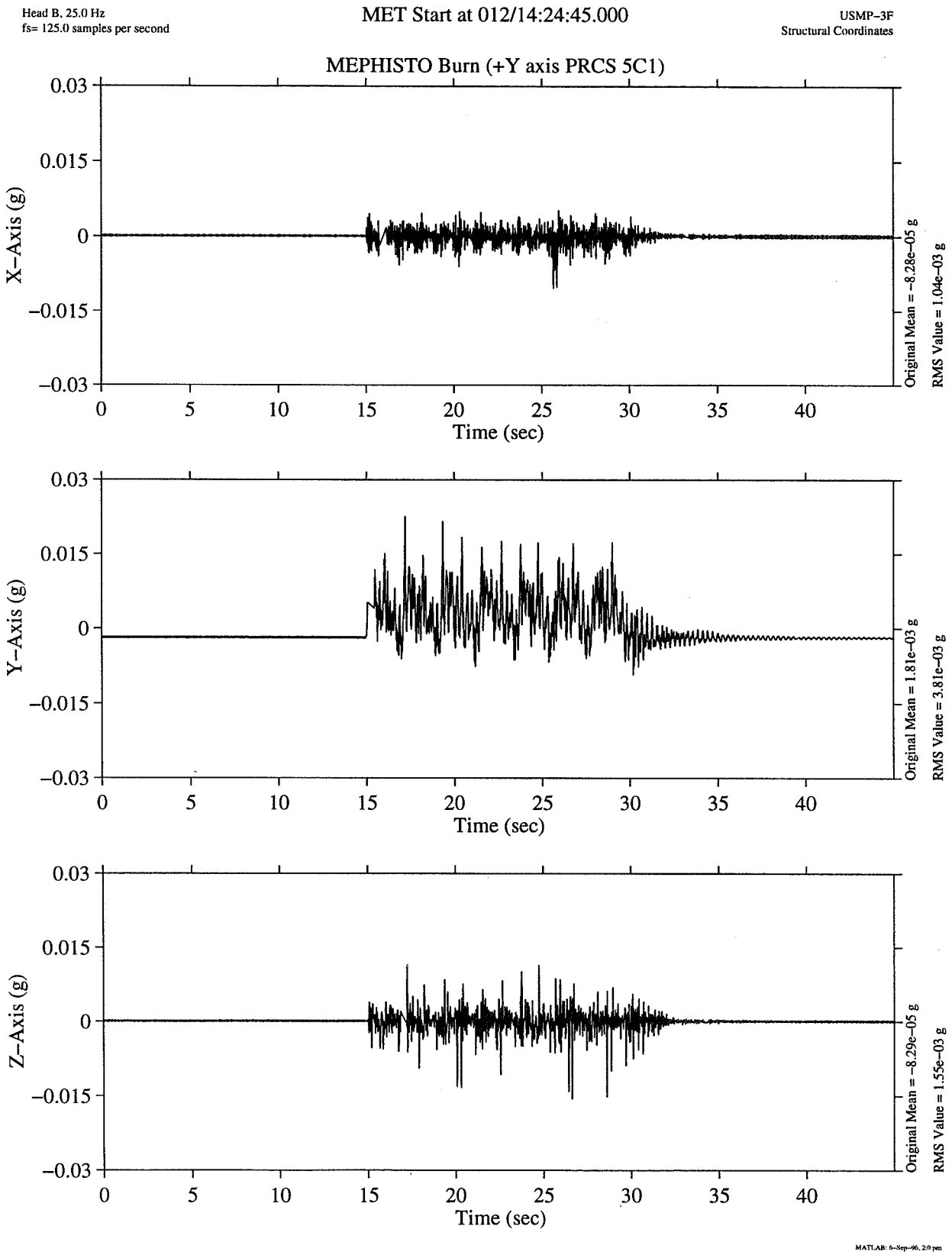

Figure 6. SAMS Unit F TSH 1B data from MEPHISTO PRCS 5C1 ($+Y_b$) event. MET start 012/ 14:24:45

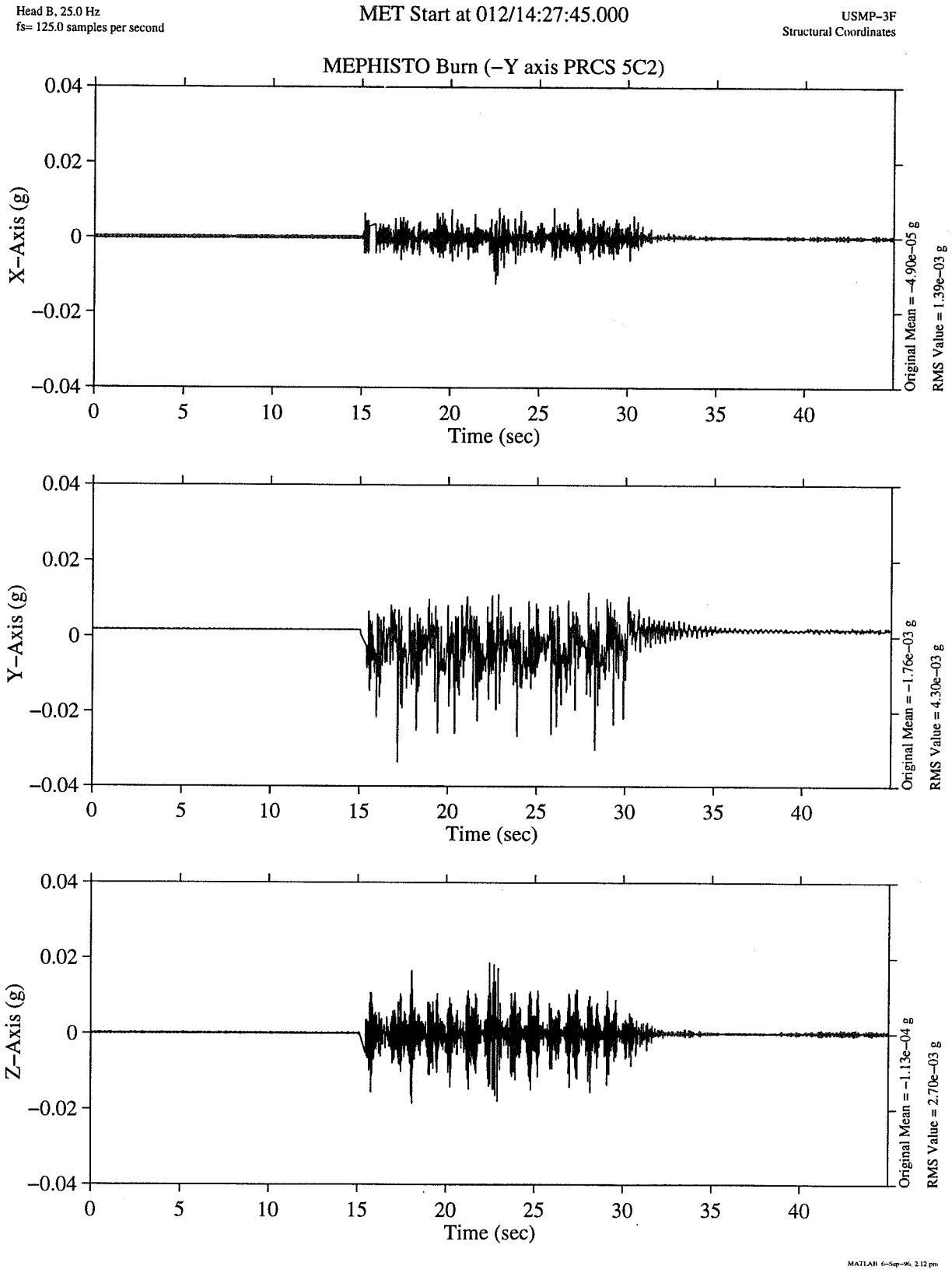

Figure 7. SAMS Unit F TSH 1B data from MEPHISTO PRCS 5C2 ($-Y_b$) event. MET start 012/ 14:27:45.

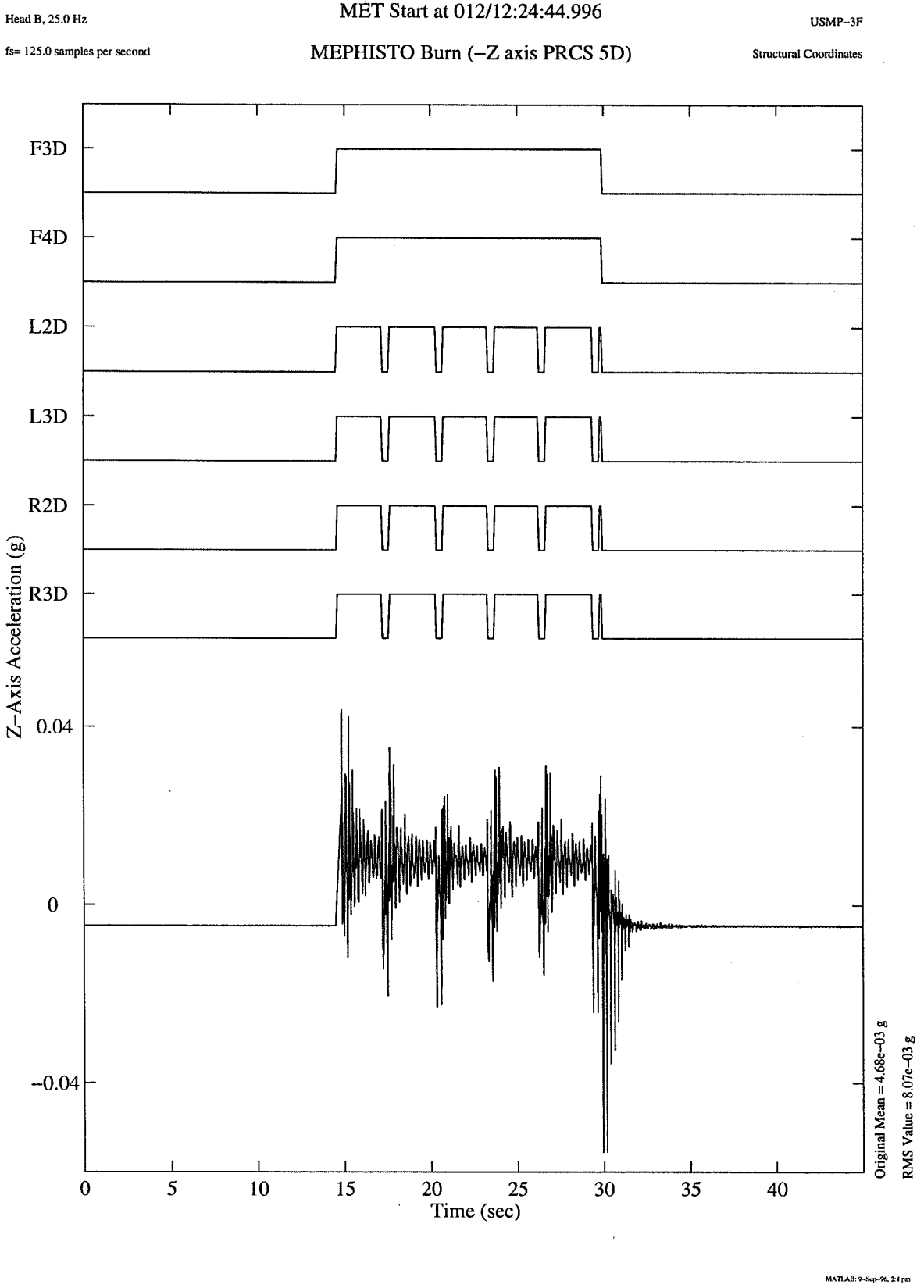

Figure 8. SAMS Unit F TSH 1B data from MEPHISTO PRCS 5D ($-Z_b$) event, Z_O axis of data shown. PRCS jet usage indicate on top section of plot. MET start 012/12:24:45

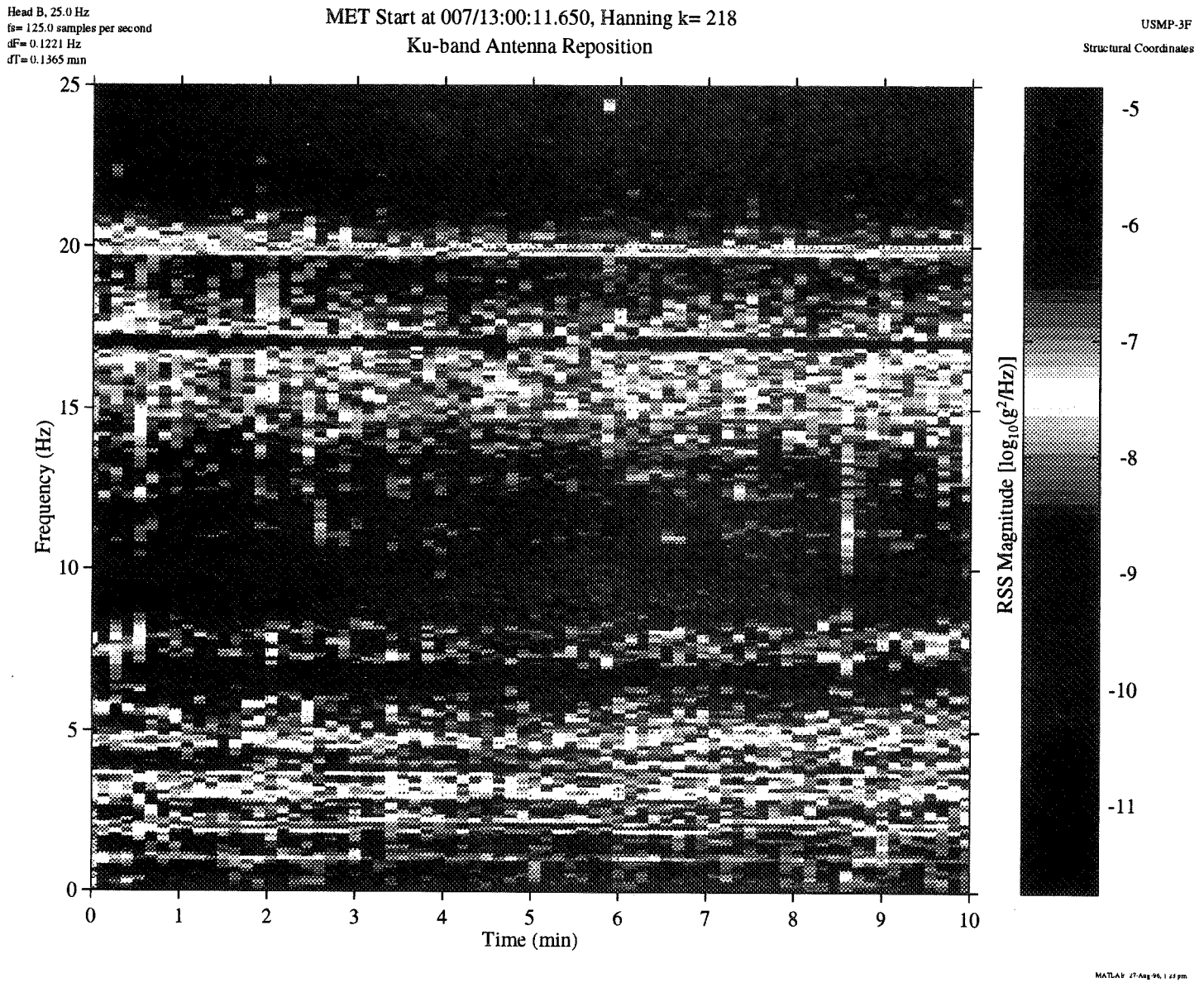

Figure 9. SAMS Unit F TSH 1B spectrogram showing data collected during Ku band antenna reposition. MET start 007/13:00:12. Note interruption of 17 Hz signal at 007/13:05:25 for 17 seconds.

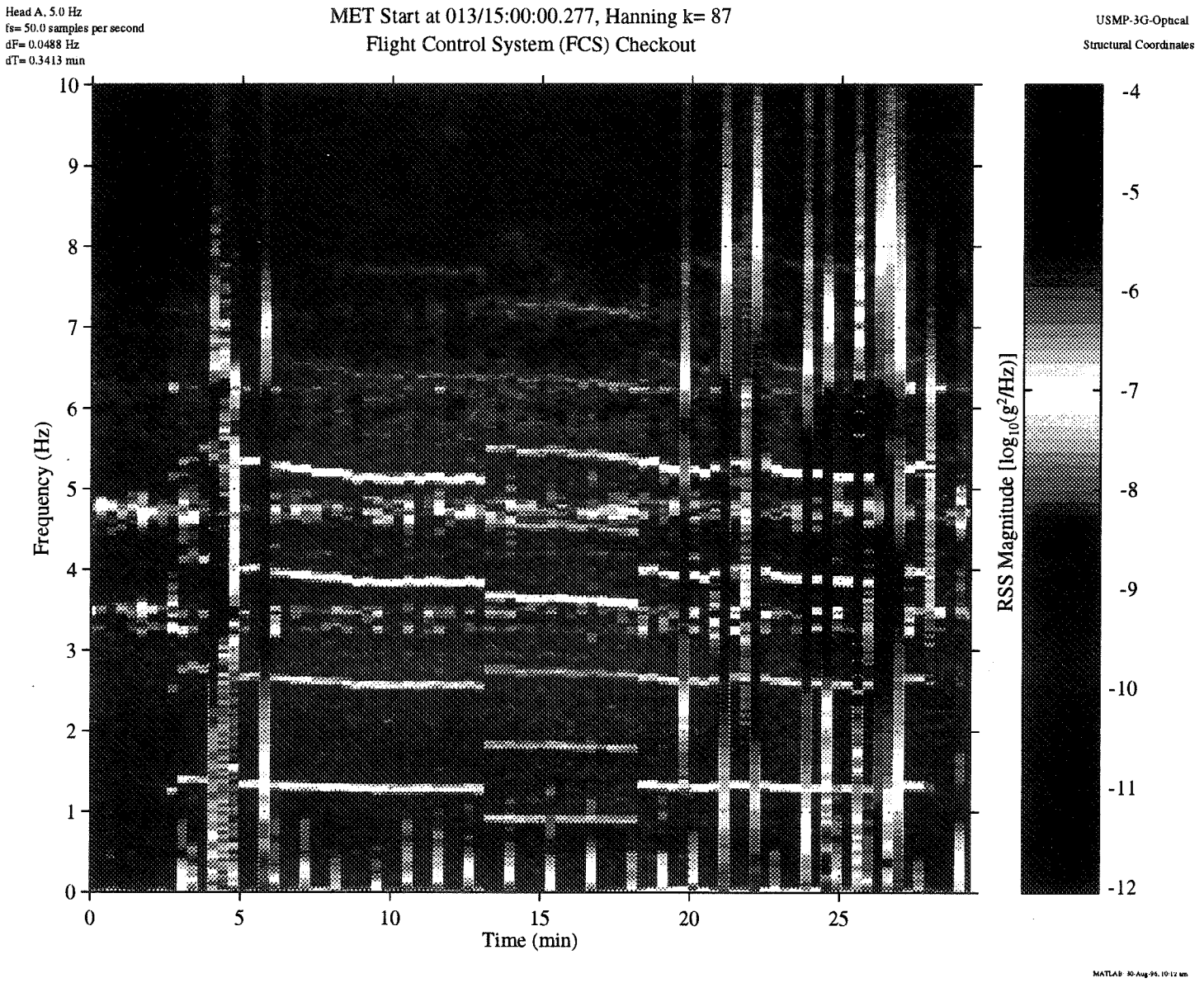

Figure 10. SAMS Unit G TSH 2A spectrogram showing data collected during Flight Control System checkout. MET start 013/15:00:00. Note change in signal character upon activation of auxiliary power unit one at 013/15:03.

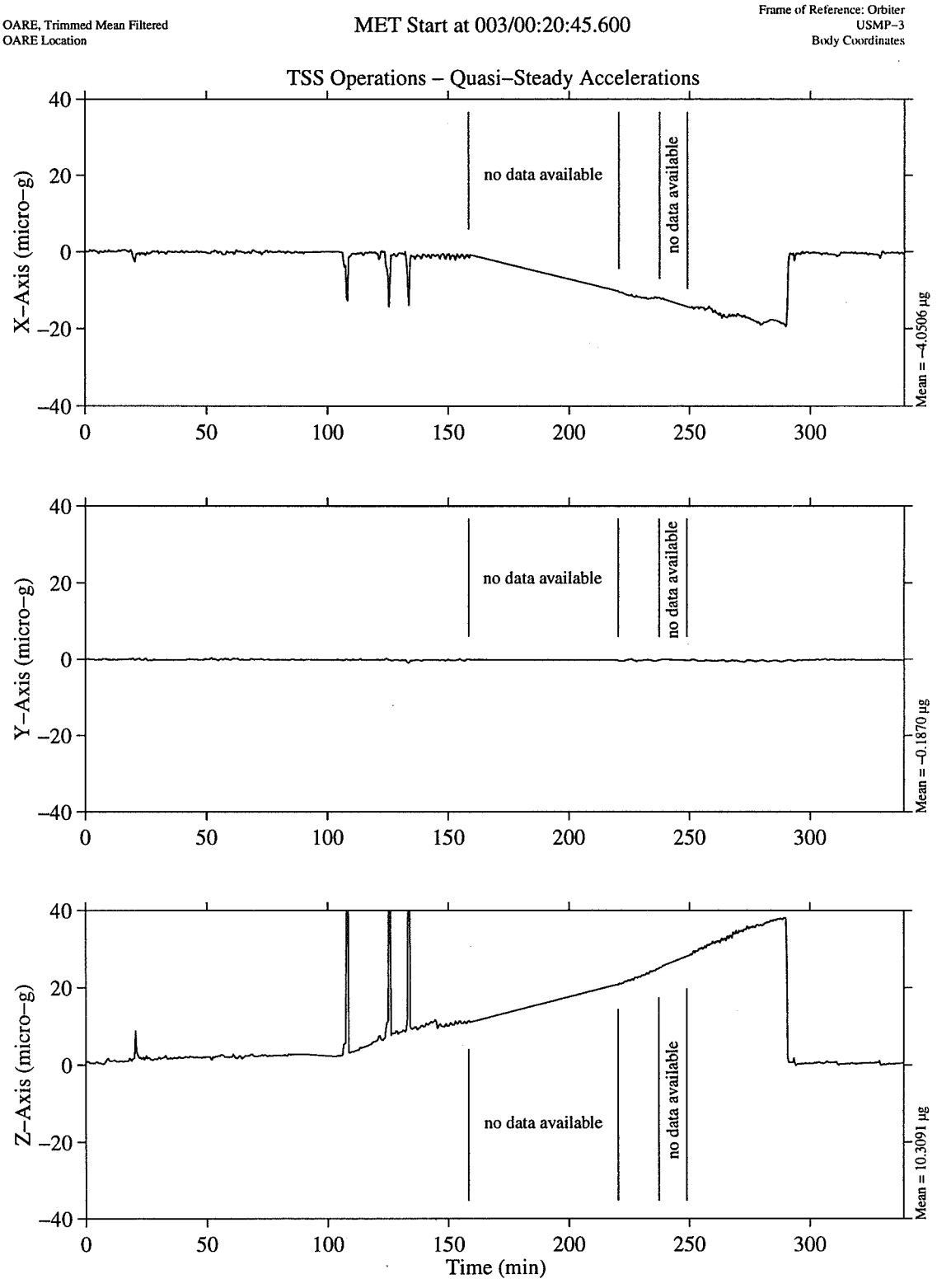

Figure 11. OARE data representing the microgravity environment at the OARE location during TSS-1R deploy operations. MET start at 003/00:00. Note TSS flyaway occurred at 003/00:27. Transient accelerations seen in the plot are due to PRCS activity to compensate for tether dynamics.

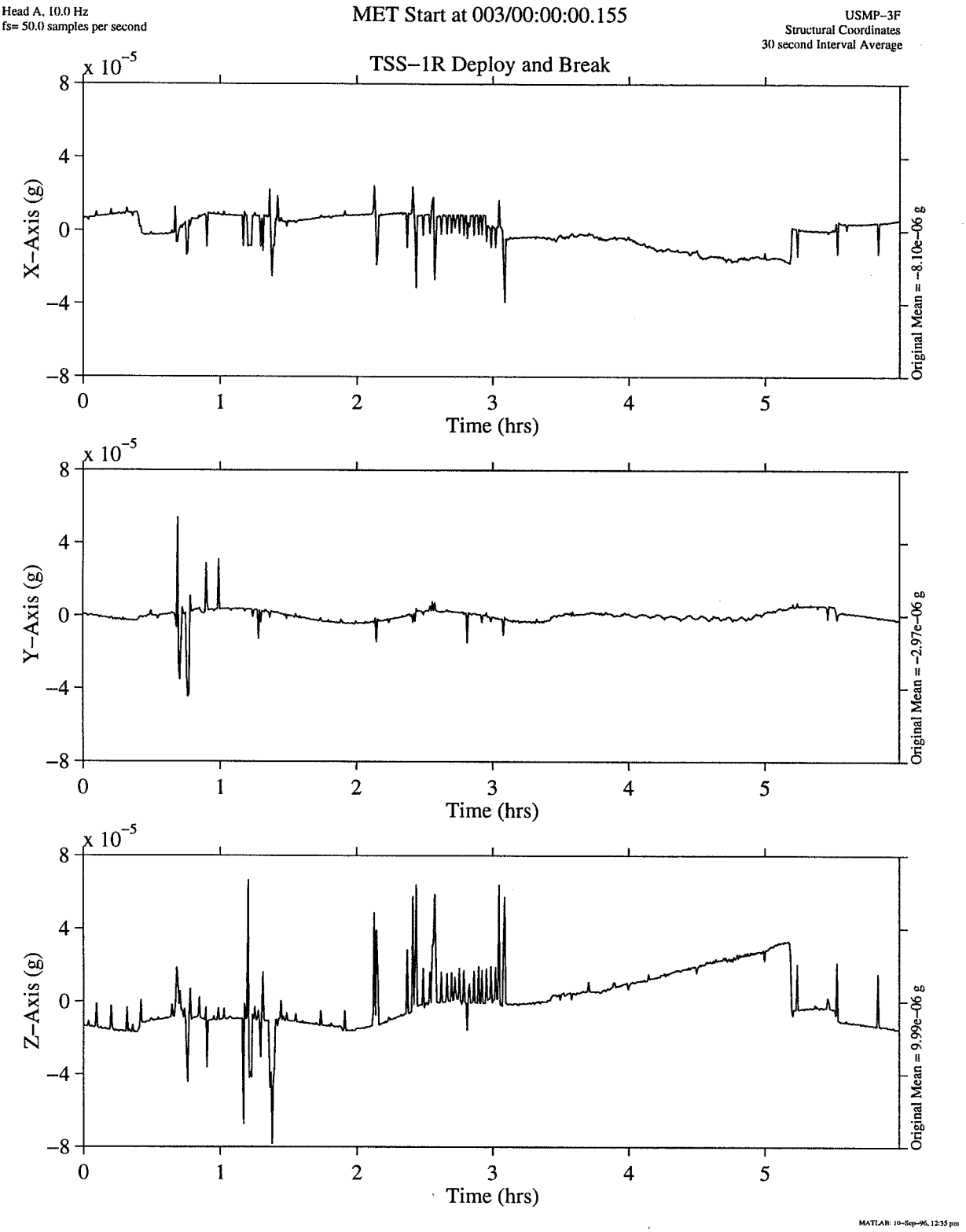

Figure 12. SAMS Unit F TSH 1A data representing the microgravity environment during TSS-1R deploy operations. MET start at 003/00:00. Note TSS flyaway occurred at 003/00:27. Transient accelerations seen in the plot are due to PRCS activity to compensate for tether dynamics.

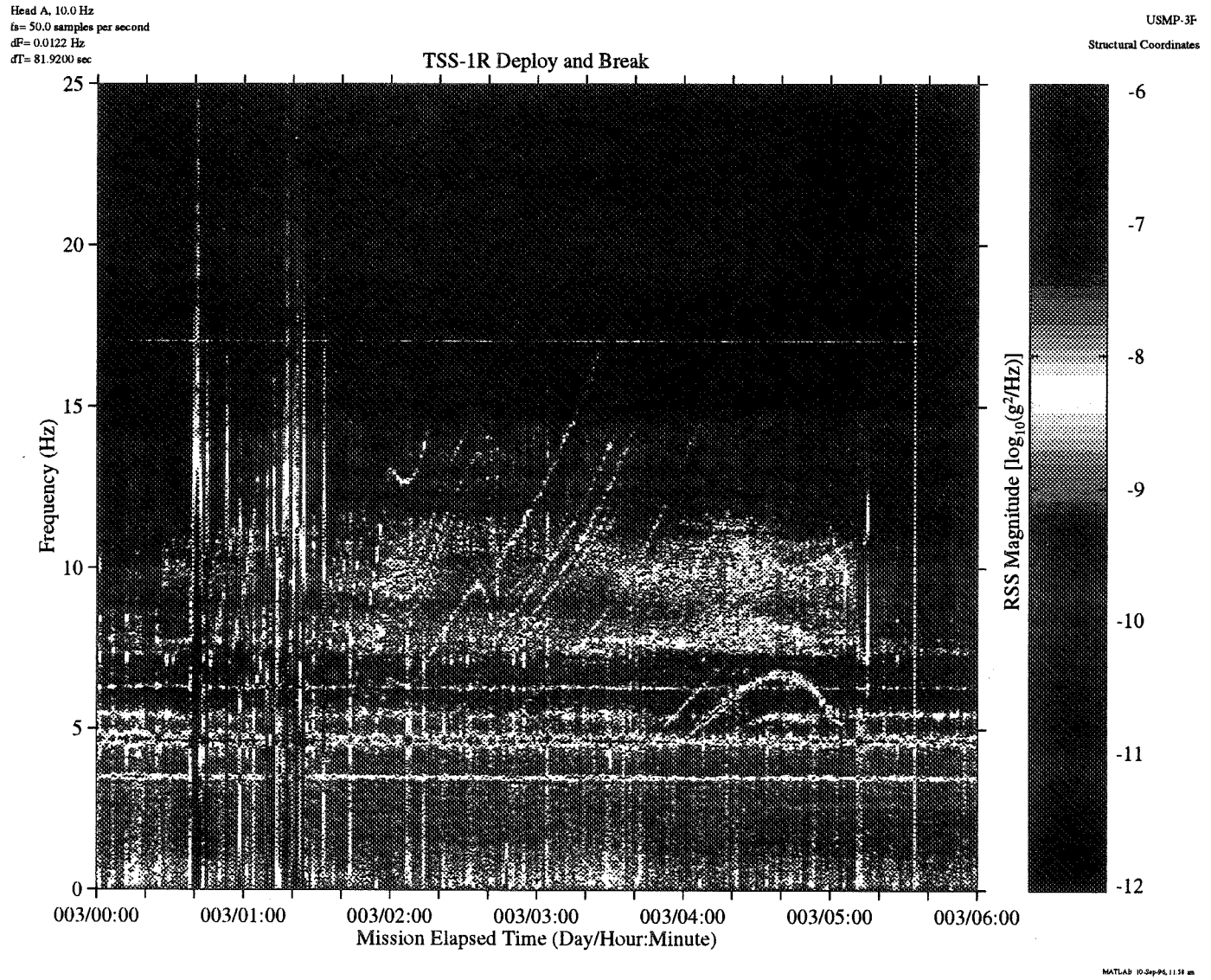

Figure 13. SAMS Unit F TSH 1A spectrogram showing data collected during TSS-1R deploy operations. MET start at 003/00:00. Note TSS flyaway occurred at 003/00:27. Transient accelerations seen in the plot as vertical stripes are due to PRCS activity to compensate for tether dynamics. Variable frequency traces are related to tether pulley rotations during tether deploy.

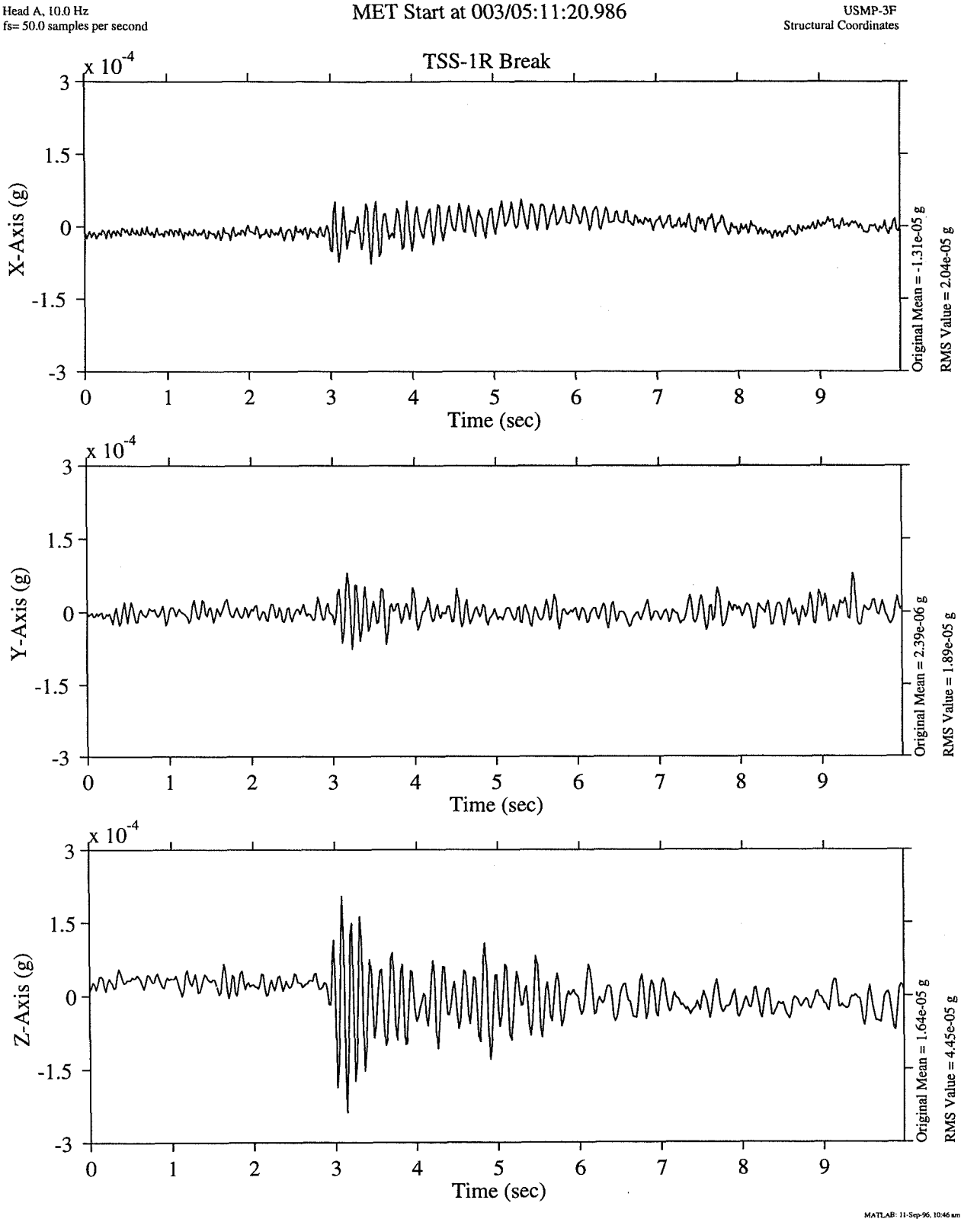

Figure 14. SAMS Unit F TSH 1A data from time of TSS-1R break. Note ringing of Orbiter structure at about 9 Hz.

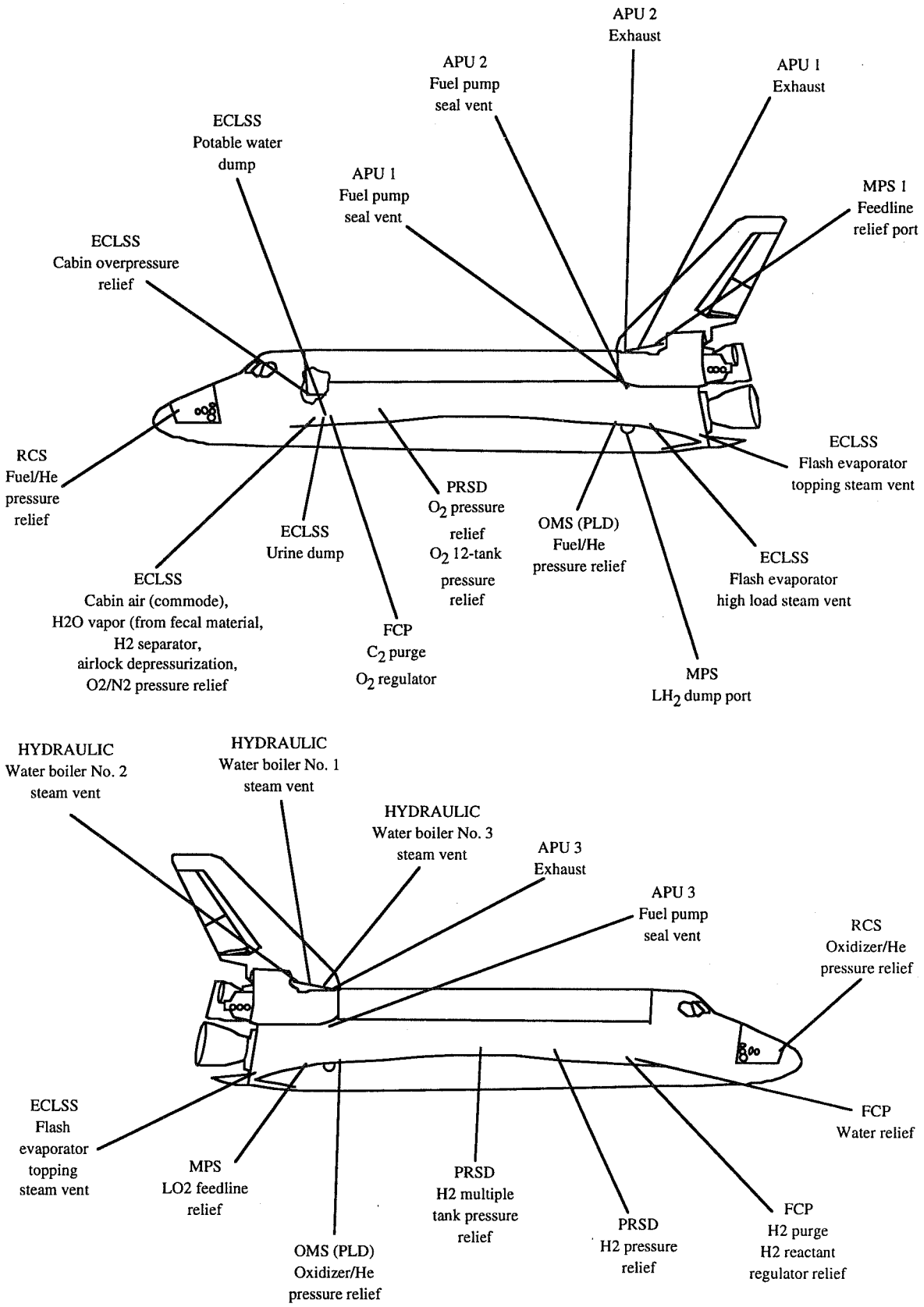

Figure 15. Orbiter venting locations [14].

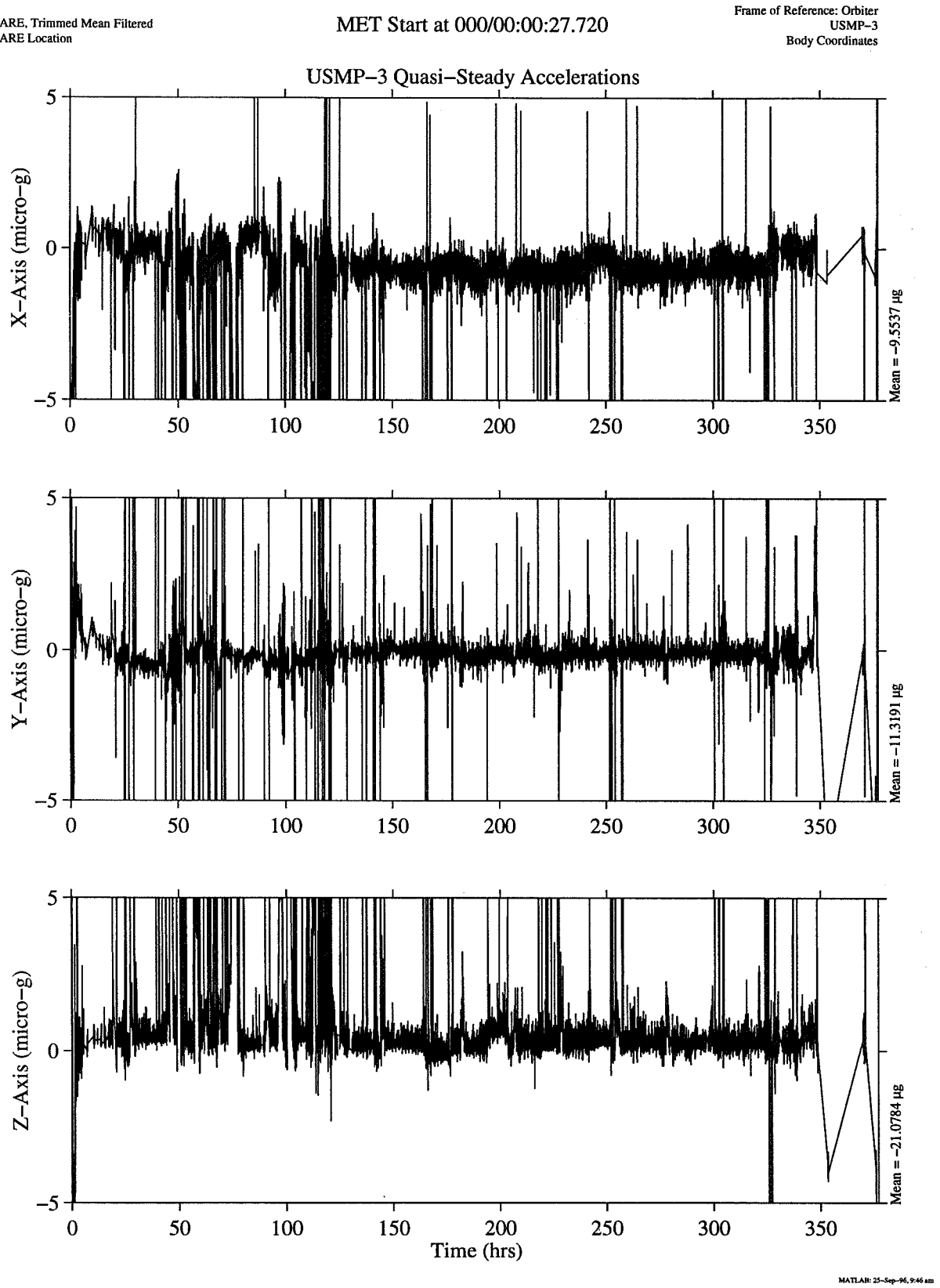

Figure 16. OARE data representing the microgravity environment at the OARE location during the STS-75 mission. MET start at 000/00:27.

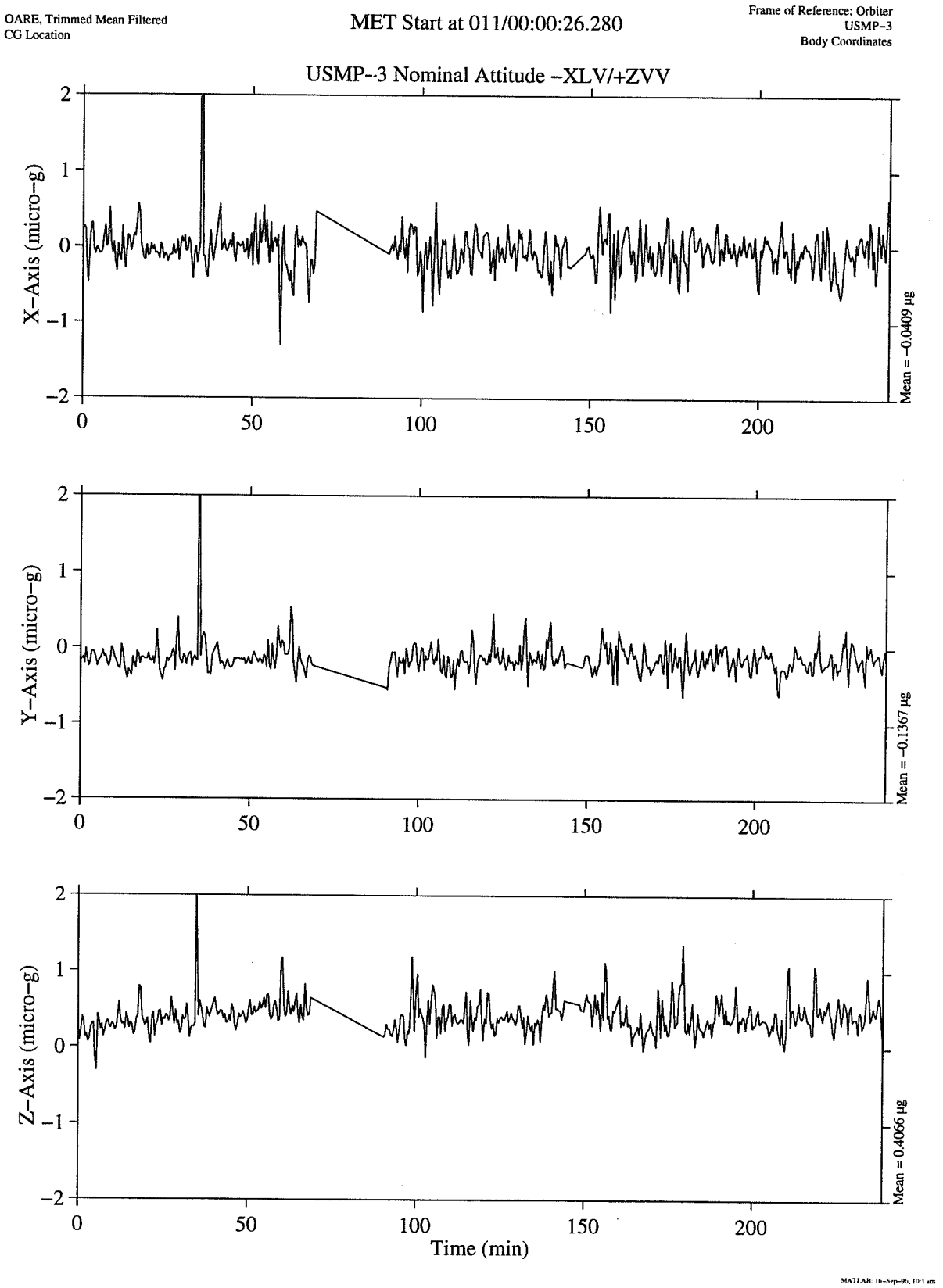

Figure 17. OARE data representing the microgravity environment at the OARE location while Columbia was in the nominal USMP-3 attitude. MET start at 011/00:00:26.

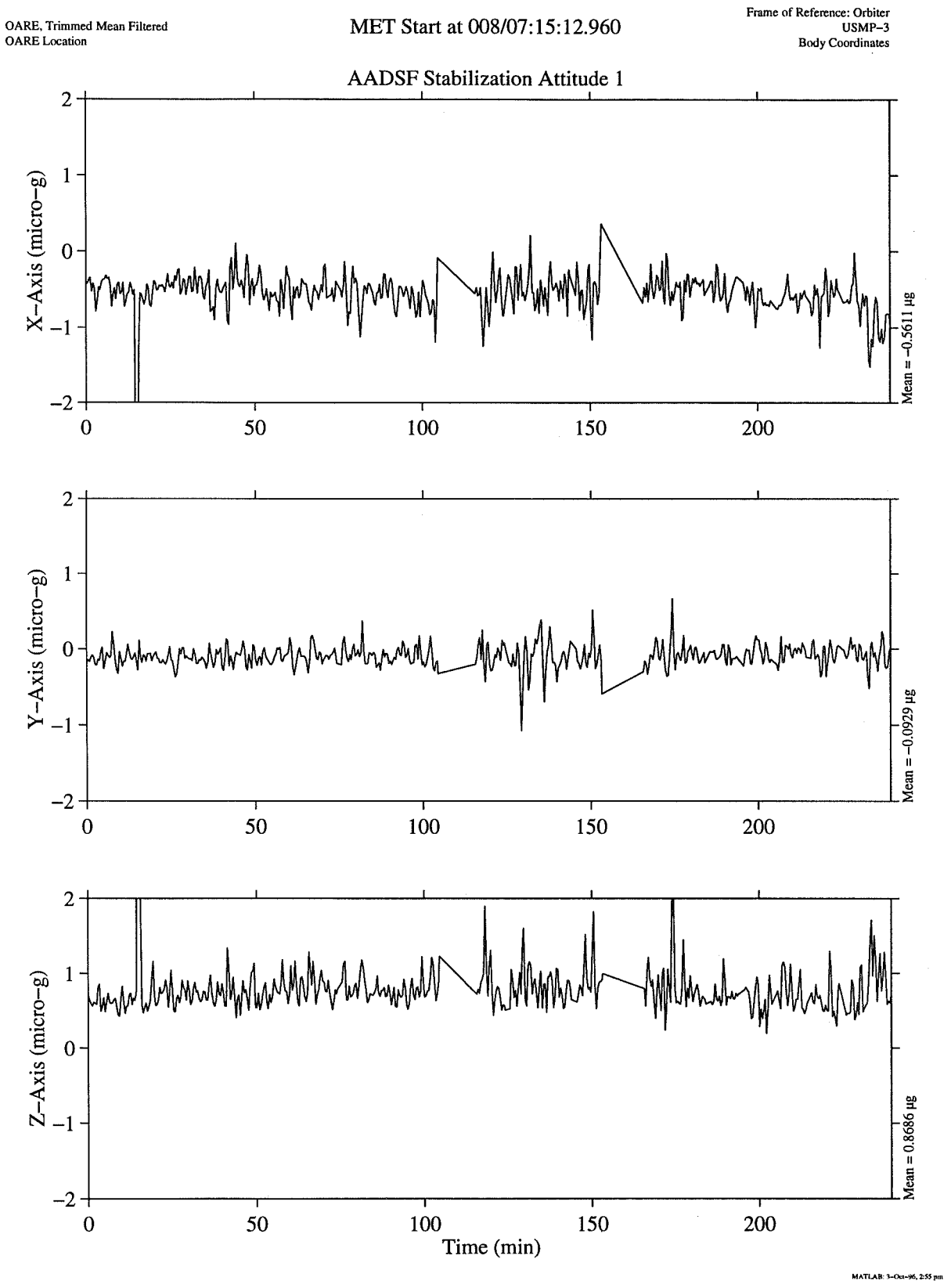

Figure 18. OARE data representing the microgravity environment at the OARE location while Columbia was in the AADSF 1 attitude. MET start at 008/07:15:13.

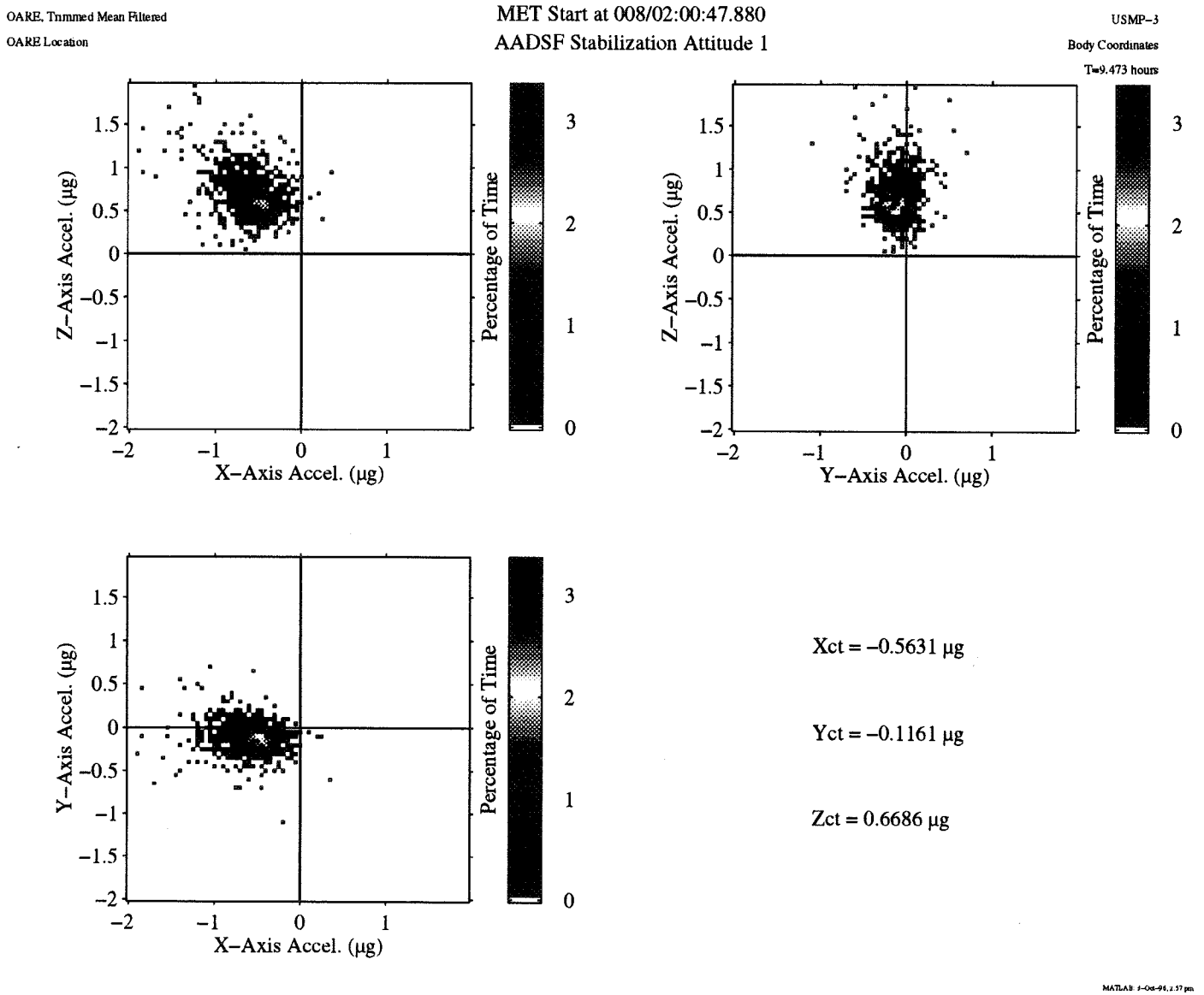

Figure 19. Three-dimensional projection of OARE data representing the microgravity environment at the OARE location while Columbia was in the AADSF 1 attitude. MET start at 008/02:00:47.

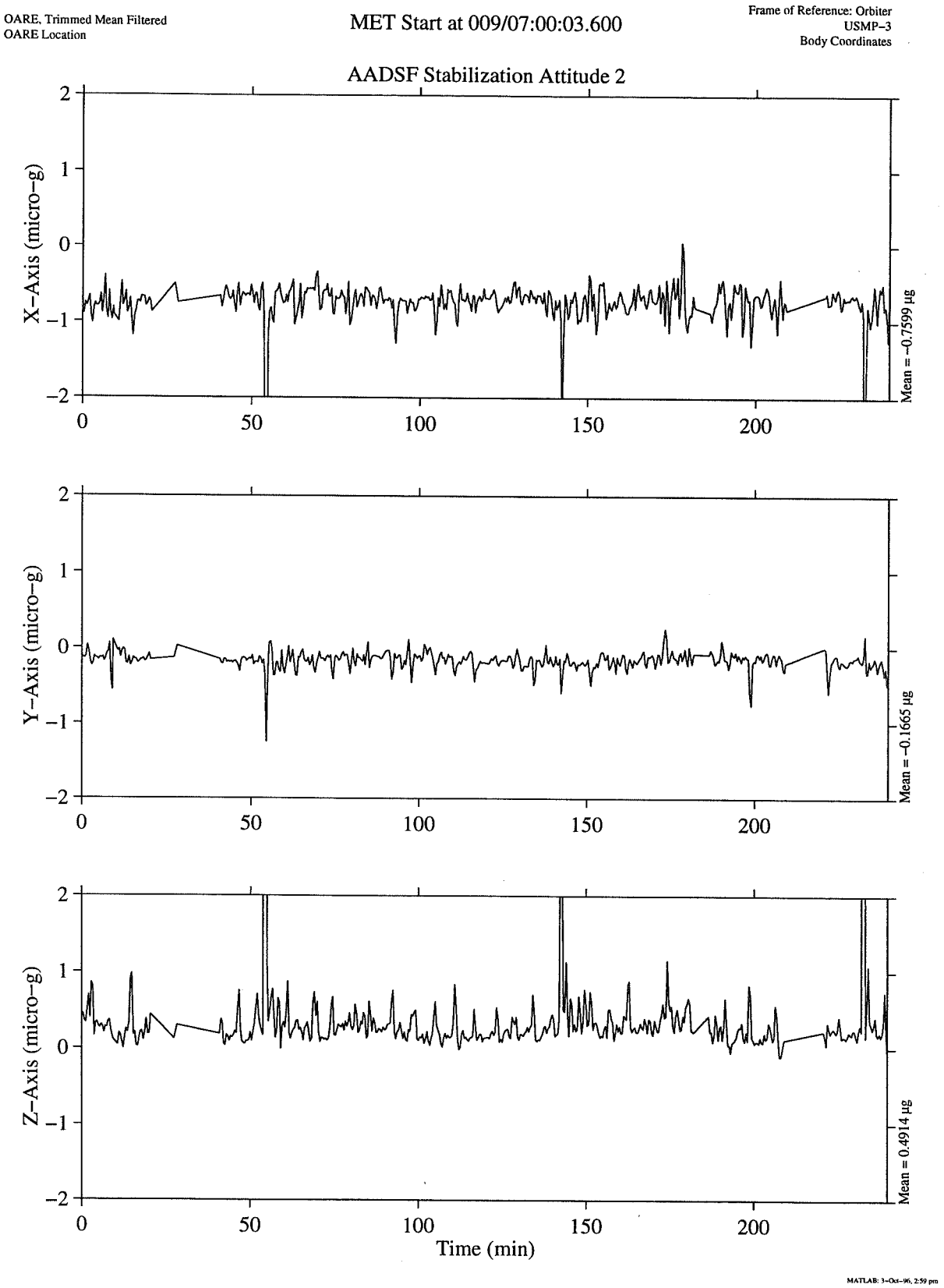

Figure 20. OARE data representing the microgravity environment at the OARE location while Columbia was in the AADSF 2 attitude. MET start at 009/07:00:03.

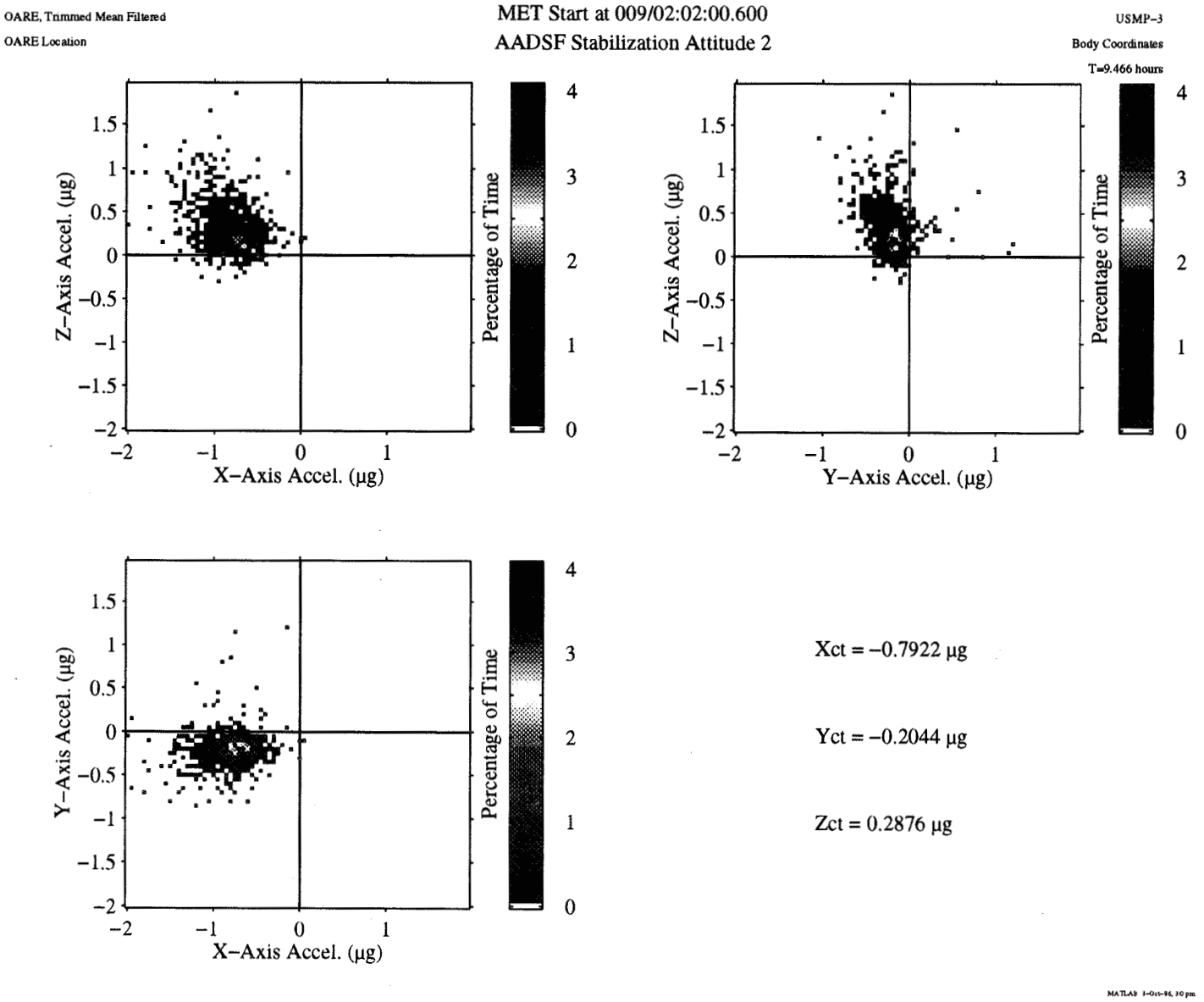

Figure 21. Three-dimensional projection of the OARE data representing the microgravity environment at the OARE location while Columbia was in the AADSF 2 attitude. MET start at 009/02:02:00.

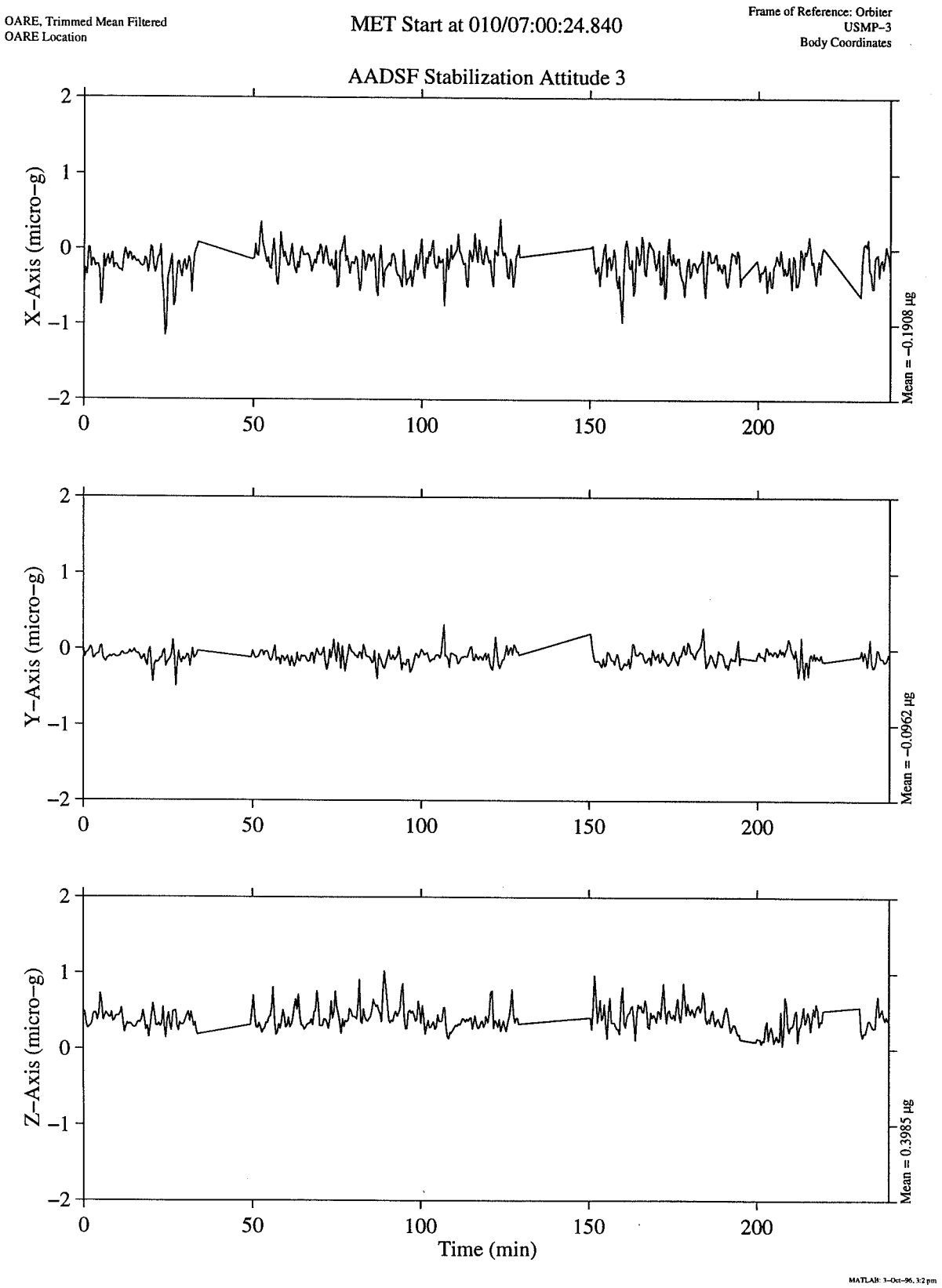

Figure 22. OARE data representing the microgravity environment at the OARE location while Columbia was in the AADSF 3 attitude. MET start at 010/07:00:24.

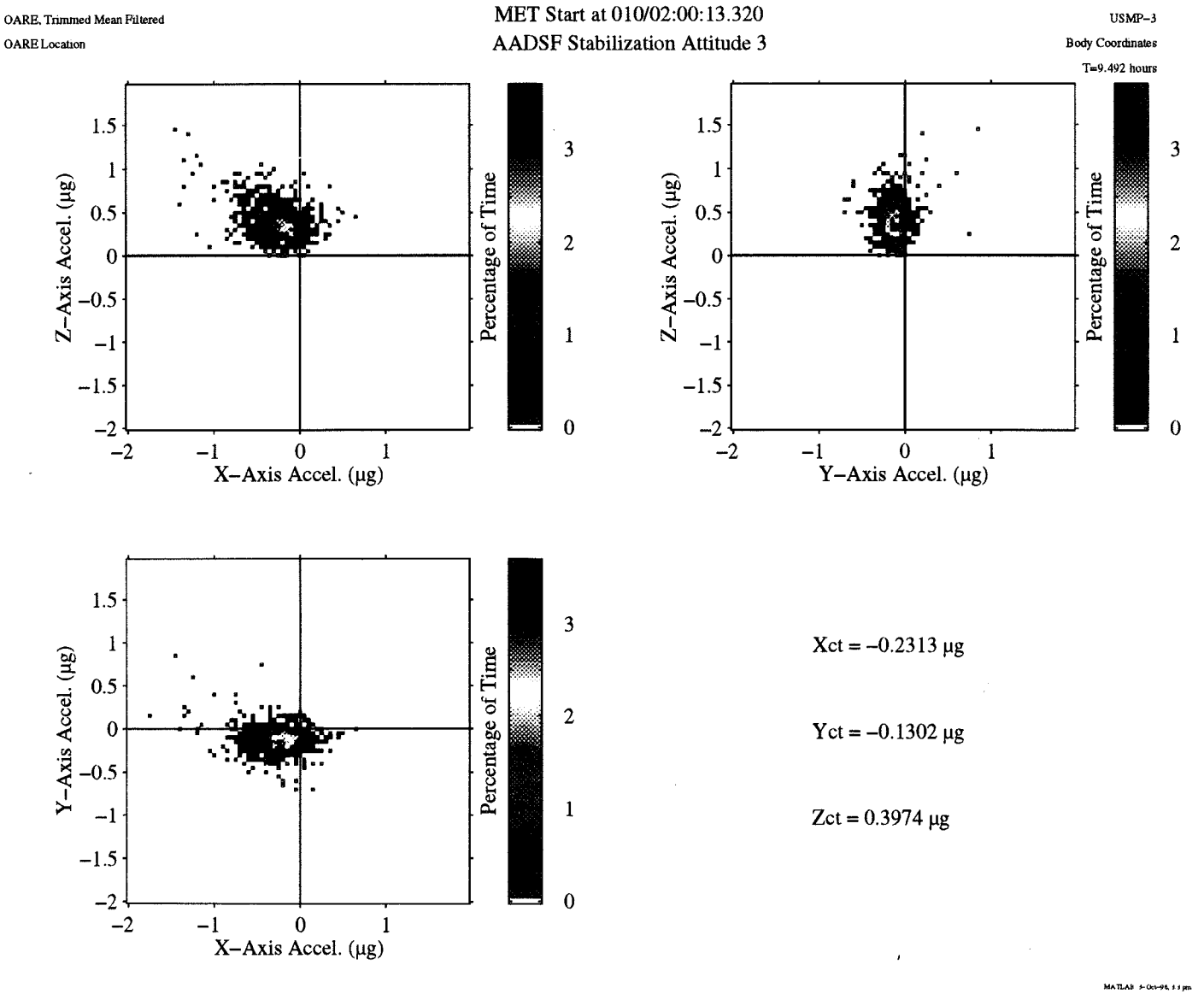

Figure 23. Three-dimensional projection of the OARE data representing the microgravity environment at the OARE location while Columbia was in the AADSF 3 attitude. MET start at 010/02:00:13.